Gas Distribution Around Galaxies in Cosmological Simulations

Mitali Damle

Universität Potsdam

Supervisors: Dr. Martin Sparre
Prof. Dr. Philipp Richter

Dissertation

zur Erlangung des akademischen Grades
doctor rerum naturalium (Dr. rer. nat.)
in der Wissenschaftsdisziplin Physik

Eingereicht an der Mathematisch-Naturwissenschaftlichen Fakultät
Institut für Physik und Astronomie
der Universität Potsdam

Potsdam, 18.04.2023

Published online on the
Publication Server of the University of Potsdam:
https://doi.org/10.25932/publishup-59054
https://nbn-resolving.org/urn:nbn:de:kobv:517-opus4-590543

Supervisors:

1. Dr. Martin Sparre
   Universität Potsdam & Leibniz Institut für Astrophysik, Germany

2. Prof. Dr. Philipp Richter
   Universität Potsdam, Germany

Referee 1: Prof. Dr. Philipp Richter
Universität Potsdam, Germany

Referee 2: Dr. Freeke van de Voort
Cardiff University, UK

Referee 3: Dr. Andrew Fox
Space Telescope Science Institute, USA

DECLARATION

I hereby declare that the contents of this thesis are based on my original work except for the citations which have been duly acknowledged. I also declare that this thesis has not been previously or concurrently submitted for any other degree at Universität Potsdam or any other university.

Mitali Damle
Universität Potsdam
Potsdam, 18.04.2023

In all chaos there is a cosmos, in all disorder a secret order.

– ***Carl Gustav Jung***, *Collected Works of C.G. Jung, Vol. 9, Part 1, Page 32, Para 66, "The Archetypes and The Collective Unconsciousness" (1959).*

Abstract

The evolution of a galaxy is pivotally governed by its pattern of star formation over a given period of time. The star formation rate at any given time is strongly dependent on the amount of cold gas available in the galaxy. Accretion of pristine gas from the Intergalactic medium (IGM) is thought to be one of the primary sources for star-forming gas. This gas first passes through the virial regions of the galaxy before reaching the Interstellar medium (ISM), the hub of star formation. On the other hand, owing to the evolutionary course of young and massive stars, energetic winds are ejected from the ISM to the virial regions of the galaxy. A bunch of interlinked, complex astrophysical processes, arising from the concurrent presence of both infalling as well as outbound gas, play out over a range of timescales in the halo region or the Circumgalactic medium (CGM) of a galaxy. It would not be incorrect to say that the CGM has a stronghold over the gas reserves of a galaxy and thus, plays a backhand, yet, rather pivotal role in shaping many galactic properties, some of which are also readily observable.

Observing the multi-phase CGM (via spectral-line ion measurements), however, remains a non-trivial effort even today. Low particle densities as well as the CGM's vast spatial extent, coupled with likely deviations from a spherical distribution, marr the possibility of obtaining complete, unbiased, high-quality spectral information tracing the full extent of the gaseous halo. This often incomplete information leads to multiple inferences about the CGM properties that give rise to multiple contradicting models. In this regard, computer simulations offer a neat solution towards testing and, subsequently, falsifying many of these existing CGM models. Thanks to their controlled environments, simulations are able to not only effortlessly transcend several orders of magnitude in time and space, but also get around many of the observational limitations and provide some unique views on many CGM properties. In this thesis, I focus on effectively using different computer simulations to understand the role of CGM in various astrophysical contexts, namely, the effect of Local Group (LG) environment, major merger events and satellite galaxies.

In Chapter 2, I discuss the approach used for modeling various phases of the simulated $z = 0$ LG CGM in HESTIA constrained simulations. Each of the three realizations contain a Milky Way (MW)–Andromeda (M31) galaxy pair, along with their corresponding sets of satellite galaxies, all embedded within the larger cosmological context. For characterizing the different temperature–density phases within the CGM, I model five tracer ions with CLOUDY ionization modeling. The cold and cool–ionized CGM (H I and Si III respectively) in HESTIA is very clumpy and distributed close to the galactic centers, while the

warm-hot and hot CGM (O VI, O VII and O VIII) is tenuous and volume-filling. On comparing the H I and Si III column densities for the simulated M31 with observational measurements from Project AMIGA survey and other low-z galaxies, I found that HESTIA galaxies produced less gas in the outer CGM, unlike observations. My carefully designed observational bias model subsequently revealed the possibility that some MW gas clouds might be incorrectly associated with the M31 CGM in observations, and hence, may be partly responsible for giving rise to the detected mismatch between simulated data and observations.

In Chapter 3, I present results from four zoom–in, major merger, gas–rich simulations and the subsequent role of the gas, originally situated in the CGM, in influencing some of the galactic observables. The progenitor parameters are selected such that the post–merger remnants are MW–mass galaxies. We generally see a very clear gas bridge joining the merging galaxies in case of multiple passage mergers while such a bridge is mostly absent when a direct collision occurs. On the basis of particle–to–galaxy distance computations and tracer particle analysis, I found that about 33–48 percent of the cold gas contributing to the merger–induced star formation in the bridge originated from the CGM regions.

In Chapter 4, I used a sample of 234 MW-mass, L^* galaxies from the TNG50 cosmological simulations, with an aim of characterizing the impact of their global satellite populations on the extended cold CGM properties of their host L^* halos. On the basis of halo mass and number of satellite galaxies ($N_{\rm sats}$), I categorized the sample into low and high mass bins, and subsequently into bottom, inter and top quartiles respectively. After confirming that satellites indeed influence the extended cold halo gas density profiles of the host galaxies, I investigated the effects of different satellite population parameters on the host halo cold CGMs. My analysis showed that there is hardly any cold gas associated with the satellite population of the lowest mass halos. The stellar mass of the most massive satellite ($M_{*\rm mms}$) impacted the cold gas in low mass bin halos the most, while $N_{\rm sats}$ (followed by $M_{*\rm mms}$) was the most influential factor for the high mass halos. In any case, how easily cold gas was stripped off the most massive satellite did not play much role. The number of massive (Stellar mass, $M_* > 10^8 M_\odot$) satellites as well as the $M_{*\rm mms}$ associated with a galaxy are two of the most crucial parameters determining how much cold gas ultimately finds its way from the satellites to the host halo. Low mass galaxies are found rather lacking on both these fronts unlike their high mass counterparts.

This work highlights some aspects of the complex gas physics that constitute the basic essence of a low-z CGM. My analysis proved the importance of a cosmological environment, local surroundings and merger history in defining some key observable properties of a galactic CGM. Furthermore, I found that different satellite properties were responsible for affecting the cold–dense CGM of the low and high-mass parent galaxies. Finally, the LG emerged as an exciting prospect for testing and pinning down several intricate details about the CGM.

Zusammenfassung

Die zeitliche Entwicklung der Sternenentstehung in einer Galaxie ist ein bestimmender Faktor für deren Entwicklung. Dabei ist die Sternenentstehungsrate stark abhängig von der in der Galaxie verfügbaren Menge an kaltem Gas. Die Akkretion von Gas aus dem intergalaktischen Medium (IGM) wird als eine der wichtigsten Quellen für das Gasreservoir angesehen, aus dem sich junge Sterne bilden. Bei diesem Prozess passiert das Gas zunächst die virialisierten äußeren Regionen der Milchstraße bevor es das Interstellare Medium (ISM) erreicht, der wichtigste Ort für die galaktische Sternentstehung. Im Gegensatz dazu tragen energiereiche Winde Gas zurück in die virialisierten Außenbereiche der Galaxie. Diese entstehen aufgrund der spezifischen Evolutionsprozesse von besonders jungen und massereichen Sternen in der galaktischen Scheibe. Durch das Zusammenspiel von einfallendem und das die Galaxie verlassendem Gas entsteht eine Vielzahl von astrophysikalischen Prozessen welche auf unterschiedlichsten Zeitskalen sowie in der Haloregion der Galaxie und dem zirkumgalaktischen Medium (CGM) von besonderer Wichtigkeit sind. Es kann behauptet werden, dass das CGM maßgeblich über die Gasreserven der Galaxie entscheidet und daher eine elementare Rolle in der Bestimmung vieler galaktischer Eigenschaften spielt von denen mache direkt beobachtbar sind.

Die Beobachtung des CGM in seinen vielen unterschiedlichen Gasphasen (durch die Spektrallinienanalyse mehrerer Ionenspezies) gestaltet sich auch heute noch als kompliziert. Die geringen Teilchendichten und die schiere Größe im Zusammenspiel mit Abweichungen von sphärischer Geometrie erschweren es, vollständige, repräsentative und hochqualitative spektrale Datensätze zu erhalten welche das volle Ausmaß das galaktischen Halos in Betracht ziehen. Diese unvollständige Informationslage führt oft zu unterschiedlichen Interpretationen der Eigenschaften des CGM welche sich in verschiedenen, sich mitunter widersprechenden Modellen, widerspiegeln. In diesem Zusammenhang bieten Computersimulationen eine elegante Lösung, um viele der CGM Modelle zu testen und schließlich zu verifizieren oder falsifizieren. Die kontrollierte Umgebung erlaubt es, das CGM mühelos auf unterschiedlichsten Größenordnungen in Raum und Zeit zu untersuchen aber auch observationstechnische Limitationen zu umgehen, um ein einzigartiges Bild der Eingenschaften des CGM zu erhalten. In dieser Arbeit fokussiere ich mich auf die effektive Nutzung von verschiedenen Computersimulationen, um die Rolle des CGM im verschiedenen astrophysikalischen Kontexten zu verstehen.

Im Kapitel 2 diskutiere ich den Ansatz, welcher für das Modellieren der unterschiedlichen Gasphasen des CGM in der Lokalen Gruppe (LG) bei $z = 0$ in den "constrained" Simulationen des HESTIA Projekts angewandt worden

ist. Jede der drei Realisierungen enthält ein Milchstraßen-M31 Paar zusammen ihren Satellitengalaxien. Alle zusammen sind dabei eingebettet in den größeren kosmologischen Kontext. Für die Charakterisierung der unterschiedlichen Temperatur-Dichte Phasen im CGM habe ich eine Gruppe von fünf Ionen gewählt welche das Vorhandensein der Phasen anzeigen. Für jede der Zellen in der Simulation habe ich das CLOUDY post-processing Toolkit angewandt und die entsprechenden Anteile der Ionen im Gas bestimmt.

Das kalte und kühle CGM (entsprechend charakterisiert durch H I beziehungsweise Si III) zeigt sich sehr klumpig und ist nahe an den galaktischen Zentren verteilt während das warm-heiße CGM (charakterisiert durch O VI, O VII, O VIII) dünn verteilt und volumenfüllend ist. Durch den Vergleich der Säulendichten für H I und Si III aus den Simulationen zusammen mit Beobachtungsdaten der AMIGA Durchmusterung und Studien über andere Galaxien mit geringer Rotverschiebung habe ich herausgefunden, dass HESTIA weniger Gas in den Außenbereichen des CGM produziert als es die Beobachtungsdaten suggerieren. Mein sorgfältig entworfenes Modell für den Beobachtungsbias hat die Möglichkeit aufgezeigt, dass in Beobachtungen mache der Milchstraße zugehörigen Gaswolken als M31-zugehörig missinterpretiert werden könnten.

Im Kapitel 3 präsentiere ich Ergebnisse von vier zoom-in, major merger und gasreichen Simulationen unter dem Gesichtspunkt der Rolle des Gases, welches ursprünglich dem CGM zugehörig ist und dessen Einfluss auf einige galaktische Observablen. Die initialen Parameter sind so ausgewählt, dass die den Verschmelzungen entspringenden Galaxien eine vergleichbare Masse wie die der Milchstraße besitzen. Im Allgemeinen sehen wir eine klare Brücke von Gas im Falle von Verschmelzungen welche mehrere separate Annäherungen durchlebten. Im Vergleich dazu fehlt diese Brücke in den Fällen einer direkten Kollision. Auf der Grundlage von particle-to-galaxy Distanz Berechnungen und tracer particle Analysen habe ich herausgefunden, dass rund 33–48 Prozent des kalten Gases aus dem CGM zur Sternenentstehung, welche in Folge der Kollision erfolgt, beiträgt.

In Kapitel 4 habe ich eine Stichprobe aus 234 L^* Galaxien, jeweils mit der Masse der Milchstraße, aus der Kosmologischen Simulation TNG50 genutzt, um den Einfluss der globalen Begleitgalaxienpopulation auf die Eigenschaften des ausgedehnten und kalten CGM der Zentralhalos zu bestimmen. Auf der Basis der Halomasse habe ich die Galaxienhalos in Bins niedriger und hoher Masse eingeteilt. Dabei ist jeder dieser Bins wiederum unterteilt in das untere, mittlere und obere Quartil in Abhängigkeit der Anzahl der Begleitgalaxien ($N_{\rm sats}$) im jeweiligen Halo. Nach der Bestätigung dass Begleitgalaxien in der Tat die Gasdichteprofile ihrer Zentralgalaxie beeinflussen, habe ich die Effekte von verschiedenen Populationsparametern der Begleitgalaxien auf die CGM der jeweiligen Zentralgalaxien untersucht. Meine Analyse zeigt, dass nahezu kein kaltes Gas mit der Population der Satellitengalaxien in den Halos mit der geringsten Masse assoziiert ist. Das Gas der Halos im masseärmeren Bin ist primär beeinflusst durch die stellare Masse der massereichsten Satellitengalaxie ($M_{*\rm mms}$), wohingegen $N_{\rm sats}$ (gefolgt von $M_{*\rm mms}$) die Masse des kalten Gases der massereichsten Zentralhalos am signifikantesten beeinflusst hat. Un-

abhängig davon schien es nicht von Relevanz zu sein wie einfach das Gas von der massereichsten Satellitengalaxie abgetragen werden kann. Die Anzahl der der massereichen ($M_* > 10^8 M_\odot$) Satellitengalaxien, sowie die mit einer Galaxie assoziierten $M_{*\mathrm{mms}}$ zeigten sich als zwei der Wichtigsten Parameter um zu verstehen wie das kalte Gas von den Satellitengalaxien in den Halo transferiert wird. Im Falle von masseärmeren Galaxien scheinen sich diese in beiden Aspekten von ihren massereichen Gegenstücken zu unterscheiden und zeigen keine besondere Abhängingkeit.

Diese Arbeit behandelt einige Aspekte der komplexem physikalischen Aspekte von astrophysikalischen Gasen welche die Basis für die Untersuchung des CGM bei geringen Rotverschiebungen bildet. Meine Analyse zeigt die Wichtigkeit des Kosmologischen Umfelds, die lokale Umgebung, sowie die Verschmelzungshistorie indem sie fundamentale Observablen des galaktischen CGM beeinflussen. Des weiteren habe ich herausgefunden, dass verschiedene Satelliteneigenschaften für die Beeinflussung des kalt–dichten CGM der masseärmeren und massereichen Muttergalaxien verantwortlich waren. Schließlich stellte sich heraus, dass die LG eine vielversprechendes Beispiel zum Testen und Festhalten mehrerer komplizierter Details über das CGM darstellt.

Layman Summary

Our Milky Way (MW) galaxy, like several others in our Universe, forms new stars regularly. Cold, dense gas is the primary fuel necessary for any galaxy to sustain its star formation. Thanks to the dominant gravitational potential of a galaxy, fresh cold gas is constantly being pulled (or accreted) and fed to its star formation hub (the Interstellar medium or ISM) from faraway, low–density regions lying between two galaxies, aka the Intergalactic medium (IGM). The ISM is a region that lies very close to the galaxy but the IGM only begins outside the far–reaching galactic gravitational influence i.e. very far away from the galaxy. There exists a vast region of galactic halo between the ISM and the IGM that is associated with the galaxy.

Infalling gas from the IGM has to travel great distances through the ever increasing gravitational potential of the galaxy as it keeps falling inward, before eventually being used for star formation. On the other hand, the stars being formed by the galaxy are of varying masses. Young, hot stars, in the early stages of their lives, expel mass and metals in the form of stellar winds. A small fraction of the total stellar population of the galaxy are really massive stars that explode as supernovae at the end of their lives and in process, send out metal–enriched shockwaves of extreme energy and momentum. Both stellar winds and supernovae explosions are launched from stars sitting in the ISM to the galactic halo that begins beyond the ISM. Some of this outflowing gas is thought to escape the ISM forever and become a part of the galactic halo while some gas may eventually rain back on the galaxy after a certain timescale.

Thus, it is intuitive to think that both the incoming gas from the IGM as well as the outbound gas from the ISM has to encounter the galactic halo region, aka the Circumgalactic medium (CGM), at some point before meeting their respective fates. Despite the continuous passage of inflowing and outflowing gas, particle densities in the CGM are far lesser than those in the ISM, although they are still appreciably higher than that in the IGM. While star formation takes a clear backseat, the importance of various other astrophysical processes, like cold gas accretion, galactic outflows, turbulence mechanisms, influence of satellite galaxies, etc. simultaneously gains traction in the CGM. The combined effect of these processes ends up regulating the flow of the gas in the CGM and makes it multi-phase, meaning, pockets of different gas densities and temperatures co–exist within the same CGM environment. This gas regulation, subsequently, has a profound bearing on the star formation rates and overall evolution of that galaxy. Thus, an in-depth knowledge about the CGM is necessary for a wholesome understanding of the complex galaxy evolution process.

However, considering the fact that the number density of gas particles (i.e. number of gas particles per cubic unit) in the CGM is quite less, observing this part of the galaxy has its fair share of problems. To begin with, high–quality data is sparse and a majority of the available data contains substantial noise which cannot always be gotten rid off. Secondly, it is very difficult to observe far–flung parts of a CGM where particle densities drop even further. Add to that, the threat of data contamination from foreground objects like the Milky Way disc, ISM, etc., sparse data at higher redshifts, limiting nature of existing observational techniques, and we have a tricky problem at hand. Some of the above issues can be minimized with the help of computer simulations. It is now possible to simulate patches of the real Universe within a computer such that one can actually model the evolution of any astrophysical entity (like the galactic CGM) and smartly get around many of the above highlighted problems.

In this thesis, using computer simulations as my primary tool, I aim to answer three distinct questions– How does the CGM of our Local Group (LG) of galaxies (comprising of our Milky Way, neighbouring Andromeda (M31) galaxy, along with a bunch of smaller satellite galaxies) looks like? When two similarly massive galaxies are in the process of merging, how does the gas in the CGM impact the post–merger properties of the system? For a galaxy having its share of surrounding satellite galaxies, how do the properties of the entire satellite galaxy population affect the cold CGM gas phase of the parent galaxy?

It was reassuring to successfully reproduce the different observed gas phases (ranging from cold, dense all the way to hot, less dense gas) of the CGM using the HESTIA simulations of the Local Group of galaxies. One of the headlining results, arising from a mismatch between the HESTIA data and observations, showed that our existing observations for the outer parts of the CGMs of galaxies might be slightly overestimated or inflated due to a misidentification of some MW CGM gas clouds situated between the target galaxy and our telescopes. In other words, this work demonstrated that the simulated Local Group can be used to spot MW CGM gas clouds, that lie in the foreground of our observational field–of–view, with remarkable accuracy. This will ultimately help us interpret the observations in a more unbiased way, thereby increasing our overall knowledge about the low–redshift CGM.

Galaxy merger forms an important part in the evolution process of a galaxy. When two similarly massive galaxies merge, a lot of phenomenological changes happen in the system. Owing to the rapid changes in the separation between the merging galaxies, extreme alterations in the energy, pressure and thermal balance occur. In many cases, a short–lived bridge comprising of stars and gas forms between the galaxies. The cold gas that is compressed due to the merger event increases the star formation rate, so–called merger–induced star formation. My analysis proved that a substantial percentage of this increased star formation is caused due to the gas that was originally located out in the CGM but got driven to the central regions as a result of the galaxy merger.

Every galaxy has some smaller satellite galaxies around it. Each satellite has some cold gas reserve of its own that is likely to be affected by the galactic

potential. In the process, it is also likely that the parent galaxy's CGM (especially the cold gas phase) *feels* the presence of the satellites. I found that the low mass galaxies' cold CGM is affected to a much lesser extent by its satellite population as compared to more massive galaxies. One of the main reasons for this is the fact that low mass galaxies simply do not contain enough massive satellite galaxies that can give a portion of their cold gas away.

Acknowledgements

Working on so many exciting projects that finally culminated into this thesis has been an exhilarating journey in itself. There is a long list of people who have, in their own way, helped me during this journey and enriched both the professional as well as non-professional aspects of my life. This section, therefore, deserves to be dedicated to thanking all those wonderful people.

I cannot thank Martin enough for guiding me all through my PhD years. The best aspect of his supervision has been his unique ability to gauge when he needs to switch from a hands-on approach to a more autonomous one from time-to-time. He has also been extremely instrumental in my progress with programming in Python and my familiarity with simulation data over the years. During the numerous science discussions we have had, he always created a receptive environment where I could confidently put forward my own thoughts and ideas. Needless to say, it has also been wonderful to pick his brains on various topics in Astronomy as well as academia, in general. For all of the above as well as being a gem of a person, thank you Martin!

Equally instrumental in my PhD journey has been Philipp! One of the hallmarks during our meetings has been the sheer number of ideas that he used to put forth with absolute enthusiasm. I have also hugely admired the simplicity, elegance and variance with which he puts some really complex concepts and problems into comprehensible sentences; I certainly aim to develop this ability to some degree in the coming years. Above all, he has always found time, from his super-packed schedule, for not just the science but also the administrative aspects of my work. A special mention also needs to be made (to both him and Martin) for always being so encouraging with attending conferences and making institute visits. Thank you Philipp.

It has been a pleasure working with my TNG project collaborators, Stephanie and Drummond, for helping me shape up this project and providing helpful insights and comments all through. Thanks Stephanie for hosting me at the CCA last year! Thank you Andrew and Freeke for agreeing to act as referees and for carefully reading my thesis. It was great meeting you at the STScI in-person last year, Andrew. I hope to collaborate with both you and Freeke some time in future. Sincere thanks to Stephan and Lida for agreeing to serve as committee members for my doctoral thesis. Heartfelt appreciation also goes out to all my co-author collaborators for their contributions.

For all the super-insightful and fun conversations during our weekly group meetings as well as regular lunch outings, I would like to thank Gabor, Martin (Wendt), Moritz, Florian, Patricia and Rainer. Thank you so much Florian for providing me with the German translation of my abstract! For all the good times during the movie nights, biergarten outings, viewing sessions with the telescope, numerous cake parties in the coffee room, etc., I sincerely thank all my colleagues in the Astronomy department. Thanks Kirill for sharing your academia experiences during my early years and also for providing me with the thesis template.

A big thank you, Andrea for literally wading me through tons of documentation procedures all through these years! I have lost count of the number of occasions when you have reminded/helped me out with some really tricky paperwork. Also, the genuine considerateness you constantly showed with regards to my work, living in Germany as a foreigner or even just inquiring about my day has been absolutely endearing.

I have been extremely fortunate to have some really good friends by my side, who ensured that I could call this country a home-away-from-home. For our shared craze for cats, I mew (thank) you Anjali. For all the super-"deep" as well as dumb conversations, thank you Deep. I will absolutely miss those random Pommes (fries) trips with you guys! Adnan, thanks for being my virtual sounding board at times when I needed to vent out about something and also for encouraging me always. Sweta, it feels really nice when I look back at how our friendship has developed over the past few years– thanks for being there for me when it really mattered. Sharlene, Carissa and Nisha– I hope we can all catch up real soon and reminisce our Xavier's times. Sharlene, thanks for showing me around Washington DC last summer, I had a great time. Vrunda, I cannot wait to replicate, in-person, all those smiles and long, therapeutic virtual conversations. Thank you for being a part of my life!

Finally, the constant faith, unconditional love and support from my family cannot be undermined. Mom (Manjiri), you are my rockstar and I absolutely admire your silent strength and empathy. Dad (Makarand), I wish you were present for my defense. I miss you. My elder sister, Madhu– we are such opposites and that's why there are so many qualities in you that I adore and look up to! Thanks for always looking out for me! Much love to my nephew, Yuvraj– not being able to see you grow up saddens me; hopefully I can make it up by making a longer visit this time. Charu, my brother-in-law, I miss our fun as well as thoughtful discussions over beer– thank you for being the elder brother that I never had. Lastly, my pet cat, Rancho, whom I miss very dearly– I hope I can see you soon.

To all those who have, knowingly or unknowingly, helped me during this journey– sincere apologies for having missed out on your mentions and a big thank you!

Contents

List of Figures

List of Tables

List of Abbreviations

AGB	Asymptotic Giant Branch.
AGN	Active Galactic Nuclei.
ALMA	Atacama Large Millimeter Array.
AMIGA	Absorption Maps In the Gas of Andromeda.
AMR	Adaptive Mesh Refinement.
BH	Black Hole.
BQ	Bottom Quartile.
CDM	Cold Dark Matter.
CGM	Circum Galactic Medium.
CI	Collisional Ionization.
CIE	Collisional Ionization Equilibrium.
CLUES	Constrained Local UniversE Simulations.
CMB	Cosmic Microwave Background.
COS	Cosmic Origins Spectrograph.
CR	Cosmic Rays.
DLA	Damped Lyman Alpha.
DM	Dark Matter.
ELG	Emission Line Galaxy.
EW	Equivalent Width.
FoF	Friends–of–Friends.
FRB	Fast Radio Burst.
FUSE	Far Ultraviolet Spectroscopic Explorer.
GRB	Gamma Ray Burst.
HESTIA	High–resolution Environmental Simulations of The Immediate Area.
HMB	High Mass Bin.
HST	Hubble Space Telescope.
HVC	High Velocity Cloud.
IC	Initial Conditions.

ICM	Intra Cluster medium.
IGM	Inter Galactic Medium.
IGrM	Intra Group medium.
IllustrisTNG	Illustris The Next Generation.
IQ	Inter Quartile.
ISM	Inter Stellar Medium.
IVC	Intermediate Velocity Cloud.
JWST	James Webb Space Telescope.
K–S test	Kolmogorov–Smirnov test.
KBSS	Keck Baryonic Structure Survey.
KCWI	Keck Cosmic Web Imager.
LBT	Large Binocular Telescope.
LG	Local Group.
LLS	Lyman Limit System.
LMB	Low Mass Bin.
LMC	Large Magellanic Cloud.
LOS	Line–of–Sight.
LRG	Luminous Red Galaxy.
LU	Local Universe.
LVC	Low Velocity Cloud.
M31	Andromeda galaxy.
MAD	Mean Absolute Deviation.
MC	Monte Carlo.
MHD	Magneto–Hydro–Dynamics.
MMB	Middle Mass Bin.
MOSFIRE	Multi–Object Spectrometer For Infra–Red Exploration.
MS	Magellanic Stream.
MUSE	Multi Unit Spectroscopic Explorer.
MW	Milky Way galaxy.
P3M	Particle–Particle plus Particle–Mesh.
PI	Photo Ionization.
PIE	Photo Ionization Equilibrium.
PM	Particle Mesh.
QSO	Quasi Stellar Objects.
ROI	Region of Interest.
S/N	Signal–to–Noise.
SFR	Star Formation Rate.
SMBH	Supermassive Black Hole.
SMC	Small Magellanic Cloud.
SNe	Supernovae.

SPH	Smoothed Particle Hydrodynamics.
STIS	Space Telescope Imaging Spectrograph.
TQ	Top Quartile.
UCHVC	Ultra Compact High Velocity Cloud.
UDG	Ultra Diffuse Galaxy.
VLT	Very Large Telescope.

Chapter 1

Introduction

Under the broad umbrella of galaxy formation and evolution within the Lambda-Cold Dark Matter (ΛCDM) model, this thesis stands mainly on two pillars– *Numerical simulations* (*N*-body and cosmological, magnetohydrodynamical i.e. MHD simulations) as a method and the CGM as the subject. We begin first by providing a broad overview of the current paradigm of the evolution of the universe and its galaxies (§1.1). This will be followed by a concise summary on the advancements in the field of numerical simulations since their inception in an extremely rudimentary *N*-body form all the way up to the current state–of–the–art, much advanced and realistic, fully cosmological–MHD simulations (§1.2). Later we will discuss about the importance of CGM studies and our current knowledge about it in the broader context of galaxy evolution, highlighting different approaches, along their strengths as well as limitations (§1.3). Finally, we will round off this chapter with a brief outlook (§1.4).

1.1 Cosmology and Galaxy Formation

The evolution of our Universe is a rather complex, non-trivial process that spans orders of magnitude in both space as well as time, driven primarily (barring the extremely early inflation–epochs) by non–linear gravitational forces. Galaxies are the building blocks of the Universe. However, they were thought of more like island universes when they were first observed in the early 1700s (Kant, 1755). The extragalactic origin of galaxies (known back then as *nebulae*) only came to the fore following the distance estimates to Cepheid variable stars in other galaxies by Edwin Hubble (Hubble, 1929). Back then, the field of galaxy evolution existed primarily as a means to better explore the field of cosmology. However, since then, galaxy formation and evolution studies have grown immensely as a standalone field in its own right.

A bottom-up hierarchical growth is the most favored structure formation pathway in the ΛCDM model (Davis et al., 1985). This means that tiny density fluctuations in space, under the influence of gravitational forces, resulted in larger and larger astrophysical structures such as proto–stars, proto–galaxies, stars, galaxies, galaxy groups, clusters, etc. Post the extremely early, Planck-epoch (where our currently established laws of Physics may not hold), the Universe first underwent a neutrino decoupling phase (that gave rise to a corresponding cosmic neutrino background) at 1 second, wherein the neutrinos stopped interacting with other types of matter and started streaming freely throughout the Universe (Bernstein et al., 1989). When the Universe was aged about 370,000 years, photons decoupled (giving rise to the still observed cosmic microwave background or CMB radiation), finishing the recombination process that resulted in neutral hydrogen atoms for the first time (Peebles, 1968; Zel'dovich et al., 1969). Owing to the

expansion of the Universe, the newly decoupled photons could now stream to longer distances without being absorbed or deflected, thus making the Universe transparent.

Post this era, however, the collapsing clouds of hydrogen needed some time before they could form the first stars and galaxies. In the meanwhile, the photons were continuously losing energy as they streamed through the space and were soon shifted into non–visible wavelengths. This gave rise to the so–called Dark Ages of the Universe where no new sources of light emerged until the Universe was about 1 billion years old. Subsequently, the first stars were formed– these are believed to have enriched the Universe with all the heavy elements that we observe today (Barkana & Loeb, 2001). Visible matter (or baryons) followed the localized dark matter overdensities (or halos) to form the first galaxies. Early galaxies, mostly spirals and irregulars, matured over time to give rise to present–day ellipticals (Bouwens et al., 2012). Larger and larger structures in the form of galaxy groups, clusters and superclusters have since then been assembling. At the largest scales, a filamentary pattern, occasionally interjected by sites of huge density contrasts, emerges– this is also known as the cosmic web (Klypin & Shandarin, 1983; Springel et al., 2005c; Heitmann et al., 2010). Galaxies along the filaments are constantly being accreted onto the dense areas (nodes), while the remaining regions (voids) in the cosmic web are largely devoid of that many galaxies.

With this brief summary on the history of the Universe, we shall move on to discussing about the technique of numerical simulations and their usage in astrophysics.

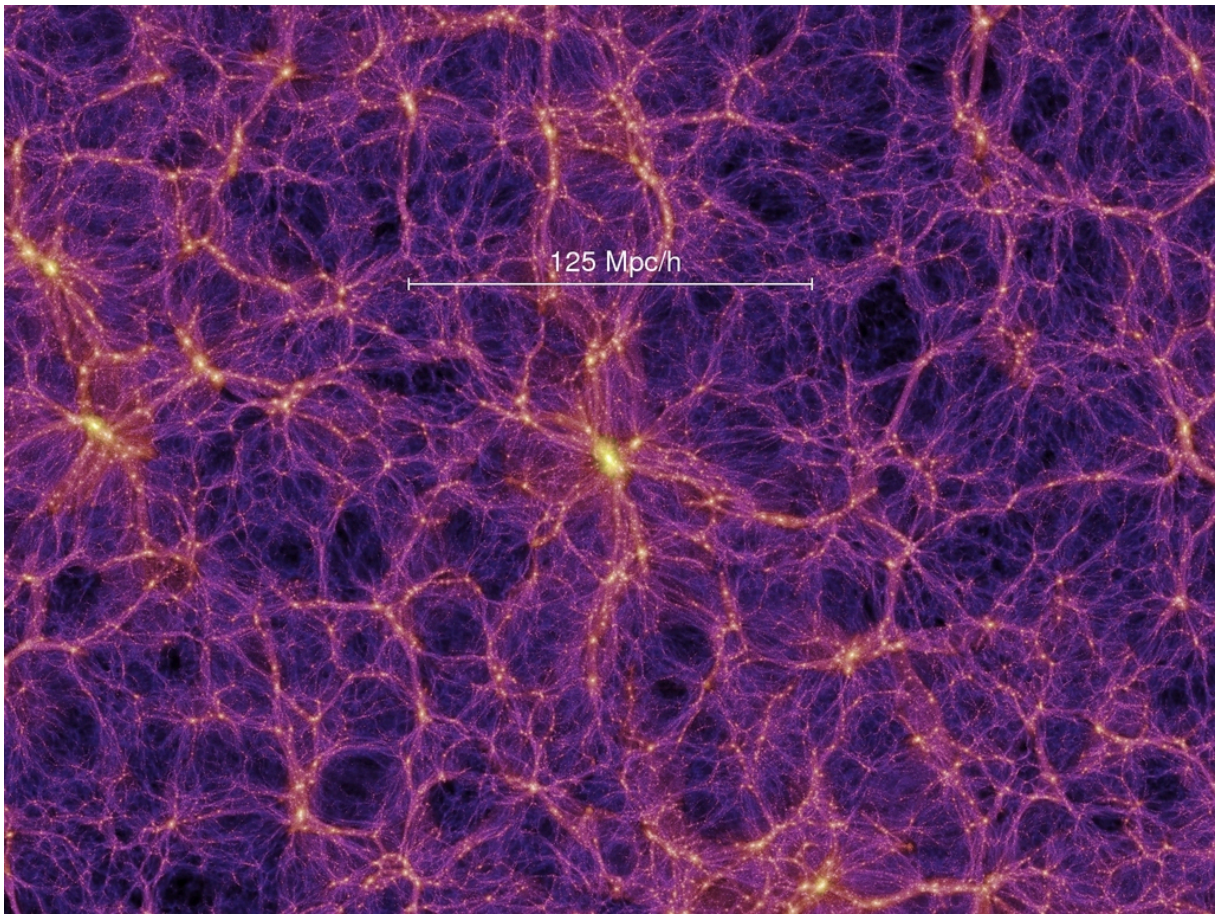

Figure 1.1: Slices of the large scale dark matter distribution from the Millennium cosmological simulations. Such simulations have proven to be extremely useful in reproducing and then investigating the large-scale density field and matter distribution in the Universe. (Credits: Simulations of the formation, evolution and clustering of galaxies and quasars; Springel et al. 2005c)

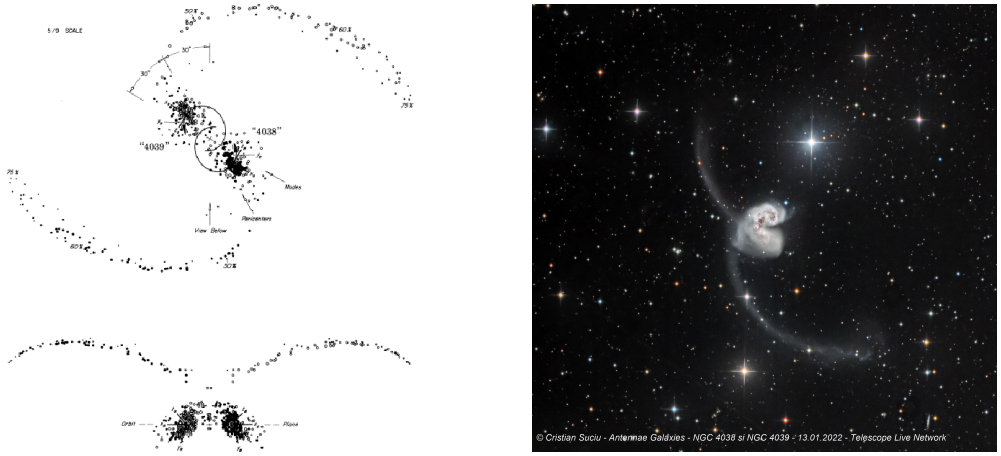

Figure 1.2: *Left:* Replication of bridges and tail–like features from a galaxy merger in a test-particle simulation from Toomre & Toomre 1972. *Right:* Observations of the interacting galaxy pair NGC 4038 and NGC 4039 aka Antennae galaxies (Credit: Cristian Suciu).

1.2 Numerical simulations

Understanding a multi–scale, multi–physics problem such as the process of galaxy formation and evolution requires a setup wherein different models and theories, inspired from a large range of observations, can be constantly tested and falsified– computer simulations fulfil these requirements perfectly! The basic idea of a numerical simulation (see an example from a simulation in Fig. 1.1) is to set up an ecosystem of particles and track their dynamical evolution over a period of time. First rudimentary test–particle simulations were run by Toomre & Toomre 1972, where they successfully reproduced bridges and elongated, tail–like features observed in the Antennae galaxies (see Fig. 1.2). Thereby, they found that one way to form present–day elliptical galaxies could be a merger between two spiral galaxies. They employed the restricted 3-body computations (like those previously used in Pfleiderer & Siedentopf 1961 and Pfleiderer 1963), wherein each of the two progenitor galaxies was represented by a total of 120 non–interacting particles whose dynamical evolution was temporally tracked. In the following subsections, I will breakdown the structural components of a computer simulation, namely the cosmological framework (§1.2.1.1), dark matter (§1.2.1.2) and baryonic matter (§1.2.1.3) and describe briefly the methodology used for modeling each of them.

1.2.1 The Assembly

1.2.1.1 Cosmological framework

The floor of any modern computer simulation, in general, is set up by the chosen cosmological model. Following this, either only gravitational interactions or both gravitational as well as hydrodynamical interactions are solved for within the simulation volume. The *cosmological framework*, dictated by fundamental parameters from observations, i.e. the adopted cosmological model, and a set of initial conditions, describing the Gaussian perturbations that are applied on top of a homogeneous expanding space–time metric, form the framework within which the corresponding computer simulation runs (Vogelsberger et al., 2020). Thereafter, a number of integral components must be put into action for incorporating a range of physical processes, either purely gravitational or gravitational plus (magneto–)hydrodynamical, that ultimately make the simulation as close to the observed reality as possible. If the cosmological framework

is the skeleton of a simulation, then surely the processes employed to simulate dark matter and baryons form its flesh. ΛCDM is the most widely adopted cosmological model as of today; collisionless cold dark matter and a cosmological constant Λ-based dark energy, which together account for $\simeq 95\%$ of our geometrically flat Universe's total energy density, are the cornerstones of this model (Planck Collaboration et al., 2016).

1.2.1.2 Simulating dark matter

Simulating dark matter, which forms the basis upon which galaxies form, is arguably one of the most fundamental steps in any simulation. Dark matter (in general, assumed to be *cold*, though other variants are also hypothesized) can be safely assumed to be collision–less on cosmological scales and can interact only gravitationally with fellow particles. Under the influence of the underlying collective gravitational potential, described by the Poisson equation (see Eq. 1.1), the evolution of the distribution function of the dark matter ($f = f(r,v,t)$) can be put forth in the form of collision–less Boltzmann equation (see Eq. 1.2),

$$\textbf{Poisson's equation:} \quad \nabla^2\Phi = 4\pi G \int f dv \tag{1.1}$$

$$\textbf{collisionless Boltzmann equation:} \quad \frac{df}{dt} = \frac{\partial f}{\partial t} + v\frac{\partial f}{\partial r} - \frac{\partial \Phi}{\partial r}\frac{\partial f}{\partial v} = 0 \tag{1.2}$$

where Φ is the gravitational potential.

Owing to the high dimensionality of these coupled equations, it is computationally impossible to fully solve them. Hence, solving these equations efficiently is one of the keys to minimizing the computational cost of that simulation. The *N-body* (or *Monte–Carlo*) technique is one of the most preferred, economical ways in the community to simulate dark matter particles (Binney & Tremaine, 2008). This method coarsely samples the phase–space density via N randomly selected points; since the sampling is subject to Poisson noise, higher the value of N i.e. more the number of points/particles, lesser is the statistical noise but also, higher is the computational cost. Gravitational forces are first computed within the sampled phase–space over which the motion of our Monte–Carlo particles will be determined. Numerical integration schemes like Symplectic integrators (which conserve the total energy in Hamiltonian systems) are then employed iteratively as the particles are advanced through the simulation space, over a series of timesteps. Applying uniform timesteps to all particles in a simulation would work well for regions of uniform density. However, in real Universe, some regions (for example, ISM, galactic outflows, etc.) are far denser than some other regions (for example, IGM). To correctly capture this range of densities in a simulation volume, one needs to use smaller timesteps for highly dense regions as compared to less dense areas i.e. individual, tailored timesteps need to be incorporated in our integration schemes. Unphysical scattering of particles is another issue that becomes relevant in dense regions. To tackle this, gravitational forces are softened beyond certain length scales (so–called softening length; Price & Monaghan 2007).

There are primarily two methods for treating gravity: Particle method (solving the integral form of Poisson equation) and Mesh method (solving the differential form of Poisson equation). Until mid–1980s, simple particle simulations, whose computational expense scaled as $\mathcal{O}(N^2)$ (where N is the number of particles), were relied upon. These are also popularly known as the particle–particle schemes. However, the introduction of tree–based codes, thereafter, greatly reduced the computational load to $\mathcal{O}(N \log N)$ (Barnes & Hut, 1986). Further optimization can be achieved via fast multipole method (which computes forces purely between tree nodes and

thus eliminates the usage of particles in force calculations entirely), which reduces the load to $\mathcal{O}(N)$ (Dehnen, 2000).

Another way to model gravity is to convert a given set of particles into a mesh or a grid (so–called particle–mesh or PM method; Hockney & Eastwood 1981). Gravitational potential is computed for this mesh and the resultant forces are then assigned to the associated particles. This scheme also results in a $\mathcal{O}(N \log N)$ complexity (where N is the number of mesh cells). PM method, used in combination with a set of nested grids of varying resolutions, results in an adaptive–mesh–refinement (AMR) scheme (Berger & Oliger, 1984; Berger & Colella, 1989). The nested grid setup of AMR allows it to adapt the grid resolution in accordance with the localized particle densities (see Fig. 1.3), thus increasing the resolution of the simulation where necessary while also maximizing efficiency.

A number of hybrid schemes, combining the particle method with mesh method have been developed. Particle–particle plus particle–mesh method (P3M; Efstathiou et al. 1985) and Tree–particle–mesh (TreePM; Bode & Ostriker 2003) method are the most commonly used ones. Some of the codes employing modified versions of PM method are ART (Kravtsov et al., 1997), RAMSES (Teyssier, 2002), Enzo (Bryan et al., 2014), etc., while GADGET–3 (Springel, 2005), AREPO (Springel, 2010), GIZMO, etc. are examples using TreePM scheme. N-body simulations, which include only gravity and dark matter interactions, are frequently employed for problem cases focusing only on halo and dark matter properties and also often serve as selection pools for more complex and computationally–heavy hydrodynamical simulations. Since they do not include any baryonic physics they are computationally less expensive to run.

1.2.1.3 Simulating baryonic matter

Even though the detailed properties of dark matter and dark energy, which constitute a major chunk of the energy budget of our Universe, remain obscure, extensive robust observations constrain their global properties and behavior pretty decently. Thus, it is comparatively easier to simulate dark matter. Normal, baryonic matter, on the other hand, makes up a very small percentage of the total energy budget but it is also the only directly observable form of matter in the Universe. It is also the most challenging component to simulate accurately. This is due to the fact that there is a huge dynamic range in space–time where a large number of interlinked astrophysical processes happen simultaneously– this is also where numerical artefacts, associated with the approach chosen for solving hydrodynamical equations of astrophysical fluids, occasionally creep up. Add to that the indispensable need for including sub–resolution level physics, arising due to an inherent computational limit to the spatial resolution of a simulation, and we have an ominous task at hand when it comes to dealing with accurate modeling of baryonic processes and associated feedback!

Baryons, initially in the form of gaseous hydrogen and helium, are thought to trace the dark matter potentials i.e. galaxy halos. They first form stars in the early Universe, which later process these primordial elements into metals during the course of stellar evolution. In astrophysical simulations, baryons are often modelled as an ideal gas with negligible viscosity. The resultant hydrodynamical equations can be expressed either in Lagrangian, Eulerian or a hybrid Lagrangian–Eulerian form (see Fig. 1.4).

Traditionally, conventional mesh–based Eulerian methods, like finite volume, finite difference, and so on have been used. The idea, for example, in case of the finite volume scheme is to calculate the mass fluxes through each cell in an underlying fixed Cartesian mesh. However, as in N-body simulations, real baryon densities vary in space and thus, call for an optimization in terms of adaptively refining (AMR) the cell sizes based on some refinement criterion (Klein et al., 1994; Bryan & Norman, 1995). These criteria are often set, basis some minimum mass/density

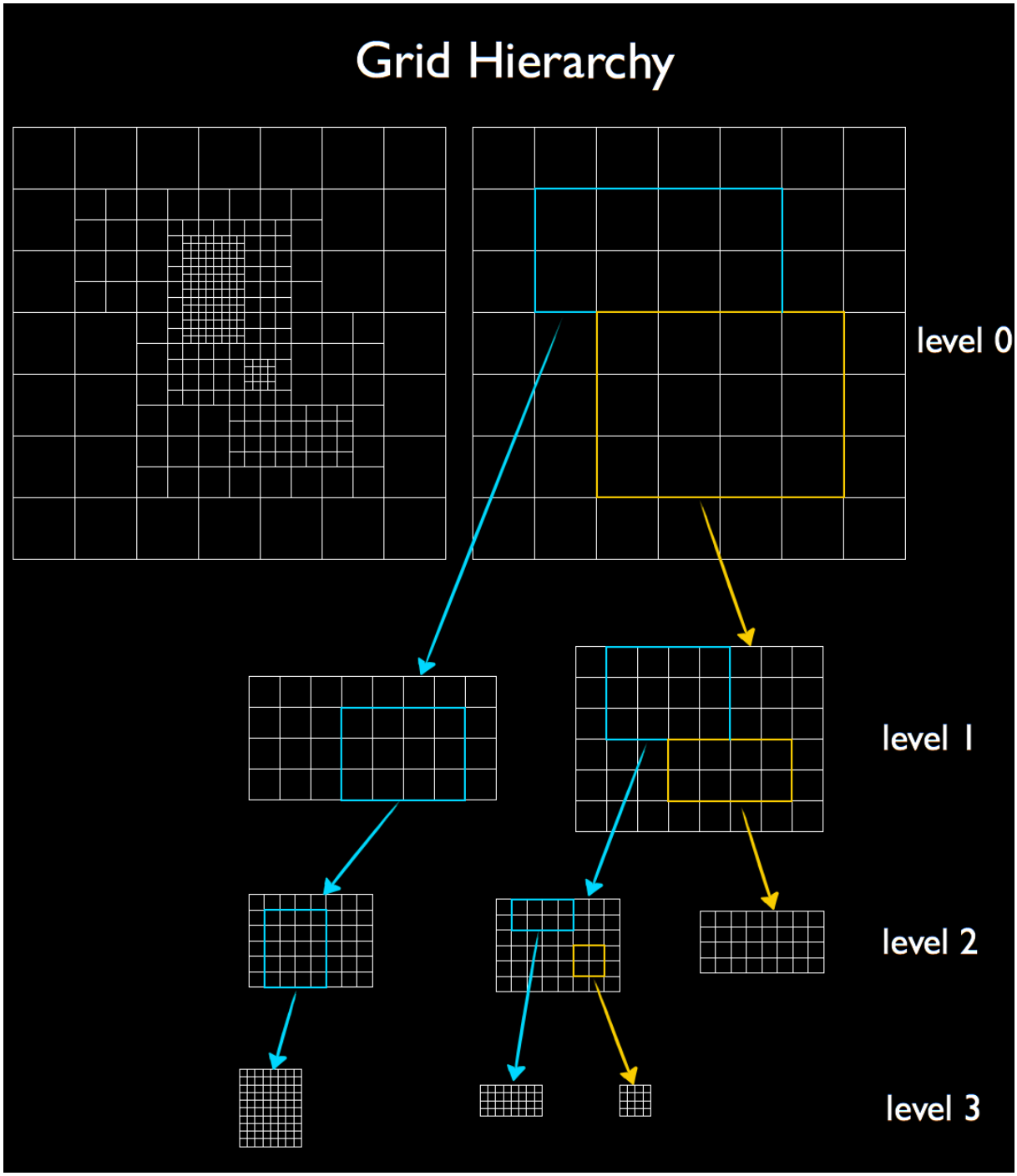

Figure 1.3: Basics of the Adaptive Mesh Refinement technique: Resolution of the underlying grid is adjusted in accordance with the local particle densities. This creates finer (coarser) grids at dense (less–dense) sites, thereby increasing the efficiency of the simulation. (Credits: https://2dshocks.wordpress.com/2013/05/07/adaptive-mesh-refinement/).

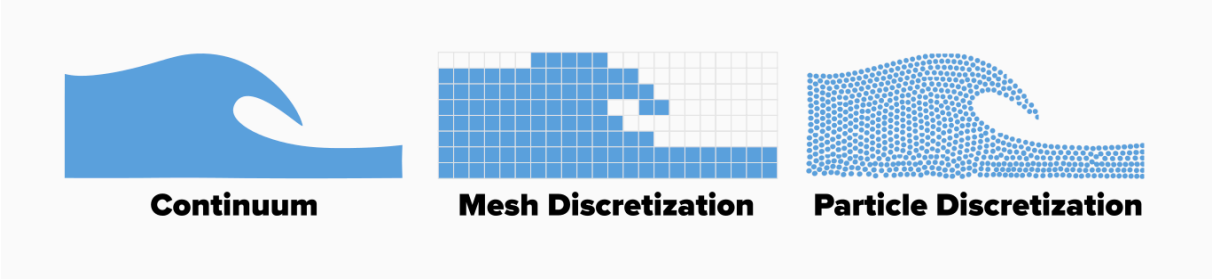

Figure 1.4: Lagrangian vs. Eulerian approach of discretizing a continuous fluid flow, such as seen in many astrophysical scenarios (Credits: Fig. 9 from https://www.dive-solutions.de/blog/sph-basics).

limit (which essentially enables higher resolution in denser regions at the expense of degraded resolution in sparser regions in space). One can also chose to do away with the mesh and instead adopt a Lagrangian approach, using a set of sampling particles to approximate fluid motions. Smoothed particle hydrodynamics (SPH) is one of the most popular methods of this kind (Lucy, 1977; Gingold & Monaghan, 1977; Monaghan, 1992; Springel, 2010; Price, 2012). This method, in general, lends itself more naturally towards modeling various astrophysical fluid flows than the Eulerian method. However, both the above methods are riddled by some glaring problems.

Shock waves in astrophysical environments are very common like, for example, supernovae explosion shocks, collisional shocks, merger–induced shocks and accretion shocks, as are sudden density jumps, for example, in cases where cold-dense clouds are embedded within a hot–ionized bubble. Mesh–free SPH codes are unable to properly treat both these situations (Agertz et al., 2007). Mesh–based AMR codes have major issues in correctly replicating fast–moving objects, particularly, relative velocities between galaxies as well as heavily refined regions that move quickly with respect to the remaining, largely–static regions (Tasker et al., 2008). Enhanced mixing as a result of limited resolution or lack of dealing with large bulk velocities is another undesired by-product (Wadsley et al., 2008).

Above issues necessitated the need for developing a hybrid Lagrangian–Eulerian method. Voronoi tessellation–based method is one of the most preferred ones. The underlying mesh, which is fixed in traditional Eulerian approach, is allowed to move here (see Fig. 1.5). The Voronoi mesh imitates the behavior of a fluid flow (as in SPH methods), thus combining the strengths of both the previous approaches (Springel, 2010). Apart from modeling the hydrodynamical behavior, one also needs to incorporate numerous astrophysical processes that govern galactic properties (see Fig.1.6). These processes largely occur at spatial resolution scales far below than what can be computationally achieved in a typical simulation. This is where inputs from observations and existing theoretical models play a major role. Relevant observations along with best suited models provide us with inputs that help us curate a unique sub-grid recipe for each major astrophysical process. These recipes are then implemented on top of the hydrodynamical solvers to complete the simulation setup. Feedback from supermassive black holes (SMBH) and active galactic nuclei (AGNs), star formation and ISM formation, stellar feedback, gas cooling, magnetic fields, cosmic ray feedback, etc. are the major sub-grid processes that are employed in most of the recent state–of–the–art simulations. We describe each of them briefly.

SMBHs are ubiquitously found at the centers of galaxies (Gehren et al., 1984; Kormendy & Richstone, 1995; Shields et al., 2008; Moran et al., 2014). The origin of the seeds of SMBHs is still unclear and they are confined to scales far lower than the resolution in simulations. Thus, they are numerically seeded in $\gtrsim 10^{10}$–10^{11} $M_\odot$ dark matter haloes. Their accretion rate is governed

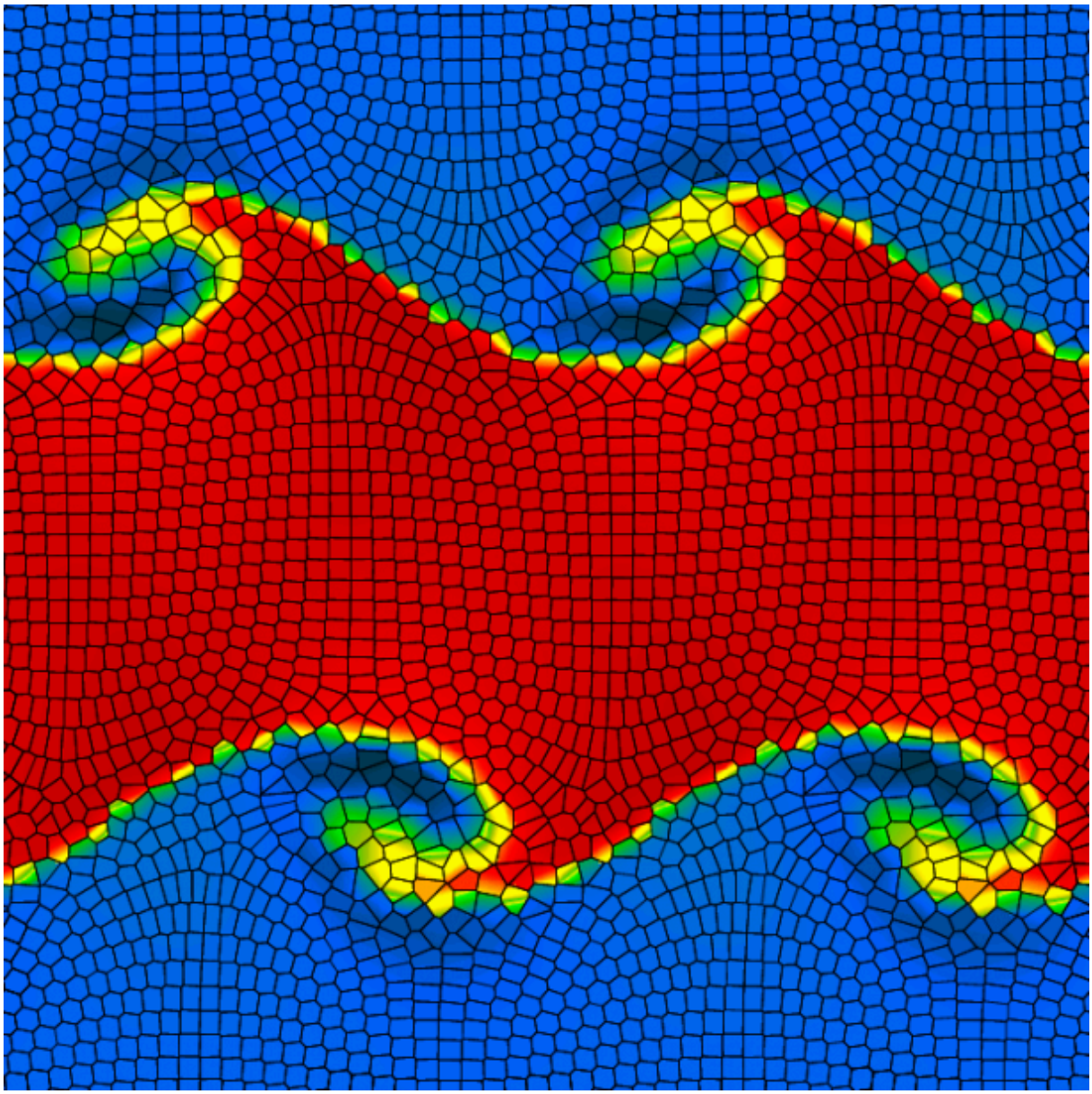

Figure 1.5: Kelvin–Helmholtz instability calculated on an underlying Voronoi moving mesh (Credits: https://virgo.dur.ac.uk/2010/01/05/AREPO/).

by the Eddington–limited Bondi–Hoyle accretion, $\dot{M}_{\rm BH} = (4\pi G^2 M_{\rm BH}^2 \rho)/(c_s^2 + \nu_{\rm rel}^2)^{3/2}$ (where, ρ is the gas density, c_s is the sound speed of the gas and $\nu_{\rm rel}$ is the relative velocity between the gas and the SMBH). Black hole growth via mergers is also accounted for by assuming instant merger once the SMBHs approach each other within their accretion radii (Sijacki et al., 2015).

AGNs are compact regions situated at some galactic centers, showing excess non-stellar emission. This AGN radiation couples with the surrounding gas, imparting energy/momentum, thus, eventually creating a feedback mechanism that regulates the SMBH's growth as well as the star formation rate (Krolik, 1999). Accretion of matter onto the central SMBH is hypothesized to be the main culprit causing this feedback. AGN feedback is thought to happen via two principal modes– high–accretion quasar mode and low–accretion radio mode. Quasar mode is known to be dominant in less massive galaxies and the resultant feedback is modelled in the form of an energy/momentum injection (Di Matteo et al., 2005; Debuhr et al., 2010; Choi et al., 2012). Radio mode feedback is prevalent mainly in massive galaxies and is evident in form of powerful jets and large-scale bubbles (Sijacki et al., 2007; Weinberger et al., 2017). These jets and bubbles originate very close to the SMBH and propagate outwards to tens of kpc distances from the SMBH (resolving such a huge dynamic range is currently out of reach for simulations). It is also currently impossible to resolve the accretion disc regions in simulations and hence, a number of assumptions regarding the relation between accretion rate of the SMBH and the observed bolometric luminosity of the AGN as well as the amount of energy deposited into the gas surrounding the accretion disc have to be made.

Since it is not possible to spatially resolve stellar scales, simulators generally implement the conversion of cold-dense molecular gas to star particles in a stochastic manner. For this, the star formation rate is first computed, assuming a Kennicutt–Schmidt relation (which depends on the gas cell/particle mass, gravitational free–fall time and an observationally motivated gas–to–stars conversion efficiency) (Kennicutt, 1998; Hopkins et al., 2014, 2018). Thereafter, based on certain density threshold criteria, some gas cells are stochastically converted into star particles (Stinson et al., 2006; Teyssier et al., 2013; Schaye et al., 2015; Wang et al., 2015). Subsequently, the stellar yields (both in terms of mass and metals) of these star particles following their evolution are tracked and are fed back to the gaseous component in simulations (Wiersma et al., 2009; Vogelsberger et al., 2013; Naiman et al., 2018).

The complex, multi–phase nature of the ISM and its stronghold over the star formation patterns of a galaxy, make it extremely important yet challenging to model. Simplistically speaking, the ISM can be thought of as a two–phase entity, wherein a mass–dominant cold phase is in equilibrium with a surrounding supernova–heated, volume–dominant hot gas phase (Springel & Hernquist, 2003; Emerick et al., 2019). The cold part of the ISM evolves on very short timescales which compels simulators to approximate it via an effective polytropic equation of state (that emerges from the aforementioned two–phase nature of the ISM) (Agertz et al., 2010; Dalla Vecchia & Schaye, 2012). Furthermore, the effect of various background ionizing sources on the ISM gas must be taken into account. Self–shielding from such radiation in the densest regions of the ISM is also accounted for (Krumholz & Gnedin, 2011; Rahmati et al., 2013).

During the course of stellar evolution, massive stars undergo supernovae explosion that deposit energy and momentum to the surrounding gas cells. This sets off a feedback channel, in the form of galactic outflows, which ultimately regulates star formation. The energy from these outflows can either be deposited thermally or kinetically. Suppressing radiative cooling or probabilistic heating of gas for a short while is needed to counter excess radiative cooling that is an artificial phenomenon of simulations (Stinson et al., 2006; Dalla Vecchia & Schaye, 2012). For the latter case, hydrodynamically–decoupled wind particles are usually employed for momentum

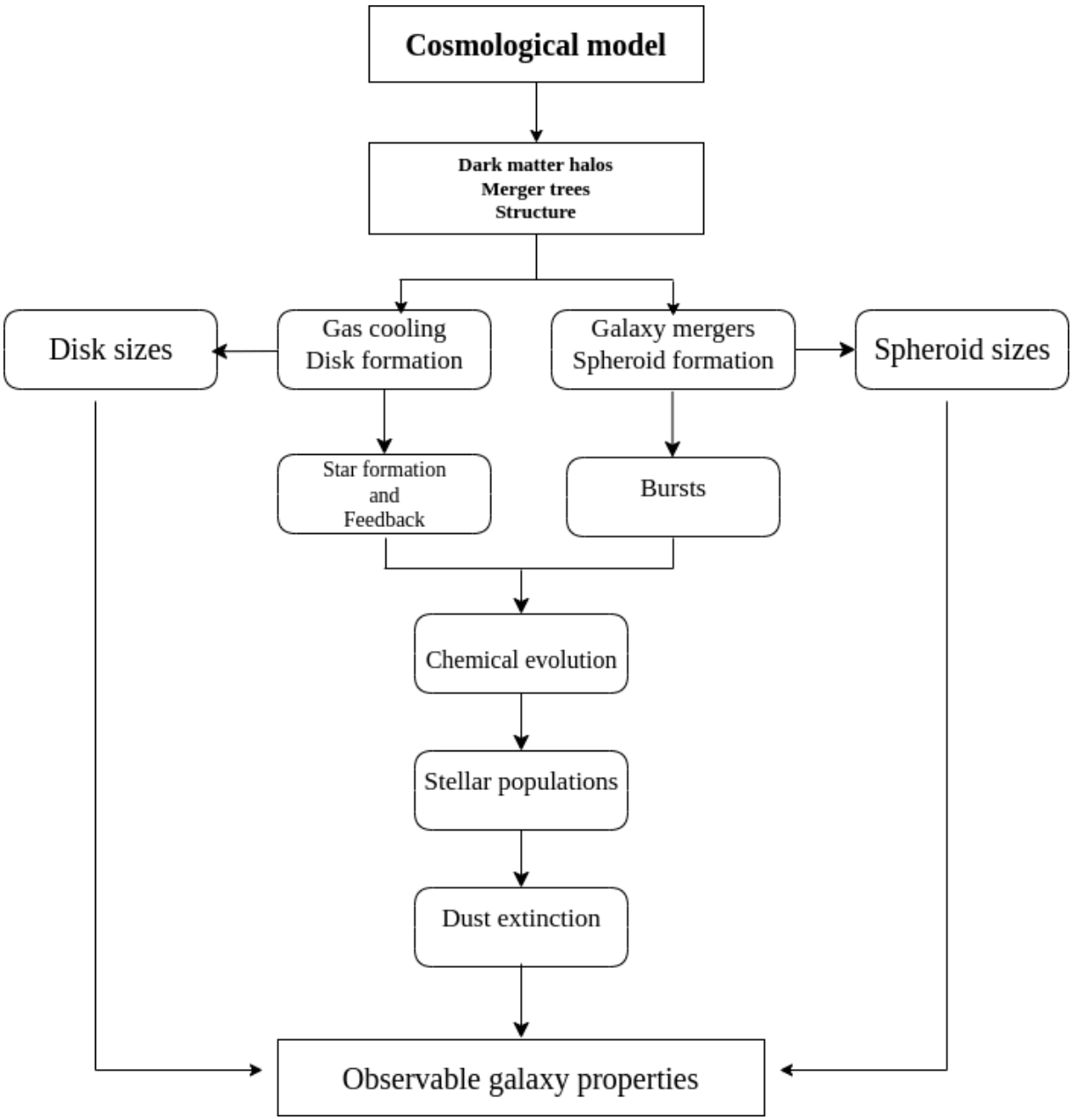

Figure 1.6: A schematic describing how different astrophysical processes, operating within the adopted cosmological framework, are linked to the observed galactic properties.
(Credits: Modified version of fig. 1 from Cole et al. 2000)

transfer from supernovae sites to outer regions (Oppenheimer et al., 2010; Vogelsberger et al., 2013). Additional processes such as feedback from stellar winds and excess radiation due to young, massive OB stars, together with galactic outflows, completes the stellar feedback library (Stinson et al., 2013; Smith et al., 2019).

Gas cooling is a conglomeration of several different processes. It is, for this reason, not implemented in simulations as a single sub–resolution model but rather constituent individual processes are incorporated. A gas parcel at a higher temperature can dissipate its energy via collisional excitation, inverse Compton process, free–free emission, recombination, etc. Along with primordial cooling, cooling due to heavy elements (so–called metal line cooling) is also important, especially at high temperatures. Cooling functions that are responsible for carrying out the aforementioned processes are extracted from well–predicted chemical networks. Apart from collisional ionization equilibrium (Sutherland & Dopita, 1993), most modern simulations also incorporate metal photo–ionization due to a spatially–uniform, time–dependent UV background radiation field (Wiersma et al., 2009; Haardt & Madau, 2012). Fine–structure cooling and molecular cooling also comes into picture in cases where gas at $T < 10^4$ K (cold ISM) is resolved (Tielens, 2005).

Magnetic fields are omnipresent throughout the Universe across spatial scales. Their effect is primarily seen on ionized gas and the dynamics of ionized gas, in turn, affects the anatomy and strength of the magnetic fields. Typically, simulations adopt the ideal MHD approach, which suffices for super–stellar spatial scales. While their impact on cosmological scales is rather subdued (Marinacci & Vogelsberger, 2016), magnetic fields are an important source for providing pressure support against gravity in the ISM regions (Ferrière, 2001) as well as affecting cosmic–ray propagation (Kotera & Olinto, 2011). A tiny seed field ($\sim 10^{-10}$ G) is generally introduced in simulations at early epochs ($z \sim 100$) in order to mimic the self–consistent inception of magnetic fields (which is prohibited in the ideal MHD realm adopted in simulations). This seed field first undergoes an exponential amplification at high redshifts via a turbulent dynamo process, post which a second, linear amplification at lower redshift occurs via a galactic dynamo (Pakmor et al., 2017).

Cosmic rays (comprising of relativistic nuclei and electrons) are another pressure support (Ferrière, 2005; Cox, 2005) and heating source in the ISM (Field et al., 1969; Wolfire et al., 1995). They also play a part in driving galactic scale outflows (Uhlig et al., 2012; Pakmor et al., 2016a; Ruszkowski et al., 2017; Farber et al., 2018). The pressure arising from cosmic rays can be described by $P_{cr} \propto \rho_{cr}^{4/3}$ and they are characterized by long cooling times (Pfrommer et al., 2016). The topology and strength of the root magnetic fields closely dictate the propagation pattern of cosmic rays. Thus, a robust treatment of cosmic rays and their effects in simulation must be preceded by an equally detailed treatment of magnetic fields. The injection, acceleration and subsequent propagation of cosmic rays happens primarily via anisotropic diffusion and streaming. Both these processes are captured in the cosmic ray energy equation. To minimize the complexities arising from the interdependence of cosmic ray energy and flux (Sharma & Hammett, 2007; Sharma et al., 2010; Kannan et al., 2016; Butsky & Quinn, 2018), diffusion and streaming are coupled to the ideal MHD equations via two separate formulations (Jiang & Oh, 2018; Thomas & Pfrommer, 2019).

1.2.2 Types of simulations

As stated earlier, the set of simulations solving only gravitational interactions are N-body, dark matter simulations. Those additionally incorporating baryon dynamics as well as other physical processes into consideration are known as hydrodynamical simulations. Further distinctions can

be made based on the spatial scales simulated (see Fig. 1.7). However, all types of simulations have to first incorporate a set of cosmological initial conditions to set the ball rolling. I will first describe the salient features of some commonly used types of simulations (§1.2.2.1, §1.2.2.2, §1.2.2.4 and §1.2.2.3), followed by some important results (§1.2.3).

1.2.2.1 Big Box simulations

Numerous observational surveys, that have been completed or are in progress, sample large swathes of areas in space (sometimes even over large cosmic timescales) and generate data, depending on the use case in consideration. In order to fully comprehend and test existing models with these observations that span such a vast range in space and time, simulated universes spanning similar ranges must be first generated. Thus, we have *Big Box* (also called as *large volume*) cosmological simulations. Statistics is the centrepiece of any such simulation. This is, of course, at the expense of spatial resolution (since running statistically–intensive as well as very high–resolution simulations becomes computationally impractical). The box–sizes of these simulations can go up to giga–parsec scales and they can be populated with trillions of particles.

One commonly employed use case, in the context of N-body simulations, is the study of large-scale structure of the Universe by tracking the dark matter distributions. The VIRGO Project (Jenkins et al., 1998) and Millennium (Springel et al., 2005c) were one of the first dark matter–only setups to adequately imitate the observed large-scale dark matter distribution; these were followed over the years by other increasingly cutting edge simulation suites like Bolshoi (Klypin et al., 2011), Millennium-XXL (Angulo et al., 2012), Dark Sky (Skillman et al., 2014), Indra (Falck et al., 2021), ABACUSSUMMIT (Maksimova et al., 2021), etc. Adding hydrodynamical processes to the fold undoubtedly increases the complexity but also enables a direct comparison between the resultant hydrodynamical simulations and datasets from the observable Universe. Soon after the emergence of N-body simulations in early 2000s, first fully cosmological hydrodynamical simulations like Horizon–AGN (Dubois et al., 2014) and Illustris (Vogelsberger et al., 2014a) were developed. Following improvements in computing techniques as well as better observationally motivated sub-grid recipes, more realistic simulations like MassiveBlack–II (Khandai et al., 2015), EAGLE (Schaye et al., 2015), Magneticum (Dolag et al., 2016), Romulus25 (Tremmel et al., 2017), IllustrisTNG (Nelson et al., 2017; Pillepich et al., 2017; Marinacci et al., 2018; Naiman et al., 2018; Springel et al., 2018; Nelson et al., 2019a,b; Pillepich et al., 2019), SIMBA (Davé et al., 2019), FIREBox (Feldmann et al., 2022), etc. have become possible.

1.2.2.2 Zoom simulations

Generally, the baryonic mass resolution of a typical hydrodynamical large–volume simulation is $\sim 10^7$–10^8 $M_\odot$; even the best resolved ones can only go up to $\sim 10^{5.5}$–10^6 $M_\odot$ (see Fig. 1.8). At these resolutions, numerous baryonic processes need to be incorporated via sub-grid recipes. These recipes involve the usage of a number of adjustable parameters. In box simulations, the parameter selection is done via a calibration procedure. First, the best possible set of parameters is obtained by exploring numerous effective models in multiple smaller volume simulations. A comparison of these parameter values with observables such as present-day galaxy stellar mass function, stellar–to–halo mass relation, etc. completes the calibration (also called as *fine-tuning*) process. This roundabout technique of implementing a model based on calibrated parameters, unfortunately, makes the model less detailed. This affects the predictive power of box simulations at galactic scales.

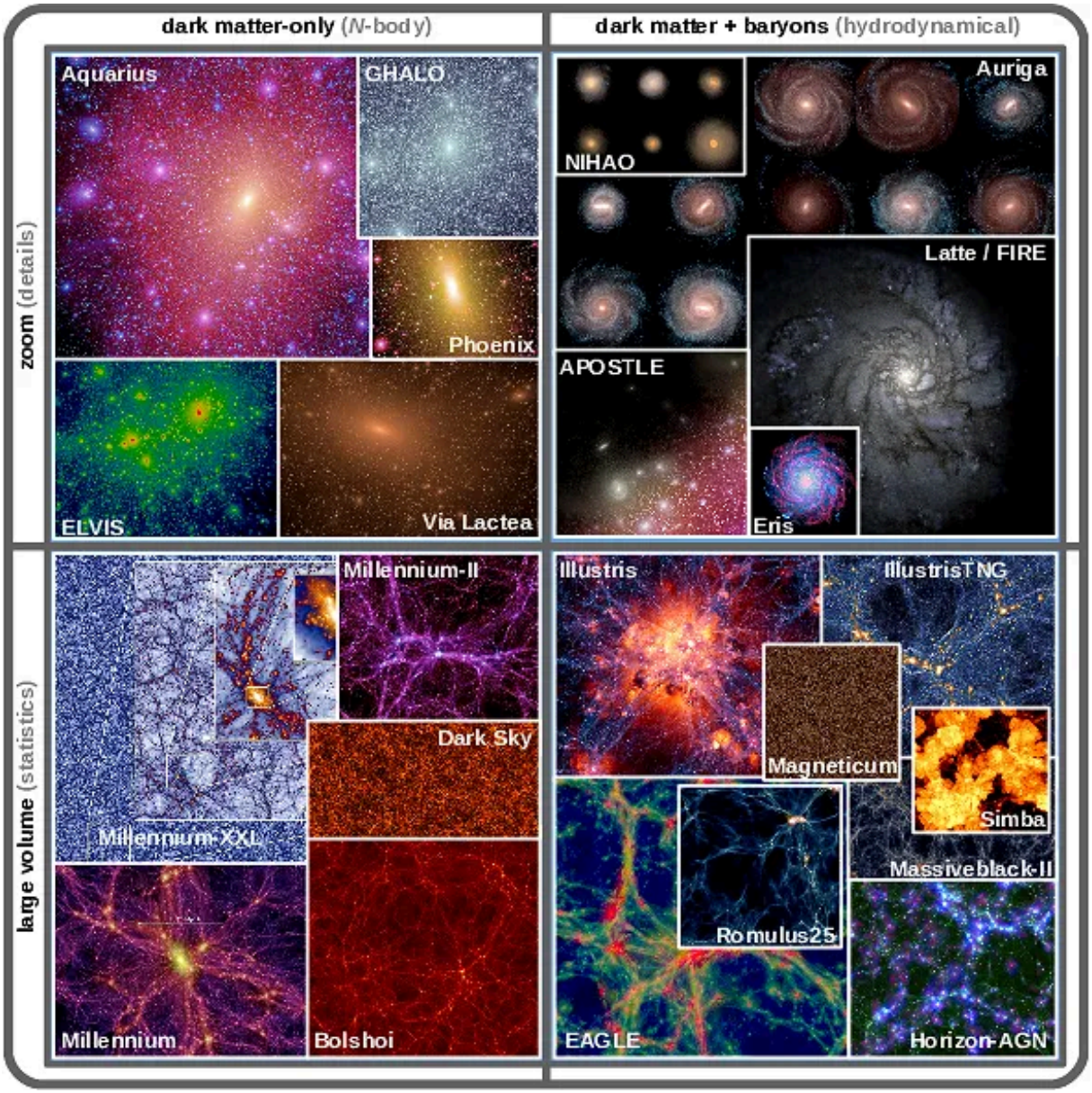

Figure 1.7: Visual slices from some of the N-body as well as hydrodynamical simulations from recent times. Detailed, zoom simulations are represented in the top half while large volume, box simulations are shown in the bottom half. On the left, we have dark matter only (or N-body) simulations while on the right we have dark matter + baryonic matter (i.e. hydrodynamical) simulations. (Credits: Cosmological Simulations of Galaxy Formation; Vogelsberger et al. 2020)

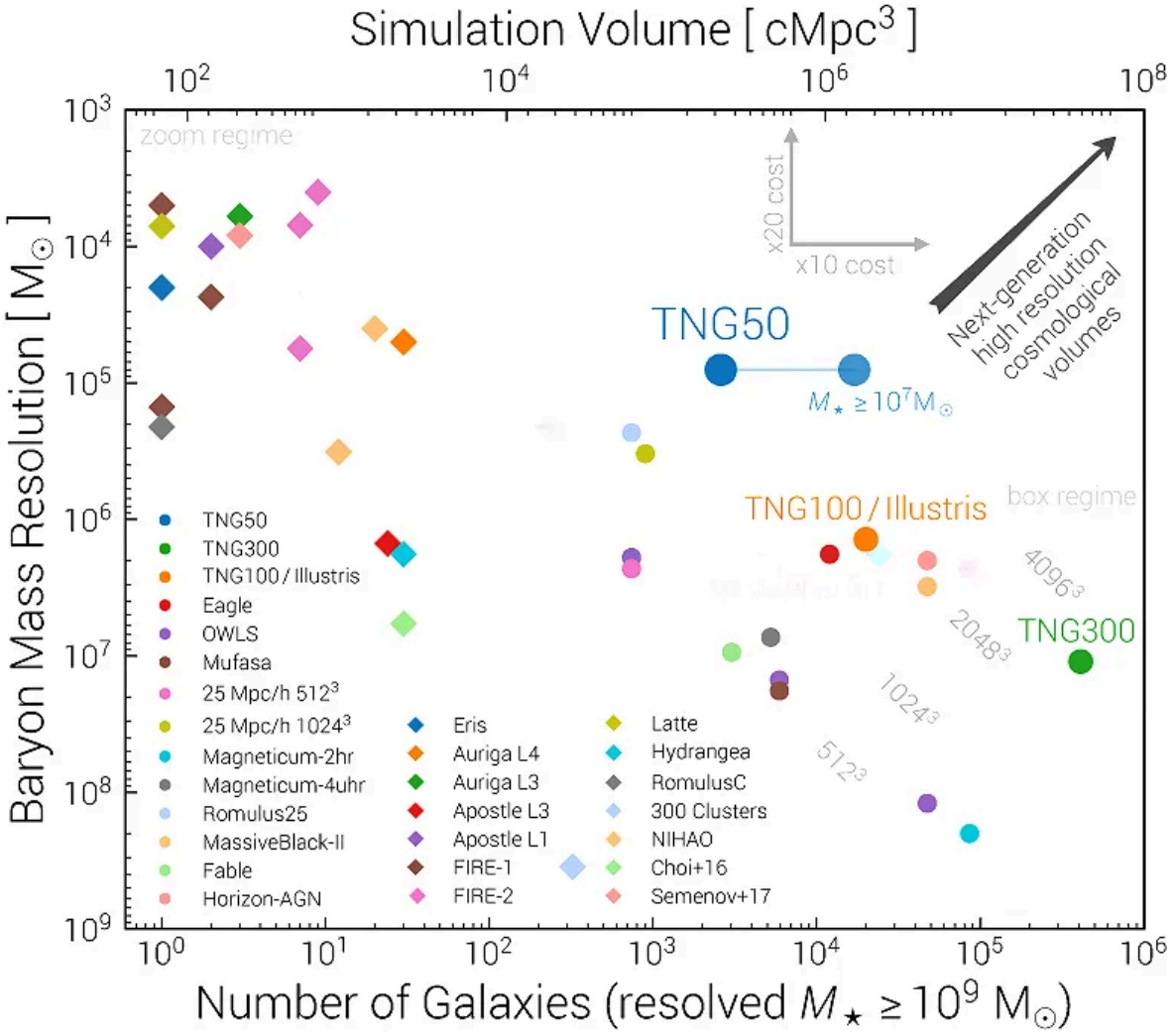

Figure 1.8: A comparison of effective volume (in terms of number of $M_* > 10^9$ $M_\odot$ galaxies resolved) vs. baryonic mass element resolution for a non–exhaustive list of hydrodynamical big box (filled circles) as well as zoom-in (filled diamonds) cosmological simulations.
(Credits: Modified version from– https://www.tng-project.org/about/)

Thus, in use cases closer to galaxy scales, simulators use the *zoom-in* technique. The essence of a zoom-in simulation lies in concentrating the bulk of its computational strength on a small region (so–called *region–of–interest* or ROI) within the total simulation volume. Thus, the ROI contains maximum number of dark matter/baryon particles; as we move away from this region, the number of particles keep reducing, i.e., the spatial resolution is degraded. Since most of the resolution elements are only distributed within a small volume, zoom-in simulations have to compromise on number statistics. However, their spatial resolution is better by a factor of 2 as compared to box simulations (see Fig. 1.8). This enables physically-motivated, calibration–free parameter selection, unlike that in case of large-volume simulations and hence, improves the sub-grid physics. Cosmological galaxy merger simulations are a subset of zoom simulations, designed specifically to cater to the use case of studying the impact of merger events on various galactic properties such as star formation rate, changes in mass and metallicity profiles, etc. Aquarius (Springel et al., 2008), GHALO (Stadel et al., 2009), Phoenix (Gao et al., 2012), ELVIS (Garrison-Kimmel et al., 2014b), COCO (Hellwing et al., 2016), etc. are some examples of dark-matter only zoom-in simulations. Eris (Guedes et al., 2011), NIHAO (Wang et al., 2015), Auriga (Grand et al., 2017), Hydrangea Project (Bahé et al., 2017), The Three Hundred Project (Cui et al., 2018), RomulusC (Tremmel et al., 2018), The FLARES Project (Lovell et al., 2021) etc. are some examples of zoom-in hydrodynamical simulations.

1.2.2.3 LG constrained simulations

Observational datasets are often more abundant and robust in the nearby universe as compared to slightly higher–z regions. This is especially true when we consider precision velocity and spatial measurements for stars and galaxies, absorption as well as emission–line measurements for gas clouds outside of galaxies and so on. This is also one of the major reasons why astrophysical objects in our surroundings are chosen as proxies for similar other distant objects. Surveys like Gaia (Gaia Collaboration et al., 2018, 2021), for example, are able to measure the positions and velocities of millions of stars in our Milky Way to an unprecedented accuracy. Similarly, CosmicFlows catalogue (Tully et al., 2013; Tully et al., 2016; Kourkchi et al., 2020) provides highly accurate direct distance estimates for thousands of galaxies in our Local Universe (LU). Such a detailed cosmographic view of our nearby environment can be effectively leveraged to create tailored simulations to better study metal-poor stars, dwarf galaxy dynamics, quenching patterns in satellites, LG CGM, etc. Thus, a demand for LG constrained simulations organically arises. Since the computational prowess is directed towards simulating a patch of the Universe surrounding us, constrained simulations can be thought of as a special class of zoom simulations itself.

Constrained simulations use the wealth of high–quality, nearby–Universe observational data as an input for their initial conditions (ICs). Thereafter, the usual approach, used for running conventional cosmological hydrodynamical simulations, is adopted. Thus, a LG constrained simulation has an added advantage of having the right local cosmography in addition to its self–consistent treatment of large-scale surroundings. The CLUES Project (Gottlöber et al., 2010), ELVIS (Garrison-Kimmel et al., 2014b), The APOSTLE Project (Sawala et al., 2016), Cosmic Dawn (Ocvirk et al., 2016), ELVIS on FIRE (Garrison-Kimmel et al., 2019a,b), HESTIA (Libeskind et al., 2020), The SIBELIUS Project (Sawala et al., 2022), The SIBELIUS-DARK Project (McAlpine et al., 2022), NIHAO–LG (Arora et al., 2022), LU constrained simulations with modified gravity (Naidoo et al., 2022), etc. are some examples of constrained cosmological simulations.

1.2.2.4 Idealized simulations

Instead of simulating whole volumes containing a number of target astrophysical objects, one can instead, also choose to model a single object. Such an approach leads us to *Idealized* simulations. Modeling a single galaxy or a galaxy cluster in a controlled manner to a very high resolution at the expense of entirely excluding its larger cosmological surroundings is a hallmark of these kind of simulations. Owing to their superior resolution, their reliance on sub-grid models can be greatly reduced. They are also usually computationally cheaper to run as compared to cosmological simulations. However, the trade off comes in the form of a lack of physical realism (a by-product of excluding the cosmological context around the simulated entity).

Idealized simulations can be viewed in a complementary light since their results can be used rather effectively in specific problem cases to gain unique insights and perhaps, also better guide cosmological simulations. They are often invoked, for example, in studies involving the classic cooling flow problem (Fabian et al., 1994; Peterson & Fabian, 2006), which dictates an unnaturally large observed cooling of infalling IGM gas (that does not translate to an expected high enough star formation rate) in case of L^* and super–L^* galaxies (Stern et al., 2019; Su et al., 2019; Stern et al., 2020). The impact of supernovae (Li & Tonnesen, 2020), stellar feedback (Fielding et al., 2017), SMBH feedback (Huško et al., 2022) as well as detailed effects of finer physical processes such as precipitation (Kopenhafer et al., 2022), turbulence (Lochhaas et al., 2020), etc. (especially on the cool phase of CGM) all benefit greatly from enhanced resolution and, therefore, are well suited for idealized setups. Furthermore, galaxy cluster merger cases, wherein it is not only necessary to have the merging systems in equilibrium at the beginning of the simulation but also have an extremely detailed prior knowledge about the initial merger parameters, could actually be better suited for idealized simulations (Chadayammuri et al., 2022).

1.2.3 Insights from simulations

Dark-matter only, cosmological simulations have contributed immensely towards improving our understanding about the large-scale structure of dark matter as well as the structure of dark matter halos (Aarseth et al., 1979; Efstathiou, 1979). Since the currently favored model remains ΛCDM, a majority of N-body simulations adopt this framework. According to this model, on large scales, dark matter is distributed in a rather non–homogeneous, cosmic web–like structure. The cosmic web, best quantified by the halo mass function and dark matter correlation function, consists of galaxy-rich nodes, less-dense filaments and walls, punctuated intermittently by sparsely populated void regions (Cautun et al., 2014; Libeskind et al., 2017). Halo mass function counts the number of dark matter halos, as predicted by the model, as a function of M_{200} (mass within a radius r_{200}, which characterizes the spherical distance from the center of a halo where the mean density equals 200 times the critical density of the Universe; Tinker et al. 2008). Today, several halo finder algorithms exist for the purpose of identifying dark matter halos (Knollmann & Knebe, 2009; Knebe et al., 2011; Behroozi et al., 2013; Hadzhiyska et al., 2021). Simulations reveal a power law slope for low-mass halos, while at the high-mass end, the slope is exponentially suppressed (Sheth & Tormen, 2002; Reed et al., 2003; Warren et al., 2006). Constraints on cosmological parameters, predictions for the nature of dark matter, testing the model–predicted spherical collapse of halos, etc. are some other important results in this regime (Eke et al., 1996; Sheth & Tormen, 2002; Angulo et al., 2013; Schneider, 2015). Simulations also robustly predict the two–point correlation function, $\xi(r)$, which contains information about the properties of cosmic web (Cooray & Sheth, 2002; Springel et al., 2018). Properties of internal structure of a dark matter halo (described by a spherically-averaged Navarro–White–Frenk

density profile; Navarro et al. 1996, 1997) as well as the substructure within that halo are key parameters for testing the ΛCDM model. Secondary halos (subhalos) residing within the parent halos have been successfully studied owing to increasing resolving power of simulations (Ghigna et al., 1998; Moore et al., 1999). Further insights about the shapes of dark matter halos (Jing, 2002; Allgood et al., 2006; Bett et al., 2007), halo formation timescales as a function of halo mass (Navarro et al., 1997), velocity dispersion profiles (Diemand et al., 2007; Navarro et al., 2010), radial distribution of subhalos as a function of parent halo mass (Springel et al., 2008), abundance of subhalos (Gao et al., 2004; Gao et al., 2012), etc. have emerged primarily as a result of testing various predictions from different models in simulations.

Unlike, predictions for dark matter (which rely heavily on well–defined theoretical models), baryonic matter additionally have an stronger pillar of observational data to lean on. Simulations can be used to generate mock datasets (most of which, nowadays, also take into consideration instrument–specific properties) which can be directly compared to actual observations. One of the biggest successes of hydrodynamical simulations has been reproducing realistic–looking galaxies having properties similar to what has been observed (Hopkins et al., 2014; Vogelsberger et al., 2014a; Schaye et al., 2015; Wang et al., 2015; Grand et al., 2017; Kaviraj et al., 2017; Springel et al., 2018). Tackling the uncertainties associated with implementing different sub–resolution models is the next challenging frontier for simulators (Mathew & Federrath, 2020; Borrow et al., 2021). Mock datasets from large–volume simulations have been compared to extensive galactic surveys for studying associated global galaxy properties like their stellar content (Schaye et al., 2015; Pillepich et al., 2018), properties of the diffuse CGM and IGM (Hernquist et al., 1996; Peeples et al., 2019; van de Voort et al., 2019; Suresh et al., 2018; Hummels et al., 2019), galaxy two–point correlation function (Meneux et al., 2008; Foucaud et al., 2010; Wake et al., 2011; Artale et al., 2017; Marulli et al., 2013), various galaxy scaling relations (galaxy color–stellar mass; Trayford et al. 2015; Nelson et al. 2017, galaxy mass–metallicity; Tremonti et al. 2004; Davé et al. 2017; De Rossi et al. 2017; Torrey et al. 2019, galaxy mass–size; Shen et al. 2003, SMBH mass–stellar velocity dispersion; Kormendy & Ho 2013, etc.).

The biggest impact of zoom simulation studies has been in the domain of global satellite population properties as well as details regarding pressure balance in the CGM (Ji et al., 2020; Lochhaas et al., 2022) and, to a smaller extent, also in the ISM (Gurvich et al., 2020). Extra spatial resolution in these setups allows to now simulate the entire mass range of satellite population around a MW–like halo (Grand et al., 2021), alleviating the planes of satellites problem to a great extent. Hafen et al. 2022 found that a prior angular momentum alignment of gas is one of the key elements to form thin stellar discs. Impact of magnetic fields in galaxy mergers (Whittingham et al., 2023) have also been studied.

On the other hand, idealized simulations have been especially useful in studying the ISM. Detailed modeling of SNe–driven winds (Fielding et al., 2017), simulating stellar feedback from individual stars in dwarfs (Emerick et al., 2019), probing the effects of variable energy SNe feedback on a dwarf galaxy ISM (Gutcke et al., 2021), development of the most–resolved ISM model for LMC–mass dwarfs (Steinwandel et al., 2022), etc. have been some of the headlining results in the past few years. Idealized setups have also proven useful at large scales– studying the co–evolution and effects of gas and SMBH feedback in large halos (Dattathri & Sharma, 2022), the brightest cluster galaxy–SMBH–ICM interaction (Nobels et al., 2022), effect of AGN feedback on the cooling flows in isolated cool–core halos (Weinberger et al., 2022), etc. are some important results.

In the recent years, constrained simulations have been finding a growing voice in the community for the use case of near field cosmology as well as extremely detailed satellite studies. Many of the resultant studies also aim to answer whether or not our LG can be considered as

a good proxy for galaxy groups elsewhere (Libeskind et al., 2020). Samuel et al. 2021 showed that the planes of satellites problem was organically resolved in their constrained realizations while Newton et al. 2022 proposed the usage of ultra–diffuse galaxies (UDGs) as test probes for current galaxy formation theories. Dupuy et al. 2022 used anisotropic satellite accretion while Khoperskov et al. 2022 employed stellar chemical abundances to study the mass assembly patterns in our LG. Biaus et al. 2022 were able to reproduce the LG–specific observed radial velocity dipole while Lovell & Zavala 2023 were able to replicate the observed MW satellite density profile diversity. Furthermore, Damle et al. 2022 (which is the chapter 2 of this thesis) showed from their HESTIA simulation–based study that observational biases in form of intervening MW CGM gas clouds could unnaturally boost absorption-line measurement values in M31 at large radii.

Despite these significant results, overcoming certain technical challenges as well as creating a better synergy with the observational community (especially in the context of CGM) are two areas that still have a healthy room for improvement. Various hydrodynamic, wind tunnel, radiative mixing layer as well as cloud crushing simulations have repeatedly established the importance of including the effect of turbulent mixing layers on the observable properties of the CGM (Sparre et al., 2018; Fielding et al., 2020; Tan et al., 2022; Abruzzo et al., 2022b). Its implementation in conventional computer simulations, however, is yet to be realized. Similarly, a lot of theoretical advancements have been taking place with respect to understanding the broader role of cosmic rays (CRs) (Buck et al., 2020), and magnetic fields, especially with respect to the cold CGM (Simpson et al., 2016; Sparre et al., 2020; Butsky et al., 2020; van de Voort et al., 2021). While only some of the very recent simulation efforts have started rudimentarily including these elements (Chan et al., 2022; Hopkins et al., 2022b; Böss et al., 2023; Butsky et al., 2023), these are yet to become mainstream. While it is no secret that an improved communication between the observers and simulators is one of the keys towards leveraging simulations to their fullest (Cole et al., 1998; Yang et al., 2004; Hayward et al., 2013), this aspect is yet to reach its full potential in the field of CGM studies. Efforts are now being increasingly made, in this context, to include an element of observational realism (in the form of accounting for instrument/survey–specific properties and limitations) in simulated datasets such that the resultant CGM predictions can be interpreted more realistically (Lokhorst et al., 2019; Oppenheimer et al., 2020; Yung et al., 2022).

1.3 CGM studies

Our earlier knowledge about the extent of a galaxy being synonymous with the outskirts of its stellar disc was fundamentally challenged after the 1950s, when Guido Münch stumbled upon the first evidence of Galactic Corona in form of Na I and Ca II absorption lines at high Galactic latitudes in the spectra of hot stars (Munch, 1952). Within a decade, a new class of astrophysical objects, quasi–stellar objects (QSOs) or quasars, were discovered (Schmidt, 1963). Extensive studies of quasar spectra soon followed (Greenstein & Schmidt, 1964; Hoyle & Burbidge, 1966). It was not long after when astronomers realized that several of the QSO spectra, in fact, were punctuated by absorption lines. Bahcall & Spitzer Jr 1969 proposed that these lines were a signature of the gas in the extended halos of foreground galaxies at various redshifts. This culminated into the establishment of the existence of Intergalactic medium (IGM) via the discovery of Lyman alpha (Ly-α) forest (Sargent et al., 1980) and the CGM via the association of QSO absorption lines with foreground galactic halos (Bergeron & Stasinska, 1986; Bergeron & Boissé, 1991).

The then widely accepted model of galaxy evolution, the simplistic closed–box model, assumed that neither the existing gas is allowed to leave nor fresh gas is allowed to enter a galaxy throughout its lifetime (Schmidt, 1959; Salpeter, 1959; Talbot & Arnett, 1971). In other words, stringent restrictions were placed on gas flows in a galaxy. However, multiple measurements from extensive spectroscopic surveys in 2000s showed a large baryon and metals deficit (Tremonti et al., 2004; McGaugh et al., 2009; Behroozi et al., 2010a; Zahid et al., 2012; Peeples et al., 2014; Somerville & Davé, 2015; Muratov et al., 2015; Oppenheimer et al., 2016), lack of efficient star formation in low–mass and high–mass galaxies and galaxy groups (Whitaker et al., 2012; Peeples et al., 2014; Pacifici et al., 2016; Wagner et al., 2017; Boogaard et al., 2018; Dou et al., 2021; Kolokythas et al., 2022), galaxy bimodality (Schiminovich et al., 2010; Gonçalves et al., 2012; Forbes et al., 2014; Brennan et al., 2015; Feldmann et al., 2017; Bremer et al., 2018; Bera et al., 2018; Hunt et al., 2020), etc. It became increasingly difficult to reconcile these observations with the closed–box galaxy formation model without resorting to an undesirable extreme fine-tuning of model parameters. Subsequent studies probing gas flows presented many clues that encouraged adopting a more dynamic gas flow model (see Fig. 1.9); one which was organically able to account for most of the above observations over the rather rigid, earlier model (Larson, 1972; Tinsley, 1974; Hunt, 1975; Yoshii, 1981; Chiosi & Matteucci, 1984; Tantalo et al., 1998; Calura & Matteucci, 2006; Colavitti et al., 2008; Lapi et al., 2020). Thus, what started as a purely serendipitous discovery soon snowballed into an increasingly physically motivated, standalone field of study.

1.3.1 Different approaches

Detecting the CGM in emission lines, aka direct detection, is naturally the most straightforward and desirable approach of studying the CGM. However, since the emission strength from radiative cooling scales as particle density squared, the typical densities in this gas remain very low (Augustin et al., 2019; Wijers et al., 2020). This results in emission lines being mostly too faint to be detected. This problem is somewhat mitigated in the LG, especially in the case of our MW's halo (Putman et al., 2012). The cold, warm and hot warm components of our Galactic CGM have been previously detected as high velocity clouds (HVCs) and intermediate velocity clouds (IVCs) via 21 cm–H I (Kerp et al., 1996; Stanimirović et al., 2008; Hsu et al., 2011; Faridani et al., 2014; Park et al., 2016; Li et al., 2021a; Lockman et al., 2023), Hα (Tufte et al., 1998; Haffner et al., 2001; Putman et al., 2002; Barger et al., 2017; Smart et al., 2019), X-ray (Henley et al., 2014; Kaaret et al., 2020; Bhattacharyya et al., 2022; Ponti et al., 2022) and even gamma–ray (Tibaldo et al., 2015; Karwin et al., 2019) emission lines. To some extent, these studies have also been extended to the halo reservoir observations of other galaxies. For example, the MHONGOOSE survey (Sardone et al., 2021) and eDIG–CHANGES (Lu et al., 2023) detected 21 cm-H I and Hα halo emission around spiral galaxies respectively while multiple metal emission lines (He II, O II, O III, Mg II, Ne V, etc.), tracing ionizing outflows, were detected in some other studies (Rupke et al., 2019; Chisholm et al., 2020; Zabl et al., 2021; Burchett et al., 2021; Leung et al., 2021; Shaban et al., 2022; Dutta et al., 2023). Molecular CO emission has also been detected recently (Cicone et al., 2021; Li et al., 2021b; Scholtz et al., 2023). Better instrument sensitivities are enabling more X–ray CGM detections around external galaxies as well (Lehnert et al., 1999; Bogdán et al., 2015; Anderson et al., 2016; Li et al., 2017; Bogdán et al., 2017; Das et al., 2020a; Comparat et al., 2022).

Nevertheless, considering the general difficulty in obtaining robust emission signatures from the CGM, quasar absorption-line spectroscopy remains the most effective method for studying the CGM (Tumlinson et al., 2017). Quasars lie at large distances from us (i.e. at high-z) and therefore, their emitted light has to travel through a lot of space. The intervening space consists

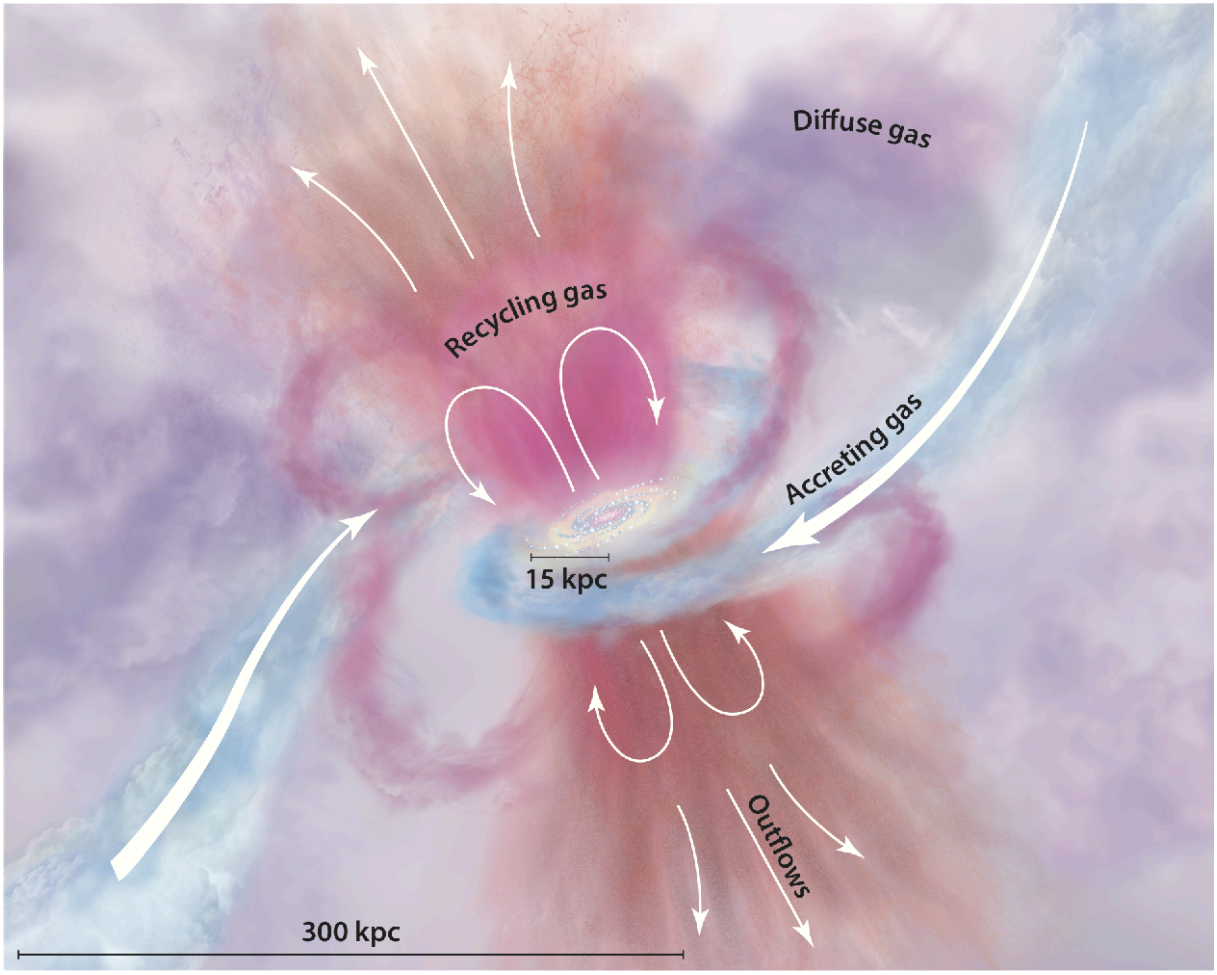

Figure 1.9: Artist's impression of the CGM. Pristine, metal-poor gas (in blue) is accreted from the IGM while outflows from hot, young stars and SNe (in brown) are ejected from the ISM. Some of the outflowing gas is recycled (in pink) on certain timescales after which it rains back onto the galaxy in a fountain flow fashion while some gas remains dormant (in purple) in the CGM (to be perhaps accreted at some later stage).
(Credits: Fig. 1 from Tumlinson et al. 2017)

not only of extremely rarefied pockets but also tenuous gas clouds that are associated with either the space between the galaxies (IGM) or the galactic haloes themselves (CGM). Depending on the chemical ionization and physical conditions, each cloud develops its own unique absorption property. The light rays emitted from a distant quasar along our line–of–sight (LOS) have to first encounter multiple gas blobs at various foreground redshifts (Putman et al., 2012). Since the area of cross-section of a light ray is minuscule as compared to that of a gas blob, this ray can be safely assumed to only pierce through the blob at a specific point. The local density and ionization conditions within each foreground gas cloud at its respective point of interjection is, thus, imprinted as a unique absorption feature in the emitted quasar spectrum (see Fig.1.10). Careful studies of such absorption spectra can reveal a lot about the local CGM properties associated with every foreground galaxy. The primary strength of this technique lies in its ability to detect very low column density (upto $N \simeq 10^{12}$ cm^{-2}; in comparison, typical ISM densities for H I are $N > 10^{20}$ cm^{-2}) gas.

The realization that the properties of the Far Ultraviolet Spectroscopic Explorer (FUSE) and its successor, Cosmic Origins Spectrograph aka COS (both operating in the UV wavelength range; Froning & Green 2009; Green et al. 2011) onboard Hubble Space Telescope (HST) are tailor made for LG and low-z CGM ($z < 1$) studies, opened up the floodgates for hordes of CGM-specific surveys. Studies of molecular hydrogen and metal lines in HVCs and IVCs (Richter et al., 2001a,b), ionized gas reservoir in our Galactic halo (Shull et al., 2009), absorption-line study of the Magellanic system (Barger et al., 2013; Fox et al., 2014), etc. have been completed. For external nearby galactic CGMs, the COS–Halos survey (Tumlinson et al., 2013a; Werk et al., 2013; Werk et al., 2014; Peeples et al., 2014; Werk et al., 2016a; Prochaska et al., 2017), which studied the CGM of L* galaxies (this was followed recently by the CGM^2 survey; Wilde et al. 2021; Tchernyshyov et al. 2022) was devised. Similar survey was designed for sub–L* galaxies (COS–Dwarfs; Bordoloi et al. 2014). Properties of CGM around galaxies falling in different sub-categories (Active Galactic Nuclei aka AGNs, starburst galaxies, Luminous Red Galaxies aka LRGs, etc.) have also been studied since then– COS–AGN (Berg et al., 2018), COS–Burst (Heckman et al., 2017), COS–LRG (Chen et al., 2018, 2019; Zahedy et al., 2019) and the Red Dead Redemption surveys (Berg et al., 2019). Studies concerning specific absorbers, like, for example, the COS CGM Compendium (Lehner et al., 2018) for probing the metallicity distribution of H I absorbers, CUBS survey (Chen et al., 2020; Zahedy et al., 2021; Cooper et al., 2021; Qu et al., 2022) for the Lyman Limit Systems (LLS), Damped Lyman Alpha (DLA) absorber studies (Rahmani et al., 2016) or the MAGIICAT survey (Nielsen et al., 2013) and COS–Weak survey (Muzahid et al., 2018) which studied the properties of weak Mg II absorbers have been carried out. Recent surveys like the COS–GASS (Borthakur et al., 2015, 2016) and COS–IGrM (McCabe et al., 2021) cater towards understanding the ISM–CGM and the CGM–IGM connection respectively.

The eBOSS emission line galaxy (ELG) survey (Lan & Mo, 2018), the CASBaH survey of Ne VIII lines tracing the warm-hot CGM (Burchett et al., 2019), the QSAGE survey of O VI absorbers (Bielby et al., 2019), etc. are some campaigns focused in the intermediate ($z < 2$) z-space. Instruments like the Keck Baryonic Structure Survey (KBSS), Keck Cosmic Web Imager (KCWI), Multi–Object Spectrometer For Infra-Red Exploration (MOSFIRE), Gemini, Large Binocular Telescope (LBT), Very Large Telescope/Multi Unit Spectroscopic Explorer (VLT/MUSE), VLT/X-Shooter, Atacama Large Millimeter Array (ALMA), etc. have been successfully used to explore the properties of the high-z CGM (Fu et al., 2016; Leclercq et al., 2017; Ginolfi et al., 2020; Muzahid et al., 2021; Langen et al., 2023). While quasars have been traditionally preferred for these LOS studies, other foreground sources such as fast radio bursts

(FRBs), gamma ray bursts (GRBs), other galaxies, etc. are being increasingly used since recent times (Adelberger et al., 2005; Steidel et al., 2010; Gatkine et al., 2019; Chen et al., 2020).

An alternative approach is to stack a large number of spectra (aka the stacking method) in a bid to clamp down the statistical noise and achieve a better signal–to–noise (S/N) ratio (York et al., 2006; Zhu & Ménard, 2013; Bordoloi et al., 2011). This, however, comes with a downside of washing out some of the kinematic and ionization information associated with individual CGMs.

One can also use the object galaxy's own starlight as a illuminating background source for studying its CGM. This is also known as down–the–barrel spectroscopy technique and is particularly useful in directly tracing inflows/outflows associated with a galaxy (Martin, 2006; Rubin et al., 2012; Henry et al., 2015). However, since the galactocentric radius traced by this method is unconstrained, baryon budget and distribution estimates are substantially difficult to obtain.

Hydrodynamical simulations can also be used as a tool to study the CGM. The CGM is a hub wherein a range of astrophysical processes (many of them rather complexly intertwined) take place. It is often impossible for observations to cleanly extract the effects of a particular process on the CGM, let alone quantify it. Controlled environments within simulations are able to solve this problem to a good extent. By introducing only a limited number of stringently modeled physical processes within mock environments, one can track their effects on the CGM with relative ease. Different types of simulations can be used for different problem tasks. However, one must be careful about the implications of the assumptions made regarding the sub-resolution physics on the CGM predictions and should, therefore, cautiously interpret subsequent results that are likely to be affected by this issue (Somerville et al., 2015).

1.3.2 Multi-phase nature

A particle can be ionized either by absorption of incoming photons from a variety of ionizing sources (aka photoionization or PI) or by electrons generated via inter-particle collisions (aka collisional ionization or CI) (Bergeron & Stasinska, 1986; Hummels et al., 2013). PI is almost purely dependant on the cloud density, as opposed to its temperature; meaning, particles in colder, denser clouds are more likely to be ionized via this mechanism. On the other hand, CI is strongly tied up with the temperature of a cloud i.e., hotter, less dense cloud particles will most likely be ionized via CI (Ji et al., 2020). Assuming that the subsequently ionized particles reach an equilibrium, we can define two distinct ionization states, photoionization equilibrium (PIE) and collisional ionization equilibrium (CIE) (Richter et al., 2008). PIE (CIE) gives a good estimate of the cloud density (temperature) and generally describes less (more) ionized species better. These processes are described in further detail in §2.4.1.

Multiple CGM observational campaigns over the last 20 years, both within and outside of the LG, have repeatedly detected a bunch of ions spanning a broad range of ionization potentials in a single absorber system within the galactic halo (Putman et al., 2011, 2012; Gupta et al., 2012; Fang et al., 2015). In other words, some of the less ionized tracer ions that are, by nature, at lower temperatures and higher densities have been found occupying similar regions as the highly ionized, hot and diffuse species within the same absorber cloud. An example of the above can be seen clearly in Fig. 1.11, wherein the absorption-line measurements for equivalent widths of H I and some other metal lines span similar radial extents. Different ionization states of these species is also indicative of different physical origins for each species.

While in principle, all metal line transitions that exist owing to the local ionization conditions within a galactic halo should have been observable, the laws of atomic physics govern that only a small subset of the resultant ions will ultimately fall in the detection range of our ground and/or

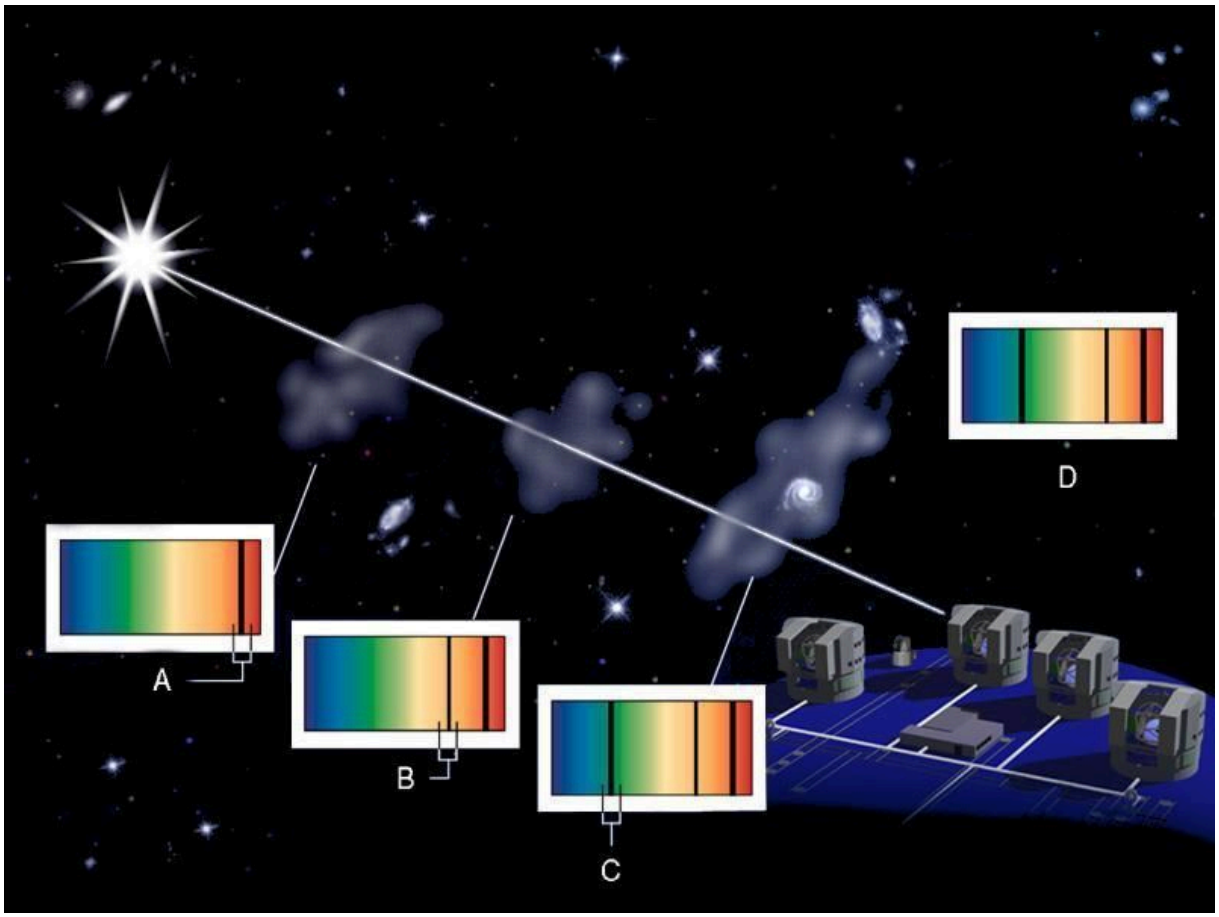

Figure 1.10: Working principle behind quasar absorption line spectroscopy. Light rays from a distant background quasar pierce through multiple gas clouds (some also associated with foreground galaxies) as they travel towards our telescopes on Earth. The ionization conditions within each cloud at the point of interjection results in an absorption signature that is unique to that particular intervening gas cloud (A, B and C). Thus, the ultimately observed quasar emission spectrum (D) consists of multiple absorption lines that are indicative of the properties of foreground gas clouds at various redshifts between the quasar and Earth.
(Credits: Ed Janssen, ESO)

space-based telescopes. This compels observers to unwillingly adopt assumption-dependent ionization models (such as PIE and CIE) to make up for the inherent lack of information. However, favoring one model completely over the other ends up suppressing the multi–phase nature of the CGM itself, something that is so vehemently proven across observations. Simulations, by nature, do not suffer from this problem of lack of information since the complete phase-space information of each gas cell is easily accessible. This has been leveraged excellently by various software codes to determine ionization fractions both as a function of temperature as well as density (Churchill et al., 2014, 2015; Hummels et al., 2017; Ferland et al., 2017; Röttgers et al., 2020). Resultant predictions are used, thereafter, to improve existing models that are better able to reproduce the observed complexity of the CGM. Newer approaches include using Bayesian (Haislmaier et al., 2020) and cloud–by–cloud modeling techniques (Sameer et al., 2021) for characterizing different CGM phases, attributing the relevant ionization mechanism using an approximate but unique temperature threshold on an ion–to–ion basis (Strawn et al., 2022), implementing an on–the–fly radiative transfer for obtaining a more realistic photoionization model (Katz, 2022), etc.

1.3.3 Insights about CGM

The advent of FUSE and HST in 1990s enabled extensive studies of the gas flows around MW (Wakker & van Woerden, 1997). These gas flows, whose signatures have been most evidently revealed by the HVCs (and later on also by the IVCs), are now known to exist in both neutral as well as ionized form, spanning different covering fractions on the sky (Desert et al., 1990; Wakker & van Woerden, 1991; Lockman et al., 2002; Fox et al., 2006; Shull et al., 2009; Lehner et al., 2012; Röhser et al., 2016; Bouma et al., 2019). Furthermore, the galactic fountain model (touted to be an important part of the larger galaxy evolution model), first favored in simulations (Kwak et al., 2009), has also recently been purported via scale-height measurement studies (Lehner et al., 2022). While much of the attention has been directed towards HVCs, a low-velocity component of the Galactic CGM has also been discovered (Peek et al., 2009; Zheng et al., 2019a; Bish et al., 2021). Giant X–ray and γ–ray bubbles, aka Fermi bubbles and eROSITA bubbles respectively, thought to be a strong evidence of the Galactic nuclear activity, have been found to extend all the way into the CGM of our galaxy (Su et al., 2019; Predehl et al., 2020). The availability of multiple QSO sightlines along with significant improvements in spectral resolution techniques enabled an unprecedented view into the CGM of Andromeda galaxy (Lehner et al., 2020). Other multi-sightline observations in the LG and low-z Universe have been instrumental in constraining key kinematic properties of the gas, albeit at lower spectral resolutions (Bowen et al., 1997; Bordoloi et al., 2014; Liang & Chen, 2014; Johnson et al., 2017; Richter et al., 2017; Zheng et al., 2019b, 2020).

Using quasar pairs and triplets has enabled us to constrain the size of the CGM (Mintz et al., 2022) as well as reveal the properties of extended discs and outflowing gas structures (Beckett et al., 2022). Moreover, gas chemical enrichment patterns using background lensed quasars (Okoshi et al., 2021), detection of giant Ly-α halos and metal content around high-z galaxies using lensed galaxy clusters (Chen et al., 2021) and galaxies (Solimano et al., 2022; Méndez-Hernández et al., 2022) and examining the LOS orientation effects on observed equivalent widths around intermediate-z galaxies using gravitational arcs (Fernandez-Figueroa et al., 2022) have all been possible recently.

Our understanding about the evolution of CGM around galaxies in earlier epochs has improved massively during the last decade. Extended Ly-α halos and emission from cosmic web have been detected via surveys like MUSE EDF, MUSE HUDF, FLASHES, SUPERCOLD-CGM and REQUIEM (Farina et al., 2019; Leclercq et al., 2020; O'Sullivan et al., 2020; Bacon et al., 2021; Li et al., 2021b). Studies focusing on the properties of galaxies surrounding strong

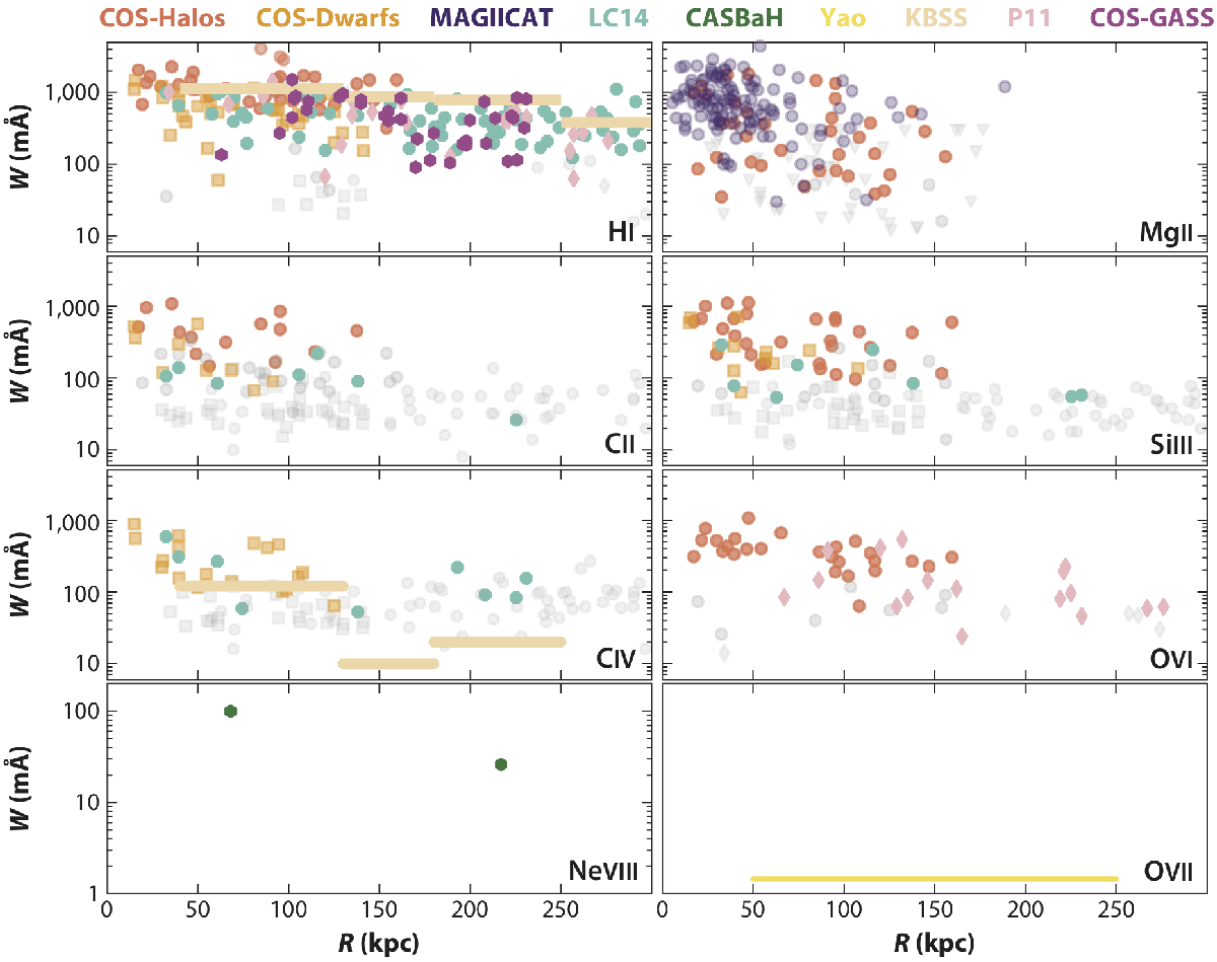

Figure 1.11: Radial equivalent width profiles for different ions tracing the multi–phase CGM in different observational surveys (COS–Halos, Tumlinson et al. 2013a; Werk et al. 2013; COS–Dwarfs, Bordoloi et al. 2014; COS–GASS, Borthakur et al. 2015; MAGIICAT, Nielsen et al. 2013; Liang & Chen 2014; KBSS, Rudie et al. 2012; Turner et al. 2015; CASBaH, Tripp et al. 2011; Prochaska et al. 2011; Yao et al. 2012). Note how these vastly different ion species are detected within a similar radial range, indicative of co-habitation of differing gas phases. (Credits: Fig. 4 from Tumlinson et al. 2017)

absorption-line systems (Lofthouse et al., 2020), kinematic and metal enrichment properties (Travascio et al., 2020), environment of high-z DLAs (Mackenzie et al., 2019), detection of pristine cold and highly ionized CGM phases (Cooper et al., 2019), detection and characterization of O I and C II halos (Becker et al., 2019; Fujimoto et al., 2019) as well as shedding light on the ISM/CGM/IGM connection (Codoreanu et al., 2018; Du et al., 2021) have been successfully carried out.

In this context, one of the earliest triumphs of simulations has been the successful reproduction of the declining trend of number of absorber clouds from early to late epochs in the Ly-α forest (Hernquist et al., 1996). Reproducing the rich, multi–phase structure of the CGM (in particular, the cold-dense gas) has been especially challenging due to a lack of clear convergence in simulations at low enough spatial scales at which these cold clouds are generally observed (Stern et al., 2016; Rubin et al., 2018). However, recent improvements in cosmological simulations, tailored specifically towards improving CGM resolution (while efficiently maintaining the computational cost), have reduced this problem to an appreciable extent (Suresh et al., 2018; Peeples et al., 2019; van de Voort et al., 2019; Hummels et al., 2019; Rey et al., 2023). The overall distribution trend of cold and hot gas around galaxies and galaxy clusters has been well reproduced in all simulations (Rhodin et al., 2019; Butsky et al., 2019; Lochhaas et al., 2020), although most of them under-predict the amount of gas at distances away from galaxies (Oppenheimer et al., 2018a; Ji et al., 2020; Appleby et al., 2021; Damle et al., 2022).

Modeling feedback properly has been another grave concern for simulators. However, many novel approaches towards accurately modeling gas flows and resultant feedback promise to soon alleviate this issue. For example, Oku et al. 2022 demonstrated the need for incorporating not just thermal but also mechanical feedback from unresolved SNe bubbles in sub-grid models for ensuring a better agreement with the K–S relation. Weinberger & Hernquist 2023 used multi–component fluid hydrodynamics in order to efficiently treat the resolved and unresolved regions without having to grapple with the spatial resolution issues that plague particularly the cold phases. Recent ISM models like TIGRESS, INFERNO, Arkenstone, etc. found that galactic outflows are characterized by a slow, cold, mass ejecting component and a fast, hot, energy ejecting component (Kim et al., 2020; Andersson et al., 2022; Smith et al., 2023).

1.4 Thesis outlook

As highlighted earlier, the overarching purpose of this thesis is to use simulations as a tool to study some of the ways in which the CGM affects and, in turn, gets affected by various galactic processes. This thesis includes a compilation of three case studies (listed as Chapters), each using a specific kind of simulation dataset, employed to ultimately probe a certain aspect of the CGM–galaxy synergy. I present a brief summary of the key aspects and science questions targeted by each use case below.

Chapter 2: Gas in the Local Group Simulations

Key aspects: I use a suite of high-resolution Local Group constrained simulations, HESTIA. The unique proposition of these simulations is the fact that the 6D spatio–kinematic observational measurements for thousands of galaxies in the Local Universe are used as an input for accurately modeling our Local neighbourhood, in addition to the conventional large-scale cosmography that is, as such, a hallmark of any state–of–the–art cosmological simulation.

Science questions posed–

1. How do various CGM phases in HESTIA look like?
2. Is HESTIA able to reproduce existing observational CGM measurements of LG and low-z galaxies?
3. If there exist some discrepancies between the simulated and observed CGM properties, what could be the reasons?

Chapter 3: Bridge Formation in Merging Galaxies

Key aspects: I use a set of four major merger zoom-in simulations to study its effects on the gas flows around the progenitor system through the merger process. These simulations are a re-run of the large volume Illustris simulations, with extra resolution elements focused on a sub-volume centered around the merger site.

Science questions posed–

1. Does a bridge always form during a major merger event? Does cold, star-forming gas land up in such bridges?
2. Is there any clear link between the gas originating from the CGM regions and merger–induced star formation in the system?
3. How do the gas kinematic profiles look like?

Chapter 4: How Satellites Influence the Cold Circumgalactic Medium in TNG50 Simulations

Key aspects: I use a sample of L* galaxies in TNG50, the highest resolution simulation suite from the IllustrisTNG project. In this study, I focus on the effects of the properties of a global satellite population on the cold halo gas of the respective parent galaxies.

Science questions posed–

1. To what extent does the overall satellite population impact the extended cold CGM density profiles of galactic halos spanning a range of halo masses?
2. Which of the global satellite properties affect the cold halo gas the most (i.e. which is the most impactful factor)?
3. Is the most impactful factor same or different for low mass and high mass halos?

Chapter 2

Gas in the Local Group Simulations

The contents of this chapter are based on the first–author publication, Damle et al. 2022, MNRAS 512, 3717.

Title: *Cold and hot gas distribution around the Milky–Way – M31 system in the HESTIA simulations.*

Complete author list: **Mitali Damle**, Martin Sparre, Philipp Richter, Maan H. Hani, Sebastián Nuza, Christoph Pfrommer, Robert J J Grand, Yehuda Hoffman, Noam Libeskind, Jenny Sorce, Matthias Steinmetz, Elmo Tempel, Mark Vogelsberger, Peng Wang.

My contributions in the context of this chapter are as follows–

- I have led the scientific analysis, co–ordinated the contributions of co–authors and have published the paper as the leading author.
- The analysis pipeline used for this chapter has been developed in a code repository by me, with the help of Dr. Martin Sparre.[1].
- Generated all the figures presented in this chapter.

2.1 Abstract

Recent observations have revealed remarkable insights into the gas reservoir in the circumgalactic medium (CGM) of galaxy haloes. In this paper, we characterise the gas in the vicinity of Milky Way and Andromeda analogues in the HESTIA (High resolution Environmental Simulations of The Immediate Area) suite of constrained Local Group (LG) simulations. The HESTIA suite comprise of a set of three high-resolution AREPO–based simulations of the LG, run using the Auriga galaxy formation model. For this paper, we focus only on the $z = 0$ simulation datasets and generate mock skymaps along with a power spectrum analysis to show that the distributions of ions tracing low-temperature gas (H I and Si III) are more clumpy in comparison to warmer gas tracers (O VI, O VII and O VIII). We compare to the spectroscopic CGM observations of M31 and low-redshift galaxies. HESTIA under-produces the column densities of the M31 observations, but the simulations are consistent with the observations of low-redshift galaxies. A possible

[1]The framework for Cloudy modeling and resulting ion tables (modified version of the ion tables developed by Dr. Martin Sparre were used) were adopted from Hani et al. (2018).

explanation for these findings is that the spectroscopic observations of M31 are contaminated by gas residing in the CGM of the Milky Way.

2.2 Introduction

Our understanding of the tenuous gas reservoir surrounding galaxies, better known as the circumgalactic medium (CGM), has dramatically improved since its first detection, back in the 1950s (Spitzer Jr, 1956; Münch & Zirin, 1961; Bahcall & Spitzer Jr, 1969). The CGM is a site through which pristine, cold intergalactic medium (IGM) gas passes on its way into the galaxy and it is also the site where metal-enriched gas from the interstellar medium (ISM) gets dumped via outflows and winds (Anglés-Alcázar et al., 2017; Suresh et al., 2019). CGM gas is often extremely challenging to detect in emission due to its low column densities. Therefore, most of our knowledge about its nature stems from absorption line studies (Werk et al., 2014; Tumlinson et al., 2017) of quasar sightlines passing through the CGM of foreground galaxies.

Observational datasets from instruments like Far Ultraviolet Spectroscopic Explorer (FUSE, see Moos et al. 2000; Savage et al. 2000; Sembach et al. 2000), Space Telescope Imaging Spectrograph (HST–STIS, see Woodgate et al. 1998; Kimble et al. 1998) and Cosmic Origins Spectrograph (HST–COS, see Froning & Green 2009; Green et al. 2011) have revolutionised our understanding of not just the MW CGM but the CGMs of other galaxies as well (Richter et al., 2001b; Lehner et al., 2012; Herenz et al., 2013; Tumlinson et al., 2013b; Werk et al., 2013; Fox et al., 2014; Werk et al., 2014; Richter et al., 2017).

Numerous studies through the last decade involving quasar absorption line studies of various low and intermediate ions tracing a substantial range in temperatures and densities have revealed the complex, multiphase structure of the CGM (Nielsen et al., 2013; Tumlinson et al., 2013b; Bordoloi et al., 2014; Richter et al., 2016; Lehner et al., 2018). Lehner et al. (2020) have gone a step ahead in quasar absorption line studies by obtaining multi-ion deep observations of several sightlines heterogeneously piercing the CGM of a single galaxy (M31).

Recent studies conclude that a significant percentage of galactic baryons could lie in the warm-hot virialized gas phase (Peeples et al., 2014; Tumlinson et al., 2017), increasingly emphasizing the importance of high ions in describing the CGM mass budget (Tumlinson et al., 2017). O VI, which is an important tracer of the warm-hot CGM ($T \sim 10^{5.5}$ K), has been detected in gas reservoirs around star forming galaxies in Far UV (Tumlinson et al., 2011). Even hotter CGM gas, traced primarily by O VII and O VIII, has been detected around galaxies in X–ray studies (Das et al., 2019a; Das et al., 2020b). Apart from these high ions, Coronal Broad Lyman alpha absorbers could also contribute towards constituting the hot CGM (Richter, 2020).

Significant progress is also being made via systematic CGM studies targeting diverse galaxy samples which provide insightful views into the synergy between the CGM and the evolution of its host galaxy. The presence of warm gas clouds around late-type galaxies at low redshift (Stocke et al., 2013), the impact of starbursts (Borthakur et al., 2013) and AGN (Berg et al., 2018), evidence of a bimodal metallicity distribution in the form of metal-poor, pristine and metal-rich, recycled gas streams (Lehner et al., 2013) have given us a peek into the interplay between the CGM and its parent galaxy. The theory of galactic winds injecting metal-rich gas from the ISM out to the CGM (Hummels et al., 2013; Ford et al., 2013) is now being supported by observational evidence (Rupke et al., 2019).

Despite all the advancements in the past few years, limited sightline observations and our technological inability to probe substantially lower column densities in the CGM of other galaxies indicate that we cannot yet fully rely solely on these studies to give us a complete picture of the workings of the CGM (Tumlinson et al., 2017). Therefore, studying the MW and the LG

CGM (which will always have better CGM datasets as compared to those for non-LG galaxies) assumes a great importance in this context.

High-velocity, warm O VI gas has been observed extensively around the MW (Sembach et al., 2003; Savage et al., 2003; Wakker et al., 2003). HST UV spectra of a list of low and intermediate ions have further helped us track the expanse of high-velocity clouds (HVCs) around our Galaxy (Lehner et al., 2012; Herenz et al., 2013). A low-velocity, cool-ionized CGM component has also been detected recently around the MW (Zheng et al., 2019a; Bish et al., 2021). Additionally, a long hypothesised hot, diffuse galactic gas phase (Gupta et al., 2012) has been observed using the highly ionized O VII and O VIII ions (Miller & Bregman, 2015; Das et al., 2019b). While the observations of the Galaxy's CGM certainly provide us with more sightlines and enable us to detect slightly lower column densities as compared to other galaxies' CGMs, galactic CGM observations are fraught with a greater possibility of contamination from sources lying in the line–of–sight of our observations, thereby masking the true nature of our galaxy's CGM.

With the advent of the above observations, complementary studies with regards to the CGMs around the galaxies, generated using cosmological galaxy formation simulations, started gaining momentum (Vogelsberger et al., 2020). Cosmological simulations, in general, have been extremely successful in replicating many pivotal observational properties central to the current galaxy formation and evolution model (Vogelsberger et al., 2014b,a). These include galaxy morphologies (Ceverino et al., 2010; Aumer et al., 2013; Marinacci et al., 2014; Somerville & Davé, 2015; Grand et al., 2017), galaxy scaling relations (Booth & Schaye, 2009; Angulo et al., 2012; Vogelsberger et al., 2013), $M_*/M_{\rm halo}$ relationship (Behroozi et al., 2010b; Moster et al., 2013), and star formation in galaxies (Behroozi et al., 2013; Agertz & Kravtsov, 2015; Sparre et al., 2015; Furlong et al., 2015; Sparre et al., 2017; Donnari et al., 2019). Like observations, cosmological simulations provide different approaches to quantify the typical baryon and metal budgets of galaxies (Ford et al., 2014; Schaye et al., 2015; Suresh et al., 2016; Hani et al., 2019; Tuominen et al., 2021). They reveal how the motions of gas manifests itself in various forms like inflow streams from the IGM, or replenished outflows from the galaxy out to its CGM, or stellar winds or supernovae and AGN feedback (Nelson et al., 2019c; Wright et al., 2021; Appleby et al., 2021).

Given that the computational studies of the CGM have provided an enormous insight into the evolution of galaxies, it is worthwhile to look back to our local environment, i.e. the Local Group (LG). Apart from tracking the formation history of MW–M31 (Ibata et al., 2013; Hammer et al., 2013; Scannapieco et al., 2015) and the accretion histories of MW-like galaxies (Nuza et al., 2019), our LG, over the past decade, has proved to be an ideal site for studies involving ΛCDM model tests (Klypin et al., 1999; Wetzel et al., 2016; Lovell et al., 2017), dwarf galaxy formation and evolution (Tolstoy et al., 2009; Garrison-Kimmel et al., 2014a; Pawlowski et al., 2017; Samuel et al., 2020), effects of environment on star formation histories of MW-like galaxies (Creasey et al., 2015), local Universe re-ionization (Ocvirk et al., 2020), and the cosmic web (Nuza et al., 2014; Forero-Romero & González, 2015; Metuki et al., 2015). Observational constraints of the Local Universe have resulted in an emergence of constrained simulations, where the large-scale structure resembles the observations (Nuza et al., 2010; Libeskind et al., 2011; Knebe et al., 2011; Di Cintio et al., 2013; Nuza et al., 2013). It is also worthwhile to note that such LG constrained simulations might be the setups best equipped to separate out any sources of possible contamination towards the MW CGM.

A simulation of a Milky-Way–like galaxy in a constrained environment was done by the CLUES (Constrained Local UniversE Simulations) project (Gottlöber et al., 2010), which were one of the first cosmological simulations to include a realistic local environment within the large-scale LG structure. Nuza et al. (2014) carried out a study on the $z = 0$ gas distribution around

MW and M31 in the CLUES simulation to characterize the effect of cosmography on the LG CGM. They analysed the cold and hot gas phases, computed their masses and accretion/ejection rates, and later compared their results with the absorption–line observations from Richter et al. (2017).

We build upon the approach adopted in Nuza et al. (2014) by analysing the constrained LG simulations, HESTIA (Libeskind et al., 2020), which in comparison to the original CLUES simulations have better constrained initial conditions. In HESTIA we, furthermore, use the Auriga galaxy formation model (Grand et al., 2017), which produces realistic Milky-Way–mass disc galaxies. In comparison to the previous CLUES simulations, we carry out a more extensive analysis to predict column densities of a range of tracer ions (H I, Si III, O VI, O VII and O VIII) selected to give a complete view of the various gas phases in and around the galaxies. This helps us, for example, with the interpretation of absorption studies of the LG CGM gas.

The aim of this paper is to provide predictions for absorption–line observations of the gas in the LG. We achieve this by studying the gas around LG galaxies in the state–of–the–art constrained magnetohydrodynamical (MHD) simulations, HESTIA (High resolution Environmental Simulations of The Immediate Area). The comparison between HESTIA and some of the recent observations makes it possible to constrain the galaxy formation models of our simulations.

This paper is structured as follows: §2.4 describes the analysis tools and the simulation. We present our results in §2.5, which include Mollweide projection maps (§2.5.1), power spectra (§2.5.5) and radial column density profiles (§2.5.6). We compare our results with some of the recent observations and other simulations in §2.5.7 and 2.5.8. Further, we discuss the implications of our results in the context of current theories about CGM and galaxy formation and evolution in §2.6. We also analyse the possibility of MW's CGM gas interfering with M31's CGM observations in §2.6.1. Finally, we sum up our conclusions and provide a quick note about certain caveats and ideas to be implemented in future projects (§2.7).

2.3 Next generation CLUES: HESTIA

2.3.1 Initial conditions: An improvement over CLUES simulations

The small scale initial conditions are obtained from a sampling of the peculiar velocity field. The CosmicFlows-2 catalog (Tully et al., 2013), used to derive peculiar velocities, provides constraints up to distances farther than that was available for the predecessor CLUES simulation. Reverse Zel'dovich technique (Doumler et al., 2013) handles the cosmic displacement field better, hence offering smaller structure shifts. A new technique, bias minimisation scheme (Sorce, 2015), has been employed for HESTIA simulations to ensure that the LG characteristic objects (e.g. Virgo cluster) have proper mass. The above mentioned new elements (see Sorce et al. 2015 for further details) in conjunction with the earlier aspects of constrained realization (Hoffman & Ribak, 1991) and Wiener Filter (Sorce et al., 2013) offer HESTIA a clear edge over the previous generation CLUES simulations.

Low-resolution, constrained, dark-matter only simulations are the fields from which halo pairs resembling our LG were picked up for intermediate and high resolution runs. Note that only the highest resolution realizations (those labelled 09−18, 17−11 and 37−11) are used for our analysis in this paper. The first and second numbers in the simulation nomenclature represent the seed for long and short waves, respectively, both of which together constitute to the construction of the initial conditions. Two overlapping $2.5h^{-1}$ Mpc spheres centred on the two largest $z = 0$ LG members (MW and M31) represent the effective high resolution fields which are populated with 8192^3 effective particles. The mass resolution for the DM particles

(gas cells) in the high-resolution simulations is 1.5×10^5 $M_\odot$ (2.2×10^4 $M_\odot$), while the softening length (ϵ) for the DM is 220 pc.

While the entire process of selecting cosmographically correct halo pairs involves handpicking MW–M31 candidates with certain criteria (halo mass, separation, isolation) that lie within the corresponding observational constraints, there are yet a few other bulk parameters (M_* vs $M_{\rm halo}$, circular velocity profile) and dynamical properties (total relative velocities) which are organically found to agree well with observations (Guo et al., 2010; Van der Marel et al., 2012; McLeod et al., 2017).

2.3.2 AREPO MHD Solver

The moving-mesh magneto-hydrodynamic code, AREPO (Springel, 2010; Pakmor et al., 2016b), has been employed for the higher resolution runs. AREPO, which is based on a quasi-Lagrangian approach, uses an underlying Voronoi mesh (in order to solve the ideal MHD equations) that is allowed to move along the fluid flow, thus seamlessly combining both Lagrangian as well as Eulerian features in a single cosmological simulation.

The code follows the evolution of magnetic fields with the ideal MHD approximation (Pakmor et al., 2011; Pakmor & Springel, 2013) that has been shown to reproduce several observed properties of magnetic fields in galaxies (Pakmor et al., 2017; Pakmor et al., 2018) and the CGM (Pakmor et al., 2020). Cells are split (i.e. refined) or merged (i.e. de-refined) whenever the mass of a particular mesh cell varies by more than a factor of two from the target mass resolution.

2.3.3 Auriga galaxy formation model

We adopt the Auriga galaxy formation model (Grand et al., 2017). A two-phase model is used to describe the interstellar medium (ISM), wherein a fraction of cold gas and a hot ambient phase is assigned to each star-forming gas cell (Springel & Hernquist, 2003). This two-phase model is enabled for gas denser than the star formation threshold (0.13 $\rm cm^{-3}$). Energy is transferred between the two phases by radiative cooling and supernova evaporation, and the gas is assumed to be in pressure equilibrium following an effective equation of state (similar to fig. 4 in Springel et al. 2005a). Stellar population particles are formed stochastically from star-forming cells. Black holes (BH) formation and their subsequent feedback contributions are also included in the Auriga framework. Magnetic fields are included as uniform seed fields at the beginning of the simulation runs ($z = 127$) with a comoving field strength of 10^{-14} G, which are amplified by an efficient turbulent dynamo at high redshifts (Pakmor et al., 2017). Gas cooling via primordial and metal cooling (Vogelsberger et al., 2013) and a spatially uniform UV background (Faucher-Giguère et al., 2009) are included. Our galaxy formation model produces a magnetized CGM with a magnetic energy, which is an order of magnitude below the equipartition value for the thermal and turbulent energy density (Pakmor et al., 2020).

In our galaxy formation model, the CGM experiences heating primarily from sources such as SNe Type II, AGN feedback (see fig. 17 in Grand et al. 2017), stellar winds and time-dependent spatially uniform UV background. Stellar and AGN feedback are especially important since they heat and deposit a substantial amount of metals as well as some baryonic material into the CGM (Vogelsberger et al., 2013; Bogdán et al., 2013).

We do not include extra-planar type Ia SNe or runaway type II SNe. We expect the uncertainty due to not including these in our physics model to be extremely small with respect to that due to treating the ISM with an effective equation of state (see for example fig. 10 in Marinacci et al., 2019).

Quasar mode feedback is known to suppress star formation in the inner disc of galaxies (particularly relevant at early times) while the radio mode feedback is known to control the ability of halo gas to cool down efficiently at late times (hence relevant in the context of this study). In general, radio mode feedback is instrumental in keeping the halo gas hot, which in turn results in lesser cool gas in the CGM (see fig. 17 from Grand et al. 2017; also fig. 9 from Irodotou et al. 2021). Hani et al. 2019 studied the effect of AGN feedback on the ionization structure within the CGM of a sample of MW–like galaxies from the Auriga simulations. On the whole, they concluded that in comparison to the galaxies without any AGN feedback, the CGMs of galaxies with an AGN feedback exhibited lesser column densities for low and intermediate ions while the column densities for high ions remained largely unchanged. While the presence of an ionizing AGN radiation field in the CGM is responsible for slightly reduced abundances of low ions, the abundances of high ions like O VI mainly arise from the halo virial temperatures and are hence, largely unaffected by the AGN feedback effects.

We use the SUBFIND halo finder (Springel et al., 2001; Dolag et al., 2009; Springel et al., 2021) to identify galaxies and galaxy groups in our analysis. When the simulations were run, black holes were seeded in haloes identified by SUBFIND.

Our simulations and analysis consistently use the Planck 2014 best-fit cosmological parameters (Planck Collaboration et al., 2014), which have the following values: $H_0 = 100h$ km s^{-1} Mpc^{-1}, where $h = 0.677$, $\sigma_8 = 0.83$, $\Omega_\Lambda = 0.682$, $\Omega_\mathrm{M} = 0.270$ and $\Omega_\mathrm{b} = 0.048$.

2.3.4 HESTIA high-resolution realizations

Table 2.1 lists key properties for the three realizations of the MW–M31 analogues, which we consider in this paper. We define R_{200} as the radius within which the spherically averaged density is 200 times the critical density of the universe. M_{200} is the total mass within R_{200}. The overall M_{200}, M_*, M_gas and R_{200} values for our MW–M31 analogues are broadly consistent with typical observational estimates (see fig. 7 in Libeskind et al. 2020; see also Bland-Hawthorn & Gerhard 2016; Yin et al. 2009). Among the two most massive galaxies in each of our LG simulations, the galaxy with a larger value of M_{200} is identified as M31, while the other galaxy is identified as MW.

Table 2.1: Properties of MW and M31 analogues at $z = 0$ for the three LG HESTIA simulations. The simulations are referred to as 09−18, 17−11 and 37−11, following the nomenclature used in (Libeskind et al., 2020). We show the *LG distance* (defined as the distance of a galaxy from the geometric centre of the line that connects MW and M31), the mass in stars and gas bound to each galaxy, and R_{200} and M_{200} of each galaxy. SFR is the star formation rate for all the gas cells within twice the stellar half mass radius. $Z_{\rm SFR}/Z_{\odot}$ is the SFR-weighted gas metallicity, normalized with respect to the solar metallicity. We also list the observational estimates for MW from Bland-Hawthorn & Gerhard (2016) as well as that for M31. The observational estimate for R_{200} of the MW is calculated as $R_{200} = 1.3 \times R_{\rm vir}$ (following Van der Marel et al. 2012) from the $R_{\rm vir}$ value for MW given in Bland-Hawthorn & Gerhard (2016).

	09−18		17−11		37−11		Obs. estimates for MW	Obs. estimates for M31
	MW	M31	MW	M31	MW	M31	(from Bland-Hawthorn & Gerhard 2016)	
LG distance (kpc)	433.19	433.19	338.01	338.01	425.29	425.29	-	-
log M_* ($M_\odot$)	10.91	11.11	11.06	11.08	10.77	10.72	10.69 ± 0.088	10.84-11.10 [a]
log $M_{\rm gas}$ ($M_\odot$)	11.08	11.20	10.92	11.21	10.76	10.87	10.92 ± 0.067	9.78 [b]
log M_{200} ($M_\odot$)	12.29	12.33	12.30	12.36	12.00	12.013	12.05 ± 0.096	12.10 [c]
R_{200} (kpc)	262.54	270.40	264.48	277.46	211.25	212.81	216.93 ± 23.075	230 [3]
log $M_{\rm BH}$ ($M_\odot$)	8.1314	8.277	7.7362	8.1838	7.7787	7.5840	6.6232 ± 0.02	8.15 [d]
SFR ($M_\odot$ yr^{-1})	9.476	3.757	3.600	4.754	1.193	2.337	1.650 ± 0.19	0.25-1.0 [e]
M_*/SFR (Gyr)	8.577	34.29	31.89	25.29	49.36	22.46	-	-
$Z_{\rm SFR}/Z_{\odot}$	3.26	3.04	3.55	3.05	3.26	3.31	-	-

[a] Sick et al. (2015); Rahmani et al. (2016)
[b] Yin et al. (2009)
[c] Lehner et al. (2020)
[d] Schiavi, Riccardo et al. (2020)
[e] Williams (2003); F. Williams (2003); Barmby et al. (2006); Tabatabaei, F. S. & Berkhuijsen, E. M. (2010); Ford et al. (2013); Lewis et al. (2015); Rahmani et al. (2016); Boardman et al. (2020)

2.3.5 Global properties of the LG analogues

The HESTIA MW analogues reveal $M_{\rm BH}$ values an order of magnitude larger than that stated in the observations of Bland-Hawthorn & Gerhard (2016). This does not, however, necessarily mean that the AGN feedback has been too strong during the simulations, because we see realistic MW stellar masses at $z = 0$. For the CGM, which we study extensively in this paper, the overestimated MW BH masses therefore do not necessarily indicate too strong AGN feedback. We also note that our MW analogues are still consistent with MW–mass galaxies (see fig. 5 of Savorgnan et al. 2016).

Similarly, the SFR at $z = 0$ is also comparable to or larger than observed. We note that the SFR of M31 is larger by a factor of a few in HESTIA in comparison to observations. The generation of winds is closely tied to the SFR in our simulations, so it is possible that the role of outflows is over-estimated by HESTIA in comparison to the $z = 0$ observations of M31. Integrated over the lifetime of the galaxies, HESTIA does, however, produce realistic stellar masses at $z = 0$[2]. We, therefore, do not regard the discrepancy between the $z = 0$ SFR as more problematic than the uncertainty already in place by using an effective model of winds, or, for example, by the simulated M31 galaxies having different merger histories or disc orientations than the *real* M31. In comparison to the SFR values from Bland-Hawthorn & Gerhard 2016, other observational studies report slightly larger SFR values for MW (1-3 $M_\odot$ yr^{-1}, 3-6 $M_\odot$ yr^{-1}, 1-3 $M_\odot$ yr^{-1}, 1.9 $\pm$ 0.4 $M_\odot$ yr^{-1}: McKee & Williams 1997; Boissier & Prantzos 1999; Wakker et al. 2007, 2008; Chomiuk & Povich 2011), but these are nevertheless lower than the HESTIA values. We also notice that the MW analogue in the 09−18 simulation exhibits a substantially higher SFR than others. However, all M_*/SFR values (except those for the MW analogue in 09−18 simulation) for our sample are still well within the observational constraints of normal star-forming galaxies with masses comparable to the MW and M31 (see fig. 8 in Speagle et al. 2014). Thus, overall, the HESTIA galaxies seem to be slightly more star-forming in comparison to the observations but this does not induce larger uncertainties in our analysis than already present due to multiple other factors which we highlighted earlier.

We also note that the SFR-averaged gas metallicity is consistent with the M31 measurement in Sanders et al. (2012).

2.4 Analysis

In this section, we describe the methodology adopted in order to compute the ion fractions in the CGM, underlying assumptions, their possible effects on the interpretation of our results and the process of creating Mollweide maps from the computed ion fractions. We make use of the photo-ionization code CLOUDY to obtain ionization fractions for the tracer ions H I, Si III, O VI, O VII and O VIII, and we generate Mollweide projection maps using the HEALPY package to create mock observations.

2.4.1 Ion fractions from Cloudy

Two principal ionization processes in the CGM and IGM are collisional ionization and photo-ionization (Bergeron & Stasinska, 1986; Prochaska et al., 2004; Turner et al., 2015). An equi-

[2]At a speculative node, it is possible that a too high SFR could be compensated by too high AGN feedback, and this would result in a stellar mass consistent with observations but at the same time a too massive BH mass. Addressing such a hypothesis would require running additional simulations which is beyond the scope of this paper.

librium scenario is generally assumed in both these processes thus resulting in a collisional ionization equilibrium (CIE) and a photo-ionization equilibrium (PIE).

Such a bi-modal attempt in the ionization modelling has to date proved to be sufficient to well explain the co-habitation of both high and low ions in different phases at the same time within a common astrophysical gas environment. Generally, high ions (e.g., O VII, O VIII, Ne VIII, Mg X) are found to be better modelled via CIE while the low and intermediate ions (e.g., Fe II, N I, S II) lend themselves better to PIE, owing to the temperatures in the various gas phases and the strength and shape of the UV background field. CIE, which assumes that the ionization is mainly carried by electrons, can be well characterised (Richter et al., 2008) using the relation,

$$f_{\rm H\,I,coll} = \frac{\alpha_{\rm H}(T)}{\beta_{\rm H}(T)}, \tag{2.1}$$

where $f_{\rm H\,I,coll}$ is the neutral hydrogen fraction in CIE, $\alpha_{\rm H}(T)$ is the temperature dependent recombination rate of hydrogen and $\beta_{\rm H}(T)$ is the collisional ionization coefficient, both for hydrogen.

PIE, on the other hand, assumes photons to be the primary perpetrators and can be better described (Richter et al., 2008) as,

$$f_{\rm H\,I,photo} = \frac{n_{\rm e}\alpha_{\rm H}(T)}{\Gamma_{\rm H\,I}}, \tag{2.2}$$

where $f_{\rm H\,I,photo}$ is the neutral hydrogen fraction in PIE, $n_{\rm e}$ is the electron density and $\Gamma_{\rm H\,I}$ is the photo-ionization rate.

We determine the ionization fractions using the CLOUDY code (version C17; Ferland et al. 2017), which is designed to model photo-ionization and photo-dissociation processes by including a wide combination of temperature-density phases for a list of elements, in order to simulate complex astrophysical environments realistically and produce mock parameters and outputs. The temperature of each AREPO gas cell is given as input to CLOUDY (in practice, we use lookup tables to speed up the calculation, see below), which determines the ionization state in post-processing. For the star-forming gas cell we directly set all atoms to be neutral, because most of the mass is in the cold phase.

We include both CIE and PIE in the modelling code. The UV background from Faucher-Giguère et al. (2009) is used. Self-shielding prescriptions, in particular for H I gas in denser regions, are adopted from Rahmati et al. (2013). We do not include AGN continuum radiation for the sake of simplicity. While excluding the AGN radiation might affect the ion fractions in regions close to the galaxy (e.g. ISM), it is much less likely to have any dominant impact in the CGM. Our CLOUDY modelling is identical to that introduced in Hani et al. (2018), with the only difference that we use a finer resolution grid for the output tables. In our analysis, we impose a metallicity floor of $10^{-4.5}$ $Z_{\odot}$ to avoid metallicity values lower than those present in our CLOUDY tables. Note that we do not include photo-ionization from stars or AGN in this work.

For this paper, we focus on the five tracer ions listed in Table 2.2 for which we generate mock observables; two of which are largely representative of the cold and cool-ionized ($T \sim 10^4 - 10^5$ K) gas (H I and Si III) and the three ions representative of the warm-hot ($T > 10^{5.5}$ K) gas (O VI, O VII and O VIII). These five ions have a host of robust corresponding observational CGM data as well (e.g. Liang & Chen 2014; Werk et al. 2014; Johnson et al. 2015; Richter et al. 2016, 2017; Lehner et al. 2020).

Si III may also be produced by photoionization at a much lower temperature than 10^5 K. However, neither does our ionization modeling include photoionization from stars nor is it optimal in describing gas colder than 10^4 K. Therefore, this remains an uncertainty in our ionization modelling.

Table 2.2: For the ions considered in our ionization analysis, we list the wavelength of the strongest tracer ion transitions, the ionization energy, characteristic temperature and characteristic density (we quote the ionization energy values from Edlén 1979; Martin & Zalubas 1983; Johnson & Soff 1985; Drake 1988; Jentschura et al. 2005– obtained from the NIST Database; remaining values are quoted from the supplemental fig. 4 in Tumlinson et al. 2017). Ionization energy is the energy required to ionize a species into its corresponding higher ion state (in this case, each of the five ions included in our analysis). Our ionization modelling is carried out with CLOUDYv17.

Ion	Wavelength (Å)	Ioniz. energy (eV)	$\log(T/\mathrm{K})$	$\log(n_\mathrm{H}/\mathrm{cm}^{-3})$
H I	1216.00	13.6	4.0-4.5	∼2.0
Si III	1206.00	33.5	¡5.0	−2.5
O VI	1031.00	138.12	5.5	−4.5
O VII	21.00	739.29	5.9	−5.0
O VIII	18.96	871.41	6.4	−5.5

The overall ion abundances are naturally depending on the gas metallicity distribution in HESTIA. In Appendix A.1 we, therefore, derive radial gas metallicity profiles for the simulated MW and M31 galaxies (see Fig. A.1). We conclude that the disc gas metallicity in HESTIA is up to 3 times higher than realistic MW- and M31–mass galaxies (Sanders et al., 2012; Torrey et al., 2014a). The gas metallicity profile of the CGM of MW and M31 is not well constrained observationally, but we speculate the HESTIA might as well have a slightly too high gas metallicity there. We will keep this in mind when comparing our simulations to observations (see Sec. 2.5.7.3).

2.4.2 The Healpy package

The analysis in this study extensively uses *skymaps* showing the column density distribution of the different ions. To define the unit vectors characterising each sightline, we use the Mollweide projection functionality from the HEALPY package (Zonca et al., 2019), associated to the HEALPix-scheme (Górski et al., 2005). Each HEALPix sphere consists of a set of pixels (12 pixels in three rings around the poles and equator) that give rise to a *base resolution*. The grid resolution, N_side, denotes the number of divisions along the side of each base-resolution pixel. The total number of equal-area (Ω_pix) pixels, N_pix, can be expressed as, $N_\mathrm{pix} = 12N_\mathrm{side}^2$. The area of each pixel is, $\Omega_\mathrm{pix} = \pi/(3N_\mathrm{side}^2)$ and the angular resolution per pixel is, $\Theta_\mathrm{pix} = \Omega_\mathrm{pix}^{1/2}$. We select $N_\mathrm{side} = 40$ for all the Mollweide projection plots in this paper. This yields the total number of pixels (which we hereafter refer to as *sightlines*) $N_\mathrm{pix} = 19,200$, and an angular resolution $\Theta_\mathrm{pix} = 1.46°$.

Each sightline starts in $(x, y, z) = (0, 0, 0)$ (we shift our coordinates to our desired origin; see § 2.5 for further discussion) and ends 700 kpc away in the direction of the unit vector defined by the HEALPix-pixel. A sightline is binned into 50,000 evenly spaced gridpoints, so we get a grid-size of 14 pc. At each gridpoint we set the ion density equal to the value of the nearest gas cell (we use the SCIPY-function, KDTree, to determine the nearest neighbour). The projected ion column density for a sightline is then calculated by summing the respective ion number densities over the grid-points constituting a sightline.

2.5 Results

2.5.1 Skymaps

We create skymaps centred on the geometric centre of the LG, which we define to be the midpoint between MW and M31. Based on such skymaps we will later compute projected column density profiles of M31 (see § 2.5.6), which makes it possible to directly compare our simulations to observations. A similar frame–of–reference also proved useful for Nuza et al. (2014); though they used it to obtain plots for studying the entire LG but did not produce whole skymaps from this point.

Fig. 2.1 shows Mollweide projections of the skymaps for each of the five ions – H I, Si III, O VI, O VII and O VIII – for each LG realization (Table 2.1). All ions reveal an over-density centred on the MW and M31. In this order, the ions trace gradually warmer gas, and it is, therefore, not surprising that we see a gradually more diffuse distribution in the projection maps. H I and Si III are much more centred on the inner parts of the haloes in comparison to O VI, O VII and O VIII, the latter filling the space all way out to R_{200} (and even beyond). R_{200} is shown as dashed circles around MW and M31 – note, that a circle in a Mollweide projection appears deformed.

We see that all dense gas blobs with $N_{\rm HI} > 10^{20}$ cm^{-2} are associated with regions overlapping with the galaxies from our catalogue (see Appendix A.2). It fits well with the expectation that such high column densities are typically associated with the ISM of galaxies. The CGM regions of the MW and M31 analogues show a rich structure of H I-features. In 09−18, the M31 analogue, for example, reveals a bi-conical structure, characteristic of galaxy outflows. Many of the extended, diffuse gas streams (particularly in Si III, but also in H I) go far beyond the haloes of the MW and M31 analogues. We see varying distributions of Si III gas across the three simulations in corresponding skymaps. While the 17−11 and 09−18 simulations show an excess of higher column density, clumpy Si III, 37−11 shows an excess of lower column density, diffuse Si III (See § 2.5.5.3 and 2.5.6 for further discussion). Smaller stellar mass and R_{200} values for MW-M31 in case of 37−11 (in comparison to the other two simulations) could be one possible reason for such a heterogeneity across the Si III distributions.

2.5.2 Satellite galaxies in the LG

The satellite galaxies in the simulations have been marked with a galaxy number in each panel, and their properties are summarised in the catalogue tables in Appendix A.2. We include those galaxies which have $M_{\rm gas} > 0$ (as identified by the SUBFIND halo finder) and are within 800 kpc of the LG centre. The 800 kpc cutoff is slightly larger in comparison to the 700 kpc cutoff, used when generating the skymaps; we have chosen this slightly larger cutoff for the satellite galaxy catalogue to ensure that all galaxies contributing to the skymaps are included. Below, we show that all dense H I blobs are associated with a galaxy from our catalogues, so a 800 kpc cutoff sufficiently selects all the galaxies contributing to the skymaps.

The satellite galaxies are generally more prominent in H I and Si III in comparison to the higher ions. Galaxy 12 from the 37−11 simulation does, however, reveal significant amounts of O VI, O VII and O VIII. This satellite has a stellar mass of $M_* = 3.2 \times 10^9 M_\odot$, which is comparable to the LMC galaxy in the real LG (it has $M_* = 3 \times 10^9 M_\odot$ following D'Onghia & Fox 2016). Recently, it has been suggested that the LMC galaxy may have a warm-hot coronal halo (Wakker et al., 1998; Lucchini et al., 2020) that is responsible for the presence and spatial extent of the Magellanic Stream (MS).

Adams et al. (2013) presents a study of 59 ultra compact high-velocity clouds (UCHVCs) from the ALFALFA H I survey while Giovanelli et al. (2013) reports the discovery of a low-mass

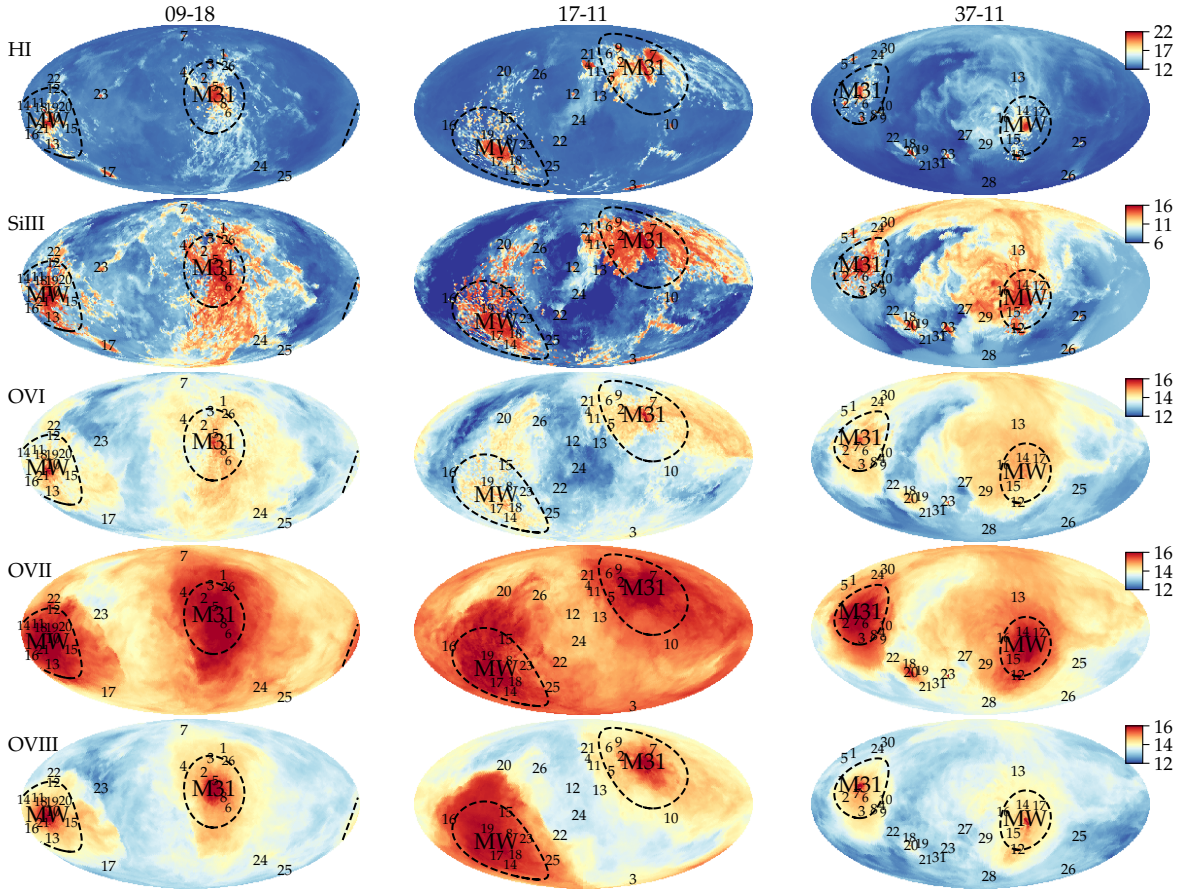

Figure 2.1: Skymaps showing the gas column densities in our three LG realizations. The maps are generated from an observer located in the LG centre, so we can see the predictions for both MW and M31 simultaneously. H I and Si III trace cold-dense gas in and around the ISM, whereas O VI, O VII and O VIII trace gradually more hot-diffuse halo gas. Colour-bars show the log column densities, N, for each ion (N in units of cm^{-2}). Dashed lines indicate R_{200} of MW and M31. Small numbers indicate the location of galaxies other than M31 and MW. All dense H I absorbers with $N_{\rm HI} > 10^{20}$ cm^{-2} are associated with a galaxy. The distributions of the oxygen ions tracing warmer gas reveal a less clumpy and more spherical distribution around the massive galaxies.

halo in the form of a UCHVC. From both these studies, a common conclusion emerges: low-mass, gas-rich halos (detected in the form of Compact HVCs/UCHVCs), lurking on the fringes of the CGMs of massive galaxies in our Local Volume (MW–M31, for example), are more likely to be discovered through their baryonic content (traceable primarily via H I). Other observational papers (de Heij et al., 2002; Putman et al., 2002; Sternberg et al., 2002; Maloney & Putman, 2003; Westmeier et al., 2005a,b), based on objects detected around MW and M31, also support this hypothesis. We find similar H I column densities ($\sim 10^{19}$ cm^{-2}) at $R_{\rm proj} \lesssim R_{200}$ ($\lesssim 200$ kpc), as reported in the above observations. One can also very clearly notice the presence of such small halos in our skymaps. Hence, we can safely conclude that our results also support the existence of low-mass halos at circumgalactic distances.

2.5.3 Ram pressure stripping in the LG

Many of the satellite systems show *disturbed* H I and Si III gas distributions (see the satellite galaxies with galaxy numbers 4 and 13 for simulation 09−18; 2, 5 and 7 for simulation 17−11; 2 for simulation 37−11) to varying degrees. The satellite galaxies' proximity to either of MW or M31 certainly plays a pivotal role (as do their own kinematic motions through their surroundings) in producing ram pressure stripping in their ISMs as well as generating asymmetries in their respective CGMs (Simpson et al., 2018; Hausammann et al., 2019). The ions tracing the warmer gas appear to be less sensitive to such disturbances.

In the context of galaxy clusters, ram-pressure stripping of the ISM gas is an important process in quenching galaxies (Gunn & Gott, 1972a; Abadi et al., 1999). *Jellyfish galaxies* are examples of galaxies experiencing such stripping, where the ram-pressure from intracluster gas strips and disturbs the ISM of star-forming galaxies (Poggianti et al., 2017; Cramer et al., 2019). Such galaxies have long extended tails, which are stabilised by radiative cooling and a magnetic field (Müller et al., 2020). Given the many disturbed galaxies with extended tails in our simulations, we argue that observations of such galaxies may provide insights into the same processes, which are usually studied in jellyfish galaxies in galaxy clusters. It would specifically be interesting, if such examples of jellyfish galaxies in the LG could be used to provide insights into the growth of dense gas in the galaxy tails. The growth of dense gas in such a multiphase medium has recently been intensively studied in hydrodynamical simulations of a cold cloud interacting with a hot wind (Gronke & Oh, 2018; Li et al., 2019; Sparre et al., 2020; Kanjilal et al., 2021; Abruzzo et al., 2022a). We further discuss the possibility of constraining gas flows in the tails of LG satellites in § 2.6.

2.5.4 Cartesian projections

The inescapable nature of skymap projections often teases one into a likely misinterpretation of the angular extent spanned by objects within them. This misinterpretation, however, is circumvented by Cartesian projection plots. An example for this is the case of satellite galaxy number 7 in the 17−11 realization. Its distance to the LG midpoint is only 114 kpc (see Table A.2 in Appendix A.2), which is much smaller in comparison to M31 (338 kpc). In the H I skymap, this galaxy appears much larger in comparison to the Cartesian projection, which we present in Fig. 2.2. This galaxy, hence, appears to be visually dominant in the Mollweide projection map simply because of its proximity to the LG centre, and its location on the skymap, where it appears to be in the direction of the M31 analogue. Thus, this example demonstrates that it is much harder to distinguish galaxies in the skymap in comparison to a Cartesian projection, which should be kept in mind when it comes to the visual interpretation of the skymaps.

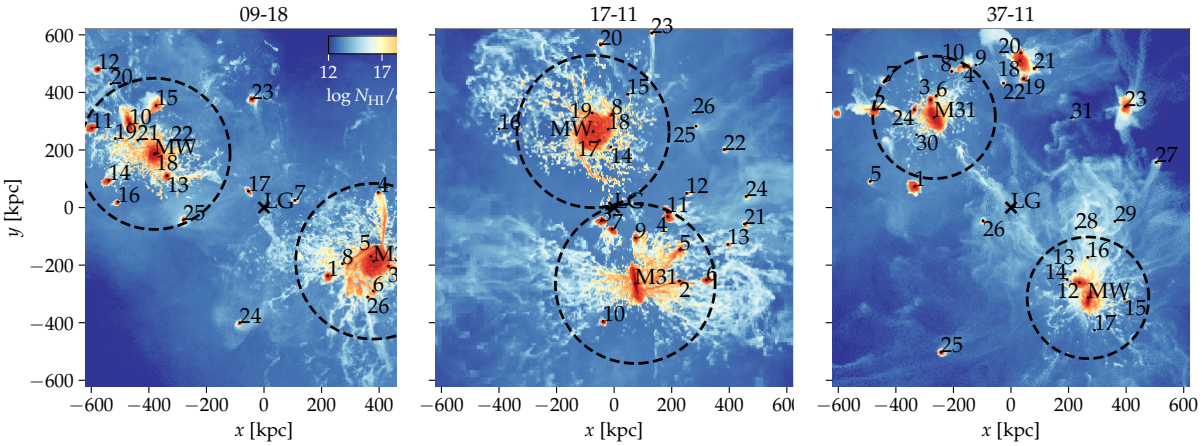

Figure 2.2: H I column density projection maps for each realization. The colour-bar denotes the range of log H I column densities (N in units of cm^{-2}). The dashed circles indicate R_{200} of M31 and MW. Note that the actual spatial extent spanned by galaxy number 7 in the 17−11 realization is far smaller as compared to its projected spatial extent in the corresponding skymap (Fig. 2.1; see also § 2.5.4).

In our analysis, all large and dense H I blobs with $N_{\rm HI} > 10^{20}$ cm^{-2} are associated with a galaxy from our galaxy catalogue. There is a minor blob at $x < -600$ kpc in the 37−11 H I projection map (Fig. 2.2), which is not included in the catalogue, because its distance to the LG centre is larger than our cutoff value of 800 kpc – hence it is not present in the skymaps, but only visible in the Cartesian projection.

We also see that the satellite galaxies, which we described in § 2.5.1 as having *disturbed* gas distributions according to the skymaps, also look disturbed in Fig. 2.2. Indeed, the deformed nature seems even more pronounced in the Cartesian projection.

2.5.5 Power Spectra

In the previous subsections, we have clearly seen that the low ions largely follow a clumpy distribution while the high ions follow a much smoother profile. One way to neatly quantify such distribution patterns is by creating power spectra for each ion and capture the scales over which the corresponding ion exhibits most of its power.

2.5.5.1 Formalism

The spatial scales contributing to a skymap can be quantified by a power spectrum. First, the column density of a given ion is decomposed into spherical harmonics as

$$N_{\rm ion}(\boldsymbol{r}) = \sum_{lm} a_{lm} Y_l^m(\boldsymbol{r}), \tag{2.3}$$

where $\boldsymbol{r}$ is a pixels unit vector, l is the multipole number, and a_{lm} is the coefficient describing the contribution by the mode corresponding to a spherical harmonics base function (Y_l^m). The angular power spectrum is then defined as,

$$C_l = \frac{1}{2l+1} \sum_m |a_{lm}|^2. \tag{2.4}$$

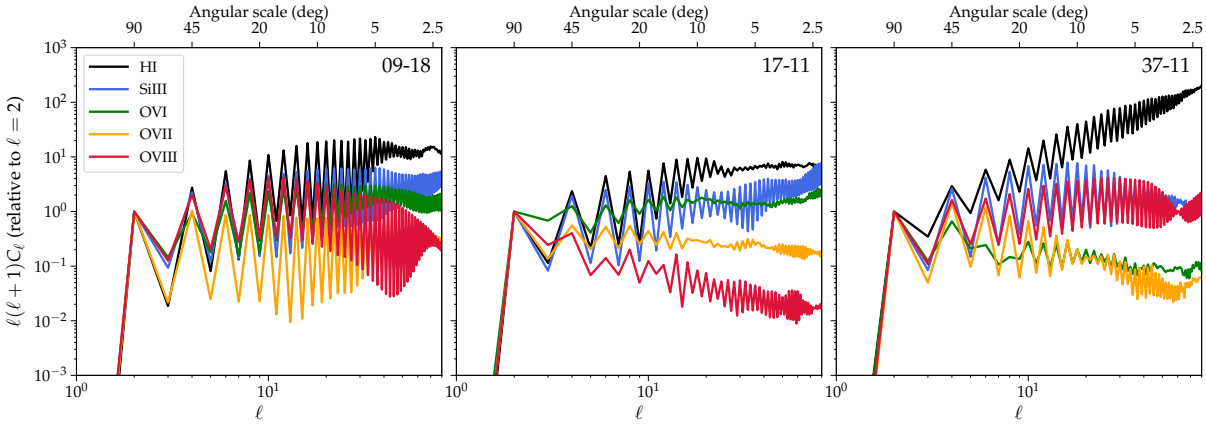

Figure 2.3: We show power spectra generated based on the ion skymaps (Fig. 2.1). The power spectra are normalised to the $l = 2$ value. The ions tracing the coldest gas (H I and Si III) have more power on small angular scales ($\lesssim 10°$) in comparison to the high ions O VI, O VII and O VIII. This fits well with the visual impression from the skymaps in Fig. 2.1. The power spectra reveal a preference for modes with even l-values. This is because the skymaps have a contribution from a reflective component, with MW and M31 being in opposite directions (as seen from the frame–of–reference of the skymap's observer).

We use the HEALPY function *anafast* to compute C_l for each of the column density skymaps. We have subtracted the monopole and dipole moments, and we constrain the power spectrum to $l \leq 2N_{\rm side} = 80$, because contributions at higher l may be dominated by noise (following the HEALPIX documentation for the anafast function).

In Fig. 2.3, we show the power spectra for the different ions. We show the power relative to $l = 2$, which makes the l-dependence for the different ions easy to compare. We have scaled the C_l by a factor of $l(l + 1)$, so the plot shows the total power contributed by each multipole. The angular scale corresponding to each multipole number is estimated as $180°/l$.

2.5.5.2 Contributions from odd and even modes

We start by characterising the 09−18 simulation. The modes with even l-values are systematically larger in comparison to the modes with odd l-values. This *zigzagging* could easily be misinterpreted as an effect of noise, but we remark that it has a physical origin caused by the MW and M31 having a similar angular extent, a similar column density and being located in opposite directions (as seen from the skymap-observer's position). These two galaxies, hence, contribute with an approximate reflection-symmetric signal. Due to the identity, $Y_l^m(-\boldsymbol{r}) = (-1)^l Y_l^m(\boldsymbol{r})$, only the modes with even l contribute to a reflection-symmetric map, so this explains the domination of even modes.

A domination of even modes is especially visible for $l \lesssim 10$ for all ions in all three simulations. For 09−18 the domination is also present for higher l for all ions, but for 17−11, the signal vanishes at $l \gtrsim 10$ for O VI and O VII.

2.5.5.3 The angular coherence scale

From the behaviour of the power spectra for 09−18, we see that the H I skymaps have more structure on small scales of $\simeq 5°$ (relative to a larger scale of $l = 2$) in comparison to the other ions. The amount of power on this angular scale ($\simeq 5°$) is indeed gradually decreasing from H I,

Si III, O VI, O VII to O VIII (with the only exception being O VIII in 37−11, which shows higher power on this scale than O VI and O VII). This is completely consistent with the picture that we get from visually examining the different skymaps in Fig. 2.1, where the ions tracing the coldest gas also seem to have the clumpiest distribution on small angular scales.

The behaviour of the power spectra for 17−11 and 37−11 are broadly consistent with this picture. H I has more power at smaller scales ($l \gtrsim 20$) across all simulations in comparison to the other four ions. For 37−11, O VIII shows more power on small scales in comparison to O VI and O VII, which is most likely an effect of the O VIII ion being influenced by outflows (this ion, for example, reveals a bi-conical outflow for MW for 37−11 in Fig. 2.1).

For 37−11, the H I spectrum reveals the most power on small angular scales – this fits well with our scenario that H I gas is clumpy on small scales. For the warmer ions such as O VII the power is a decreasing function of l (if we ignore the fluctuations caused by even modes having more power in comparison to odd modes), implying that fluctuations on large angular scales are dominating. Similar trends are found in the other simulations.

Intriguingly, the Si III power spectra for 09−18 and 17−11 show an *increasing* trend at small scales ($\lesssim 10^{\circ}$), while 37−11 Si III power spectra shows a *decreasing* trend at similar scales. This pattern is, indeed, coherent with our observations regarding the Si III skymaps (see § 2.5.1). We discuss this aspect a bit further in § 2.5.6, where we introduce the column density distributions.

2.5.6 Column density profiles

Radial column density profiles are often used as an observational probe of the spatial distribution of the CGM in galaxies. In Fig. 2.4, we show the M31 radial profiles for our ensemble of ions with a particular focus on the median and 16-84th percentile of the distributions. The background points show all our sightlines.

2.5.6.1 Overall trends

As expected, the median column density is a declining function of radius for all ions in all simulations. The scatter is, however, behaving differently. Ions tracing the warm-hot gas (O VI, O VII and O VIII) have a much lower scatter in comparison to the ions characteristic of dense-cold gas (H I and Si III). The profiles of the former ions are *well-behaved* and the column density profiles can be well-described as a monotonic decreasing function of projected distance (this feature is well documented for O VI; Werk et al. 2013; Liang et al. 2018) with a scatter of 0.1-0.2 dex. On the other hand, H I and Si III reveal extreme outliers. In simulation 17−11 galaxies 4, 11 and 21 (see Fig. 2.1), for example, contribute with high H I column densities ($\gtrsim 10^{20}$ cm^{-2}) at a projected radius of $R_{\rm proj} = 1.5 \pm 0.5 R_{200}$. This shows that the H I column density is clumpy and influenced by satellite galaxies.

Similarly, Si III show multiple clumps, but their correlation scales seem slightly larger in comparison to H I, which is consistent with our power spectrum analysis. Despite the clumpy nature of Si III, we still find the mean of the projected column density profile to be decreasing (as, for example, is also seen in the observed sample of galaxies from Liang & Chen (2014)).

These trends are also applicable to the projected column density profiles of the MW, which we show in the Appendix Fig. A.2. H I is again influenced by individual satellite galaxies, and there is generally an increased scatter for ions tracing low-temperature gas in comparison to the high ions.

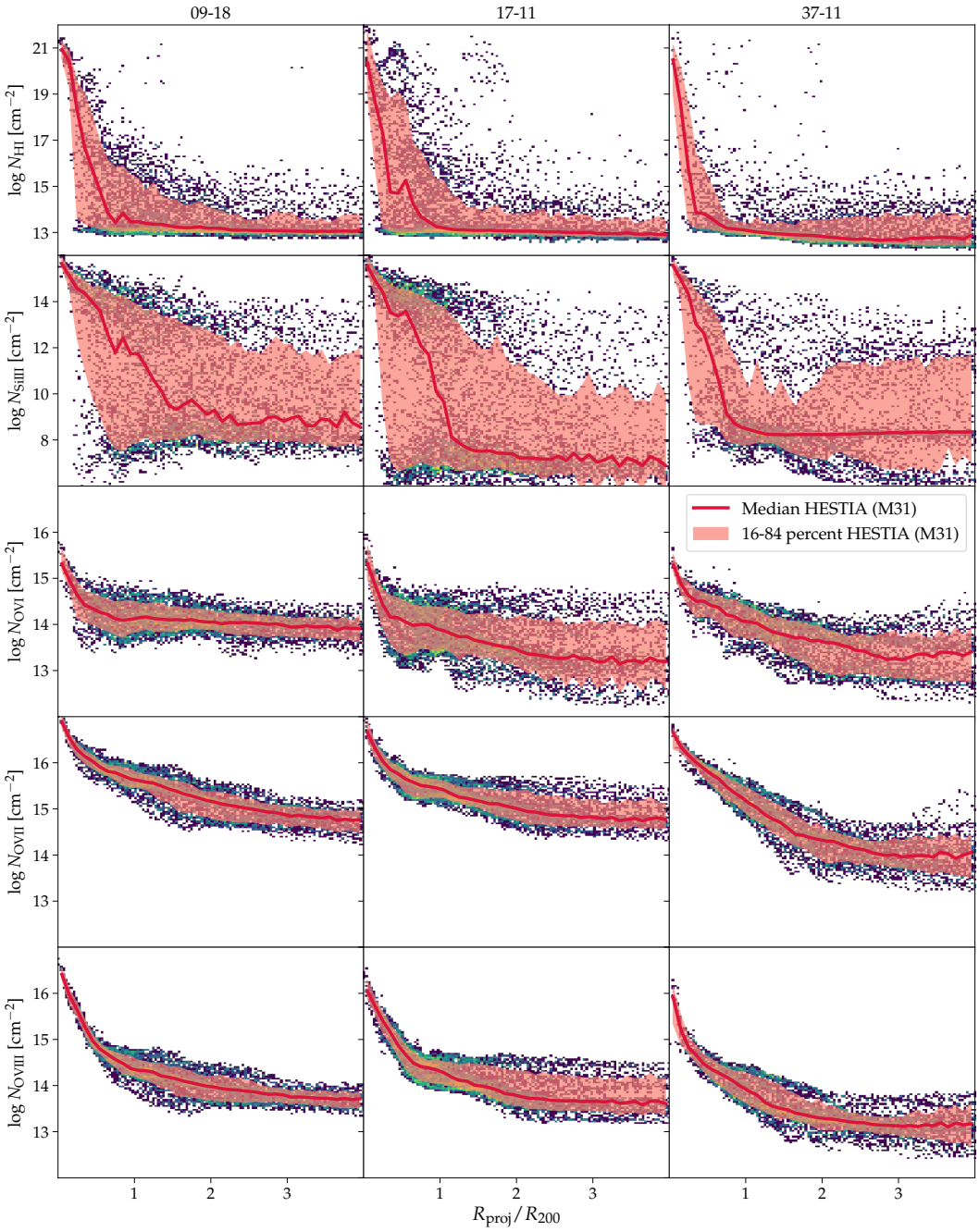

Figure 2.4: *Top-Bottom*: 2D log radial column density profiles for M31 for H I, Si III, O VI, O VII and O VIII. Thick, red curve signifies median values while the red, shaded region denotes 16-84th percentile values. The background points depict the ion column density contributions arising from the remaining gas cells. A distinct blob of high column density H I absorbers, which can be seen at a distance of $\sim 1.5\ R_{\rm proj}/R_{200}$ in the H I profile for 17−11, can be correlated with satellite galaxies numbered 4 and 11 in the corresponding skymap (H I skymap for 17−11 in Fig. 2.1).

2.5.6.2 Origins of the clumpy CGM at large radii

The presence of H I sightlines mimicking Lyman limit-like column densities ($\sim 10^{17}$ cm^{-2}) in Fig. 2.4 as well as Si III sightlines lying above $\gtrsim 10^{12}$ cm^{-2}, out to R_{200} in our simulations, indicate that the cool-clumpy CGM extends to large distances up to virial radii. In fact, using VLT/UVES and HST/STIS data, Richter et al. (2003) as well as Richter et al. (2009) have identified such a population of Lyman-limit like optical and UV absorption systems in the Milky Way halo at high radial velocities, most likely representing the observational counterpart of CGM clumps far away from the disk. It is then worthwhile to contemplate about the physical origins of this clumpy CGM gas. A comparison with corresponding H I data from Liang & Chen (2014) (henceforth, LC2014) reveals that the cool, clumpy CGM ($\log N(\mathrm{H\,I}) > 10^{16}$ cm^{-2}) has a similar spatial extent (> 2–$3\ R_{\rm proj}/R_{200}$) as seen in our data.

It is important to note that most of this clumpy CGM gas is not associated with the ISM of the satellite galaxies because those regions have far greater densities (a factor of $\sim$ 4-5 times higher) than that being discussed here. However, ram pressure stripping from the motions of many of the satellite galaxies within the R_{200} of MW-M31 can deposit such intermediate-column density cool gas at these distances. We elaborate on ram pressure stripping and its effects on the CGM of LG in § 2.6.2.

Gas accretion mechanisms onto the host galaxy, in itself could be a potential source for cool, slightly under-dense gas clumps manifesting as cold CGM at large distances.

Galactic fountain flows have long been hypothesised as a possible means to efficiently circulate gas, metals and angular momentum between the ISM and the CGM (Fraternali et al., 2013; Fraternali, 2017). Thermal instabilities arising from cold gas parcels from the ISM regions moving outward rapidly through the warm ambient CGM regions can result in the growth of intermediately dense cool gas. However, it is not immediately clear which of the above three processes could be the most dominant. While carrying out an elaborate tracer particle analysis or delving deeper into the ram pressure stripping processes could provide better clarity about the root cause of this distant cold CGM, it is beyond the scope of this paper.

2.5.6.3 The bi-modal distribution of Si III

Interestingly, Si III column density distributions show a strong bi-modality, with a higher sequence of sightlines clustered around $\sim 10^{14}$ cm^{-2} and another lower sequence clustered around $\sim 10^{8}$ cm^{-2}. This bimodality is expected due to the bi-conical outflows, which we identified in Fig. 2.1. This bimodal feature is indeed most prevalent for M31 in 09-18 and 17-11, where the bi-conical outflows were most visible. However, it is practically highly unlikely to detect the lower sequence of Si III column densities in near future; hence this bi-modal feature will not show up in the Si III observational datasets.

2.5.7 Comparison with observations

While the previous subsections primarily dealt with the theoretical interpretations of our results from the power spectra and column density profiles, this subsection is dedicated to analysing how well these results match with data from observations and other simulations. We base our comparison on three different observational datasets:

- **M31 observations from the Project AMIGA** (Absorption Maps in the Gas of Andromeda; Lehner et al., 2020). Project AMIGA is a UV HST program studying the CGM of M31 by using 43 quasar sightlines, piercing through its CGM at different impact parameters ($R_{\rm proj} = 25$ to 569 kpc). Such a large number of sightlines for the Andromeda galaxy

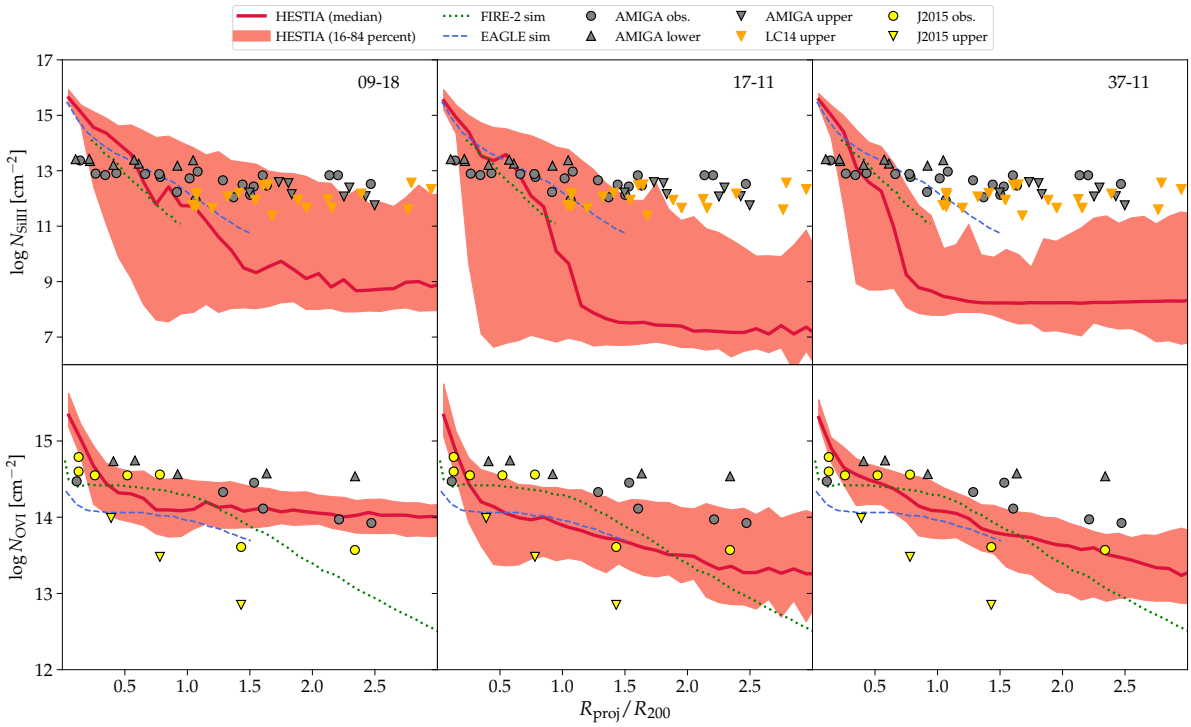

Figure 2.5: The top (bottom) panel shows the Si III (O VI) radial column density profiles for our three realizations for M31. The thick red curve denotes the median values while the red, shaded region denotes the 16-84th percentiles for our realizations. Circles refer to the detections while the downward and upward triangles, respectively, denote the upper and lower limits in the Project AMIGA survey (Lehner et al., 2020). The blue dashed line denotes the data from EAGLE simulations (Oppenheimer et al., 2017) while the green dashed-dot line denotes the data from FIRE-2 simulations (Ji et al., 2020). Downward orange triangles in the upper panel are Si III upper limits from the Liang & Chen (2014), while the yellow filled circles and downward triangles in the lower panel are O VI measurements from Johnson et al. (2015). The Si III profile from HESTIA is consistent with the LC14 upper limits, but there is an inconsistency between these and the Project AMIGA observations. Similarly, the J2015 and Project AMIGA observations of O VI are inconsistent, and HESTIA is only in reasonable agreement with J2015. In Fig. 2.6 we discuss that a likely explanation for the offset between HESTIA and the AMIGA observations is contamination of gas from the MW to the AMIGA dataset.

enables a constraining quantitative comparison to the corresponding mock data from our simulations.

- **Absorption-line measurements of Si III from LC2014**. They present a study of low and intermediate ions in the CGMs of a sample of 195 galaxies in the low-redshift regime. However, 50% of the LC2014 sample consists of dwarf galaxies. To enable a fair comparison, we select only galaxies in a comparable mass range to our M31 simulations. We specifically only include their galaxies with $10^{10.6}$ $M_\odot \leq M_* \leq 10^{11.1}$ $M_\odot$. In our context, the data pertaining to Si III (1206 Å) ion is relevant. Since this is an absorption-line study, they measure all ion abundances in terms of equivalent width (EW). In order to translate their EW measurements into column density values, we plot a corresponding curve of growth for different "b" parameters. From the curve of growth it is clear that for $\log N(\mathrm{Si\,III}) < 12.0$ and $\log N(\mathrm{Si\,III}) > 18.0$, translating EW into column densities is straightforward. However, in the $12.0 < \log N(\mathrm{Si\,III}) < 18.0$ regime, b-parameter degeneracy sets in and a single EW measurement can result in different values for column densities depending on the b-parameter adopted. For this reason we exclude the sightlines from LC2014 at distances $d/R_{200} < 1$ (where this degeneracy is present).

- **O VI ion measurements from Johnson, Chen, & Mulchaey (2015) (henceforth J2015)**. They present a study of distribution of heavy elements of sight-lines passing galaxies with different impact parameters. Like LC2014, the eCGM galaxy sample in J2015 also comprises of galaxies spanning a range of stellar masses ($\log M_*/M_\odot = 8.4$-11.5), so we again apply a mass cut of $10^{10.6}$ $M_\odot \leq M_* \leq 10^{11.1}$ $M_\odot$ and we also only include late-type galaxies.

In Fig. 2.5 we compare the projected Si III and O VI profiles for M31 from HESTIA to these observational datasets, and we also show the EAGLE simulations (Oppenheimer et al., 2017) and the FIRE-2 simulations (Ji et al., 2020). We discuss the comparison to the other simulations in Sec. 2.5.8.

2.5.7.1 Comparing hestia to Si III observations

At low impact parameters, $R_{\rm proj} \lesssim R_{200}$, the observed range of Si III column densities in AMIGA and our simulations are consistent[3]. For sightlines probing $R_{\rm proj} \gtrsim 1.5R_{200}$, our simulations under-predict the observed column densities. Some of the shown observational data points are upper limits, implying that the observations leave the possibility for individual sightlines with column densities as low as ours, but the simulations generally fall short by at least an order of magnitude at $R_{\rm proj} \gtrsim 1.5R_{200}$.

On the other hand, HESTIA is perfectly consistent with the upper limits from LC2014. Indeed, there are tensions between the high Si III column densities reported by Project AMIGA (in M31) and the upper limits from LC2014. A possible reason for this could be contamination of gas from the MW halo or Local Group environment for the M31 observations. We will further assess this hypothesis in Sec. 2.6.1.

[3]This is, of course, keeping in mind the uncertainties associated with the ion column densities in the innermost regions of the galaxies in our simulations i.e. regions where the ISM is dominant.

2.5.7.2 Comparing hestia to O VI observations

When comparing the O VI column density in AMIGA and HESTIA we again see larger values in the former. At the same time, HESTIA reveals larger column densities in comparison to the J2015 observations of galaxies from the low-redshift Universe.

The offset between the observed J2015 and AMIGA might again be caused by contamination of MW absorption in the latter dataset, or an alternative possibility for the offset is that one dataset is the mean of a sample of low-redshift galaxies and the other only takes into account a single galaxy's profile (M31).

2.5.7.3 The normalization of the metallicity profile in hestia

In Appendix A.1 we show that the gas metallicity in the disc of the HESTIA galaxies is up to a factor of 3 higher in comparison to observations. The naïve expectation is that the CGM gas metallicity is too high by a similar factor, and this would cause the HESTIA column density profiles in Fig. 2.5 to be overestimated by up to 0.5 dex. If we scale the HESTIA M31 Si III and O VI column density profiles down by 0.5 dex, the agreement with LC14 and J2015 improves, whereas the tension between the AMIGA observations and HESTIA becomes stronger. This supports our conclusion that HESTIA is well consistent with these observations of low-redshift galaxies.

2.5.8 Comparison with other simulations

Fig. 2.5 also shows the profiles for Si III and O VI for EAGLE-based (Oppenheimer et al., 2017) and FIRE-2 (Ji et al., 2020) based simulation datasets. For the comparison with EAGLE, we use the Si III and O VI profiles from their $L_\star$ subsample, which has $\log M_{200} = 11.7 - 12.3$ $\mathrm{M}_\odot$. It contains 10 haloes hosting star-forming galaxies. These are zoom simulations with non-equilibrium cooling. The corresponding average R_{200} for this subsample is $\simeq 195$ kpc (see fig. 2 in Oppenheimer et al. 2016). This dataset is at $z = 0.2$, since the authors compare it with the COS-Halos data which covers the same redshift. For the FIRE-2 simulation comparison we compare to the m12i halo ($\log M_{200} \simeq 12$ $\mathrm{M}_\odot$ at $z = 0$) using the FIRE-2 model with cosmic ray feedback (their simulation data is taken from fig. 17 in Lehner et al. 2020). Further details about the simulations and CGM modelling in FIRE2 simulations can be found in Ji et al. (2020).

The HESTIA simulations show many similar trends to EAGLE and FIRE-2 and they, furthermore, *all* under-predict the AMIGA column densities of Si III and O VI at $R_{\mathrm{proj}} \gtrsim 1.0 R_{200}$. On the other hand, all the simulations are broadly consistent with the observational datasets we have compiled based on LC2014 and J2015.

2.5.9 Convergence test

In Appendix A.4 we compare the high-resolution HESTIA simulations analysed in Fig. 2.5 with intermediate-resolution simulations having an eight times larger dark matter particle mass. This convergence test does not challenge our derived column density profile.

Using the same simulation code and galaxy formation model as in our paper, van de Voort et al. (2019) showed that increasing the spatial resolution significantly boosts the H I column density in the CGM. Idealised simulations furthermore reveal the possibility of gas to fragment to the cooling scales (McCourt et al., 2018; Sparre et al., 2019), which for dense gas is significantly below our resolution limit. Exploring the resolution requirement in the CGM of cosmological simulations is, however, still a field of ongoing research, so it is still a possibility that the idealized simulations over-estimate the needed spatial resolution.

We note that Si III and O VI trace warmer gas in comparison to H I, so these ions are expected to be less affected by resolution issues than H I. Even though our convergence test does not reveal any signs of a lack of convergence, it is still a possibility that our column densities are affected by a too low spatial resolution.

2.6 Discussion

2.6.1 Biased column density profiles caused by the MW's CGM?

We have found that observations of low-redshift galaxies disagree with the observed column densities of the M31 by the Project AMIGA. A possible explanation for this finding could be observational biases, for example, caused by gas clouds in the CGM of the MW contributing to the projected column density profile of M31. Such a bias does not play a role in our previous skymap analysis, because the skymaps are created by an observer in the geometric centre of the LG, and hence, the MW's CGM does not contribute to the sight-lines towards M31.

We now turn to addressing the role of such a bias in the three realizations of the HESTIA simulations. We re-analyse our simulations with an observer located in the MW centre, and create skymaps of the different ions as before. In order to incorporate the larger distance from the MW to M31 (as opposed to the smaller distance from the LG centre to M31 in earlier analysis), we use longer sightlines (each 1400 kpc in length). To ensure grid-size uniformity with respect to the earlier analysis, we increase the number of gridpoints from 50,000 to 100,000. To determine the role of the MW's CGM, we create skymaps excluding gas within 10, 30, 60, 90, 120 and 150 kpc of the MW's centre. The corresponding projected radial column density profiles are seen as solid lines in Fig. 2.6. The three different realizations show a significant amount of Si III and O VI residing in the MW's CGM at a distance of 10–120 kpc from the MW's centre.

Observationally, a hint of the gas clouds' spatial origin can be obtained by looking at its line-of-sight velocity. In Fig. 2.6 we also construct profiles, where we exclude gas clouds with a line-of-sight difference ($|\Delta v|$) exceeding 100 km s^{-1} from M31's velocity (see dashed lines in Fig. 2.6). From our different realizations we see a different behaviour. For 09−18 and 37−11, the column density profiles of Si III and O VI increase up to 10^{15} cm^{-2} and by 1.0 dex, respectively (this is the difference between dashed lines indicating a cutoff of 10 kpc and 120 kpc in Fig. 2.6), caused by gas residing between 10–120 kpc of the MW's CGM. For 17−11, the situation is less extreme, and the inferred column density profile of M31 is unaffected by the MW, when a velocity cut in the line-of-sight velocity is applied.

This analysis shows that the MW's CGM can substantially bias the inferred projected column densities of M31. For Si III, the potential bias is stronger in comparison to O VI. For O VI in 17−11, a velocity cut alone is successful in completely removing MW contributions. As seen from the lower middle panel in Fig. 2.6, this still gives us a small discrepancy ($\sim$ 0.5 dex) with AMIGA observations. This means that our 17−11 analogues inherently do not produce enough O VI to completely match the AMIGA observational trends. However, the opposite is true for the other two simulations where we clearly see our results matching fairly well with the AMIGA observations, when we include the contribution of gas from the MW halo. Overall, we infer that the biases estimated by our MW centred skymaps provide a likely explanation for the differences between the HESTIA simulations and the AMIGA observations (seen in Fig. 2.5). At the same time, it also provides a likely explanation for the differences between the low-redshift galaxy samples (LC2014 and J2015) and the Project AMIGA[4].

[4]However, we do note here that both LC2014 and J2015 are a representative sample as opposed to the Project AMIGA observations which pertain to a single galaxy.

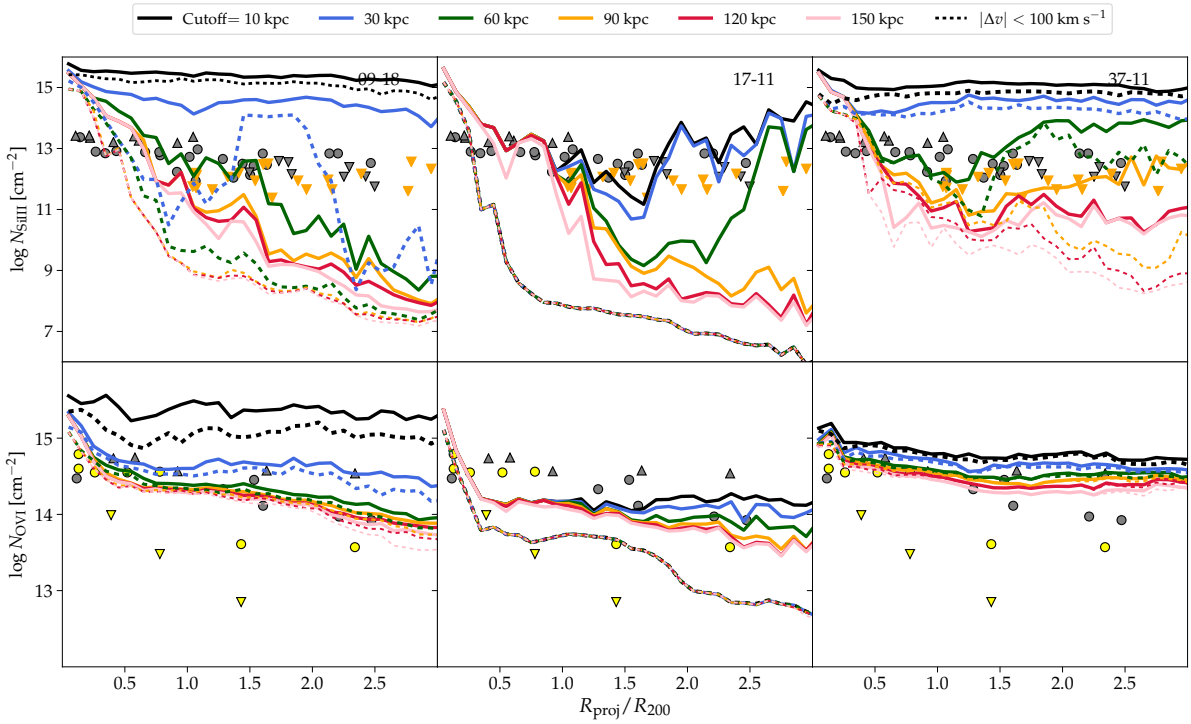

Figure 2.6: We demonstrate how the gas in the MW's CGM may influence the observationally derived median column density profiles around M31. We have generated skymaps centred on the MW (instead of the LG, as done in previous figures), where we remove gas lying within a radial cutoff ranging from 10 to 150 kpc from MW (solid lines). For the dashed lines we additionally constrain gas to be within 100 km s^{-1} of the M31. As in Fig. 2.5, the data points from Project AMIGA survey (filled grey markers), LC2014 (orange downward markers) and J2015 (filled yellow markers) have been overplotted. Even when only including gas within 100 km s^{-1} of M31, the Si III profile of 09-18 and 37-11 is increased to $\simeq 10^{15}$ cm^{-2} by clouds within 10–120 kpc from the MW centre. For 17-11, a velocity selection of gas very well removes gas within 150 kpc of the MW. For O VI, the contamination from the MW's CGM is also significantly changing the profiles in 09-18 – here gas residing within 150 kpc of the MW may boost the column density by 1.0 dex.

In reality, contamination of the gas from the MS to the M31 CGM observations is also a possibility. The MS passes just outside of the virial radius ($R_{\rm vir}$ = 300 kpc) of M31 (see fig. 1 in Lehner et al. 2020). For the purpose of ascertaining the level of MS contamination, Lehner et al. (2020) use Si III as their choice of ion (mainly because it is most sensitive to detect both weak as well as strong absorption). However, they do not remove entire sightlines merely on the suspicion of possible MS contamination. Instead, they analyze individual components and find that 28 out of 74 (38%) Si III components are within the MS boundary region (and having Si III column density values larger than 10^{13} cm^{-2}). These are not included in the sample from then on. For the remaining *non-MS contaminated* components, they find a trend of higher Si III column density at regions away ($b_{\rm MS} > 15°$) from the MS main axis ($b_{\rm MS} = 0°$). This shows that the MS contamination is negligible for these components.

However, they do find a fraction (4/22) of dwarf galaxies out of their M31 dwarf galaxies sample falling in the MS contaminated region. This means that while they do take utmost care to avoid any MS contamination in their results, there could still be some residual contributions (especially in the cold gas observations of M31's CGM) from the MW CGM. These could manifest in the form of slightly enhanced column densities in observations at regions beyond M31's virial radius.

2.6.2 Gas stripping in the Local Group

A characteristic that appears across all our realizations is the distorted nature of the CGMs of many satellite galaxies. High-velocity infall motions of dwarf galaxies through complex gravitational potential fields, typical in galaxy groups and clusters results in the dwarf galaxy CGM becoming structurally disturbed. In some extreme cases this can also result in trailing stripped gas tails (Smith et al., 2010; Owers et al., 2012; Salem et al., 2015a; McPartland et al., 2016; Poggianti et al., 2017; Tonnesen & Bryan, 2021). While a few very clear examples of such galaxies have been described in detail in §2.5.1, there are certainly many more.

The role of stripped gas from the CGMs of satellite galaxies towards augmenting the pre-existing gas reserves of the host galaxy and thereby influencing the CGM of the host galaxy is rather well known from the observations of the MS, which emanates from the interaction of the Small and Large Magellanic Clouds on their approach towards the MW (e.g. Fox et al. 2014; Richter et al. 2017). However, a scarcity of deep observations means that very little is known about the part played by the diffuse gas from other satellite galaxies in our LG. Few studies pertaining to such observations reveal low neutral gas abundances around dwarf galaxies, though they might still harbour sizeable reserves of ionized gas (Westmeier et al., 2015; Emerick et al., 2016; Fillingham et al., 2016; Simpson et al., 2018).

By carefully analysing the gas flow kinematics across time-frames for these dwarf galaxies within HESTIA, it will be possible, in future studies, to obtain not just their mock proper and bulk gas motions, but also various parameters regarding their stripped gas such as its spatial extent, cross-section and physical state. The Gaia DR2 proper motions of MW and LG satellites (Pawlowski & Kroupa, 2020), along with corresponding comprehensive UV, optical and X-ray datasets from HST-COS, UVES, Keck and Chandra, can then provide us with clues regarding which HESTIA realizations are most likely to produce these real observations. Furthermore, implementing similar sightline analysis, done in this paper for MW-M31, for multiple satellite systems over a range of their respective impact parameters, can yield extensive mock datasets that could then prove useful in the wake of future surveys that will be sensitive to even lower column density gas.

2.6.3 Physical modelling of the CGM

In recent years, our understanding of the CGM has dramatically improved, and it is encouraging that our simulations are broadly consistent with observations. This is despite of our relatively simple physics model.

Theoretical work has for example suggested that parsec-scale resolution, which is so far unattainable in cosmological simulations like HESTIA, may be necessary to resolve the cold gas in galaxies (McCourt et al., 2018; Sparre et al., 2019; Hummels et al., 2019; van de Voort et al., 2019, – we note, however, that these results are so far only suggestive and the need for parsec-scale resolution has so far not been demonstrated, yet this could be a potential reason for the offset). Results from van de Voort et al. (2019) proved that ~ 1 kpc resolution in the CGM boosts small-scale cold gas structure as well as covering fractions of Lyman limit systems; this might also hold true for slightly less dense but slightly more ionized cool gas. McCourt et al. (2017) proposed a cascaded shattering process via which a large cloud experiencing thermal instability can cool a couple of orders of magnitude (from $T \sim 10^6$ K to $\sim 10^4$ K), mainly as a result of continued fragmentation within the larger cloud. They compute the characteristic length scale, associated with shattering, to be $\sim 1 - 100$ pc. Multiple observations also show that cool gas is indeed present in form of small clouds out to $\sim R_{\rm vir}$ in galaxy haloes (Lau et al., 2016; Hennawi et al., 2015; Stocke et al., 2013; Prochaska & Hennawi, 2008). Using Cloudy ionization models, Richter et al. (2009) have determined the characteristic sizes of the partly neutral CGM clumps in the MW halo based on their HST/STIS absorption survey, leading to typical scale lengths in the range 0.03 to 130 pc (see tables 4 & 5 in Richter et al. 2009). From their absorber statistics, these authors estimated that the halos of MW-type galaxies contain millions to billions of such small-scale gas clumps and argue that these structures may represent transient features in a highly dynamical CGM. Thus, it is clear that the length scales involved in these processes are still at least an order of magnitude below what is currently achievable in the highest resolution zoom-in simulations. It is also worth mentioning that Fielding & Bryan (2022) have recently introduced a novel framework modelling multiphase winds, which may be relevant for future cosmological simulations of the CGM.

Lehner et al. (2020) discusses feedback processes, which may also affect how gas and metals are transported to large radii. The role of cosmic ray feedback in influencing the CGM has recently gained interest from multiple research groups (Salem et al., 2014, 2016; Buck et al., 2020; Ji et al., 2020; Hopkins et al., 2020), and it has been shown to significantly alter gas flows in the CGM of simulations. CR-driven winds from the LMC (Bustard et al., 2020) as well as those from the resolved ISM (Simpson et al., 2016; Girichidis et al., 2018; Farber et al., 2018) have been shown to change both the outer and inner CGM properties, respectively. Similarly, magnetic fields have been shown to influence the physical properties of the CGMs of simulated galaxies, thereby modifying the metal-mixing in the CGM (van de Voort et al., 2021).

Despite of HESTIA agreeing relatively well with the observations, we note that there are still some important challenges for future galaxy formation models in terms of understanding physical processes in the CGM.

2.7 Conclusions

We have analysed the gas, spanning a range of temperatures and densities, around the MW-M31 analogues at $z = 0$ in a set of three HESTIA simulations. These LG simulations use the quasi-Lagrangian, moving mesh AREPO code, along with the comprehensive Auriga galaxy formation model. We have set our frame of reference to the LG geometrical centre and generated ion maps

for a set of five ions, H I, Si III, O VI, O VII and O VIII. Some important conclusions have emerged from our study:

- We have created mock skymaps of the gas distribution in the LG. All dense gas blobs with $N_{\rm HI} > 10^{20}$ cm^{-2} are associated with a galaxy; either a satellite galaxy or MW/M31 themselves. The skymaps of H I and Si III reveal strong imprints of satellite galaxies, whereas the tracers of warmer gas (O VI, O VII and O VIII) are mainly dominated by the haloes of MW and M31. The projected column density profiles of the latter ions are, indeed, well-described by monotonic decreasing functions of the impact parameter. In comparison, the projected H I- and Si III-profiles have a much higher scatter caused by blobs associated with the satellite galaxies.

- A power spectrum analysis of the skymaps shows that H I, Si III, O VI, O VII and O VIII have a gradually higher coherence angle on the sky – ions tracing the coldest gas are most clumpy. This confirms the impression we get by visually inspecting the skymaps, and it is also consistent with the behaviour of the column density profiles.

- The visual inspection of the simulated skymaps reveal multiple satellite galaxies with disturbed gas morphologies, especially in H I and Si III. These are LG analogues of jellyfish galaxies. Future simulation analyses and observations can give a unique insight to the physical processes in the ISM and CGM of these galaxies.

- For the HESTIA M31 analogues we compare the Si III and O VI column density profiles to observations of M31 and low-redshift galaxies. The spectroscopic observations of M31 and low-redshift galaxies reveal remarkably different column density profiles. Using our simulations, we find that the gas residing in the Milky Way may contaminate the sight-lines towards M31, such that the M31 column densities are boosted. For Si III and O VI we see this contamination boosting the column density profiles up to as much as 10^{15} cm^{-2} and by 1.0 dex, respectively, even when only including gas within a 100 km s^{-1} of the M31 velocity. Contamination of gas from the MW, hence, provides one of the likely explanations for the offset between observations of M31 and low-redshift galaxies.

- The M31 analogues from HESTIA have Si III and O VI column density profiles broadly consistent with low-redshift galaxy constraints. If we include a contamination from MW gas, then in 2 out of 3 M31 realizations we can also reproduce the large column densities observed in the direction of M31 in Project AMIGA.

Data availability

The scripts and plots for this article will be shared on reasonable request to the corresponding author. The AREPO code is publicly available (Weinberger et al., 2020).

Acknowledgements

We thank Moritz Itzerott, Martin Wendt, Gabor Worseck for useful comments and discussions. We also thank the anonymous referee for some very constructive comments which greatly improved the quality of this paper. MS acknowledges support by the European Research Council under ERC-CoG grant CRAGSMAN-646955. MHH acknowledges support from William and Caroline Herschel Postdoctoral Fellowship Fund. SEN is a member of the Carrera del

Investigador Científico of CONICET. He acknowledges support by the Agencia Nacional de Promoción Científica y Tecnológica (ANPCyT, PICT-201-0667). RG acknowledges financial support from the Spanish Ministry of Science and Innovation (MICINN) through the Spanish State Research Agency, under the Severo Ochoa Program 2020-2023 (CEX2019-000920-S). MV acknowledges support through NASA ATP grants 16-ATP16-0167, 19-ATP19-0019, 19-ATP19-0020, 19-ATP19-0167, and NSF grants AST-1814053, AST-1814259, AST-1909831 and AST-2007355. ET acknowledges support by ETAg grant PRG1006 and by EU through the ERDF CoE grant TK133. The authors sincerely acknowledge the Gauss Centre for Supercomputing e.V. (https://www.gauss-centre.eu/) for providing computing time on the GCS Supercomputer SuperMUC at the Leibniz Supercomputing Centre (http://www.lrz.de/) for running the HESTIA simulations. We thank the contributors and developers to the software packages YT (Turk et al., 2011) and ASTROPY (Astropy Collaboration et al., 2018), which we have used for the analysis in this paper.

Chapter 3

Bridge Formation in Merging Galaxies

The contents of this chapter are based on Sparre et al. 2022, MNRAS 509, 2720.

Title: *Gas flows in galaxy mergers: supersonic turbulence in bridges, accretion from the circumgalactic medium, and metallicity dilution.*

Complete author list: Martin Sparre, Joseph Whittingham, **Mitali Damle**, Maan H. Hani, Philipp Richter, Sara L. Ellison, Christoph Pfrommer, Mark Vogelsberger.

My contributions in the context of this chapter are as follows–

- I have contributed to the scientific analysis and provided technical support and am a co-author on the paper.
- Generated the preprocessed versions of figs. 2, 3, 4, 5, 6, 8, 9 and 10 from the paper (see Figs. 3.2, 3.3, 3.4, 3.5, 3.6, 3.8, 3.9, 3.10 in this chapter). All the analysis presented in this chapter has been done in a code repository jointly developed by Dr. Martin Sparre and me.
- Developed a python analysis pipeline[1] for defining the distances between gas particles of merger progenitors (See §3.2.1 in the paper; §3.3.3 in this chapter) as well as implementing Cloudy ionization modeling[2] to get H I distributions.
- Worked on and tested the tracer particle analysis pipeline.

3.1 Introduction

Galaxy mergers are among the many processes that impact the gas dynamics of a galaxy in a rather non-trivial manner (Struck, 1999). In general, major mergers are known to occur preferentially in massive galaxies than less massive ones (Bundy et al., 2009). Observational evidences of links between a major merger followed by an enhancement in AGN activity (Schawinski et al., 2010) have been found. Increased gas densities during mergers are known to disrupt low-mass

[1]Parts of the pipeline which involve reading-in the simulation data, subhalo tracking using SUBFIND, extracting relevant attributes and developing the tracer library were written by Dr. Martin Sparre.

[2]The framework for Cloudy modeling and resulting ion tables were adopted from Hani et al. (2018).

stellar clusters (Kruijssen et al., 2012; Renaud & Gieles, 2013). Both observations as well as simulations find mergers to be a significant contributor towards the mass growth of quenched ellipticals (Khochfar & Silk, 2006; Boylan-Kolchin et al., 2006; Ciotti et al., 2007; Niemi et al., 2010; Huang et al., 2016; Deeley et al., 2017; Frigo & Balcells, 2017; Yıldırım et al., 2017). However, the most unmistakable effect of gas-rich mergers has been observed in terms of changes in star formation rates pre- and post-merger (Sanders & Mirabel, 1996; Lin et al., 2007; Di Matteo et al., 2008; Hayward et al., 2012; Elmegreen et al., 2021); an effect that seemingly outlives merger-induced morphological changes in its progenitors (Lotz et al., 2008).

Many of these above mentioned changes occur at regimes far beyond the resolving capabilities of cosmological simulations– this is where idealized simulations provide great insights. Multiple studies point to the presence of strong merger-induced starbursts (Mihos & Hernquist, 1996; Springel & Hernquist, 2005; Martig & Bournaud, 2008; Di Matteo et al., 2008; Karman et al., 2015; Gabor et al., 2016; Hani et al., 2020) as well as transformation of star-forming disc galaxies into quenched ellipticals (Springel et al., 2005b; Bekki et al., 2005; Hopkins et al., 2008; Wild et al., 2009; Snyder et al., 2011; Pawlik et al., 2019).

The subsequent setting-in of merger-induced turbulence perturbs the stellar orbits in progenitors which, in many cases, gives rise to tidally stripped stellar tails as well as bridge-like structures connecting the merging galaxies. Both simple test-particle simulations (Pfleiderer, 1963; Toomre & Toomre, 1972; Privon et al., 2013) as well as more advanced merger simulations involving self-gravitating stellar discs (Barnes, 1992) attest the above features.

Interestingly, the elementary gravity-only closed environment-based particle simulations in Toomre & Toomre 1972 predicted and, in some cases, also recreated the bridges and tails (see Fig. 1.2) despite the fact that all of their scenarios only had interacting systems but not actual mergers. They concluded that the time taken to form and sustain a bridge/tail depended strongly on the mass ratios of the progenitors. They also stated the possibility of fresh in-falling gas fueling additional star formation during such interactions. More complex simulations by Renaud et al. 2014 indeed corroborated this and found gas clumping under self-gravity, giving rise to clustered star-formation sites within bridges. However, it is important to note that the morphological disturbances in these and studies from a few other such closed-box environments arise purely from the galactic discs, since, by nature, the involvement of gas reservoir outside the ISM of these galaxies is not taken into account (Cox et al., 2006; Hayward et al., 2014; Moreno et al., 2019).

This gas reservoir, also known as the circumgalactic medium (CGM), has proven to be increasingly important in context of galaxy evolution over the last decade or two. Numerous observational campaigns like the FUSE, STIS, HST/COS have all found evidences of its multiphase nature as well as its non-negligible contribution towards the baryon budget of haloes (Werk et al., 2014, 2016b; Richter et al., 2017; Li et al., 2018; Zhang et al., 2021). Simulations as well as semi-analytic models have also supported these observations and furthermore, have established a chain of continuous gas transfer between the ISM, CGM and the intergalactic medium (IGM) (Wang et al., 2017; Tuominen et al., 2021; Appleby et al., 2021; Faerman et al., 2022; Pandya et al., 2022).

In this chapter we aim to study the role of CGM in cosmological merger simulations. To do this, we use the bridge formed between the merging galaxies as our reference point. We track the gas cells in this bridge in time before, during and after the merger in order to find out whether some of them originate from the CGM of the galaxies or if they actually only originate from the galactic discs (as seen from closed-box simulations). Further, we quantify the gas that is believed to have travelled from the CGM all the way to the ISM and determine the fraction of merger-induced star-formation that results from this gas. We introduce our simulations in §3.2,

state our methods in §3.3, present our results in §3.4 followed by a brief discussion in §3.5 and conclusions in §3.6.

3.2 Simulations

We probe the origins of the gas in bridges, formed during two major merger events, in four cosmological zoom simulations from Whittingham et al. (2021) (Henceforth, W21). We note that the four simulations A, B, C and D in this study refer to 1330-3M, 1349-3M, 1526-3M and 1605-3M simulations, following the nomenclature in W21. These are AREPO-based simulations which employ a moving mesh Voronoi grid for modeling MHD equations. The initial conditions have been selected from the Illustris simulation (Vogelsberger et al., 2014b,c; Genel et al., 2013). Our simulations have a dark matter (gas) mass resolution of $1.64 \cdot 10^5$ $M_\odot$ ($2.74 \cdot 10^4$ $M_\odot$) with a dark matter softening length of 220 pc.

Sparre & Springel (2016) and Sparre & Springel (2017) introduced the original set of major merger simulations chosen on the basis of the following four initial conditions:

- Only galaxies which have experienced a major merger at $z \leq$ 0.5-1.0.[3]
- The galaxies should have a merger mass ratio greater than 1:2.
- The merger progenitors are less massive than MW such that the post-merger remnant galaxies have MW-like stellar and halo masses.
- The mergers are gas-rich which means that quenching is not important for the progenitors.

The simulations used in this study (W21) include two major additions to the original set of simulations. These are the inclusion of magnetic fields (ideal MHD) (Pakmor & Springel, 2013) and Monte–Carlo (MC) tracer particles (Genel et al., 2013). Recent results from van de Voort et al. (2021) and W21 reveal that magnetic fields can induce pronounced discs as well as spiral structures in the merger remnants in addition to reducing the efficiency of metal mixing in the CGM. Thus, the W21 simulations used here are certainly more advanced than many other contemporary simulations without magnetic fields.

Since the primary goal of this paper is to track the contribution and role of CGM in the formation of a bridge, it is necessary to track the spatial evolution of each gas particle through the entire merger process. AREPO-based simulations involve a moving mesh that transforms according to the fluid flows but the gas cells themselves remain fixed. In other words, gas cells are constantly mixed based on the underlying fluid flows and their past history is not retained. Adding MC tracers (Genel et al., 2013) to the fold becomes an efficient way to track the evolution of these gas particles. Based on the initial conditions of the fluid, we use five tracer particles per gas cell at the start of the simulation. We describe the tracer particle analysis in further detail in §3.3.1.

Our simulations use the Auriga galaxy formation model (Grand et al., 2017), which we also use in the previous chapter (see §2.3.3). Star-forming gas cells are described by a two-phase subgrid model and an equilibrium between the phases is assumed via radiative cooling and supernovae heating. The model also includes a uniform UV background (Faucher-Giguère et al., 2009), black-hole (BH) seeding and growth (Bondi & Hoyle 1944; Bondi 1952) as well as quasar mode feedback. Interested readers are encouraged to have a closer look at the Grand et al. 2017 paper for a complete description of the galaxy formation model. For a full description about the simulations, refer to W21.

[3]This redshift interval is chosen in order to allow the galaxies to attain a relaxed phase by the time the simulation stops i.e. at z = 0.

3.3 Methods

3.3.1 Monte Carlo tracers

In AREPO-based simulations such as ours, the treatment of gas cells themselves is not Lagrangian unlike that for the underlying mesh (which moves in accordance to the fluid motions). As the simulation progresses, mass transfer happens between AREPO cells and their past history is thus continually lost.

Our study relies on being able to track the motions of gas over the course of a major merger, something that requires explicit information about the spatial history of each gas cell. Tracers are a great way to achieve this goal. These can be imagined as *unique tags* associated to each gas cell. Each tracer particle has its own unique ID that remains unchanged throughout the simulation. Thus, they passively move according to the mass transfer patterns while retaining their IDs, which makes cell tracking possible (Genel et al., 2013).

Every parent cell is evolved at each time step based on a Voronoi/Delauney tessellation, which is a scheme for fragmenting a plane into regions or cells (see Fig. 1.5). In any given simulation setup, tracers can be attached onto the constituent resolution elements (a star, AGN, wind particle or a gas cell). Finite volume fluxes are computed at each time step and tracer particles are exchanged accordingly between the Voronoi cells. More the mass transfer, more are the number of tracers exchanged between two cells. The overall tracer particle distribution follows a Monte Carlo sampling (hence, the name Monte Carlo tracers or MC tracers) of the underlying mass flux in the cells, since the total number of tracers is fixed. Thus, the tracers are forced to accurately follow the mass fluxes.

MC tracers do not have further sub-resolution elements within them i.e. they share the same resolution as the fluid flows they follow. However, they do retain their unique IDs even after mixing with neighboring cells. Among many other properties, baryonic phase-wise exchange of tracers is also recorded. This is particularly helpful in self-consistent tracking of mass exchange between various resolution elements (like gas to stars, gas to winds, stars to gas, etc.) within a simulation.

3.3.2 Ionisation modeling

The basic principles behind ionization modeling as well as specifications about the Cloudy ionization modeling code (Ferland et al., 2017) used for this paper have already been described in full detail in §2.4.1. For this study we target the H I distributions in the merging galaxies.

3.3.3 Ad-hoc definitions for the ISM, CGM and IGM

A precise definition of the CGM does not make much sense because it is indeed very hard to tell the upper and lower bounds of the ISM and IGM for any galaxy respectively. However, within a particular analysis such as this, it is imperative to specify an ad hoc definition for the CGM. We base our definition of the CGM boundary on a variable, s, that is computed for each gas cell in our simulation box. s depends on r_1 (the distance of a gas cell from galaxy 1), $R_{200,1}$ (radius at which the spherically averaged density for galaxy 1 equals 200 times the critical density of the Universe), r_2 (the distance of a gas cell from galaxy 2) and $R_{200,2}$ (radius at which the spherically averaged density for galaxy 2 equals 200 times the critical density of the Universe). We depict the above quantities in a sketch format in Fig. 3.1 and use them while tracing the origin of gas mass budget later on in Fig. 3.7.

Thus,

$$s = \min(r_1/R_{200,1}, r_2/R_{200,1}). \tag{3.1}$$

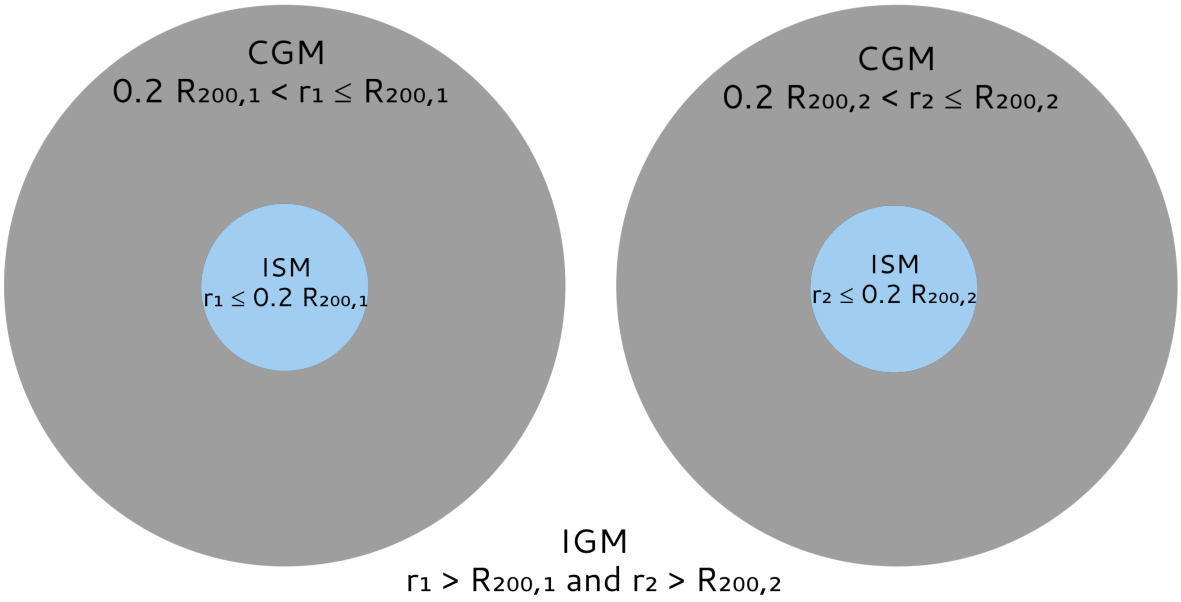

Figure 3.1: Each gas cell is assigned to one of the three reservoirs– ISM (if a gas cell lies within $r < 0.2\ R_{200}$), CGM (if $0.2\ R_{200} r < R_{200}$) or the IGM (if $r > 0.2\ R_{200}$) of either of the progenitors.

Based on the unique value that s takes, each gas cell is assigned either to the ISM, the CGM or the IGM (i.e. lying outside the merging haloes) of galaxy 1 or galaxy 2 in the following manner:

- **ISM**: If $s \leq 0.2$, a gas cell is assigned to the ISM.
- **CGM**: If $0.2 < s \leq 1.0$, then a gas cell is assigned to the CGM.
- **IGM**: If $s > 1.0$, then a gas cell is assigned to the IGM.

We assume spherical surface boundaries for the CGM because the warm gas ($\simeq 10^5$ – 10^6 K), which has a nearly spherical distribution (barring a weak contribution from biconical outflows; Oppenheimer et al. 2016, 2018a), typically dominates the volume of the CGM. The boundary values are set rather conservatively, keeping in mind that the disc and ISM of a galaxy generally extend upto 10-15 per cent of R_{200} (Marinacci et al., 2013). Both the above choices suffice for quantifying the transfer of gas across and from the CGM to the bridge and ISM of merging galaxies.

3.4 Results

3.4.1 Merger orbits and subsequent SFR peaks

The orbital patterns of a merger system primarily determine how turbulence sets into the system and how exactly gas is funneled towards the center–of–mass during the process. For this reason, we first take a look at the merger orbits of our sample and their corresponding effect on the SFR evolution, as in Fig. 3.2. Mergers B and D are *direct collisions* (i.e. they merge at their

first pericentric[4] passage) while mergers A and C involve multiple passages. The participation of multiple galaxies sets merger B apart from others. The final coalescence in merger A is preceded by a $\sim$ 2 Gyr orbiting of the progenitors around each other. SFR peaks occur approximately 1 Gyr post final coalescence.

The enhanced SFRs post coalescence in case of mergers A and B (involving multiple passages and multiple galaxies, respectively) are sustained well after the mergers are completed; unlike those in mergers C and D (involving multiple passages and direct collision respectively) wherein the SFR spikes die down much faster after the merger.

A corresponding visual inspection at respective timestamps in each case reveals that these star formation peaks are a result of the interaction between the progenitor nuclei. Indeed, our halo finder already marks the merger as finished slightly *before* the galactic nuclei have actually merged. We find the merger orbits and SFR patterns to be broadly consistent with the results from Sparre & Springel 2016 (which have the same initial conditions but slightly different physical model; see Sec. 3.2).

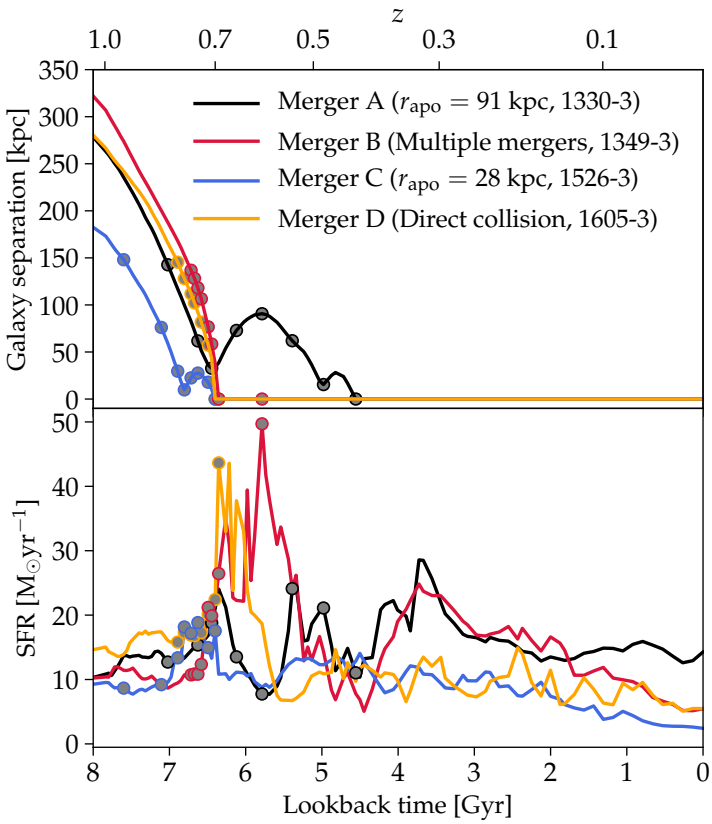

Figure 3.2: The evolution of galaxy separation for the merger progenitors (upper panel) and the star formation rate (lower panel). Of the four merger scenarios, two involve multiple passages (A and C) while the other two are direct collisions (B and D). Bursts of star formation follow soon after their pericentric passages or the final coalescence in all the mergers. For mergers A and C, we also mark the apocentric separations (r_{apo}). Grey-filled circles denote the merger time-stamps that will be studied in further detail.

[4]The midpoint of the axis joining the progenitors when they are at the closest from one another during the merger process.

3.4.2 Bridge formation and properties

Both earlier basic generations of idealized mergers (Toomre & Toomre, 1972) as well as more modern replications of galaxy mergers (Privon et al., 2013) predict the formation of a bridge post the first pericentric passage between the progenitors. The timeline of a bridge formation usually coincides with the most extreme conditions setting into the merger system such as dynamical turbulence causing gas sloshing motions, stellar orbits getting disturbed and the overall morphology of the progenitors beginning to get affected. Thus, studying the global properties of the system through bridges allows us to better characterize the immediate effect of major mergers on the whole system. The bridges in closed-box merger simulation models can only form via stellar and gas components from the galaxy discs themselves because extraneous gas flows (for example, from the CGM or IGM) are simply not a part of the setup. This is, however, not the case for cosmological simulations.

In order to identify the gas in the bridge in each merger case, we project the H I column density in Figs. 3.3–3.6. Each panel spans 150 kpc in width and we use a random projection direction (z-axis in this case). The redshift stamps marked for each panel correspond to the grey filled circles in Fig. 3.2. We include the pericentric passage and apocentre[5] in case of mergers with non-zero impact parameters (mergers A and C).

3.4.2.1 Multiple passage mergers

Both simulations A and C involve multiple passages and a bridge connects the two progenitors at apocentre (see Figs. 3.3 and 3.4). The apocentre is also where the bridge is most well-formed and hence we select the gas cells in the bridge at this epoch and track their motions, before and after, using tracer particles. Firstly, we take into account a unique vector associated with each gas cell in the bridge that connects it with the two merging galaxies. Further, we decompose this vector into a perpendicular ($d_\perp$) and a parallel ($d_\parallel$) component. These are defined as follows–

$$d_\perp = \frac{|(x_2 - x_1)\ \mathbf{x}\ (x_{\rm gas} - x_1)|}{|x_2 - x_1|} \tag{3.2}$$

$$d_\parallel = \frac{|(x_2 - x_1) \cdot (x_{\rm gas} - x_1)|}{|x_2 - x_1|} \tag{3.3}$$

where, x_1 and x_2 are the coordinates of the primary and secondary progenitors respectively and $x_{\rm gas}$ is the coordinate of a gas cell. $d_\perp$ measures the absolute distance from each gas cell to the vector joining x_1 and x_2 and hence is unsigned. $d_\parallel$, on the other hand, is signed and takes values between 0 and $|\mathrm{x_2} - \mathrm{x_1}|$. The apocentres occur at $z = 0.60$ and $z = 0.74$ for simulations A and C respectively. These are also the timestamps where the tracers are selected in both cases. We impose two criterion for tracer selection as follows–

1. Gas cells should be located between the galaxies and should specifically satisfy $0.4 < d_\parallel/|\mathrm{x_2} - \mathrm{x_1}| < 0.6$ and $d_\perp < 20$ kpc.

2. The gas cells should have a number density $n \geq 0.13$ cm^{-3} i.e. only dense gas is selected.

We depict the tracers by drawing contours at 50, 70 and 90 per cent of their distribution. In both cases, we see maximum distribution at the apocentre, as expected. For simulation A (Fig. 3.3), at $z = 0.74$ (i.e. prior to apocentre), majority of the gas tracers reside in the galactic

[5]The midpoint of the axis joining the progenitors when they are at the farthest from one another during the merger process.

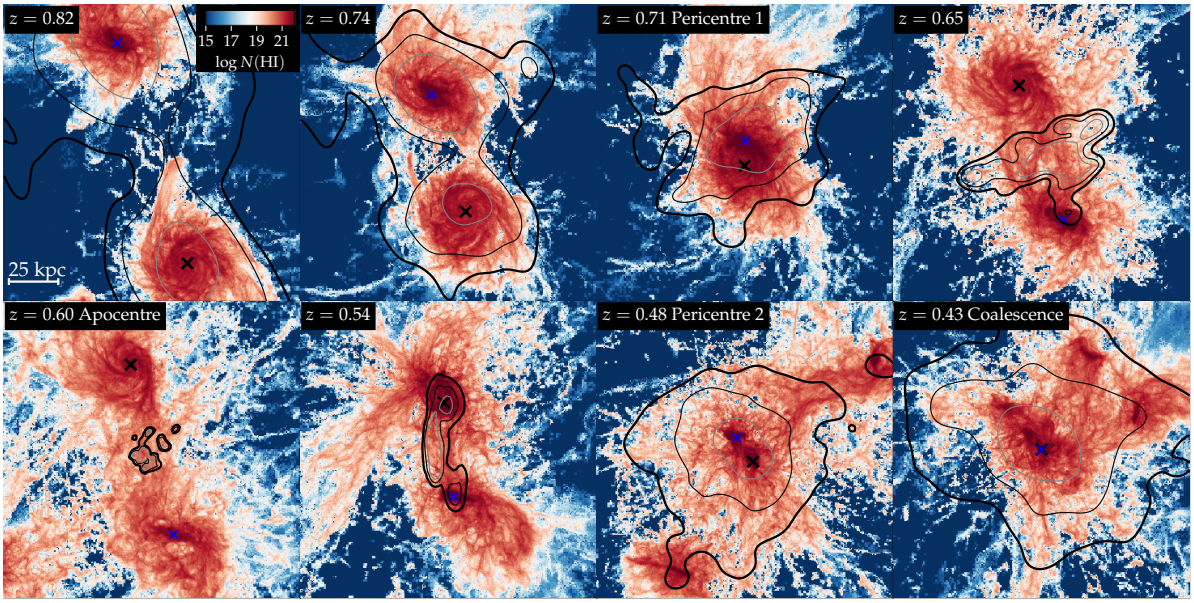

Figure 3.3: We track the changes in H I column density for the simulation A ($r_{\rm apo}$ = 91 kpc) across a redshift interval. The centres of the merger progenitors are marked by cross-symbols. Contours generated from tracer analysis reveal the presence of a dense H I bridge between the first and second passage (see panels from $z = 0.65$ to $z = 0.54$). Contour levels shown here encompass 50, 75, and 90 percent of the tracer particles that are selected to be in the galaxy bridge at $z = 0.60$. H I gas in the bridge is stripped not just from the galaxy discs but also accrued from the CGM.

discs. However, there is still a non-negligible fraction that originates *outside* the disc regions. At coalescence, tracers are concentrated in the central parts as well as outside of the merger remnant.

We repeat the procedure for simulation C (Fig. 3.4), albeit with a modified cutoff for the perpendicular distance, $d_\perp < 10$ kpc, since the separation between the progenitors is smaller in this case. The second criterion for gas cell density remains unchanged. Like in simulation A, majority of the gas originates from the discs but there is again a component from a satellite galaxy (see the panels showing $z = 0.94$ and $z = 0.83$ in Fig. 3.4).

3.4.2.2 Direct collision mergers

The galaxies in simulations B and D undergo direct collisions. There are multiple galaxies involved in the merger process in simulation B (Fig. 3.5), which is the primary reason for not implementing tracer analysis in this case. An extended tail also forms for one of the progenitors (marked by blue cross between $z = 0.75$ to $z = 0.73$). Morever, we see semblance of a bridge-like structure joining the two main galaxies at $z = 0.72$. We remark again that the presence of other galaxies around the main progenitors complicates the situation of gas tracking. The fact that this is a direct collision could also be the reason why there is no clear bridge formation. The involvement of multiple galaxies in such merger processes highlights the importance of including the larger cosmological context within such merger simulations. We note that simulation B will be excluded from our analysis henceforth due to the involvement of more than two merger progenitors.

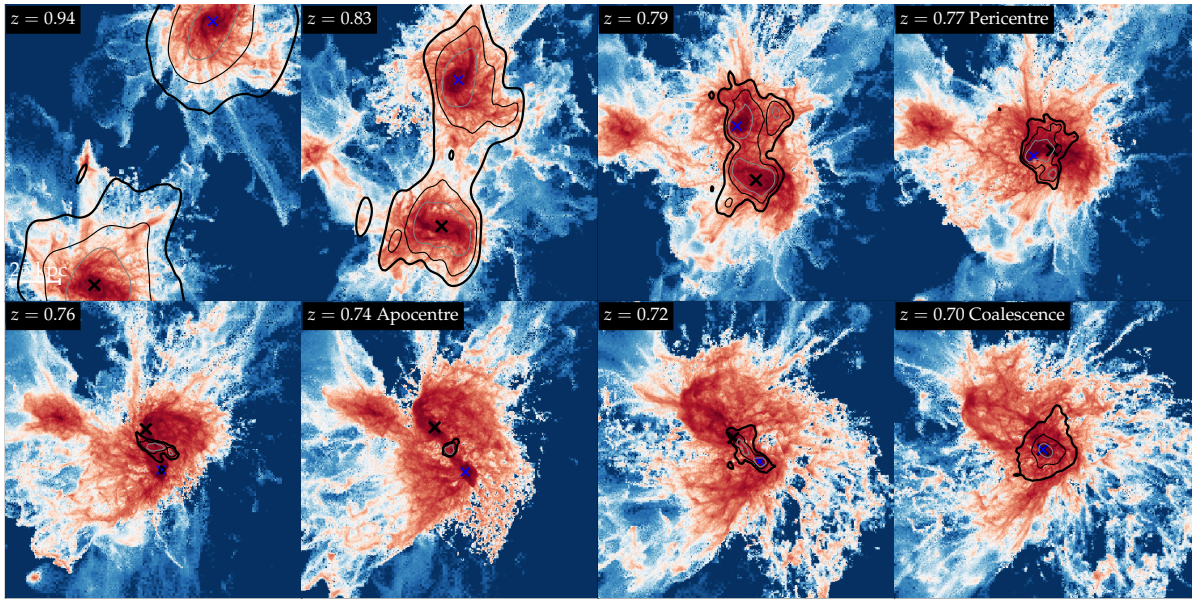

Figure 3.4: Simulation C ($r_{\rm apo} = 28$ kpc) again involves multiple passages and also reveals the presence of a bridge (formed at the apocentre at $z = 0.74$). In this case, most of the H I gas in the bridge emanates from the galactic discs of the progenitors.

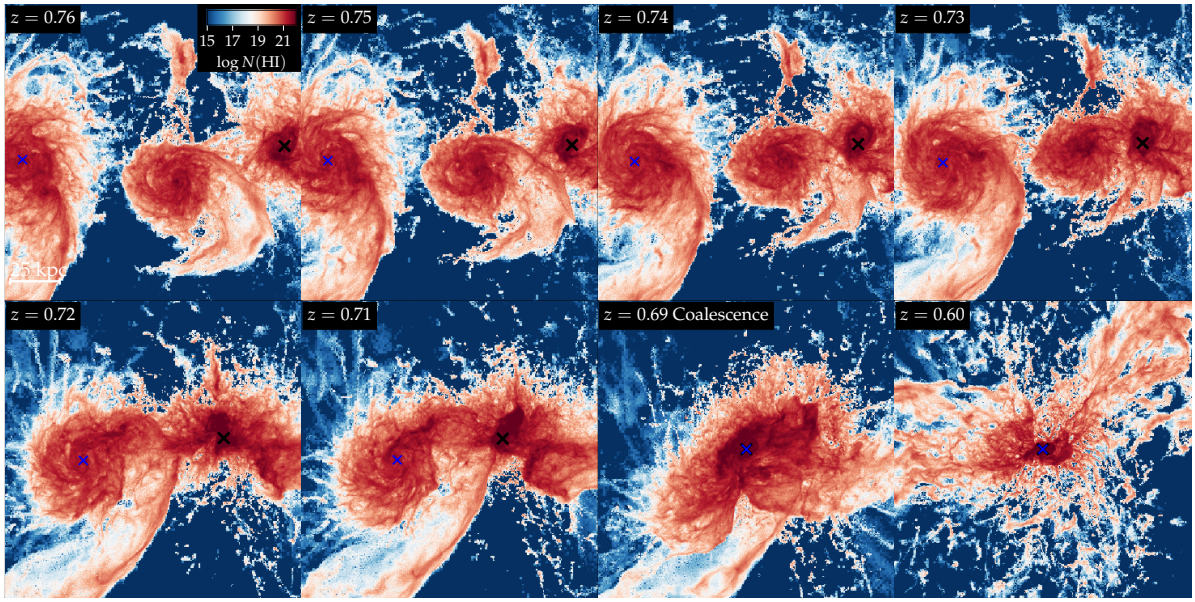

Figure 3.5: Simulation B involves a direct collision major merger with multiple participating galaxies. For the secondary progenitor (blue cross-symbol), gravitational forces due to the merger process give rise to an extended tail (at $0.73 \leq z \leq 0.76$). Detailed analysis shows that this rather messy system gives rise to rich, complex gas structures around the galaxies but we do not see any clear bridge formation.

Unlike simulation B, simulation D (Fig. 3.6) is fairly uncomplicated since there are no extra galaxies involved. Like earlier, this also being a direct collision probably results in the absence of a long-lived bridge. That said, there is still dense gas seen between the galaxies (see panel

at $z = 0.73$ in Fig. 3.6). It could be caused due to a tidal compression, shocks or ram pressure stripping. A trace-back to $z = 0.79$ shows that this stripped gas originates not just from the galaxies themselves but also from their CGMs.

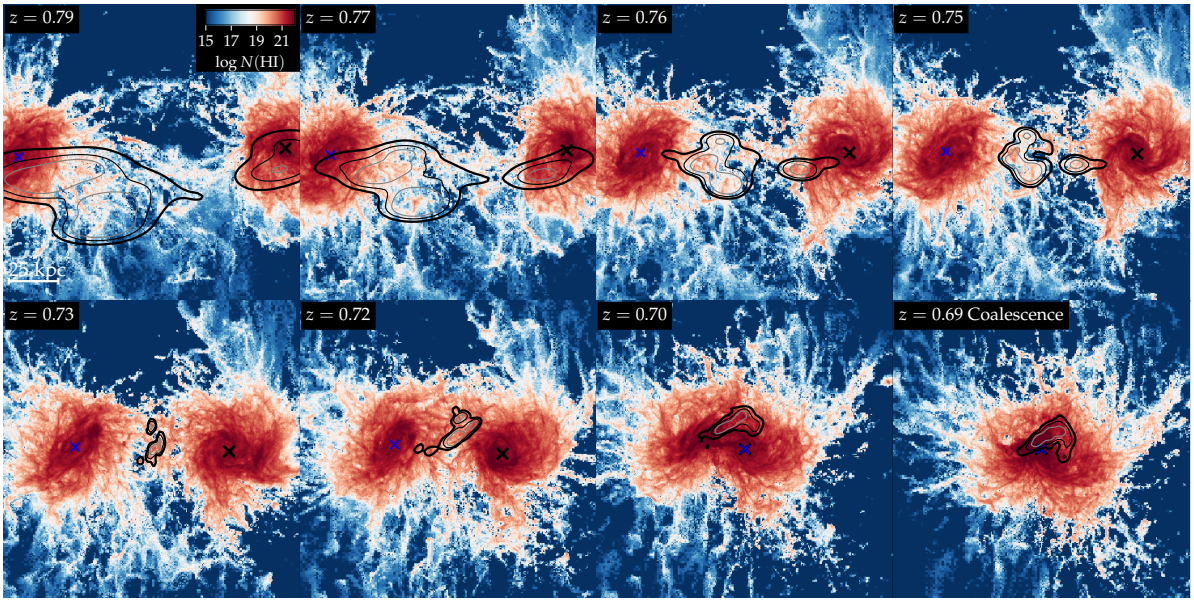

Figure 3.6: Like simulation B, the merger in simulation D is also a head-on collision (i.e. there is no second passage). While a clear bridge never forms, tracer contours mark the existence of dense gas between the progenitors (resembling a very weak bridge) at $z = 0.73$. This gas is seen to emanate partly from the galactic discs and from the CGM.

3.4.3 Origins of the bridge

Gas tracking via tracer analysis reveals that the gas in the bridge, formed between the merging galaxies, finds its way there not just from the ISM and disc regions of the galaxies but also from their circumgalactic mediums. As seen earlier, this gas is best observed in H I. Typical merger systems also exhibit the formation of a stellar bridge, attributed to the tidal stripping of material from the galactic discs (Toomre & Toomre, 1972). Tidal stripping is known to sweep away stellar as well as gaseous material from and around the disc and hence can be safely held responsible for the creation of bridges that have both stellar as well as H I component. On the other hand, bridges with a pure gaseous component are most likely to arise from predominant gaseous processes like ram pressure stripping, shocks and gas accretion. Thus, the visibility of the bridges in H I confirms that gaseous processes do play an unmistakable role along with the likely involvement from tidal stripping.

3.4.4 Gas mass fractions in bridges

In Fig. 3.7, we track the evolution of gas mass fractions, partitioned into three gas reservoirs– ISM, CGM and IGM. The timestamp at which we identify the tracers in the bridge is marked by the vertical dashed black line. In each case, the coalescence is marked by the vertical dashed red line. When the bridge is most conspicuous, the associated gas is found to lie either in the CGM (as in case of mergers A and D) or in the ISM (in case of merger C). It is worth noting

that the apocentre separation for merger C is quite small ($r_{\rm apo}$ = 28 kpc), which allows the bridge region to be within our ISM boundary definition ($< 0.2\ R_{200}$ of the merging galaxies).

About 1 Gyr prior to the apocentre, 47-67 per cent gas lies in the ISM while 33-48 per cent lies in the CGM (remaining 0-5 per cent is traced to the IGM). Our tracer analysis confirms that much of the gas in the bridge is funneled not just from the inner regions of the galaxy (driven by the simplest and most intuitive explanation) but also significantly from the CGM. Shortly after this epoch, merger-driven turbulence drives most of the gas into the ISM. Few Gyrs later, this gas is gradually ejected first to the CGM and then outside the haloes owing to the feedback from supernovae, winds, cosmic rays and black holes.

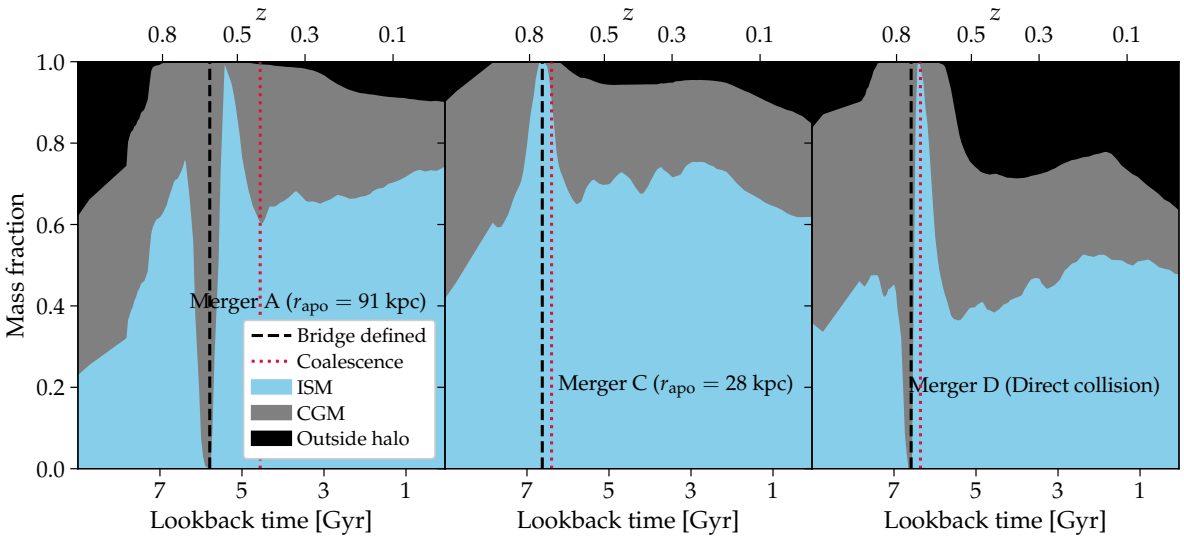

Figure 3.7: We track the same gas reservoirs in time as in Figs. 3.3, 3.4 and 3.6 for mergers A, C and D respectively. Each gas cell is assigned to one of the three gas reservoirs– ISM (blue), CGM (grey) or IGM (black). This enables us to obtain the *individual gas mass fraction evolution* for the three reservoirs. The coalescence epoch and that at which our bridge is defined are marked by the vertical dashed red and black lines respectively. For mergers A and C, just before the bridge is identified, most of the gas emanates from both the ISM as well as the CGM. Just after the apocentre, most of this gas is sloshed into the ISM of the progenitors. A part of this gas eventually ends up being expelled to the CGM and later to the IGM.

3.4.5 Star formation in bridges

Many studies have tracked the changes in star formation during the course of a merger. Indeed, merger environments are some of the most dynamic and extreme sites impacting both the gas and stellar motions of the participating galaxies immensely. In particular, the Arp and Taffy galaxies, systems undergoing some of the most striking mergers ever observed, have been a target of multiple studies in this regard; the setting-in of supersonic turbulence has been inferred to be the main cause in these cases (Braine et al., 2003; Smith et al., 2007; Vollmer, B. et al., 2012; Yeager & Struck, 2020; Vollmer, B. et al., 2021; Appleton et al., 2022).

As before, we show the H I gas column densities along with the star formation surface density and radial velocities in Figs. 3.8, 3.9 and 3.10. Because our subgrid model is tuned to reproduce the ISM characteristics of disc galaxies, it does not account for potential effects that may impact star formation in the bridge. In order to compute the SFR surface density, we select gas cells

within $d_\perp \leq 3$ kpc from the axis joining the merger progenitors. We create 3 kpc wide bins along the $d_\parallel$ axis. The first bin's centre lies at 5 kpc away from the main progenitor while the last bin's centre is 5 kpc from the second progenitor. Thus, following volume = π **x** (3 kpc)^3, each bin has a volume of $\simeq$ 85 kpc^3 and a corresponding spatial size of 4.4 kpc (size = volume$^{1/3}$). We also plot the parallel velocity component ($v_\parallel$) i.e. the velocities along the axis connecting the galaxies.

A gas bridge, traced in H I, is seen in simulations A and C (left panels in Figs. 3.8 and 3.9). We exhibit its formation by selecting a timestamp well before the first pericentric passage (upper panels) and the first apocentre (lower panels). A comparison between these two epochs reveals that the bridge is most well-formed at the apocentre in comparison to the first pericentric passage. Additionally, the presence of some star-forming clumps is also seen (middle panels in Figs. 3.8 and 3.9). In the velocity profile plot (right panels in Figs. 3.8 and 3.9), we see a transition between a negative gradient to a positive gradient between the two redshifts considered. In other words, the gas that is initially funneling towards the centre of the bridge ($d_\parallel = 0$) and is later being pushed outwards. Thus, extreme physical conditions come to the fore at the apocentre which makes mergers ideal laboratories for studying star formation in these special environments.

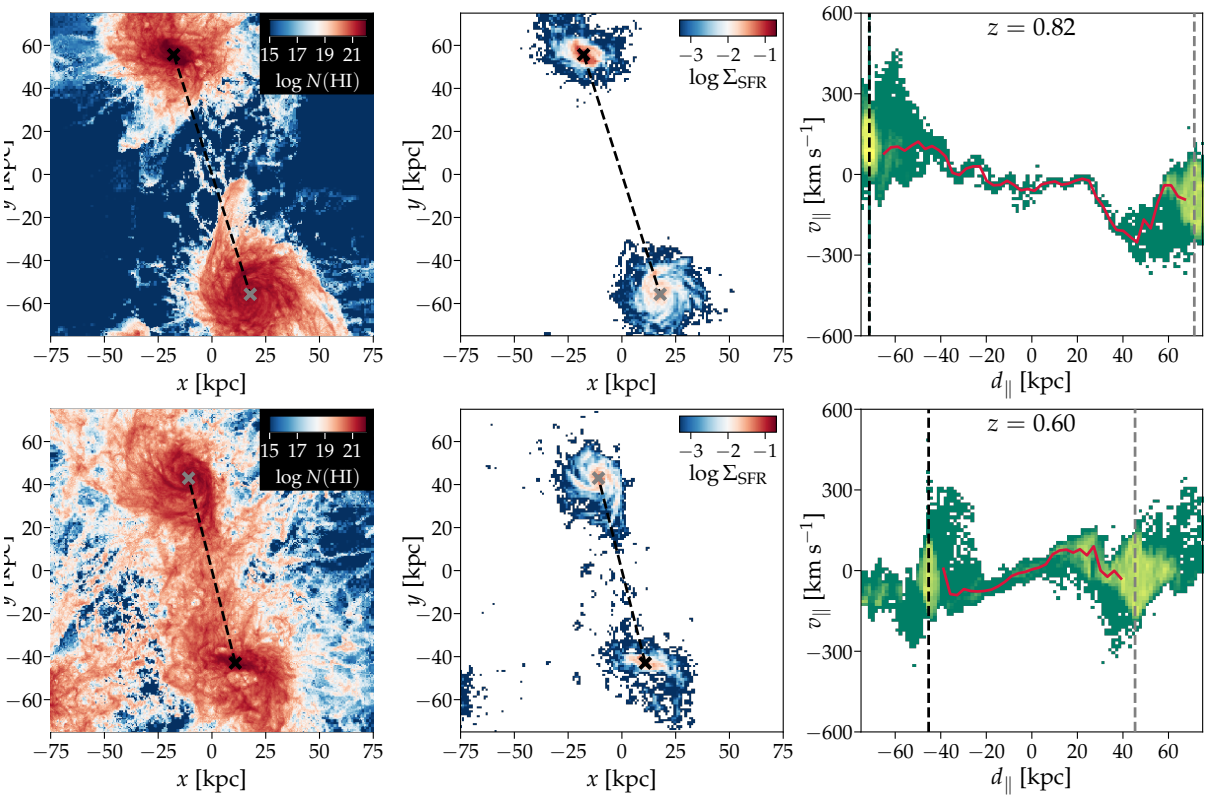

Figure 3.8: **L–R**: We show the H I gas column densities (in cm^{-2} units), SFR surface density ($\Sigma_{\rm SFR}$, in M$_\odot$ yr^{-1} kpc^{-2} units) and radial velocity (in km s^{-1}) profile along the parallel component, $d_\parallel$ for simulation A. The upper panels display the quantities captured at a snapshot before the first pericentric passage while the bottom panels are for the first apocentre. The merging galaxies are marked in the left and middle panels by grey and black crosses and by similarly colored dashed vertical lines in the rightmost panels.

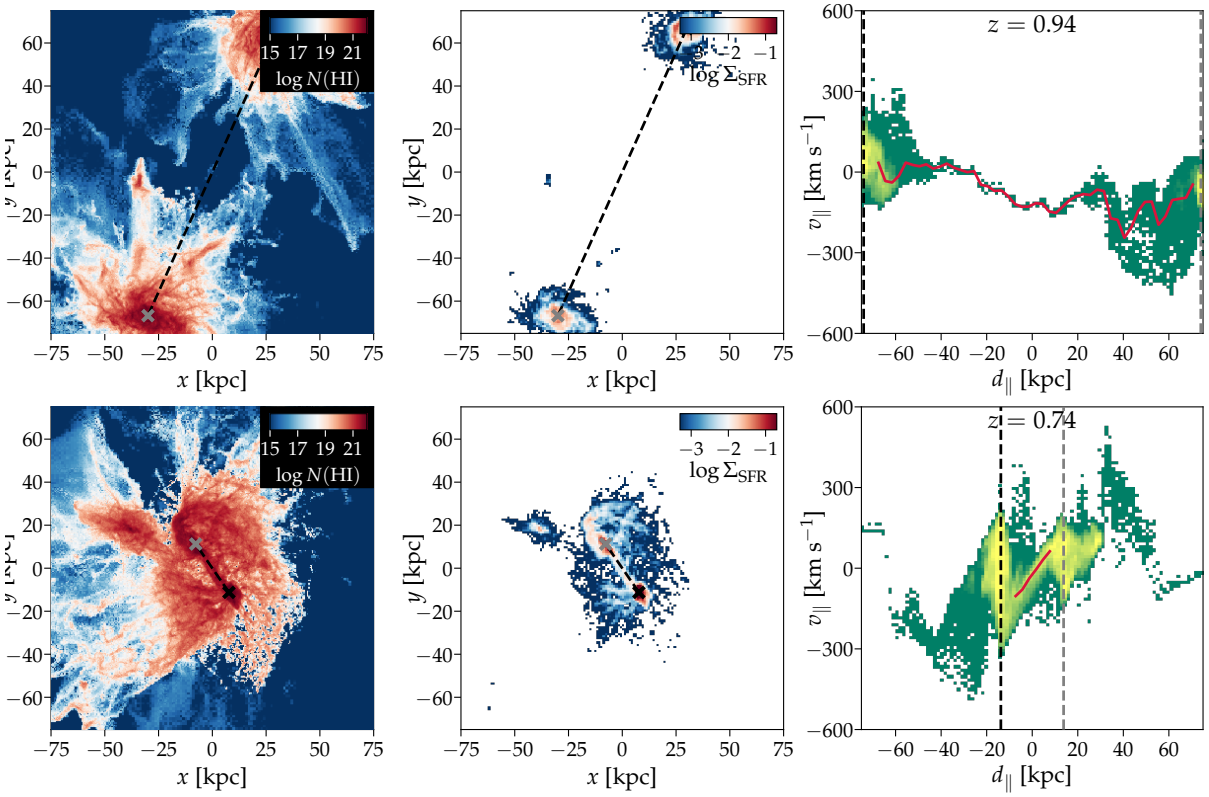

Figure 3.9: Same as Fig. 3.8, but for merger C.

For simulation D, a direct merger case, we select the redshift ($z = 0.73$) at which the bridge or the dense gas which gives the semblance of a bridge, is most visually pronounced (selected from a visual inspection of the most concentrated H I contours from Fig. 3.6). This epoch occurs just before the coalescence. The bridge in this case shows some characteristics similar to that in the case of the previous two mergers (with multiple passages). Active star formation occurs here as well and the velocity gradient shows gas flowing towards the centre of the bridge.

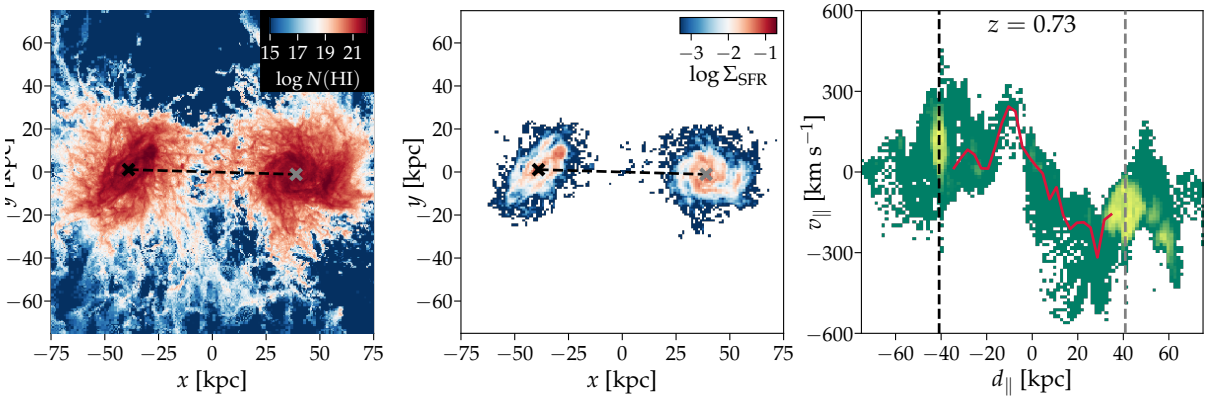

Figure 3.10: Same as Fig. 3.8, but for merger D. We remind the readers that there is no evident bridge formation in this case, but there is certainly the presence of dense gas between the merging galaxies. Accordingly, the relevant quantities are plotted corresponding to the snapshot where the interposing dense gas is at a maximum.

3.5 Discussion

All our merger remnants are found to be star-forming. Generally, this is at odds with the expectation from a major merger, wherein post-merger the galaxies hardly form stars (Martig et al., 2009; Man & Belli, 2018). However, considering the fact that the galaxies in our simulations are gas-rich (and hence the mergers are wet), it is less surprising to see a lack of quenching (Weigel et al., 2017; Ellison et al., 2018). Our analysis also revealed that some of the gas driving the post-merger star formation actually originates from the CGM of the progenitors in the pre-merger epoch. Idealized simulations mostly do not account for this additional source of gas and hence, might have overestimated the importance of quenching in mergers. On the other hand, the possibility of a more efficient AGN feedback model being employed in idealized simulations cannot be ruled out. The AGN feedback model used in our simulations has been tuned to reproduce observed scaling relations and abundance matching measurements. Such a tuning does not result in quenched merger remnants.

The Auriga galaxy formation model used in these simulations produces both MW-mass galaxies that are quenched or those having elliptical stellar structure (Grand et al., 2017). This means that we do not necessarily need mergers to produce non star-forming ellipticals. But since our model has not been tested on cosmological box simulations, it is difficult to predict whether the model over- or under-predicts the fraction of quenched ellipticals in different environments.

In the halo mass range being considered ($M_{200} \simeq 10^{12} M_{\odot}$), a number of other simulations as well as observations have found evidences for star-formation in their merger remnants. The role of mergers at high-z in Horizon-AGN simulations (Kaviraj et al., 2015), analysis of stellar components of merging galaxies in zoom-in simulations (Sparre & Springel, 2017), mergers in Auriga simulations (Bustamante et al., 2018) and the VINTERGATAN simulation (Agertz et al., 2021; Renaud et al., 2021), post merger galaxies' star formation patterns in Illustris (Rodriguez-Gomez et al., 2017) and IllustrisTNG (Patton et al., 2020; Quai et al., 2021) are some examples. Thus, simulations generally favor a lack of quenching in post merger galaxies.

Recent observations from the CALIFA survey (Barrera-Ballesteros et al., 2015) found enhanced star formation in interacting or merging systems as compared to non-interacting ones. Thorp et al. 2018 found similar results from their MaNGA survey sample. In some cases, reservoirs of molecular gas (Alatalo et al., 2016; Thorp et al., 2018) and H I (Ellison et al., 2018) (both acting as primary fuel sources for future star formation) were observed in post merger systems, casting aspersions on the *gas-blowout-phase* proposed in Hopkins et al. 2008. Indeed, the presence of H I gas, both before and after the merger, is seen not just in some of the aforementioned observational studies but also in our results (see Figs. 3.8, 3.9 and 3.10). Few studies also found that mergers may not be the predominant path towards quenching in galaxies (Violino et al., 2018; Pan et al., 2018). However, one must also keep in mind that the applicability of the above results is only confirmed currently for MW-mass galaxies at low redshifts. It is possible that mergers become more efficient in quenching more massive galaxies or MW-like galaxies at earlier epochs. New observations find massive galaxies being victims to fast quenching as compared to their less massive, younger counterparts (Forrest et al., 2020; Belli et al., 2021; Spilker et al., 2022).

All of our mergers happen between $z = 0.3$ and $z = 0.8$. This means that all of our above conclusions may not hold true for mergers outside this redshift range. The progenitor galaxies in our study have strong disc morphologies (for example, clearly evident spiral arms). Thus, our analysis can only be compared in the context of *low-redshift, gas-rich major mergers*. Studies point to the possibility that dense clumps (Buck et al., 2017; Zanella et al., 2019) and bursty star formation (Faucher-Giguère, 2017; Flores Velázquez et al., 2020; Orr et al., 2021) may

become more important in high-redshift galaxy mergers. These factors cloud the specifics of gas accretion in mergers at earlier epochs. Analogous to these low-redshift simulations, high-redshift simulations would be required to understand the role of gas accretion via CGM in the merger context.

3.6 Conclusions

We have used four gas-rich major merger simulations to study the gas flows and star formation evolution through each merger process. In accordance with the predictions from galaxy formation models, gas travels to and fro between the ISM and the CGM also in case of galaxies undergoing a major merger. The primary conclusions emerging from our study are as follows–

- A clear bridge is identified in a total of three out of the four merger simulations. Tracer particle analysis in the bridges reveals the presence of gas during coalescence.
- Roughly 47-67 per cent of this gas originates in the ISM of the progenitor galaxies approximately 1 Gyr before coalescence. However, about 33-48 per cent of gas is also found to lie initially in the CGM, only to be funneled in towards the bridge centre later.
- H I clumps can be seen in the bridge just before or during the coalescence, followed by bursts in star formation shortly after. These observations further support the role of CGM in merger-induced star formation in galaxies.
- The inflow and outflow of gas to and from the centre of the merging systems is clearly imprinted in the radial velocity profiles via a transition from a negative to a positive velocity gradient.

Chapter 4

How Satellite Galaxies Influence the Cold Circumgalactic Medium Around TNG50 Galaxies

The contents of this chapter are based on an ongoing publication effort that will soon be submitted to a peer-reviewed journal.

Title: *How satellite galaxies influence the cold circumgalactic medium around TNG50 galaxies.*

Complete author list: **Mitali Damle**, Stephanie Tonnesen, Drummond Fielding, Martin Sparre, Philipp Richter.

My contributions in the context of this chapter are as follows–

- I have led the scientific analysis, co-ordinated the contributions of co-authors and have published the paper as the leading author.
- The analysis pipeline used for this chapter has been developed in a JupyterLab workspace by me, with occasional inputs from Dr. Stephanie Tonnesen.
- Generated all the figures presented in this chapter.

4.1 Abstract

Cold halo gas is known to impact various evolutionary processes like, for example, accretion rates and star formation histories, during the lifespan of a galaxy. Satellite galaxies form a potentially important contributing channel in the cold gas assembly of a halo. We investigate the impact of satellite galaxies on the cold gas budgets of 234 parent L* halos in TNG50 simulations. Most of the cold gas in low mass halos ($M_{\rm h} \lesssim 10^{11.80}\ M_{\odot}$) is within the central galaxy, rather than the satellite population. Generally, higher mass halos ($M_{\rm h} \gtrsim 10^{11.80}\ M_{\odot}$) are consistently fed with cold gas by their primary (i.e. most massive) satellite but the ease with which cold gas is stripped off this satellite hardly makes any difference. Among all the global satellite properties considered, for low mass halos, the stellar mass of the primary satellite impacts the halo cold gas the most while for the massive halos, number of satellites emerges as the winner. Primary satellites (associated with high mass halos), whose mass is comparable to LMC/SMC ($M_{*} \sim 10^{9.5}$–$10^{10.0}\ M_{\odot}$), are less efficient in retaining cold gas with themselves as compared to their

less massive counterparts ($M_* \sim 10^{8.5}$–$10^{9.5}$ $M_\odot$) in the same halo mass bin. It is important to not just have massive satellites ($M_* > 10^8$ $M_\odot$) but also have enough number of them, such that they can meaningfully contribute cold gas to their parent halos. Our results reinforce earlier findings that satellite stripping is one of the many channels for depositing cold gas into a halo.

4.2 Introduction

Galaxies undoubtedly remain the building blocks of our universe. The life-cycle of a galaxy is largely governed by its immediate large-scale environment as well as the properties of the gas gravitationally associated with it (jie Peng et al., 2010; Kraljic et al., 2017). It is now well-known that baryons are accreted onto galaxies via filaments in the Cosmic web (Aragon-Calvo et al., 2016; Kleiner et al., 2017). The magnitude and rate of this accretion can vary depending on the environment that a galaxy finds itself in– galaxies near nodes generally experience much more baryon inflow as compared to those near voids or rarer environments (Kraljic et al., 2020; Zhu et al., 2022).

The in-falling gas from the Cosmic web must pass through the circumgalactic medium (CGM) before it can interact with the gas disk (interstellar medium or the ISM) of a galaxy (Cicone et al., 2019). The CGM is the primary site where the interaction between the effects of large-scale structure and that from the galaxy and its ISM constantly occurs (Putman et al., 2012). Feedback from AGN, supernovae, hot asymptotic giant branch (AGB) stars, etc. deposit baryons and metals into the CGM. External sources of radiation such as a temporally-varying UV background, the radiation from background AGNs and cosmic-rays, etc. as well as pristine cool gas influxes from the intergalactic medium (IGM) induce local as well as large-scale variations in the CGM temperature and density making it multi-phase in nature (Tumlinson et al., 2017). Baryons and various metals respond quite differently to these variations producing a whole range of ions in the CGM (Werk et al., 2016a; Oppenheimer et al., 2018b). Thus, the distribution, kinematics and mass budgets of these ions ultimately shapes the CGM at various epochs (Ford et al., 2013; Stern et al., 2018; Damle et al., 2022).

Depending on the cosmological environment, galaxies can enter the CGMs of more massive galaxies and become their satellites, spending a large part of their lives bound to their host galaxy. Their life-cycle is mostly at the mercy of their immediate large-scale environments (Martín-Navarro et al., 2021). Depending on the proximity of this satellite from the host galaxy, surroundings could be dictated by a fellow satellite galaxy or by its host. In any case, the global and statistical properties of a satellite population has a definite bearing on the extended CGM of their associated hosts and vice-versa (Fillingham et al., 2016; Simons et al., 2020; Wright et al., 2022). Thus, studying various properties of satellites is a great tool to closely scrutinize the local morphology of its host galaxy's CGM out to large impact parameters– something that would otherwise be far out of reach because of the low column densities in the CGM (Salem et al., 2015b; Richter et al., 2016; Armillotta et al., 2017).

Satellites experience numerous processes such as gas feeding from satellites onto hosts (Sanchez et al., 2018), ram-pressure stripping (Gunn & Gott, 1972b), tidal stripping (Bullock et al., 2001; Somerville et al., 2008), strangulation (Larson et al., 1980; Van Den Bosch et al., 2008; Peng et al., 2015), harassment (Moore et al., 1996; Davies et al., 2019), etc. during the course of their lives. The host galaxies, on the other hand, also find themselves impacted to varying degrees in terms of heightened bursts of star formation (Di Cintio et al., 2021), excess low-metallicity stars in the outskirts (Annem & Khoperskov, 2022), replenishment of their star-forming gas reservoirs (Leitner & Kravtsov, 2011), loss of momentum and energy in case of flyby/splash-back dwarf galaxies (Diemer, 2021) and baryon and metal enrichment in their

outskirts (Rubin et al., 2012). In general, satellites finding themselves closer to a host galaxy or a group environment tend to exhibit shallower gas reservoirs, lower star formation rates and enhanced mass loss from their ISM/CGMs as opposed to isolated ones (Spekkens et al., 2014; Stierwalt et al., 2015; Putman et al., 2021; Li et al., 2022). The knowledge about the properties and fate of a satellite galaxy, thus, unfolds an extra layer of information about the surrounding gas environment it finds itself embedded in.

To define different CGM phases certain fiducial temperature cuts have been generally agreed upon over the last decade. Thus, we have the cold-dense phase ($T < 10^4$ K), warm-hot-ionized phase ($10^4 < T < 10^5$ K) and hot-ionized-diffuse phase ($T > 10^5$ K). A MW-like galaxy (halo mass, $M_h \simeq 10^{12}$ $M_\odot$; Gnedin et al. 2010; Piffl et al. 2014; Bland-Hawthorn & Gerhard 2016; Patel et al. 2018; Posti & Helmi 2019), is known to harbor a baryonic mass of around $10^{11.5}$ $M_\odot$ (Werk et al., 2014; Miller & Bregman, 2015; Salem et al., 2015b; Nicastro et al., 2016; Kaaret et al., 2020; Faerman et al., 2022). These numbers are relevant because we focus only on MW-like, L^* galaxies and their satellite populations in this paper.

While the hot CGM is known to largely dominate (up to 50%) the total CGM mass budget for galaxies in the considered mass range (Peeples et al., 2014; Werk et al., 2016a), an accurate accounting of the non-negligible cold phase CGM (which is omnipresent in not just spiral galaxy halos but also across elliptical galaxy populations) is nonetheless important. There exist varying estimates for the mass in the cold CGM both from observations and simulations. 21-cm line estimates from the high-velocity clouds (HVCs) in the MW (Putman et al., 2012; Richter et al., 2017) predict less than 10^9 $M_\odot$ in the cold CGM, while the low-z universe COS-Halos observations (Werk et al., 2014) put this number at $\sim 5 \times 10^{10}$ $M_\odot$. Simulations from TNG50 galaxies (Ramesh et al., 2022) estimate less than 3×10^9 $M_\odot$ cold gas. Similar study from FIRE-2 galaxy samples (Hafen et al., 2019) reveals $\sim 5 \times 10^9$ $M_\odot$ amount of cold CGM gas. Overall, these numbers constitute to less than 25% of the total baryon mass of an L^* galaxy.

Multiple line–of–sight observations (Tripp et al., 2008; Kacprzak et al., 2012; Crighton et al., 2015; Borthakur et al., 2016; Ponti et al., 2022) as well as simulations (Oppenheimer et al., 2018b; Buie et al., 2018; Butsky & Quinn, 2018) present small volume filling factors but pretty large covering fractions for the cold CGM. This establishes the small-scale yet well-distributed nature aka patchy nature of the cold CGM throughout the galactic halo (also predicted by theoretical models such as (Liang & Remming, 2020; Gronke et al., 2021)). This, coupled with the unexpected presence of abundant cold gas in massive galactic haloes with super-hot virial temperatures (Prochaska et al., 2013; Smailagić et al., 2018; Chen et al., 2018), adds to the intrigue about the origins of this particular CGM phase.

Accretion of metal-poor, cold gas from the IGM is thought to be an important source for depositing cold gas clumps into the CGMs of galaxies on its way towards the ISM (Kereš et al., 2005; Kereš & Hernquist, 2009; Nelson et al., 2013). Galactic outflows and fountain flows could export some cold gas from the inner regions of a galaxy to its outer regions (Ford et al., 2013; Thompson et al., 2016). Minor mergers could also result in some cold gas from the smaller progenitor being dumped into the CGM of the main galaxy during the process of merger (Sancisi et al., 2008). Mihos & Hernquist 1994 noted a surge in star formation rates of the centrals owing to their involvement in minor mergers. Some other observational studies (Di Teodoro & Fraternali, 2014; Janowiecki et al., 2017) attribute excess gas content in low-mass group centrals partly due to an earlier history of H I-rich minor mergers (though it is unlikely that minor mergers are entirely responsible for this excess gas; Lehnert, M. D. et al. 2016). The motion of cool clouds embedded within a surrounding hot medium through the CGM of a galaxy gives rise to an interface which facilitates cooling as a result of thermal instabilities, condensation and so on (Maller & Bullock, 2004; Voit et al., 2015).

Satellite galaxies themselves, to some degree, contribute to the patchiness of the cold CGM. Gas getting stripped from a satellite population and accreting onto the host galaxy can induce localized cold and cool gas clumps in the extended CGMs of the host (Nelson et al., 2020; Dutta et al., 2021; Tonnesen & Bryan, 2021). The size of these clumps could go from hundreds and thousands of parsecs (for example, the Magellanic Stream) (Wannier & Wrixon, 1972; Mathewson et al., 1974; Rauch et al., 1999) to as small as a few parsecs (McCourt et al., 2017) or even sub-parsecs (Richter et al., 2005). Insights from recent wind-tunnel and radiative turbulent mixing layer simulations as well as theoretical models tell us that the survival and/or growth of these clumps, that travel through a hot ambient medium, majorly depends on whether or not radiative cooling dominates over destructive fluid instabilities (Sparre et al., 2018; Gronke & Oh, 2020; Fielding et al., 2020). Idealized simulations of cold cloud-hot wind interactions in peculiar cases such as that in Jellyfish galaxies further reveal the possibility of highly ordered magnetic fields that are aligned with the tails of such galaxies (Sparre et al., 2020). Recently, 3D hydrodynamical simulations (specifically modelling the Magellanic Stream's fate as it hurtles through the outer halo of our Milky Way) have provided some concrete constraints on the surrounding pressures, velocities as well as cooling times for the preservation and subsequent growth of cold clumps in the CGMs of galaxies (Bustard & Gronke, 2022; Tan et al., 2022).

Our motivation for this study is to highlight the effect of satellite populations on their (MW-like) host halo CGMs in TNG50 simulations. We attempt to determine whether satellites affect the cold gas mass and distribution of the CGM. Furthermore, we find out which of the global properties of satellites (number of satellites per halo, total mass in satellites or the stellar mass of the most massive satellite) actually end up impacting the mass in cold phase of the CGM.

This paper is structured as follows: We briefly describe the numerical setup and galaxy formation model of TNG50 in §4.3.1 and establish the nomenclature (used throughout the paper) in §4.3.2. §4.3.3 describes the sample selection process, §4.3.6.1 lays down the approach adopted for binning and slicing the sample and in §4.3.5 we define cold gas in our simulations. §4.3.7 describes our controlled experiment designed to bring out the satellite–CGM connection. We present our results in §4.4. The implications of our results in the context of current theories about CGM and galaxy formation and evolution are stated in §4.5. Finally, we sum up our conclusions and provide a quick note about certain caveats and ideas to be implemented in future projects (§4.6).

4.3 Methods

4.3.1 Simulations

The TNG50 (Nelson et al., 2019a,b; Pillepich et al., 2019) is the third simulation volume (other two being TNG100 and TNG300) in the IllustrisTNG series (hereafter, TNG) (Nelson et al., 2017; Pillepich et al., 2017; Marinacci et al., 2018; Naiman et al., 2018; Springel et al., 2018). It is the smallest volume (box size of 51.7 $cMpc^3$), best resolved ($m_{baryon}= 8 \times 10^4$ $M_\odot$; $m_{dm}= 4.5 \times 10^5$ $M_\odot$) realization in the TNG suite and is generated on the underlying principles of combining the statistical prowess offered by conventional large box simulations with the superior resolution offered by zoom-in simulations. This approach is quite effective in counteracting against the poor spatial resolution, typical of large-volume simulations as well as low number statistics that are a by-product of zoom-in simulations.

The ideal MHD-self gravity coupled equations that form the backbone of the TNG are solved using the moving-mesh code AREPO (Springel, 2010). The tree-particle-mesh (TreePM) algorithm handles the Poisson equations for self-gravity while a second-order, finite-volume Go-

dunov scheme (Pakmor et al., 2016b) is applied on the Voronoi mesh that continually moves in response to the underlying fluid motions. Baryon tracking is implemented via Monte-Carlo tracer particle scheme (Genel et al., 2013) while halo catalogs and subsequent subhalo associations are computed via friends-of-friends (FoF) and SUBFIND algorithms (Springel et al., 2001) respectively.

The coupled interactions between dark matter, gas, star and black hole particles are evolved from a redshift $z = 127$ to present day (i.e. $z = 0$). The TNG uses a refined version of the galaxy formation model used in the original Illustris simulation (Torrey et al., 2014b; Genel et al., 2014; Sijacki et al., 2015; Vogelsberger et al., 2014b,a). The baryonic physics components unchanged from the original Illustris are: Primordial and metal-line cooling (Vogelsberger et al., 2013) along with a spatially-uniform UV background (Faucher-Giguère et al., 2009) and self-shielding corrections in dense regions (Rahmati et al., 2013); star formation in the dense ISM implemented via stochastic sampling of particles satisfying a certain density threshold criterion; an effective equation of state for the two-phase model that enables energy transfer via radiative cooling and supernovae heating, ultimately resulting in a pressurized ISM (Springel & Hernquist, 2003); chemical enrichment and mass loss from mono-age stellar populations; supermassive blackholes' seeding and their subsequent feedback contributions. Additionally, an updated kinetic feedback model from supermassive blackholes (alongside the existing quasar-mode feedback), a revised galactic winds' prescription and inclusion of a seed magnetic field and its amplification are the novel features in the TNG model. Interested readers can find further details on the TNG model in the relevant method papers (Weinberger et al., 2017; Pillepich et al., 2018).

The initial conditions assume the best-fit cosmological parameters ($h = 0.6774$, $\sigma_8 = 0.8159$, $\mathrm{n}_s = 0.9667$, $\Omega_{\Lambda,0} = 0.6911$, $\Omega_{\mathrm{m},0} = 0.3089$ and $\Omega_{\mathrm{b},0} = 0.0486$) derived from the Planck 2016 (Planck Collaboration et al., 2016) results.

4.3.2 Object definitions

Before starting the description of our sample selection and curation, we first need to state relevant nomenclatures (as used in TNG interchangeably to refer to different astrophysical components therein) as well as a note on the TNG particle association scheme.

- All FoF groups are referred to as *Halos*. These are identified in the TNG using the Friends-of-Friends algorithm with a linking length of $b = 0.2$.
- All SUBFIND groups or galaxies are referred to as *Subhalos* and are identified in the TNG using the SUBFIND algorithm.
- Each halo consists of a primary subhalo plus a number of secondary subhalos.
- Primary subhalos (i.e the most massive subhalo) of respective FoF groups are referred to as *Centrals*.
- Secondary subhalos within a FoF group are referred to as *Satellites*. The most massive satellite galaxy within each halo is referred to as the *Primary satellite*.
- There exist primarily four types of particles/cells in TNG: Gas (PartType0), Dark matter (PartType1), Stars and wind particles (PartType4) and Black holes (PartType5). We refer to the masses associated with each of these particle types corresponding to a single halo as M_{gas}, M_h, M_*, and M_{bh} respectively.

- Each particle has a FoF halo association[1]. In the next level of particle association hierarchy, particles are associated with a particular subhalo (via SUBFIND). There also exists a (small) set of particles that are, on the virtue of their binding energy, not associated with any Subhalo but are instead only associated with the FoF halo. These particles are called the *Inner fuzz*.

Throughout this paper, we will keep referring to relevant astrophysical objects in our simulations using the above nomenclature scheme.

4.3.3 Sample selection

Our goal is to ultimately find out if there exists any correlation between the properties of the overall satellite population associated with a halo to the cold gas phase in the CGM of this halo. In the present scope of this study, we limit ourselves only to MW-like halos (L^* halos) at $z = 0$.

To unveil such halos, we adopt a set of constraints for the $M_{\rm h}$, M_* and star formation rate (SFR) values and select halos satisfying these criteria. The constraint values for the aforementioned three parameters are listed below–

- $M_{\rm h}$: $\{7 - 175\} \times 10^{10}\ M_\odot$ or $\{10 - 250\} \times 10^{10}\ M_\odot/h$
- M_*: $\{0.7 - 7\} \times 10^{10}\ M_\odot$ or $\{1 - 10)\} \times 10^{10}\ M_\odot/h$
- SFR: $\{0.7 - 3.5\}\ M_\odot\ {\rm yr}^{-1}$ or $\{1 - 5\}\ M_\odot/h\ {\rm yr}^{-1}$

A total of 234 halos are found to qualify in this selection process. Each of these halos have several satellites associated with them. As highlighted in §4.3.2, we denote the most massive subhalo of each group as the Central, surrounded by other secondary subhalos i.e. satellites. Since we want to only include systems resembling real satellite galaxies with realistic particle masses, we impose a minimum stellar mass cut ($M_* \gtrsim 10^4\ M_\odot$) on all satellites.

4.3.4 Dealing with the outlier subhalos

We discovered that some subhalos associated to the halos in our sample have an unusually high M_*/M_h ratio (in comparison to the values in Behroozi et al. 2013). We regard these as "outliers". We obtain the M_*/M_h ratios for all such "outlier satellites" and compare to the corresponding ratio range[2] for conventional subhalos. We note that typically these outliers have M_*/M_h values exceeding 1.0.

Most of these outliers have such large M_*/M_h values because of their characteristically small M_h ($M_h < 10^6 M_\odot$). This could happen if the SUBFIND associator erroneously appends a part of the halo mass from a neighbouring massive subhalo to a nearby tiny clump. We suspect (and later verify the possibility) that most of the outliers lie rather close to the centrals, within $r < 0.2\ R_{\rm vir}$ (where $R_{\rm vir}$ is the radius corresponding to a distance where the spherically averaged density equals 200 times the critical density of the universe), i.e., situated in the inner CGM or merging with the central rather than lying well within the CGM of a halo. However, we also do not reject the possibility that a small fraction of these outliers might constitute highly turbulent systems such as Jellyfish galaxies. Such galaxies are, in all likelihood, to be found only in the most massive halos from our sample (Smith et al., 2022; Zee et al., 2022). We conclude,

[1]Particles that are not associated with *any* FoF halo are referred to as *Outer fuzz* particles.

[2]For subhalos with $10^{11} \leq M_h \leq 10^{12}$, this ratio is $0.005 \leq M_*/M_h \leq 0.05$; see fig. 14 in Behroozi et al. 2013.

therefore, that doing away entirely with such possible "jellyfish" systems is likely to introduce very minor (per cent level) errors in our whole sample.

Rather than adopting a simplistic approach of eliminating such outliers entirely, we choose to deal with them in a slightly more nuanced way. Firstly, we compute the distance of each outlier from its corresponding central and inspect which of those lie within 0.2 $R_{\rm vir}$ of their centrals. We find that a majority of the outliers are indeed situated within the inner CGMs of their centrals. In the next step, we eliminate only the above selected outliers and append their stellar masses to their corresponding most massive neighbouring subhalo[3]. Appending the stellar mass of these outliers back to the neighboring most massive subhalo also ensures that some of the association errors by SUBFIND are undone.

4.3.5 Defining cold gas in TNG50

For this study, we are focused on the "cold" gas in the CGM, since the infalling gas feeding the central galaxy is mostly in this particular phase. We define "cold" gas as all gas cells in TNG50 that satisfy temperature cut criterion (defined below) as well as have a non-zero instantaneous star formation rate.

The two-phase pressurized ISM model implemented in TNG gives rise to a temperature that is not strictly physical, but "effective". This effective temperature of a star-forming gas cell is always higher in comparison to the cold-phase's temperature in the subgrid model (Kereš et al., 2012; Sparre & Springel, 2016), as each star-forming subgrid gas cell also has a contribution from a hot subgrid phase.

In the subgrid model, the unresolved cold phase has a temperature of 10^3 K and it dominates the mass-budget (in comparison to the unresolved hot phase), so in our analysis we override the "effective temperature" with a temperature of 10^3 K (as also done in e.g. Ramesh et al. 2022).

4.3.6 Binning & Slicing

In §4.3.3, we described our sample assembly process wherein we have 234 L^* halos, each having a certain number of subhalos. These halos span a fairly extensive range in halo-stellar masses as well as SFRs. Our focus in this paper is to understand how the mass in cold gas phase ($M_{\rm cg}$) is affected by different properties of the satellite population. However, to do this we must first address the positive correlation of $M_{\rm cg}$ as well as number of satellites per halo ($N_{\rm sats}$) on the corresponding halo and stellar masses of the host galaxy. Massive halos with larger stellar masses generally harbor larger reserves of cold gas as well as more satellite halos (Munshi et al., 2013; Feldmann et al., 2019; Henriques et al., 2019). The interdependence between cold gas mass and stellar masses can cloud the more subtle scaling of cold gas mass with satellite properties.

To reduce this effect, it becomes necessary to first fragment the whole sample into subgroups such that the $M_{\rm cg}$ does not monotonically increase as a function of the stellar mass of the constituent centrals for halos within individual subgroups. These subgroups (henceforth, "bins") are formed on the basis of the stellar mass values of the centrals or $M_{*\rm C}$. Thereafter, based on the $N_{\rm sats}$, we slice each bin into Bottom quartile (BQ), Inter quartile (IQ) and Top quartile (TQ). Finally, via a comparison of the stellar mass distributions between both the extreme end quartiles, we confirm that the bins do not show any correlation between their corresponding $M_{*\rm C}$ and $N_{\rm sats}$ values.

[3]Few outliers (those lying outside of 0.2 $R_{\rm vir}$ of their centrals) are, nevertheless, not eliminated from our sample. However, they constitute a tiny fraction both in comparison to the total number of eliminated outliers as well as their stellar masses ($< 4\%$), with respect to the stellar masses of the centrals. Hence, their existence in our sample can be safely allowed for, in the rest of our analysis.

Table 4.1: The 2-sample K-S test results (D-statistic and p-value), performed between the bottom and top quartiles of each respective bin, corresponding to our most optimal bin limits. Corresponding percentile as well as the $M_{*\mathrm{C}}$ ranges are also stated. Last two columns provide the $\bar{X} \pm$ MAD values for the respective quartiles per bin. Excellent agreement between these two sets of values confirms the earlier conclusion from the K-S test about the high likelihood of the underlying quartile samples having a common distribution.

Samples	Percentiles	Bin limits	2-sample K-S test results		Med_{BQ}	MAD_{BQ}	Med_{TQ}	MAD_{TQ}	$\bar{X}_{BQ}$ +	$\bar{X}_{TQ}$ -
		$(M_{*\mathrm{C}}, \log \mathrm{M}_{\odot})$	D-statistic	p-value	$(\bar{X}_{BQ})$		$(\bar{X}_{TQ})$		MAD_{BQ}	MAD_{TQ}
$\{\mathrm{LMB}\}_{\mathrm{BQ–TQ}}$	0–50th	10.060–10.417	0.24	0.41406	10.2702	0.070	10.3028	0.068	10.34	10.23
$\{\mathrm{MMB}\}_{\mathrm{BQ–TQ}}$	50th–85th	10.417–10.775	0.56	0.00197	10.4706	0.045	10.5833	0.105	10.51	10.44
$\{\mathrm{HMB}\}_{\mathrm{BQ–TQ}}$	85th-100th	10.775–11.348	0.20	0.9748	10.8638	0.081	11.0168	0.083	10.94	10.79

4.3.6.1 The Binning Process

We first bin our galaxies into smaller mass ranges such that the $N_{\rm sats}$ is not directly correlated with the $M_{*\rm C}$. To do this, we iteratively select stellar mass ranges and determine how the stellar mass distribution differs when comparing halos with high (henceforth, top quartile; TQ) versus low (henceforth, bottom quartile; BQ) numbers of satellites. To do this we use the 2-sample Kolmogorov-Smirnov (K-S) test (Kolmogorov, 1933; Smirnov, 1948) on the top and bottom quartiles of the bins of galaxies with smaller central stellar mass ranges. The 2-sample K-S test has been used as an effective statistical tool in determining the likelihood of two distributions stemming from the same sample (Peacock, 1983; Fasano & Franceschini, 1987; Babu & Feigelson, 2006).

To guide the reader, the K-S test comparing the top and bottom quartiles for the whole sample of 234 halos gives a p-value of 2.736×10^{-20}, well below any reasonable threshold that would indicate the stellar masses are drawn from the same distribution. This necessitates the need for a series of iterations to produce a Low Mass Bin (LMB) and a High Mass Bin (HMB) for which the stellar mass distributions could be roughly similar between the internal top and bottom quartiles. Our outermost bin boundaries i.e. the lower-bound of our first bin (LMB) and the higher-bound of our last bin (HMB) remain unaltered throughout this trial-and-error process (since we have fixed values for the lowest and highest $M_{*\rm C}$).

We repeatedly try out different percentile values for $M_{*\rm C}$ for the inner bin boundaries, each time performing the 2-sample K-S test between the top and bottom quartiles of $M_{*\rm C}$ values within each bin. Our goal is to include as many galaxies as possible in each bin, so we begin by using the lower 50% of galaxies in the LMB and the upper 50% of galaxies in the HMB. As seen in Table 4.1, the p-value for the LMB set is high enough so that we do not need to continue iterating any further. However, the HMB continually shows a correlation between $N_{\rm sats}$ and $M_{*\rm C}$ until we only include the most massive 15% of galaxies. We present the D-statistic and p-values for all of our bins in Table 4.1. Note that the p-value for the Middle Mass Bin (MMB) is low, indicating that there is still a correlation between $N_{\rm sats}$ and $M_{*\rm C}$. Therefore, our analysis focuses only on the LMB and HMB halos.

Unlike the LMB and MMB, the combined number of halos in the bottom and top quartiles of the HMB is quite low. The reliability of the K-S test is known to reduce significantly when the sample size is small. In such cases, the median and mean absolute deviation (MAD) values are more reliable. Thus, as a final check, we also obtain the median values of $M_{*\rm C}$ ($\bar{X}$) and the MADs for the bottom and top quartiles for the LMB and HMB halos. The MADs are computed as the median of $|X_i - \bar{X}|$, where, $\bar{X}$ is the median of X_i. If the $\bar{X}\pm$ MADs between quartiles of respective bins overlap, it indicates that the two distributions are similar. We show these values as well in Table 4.1, and it is clear that there is an overlap[4] in the mass distributions, as expected from our K-S selection technique. We also compute corresponding inter-bin parameter values for the two sets of quartiles for other halo attributes such as $\rm M_{\it h}$, $\rm M_{gas}$, $\rm M_{cg}$, $\rm M_{bh}$ and SFR for completeness purposes; the resultant values are summarized in the Appendix A.4.

4.3.6.2 The Final Binned Samples

Our K-S test defines a triad of the most optimal bins such that the stellar mass values for the centrals per halo within the bins do not directly correlate with the corresponding number of

[4]Even though the p-value for the MMB quartiles is significantly low, the corresponding $\bar{X}\pm$ MAD values are almost the same. While we do not include the MMB dataset in our analysis further on, it is, nevertheless, reassuring to see such an overlap for MMB halos as well.

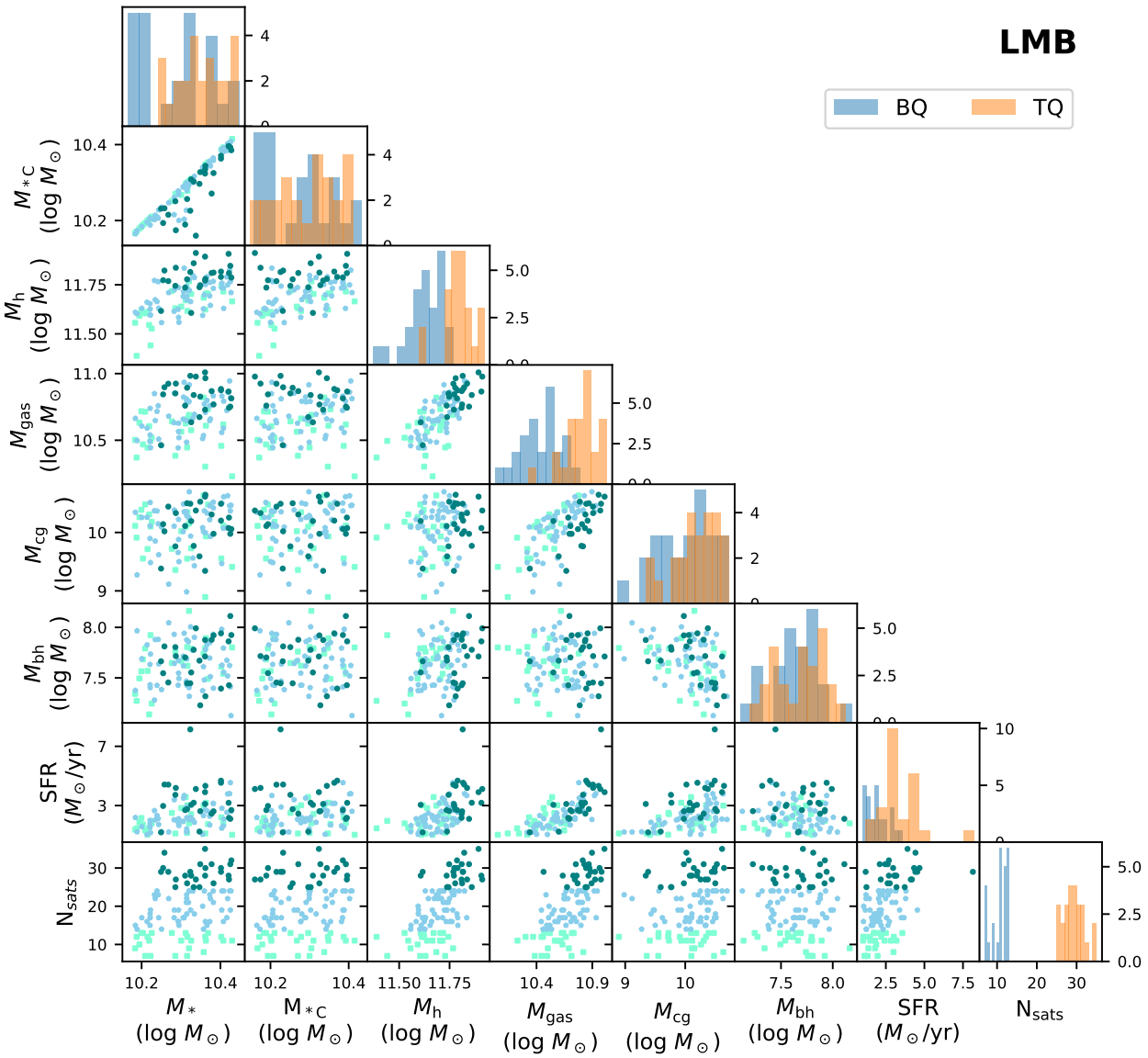

Figure 4.1: Scatter plots for the LMB halos probing correlations between Number of satellite galaxies per halo ($N_{\rm sats}$), M_*, $M_{*\rm C}$, $M_{\rm h}$, $M_{\rm gas}$, $M_{\rm cg}$, $M_{\rm bh}$ (all in log $M_\odot$), and SFR (in $\rm M_\odot\ yr^{-1}$). 25th, 50th and 75th quartiles are shown as aqua, blue and teal points respectively. Histograms for the 25th (Bottom) and 75th (Top) quartiles for corresponding halo attributes are also shown in the form of blue and orange bars respectively.

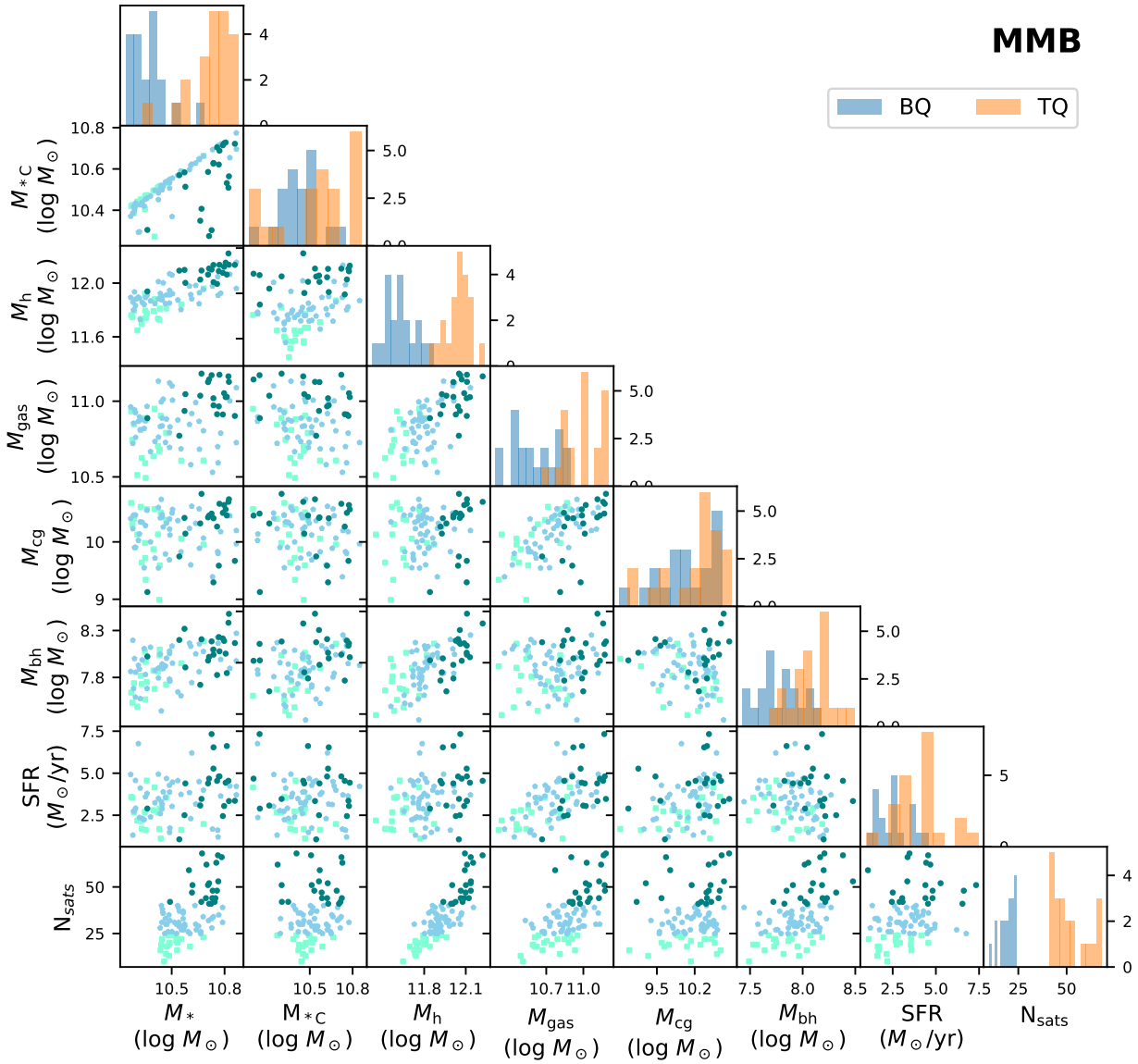

Figure 4.2: Same as Fig. 4.1, but for MMB halos.

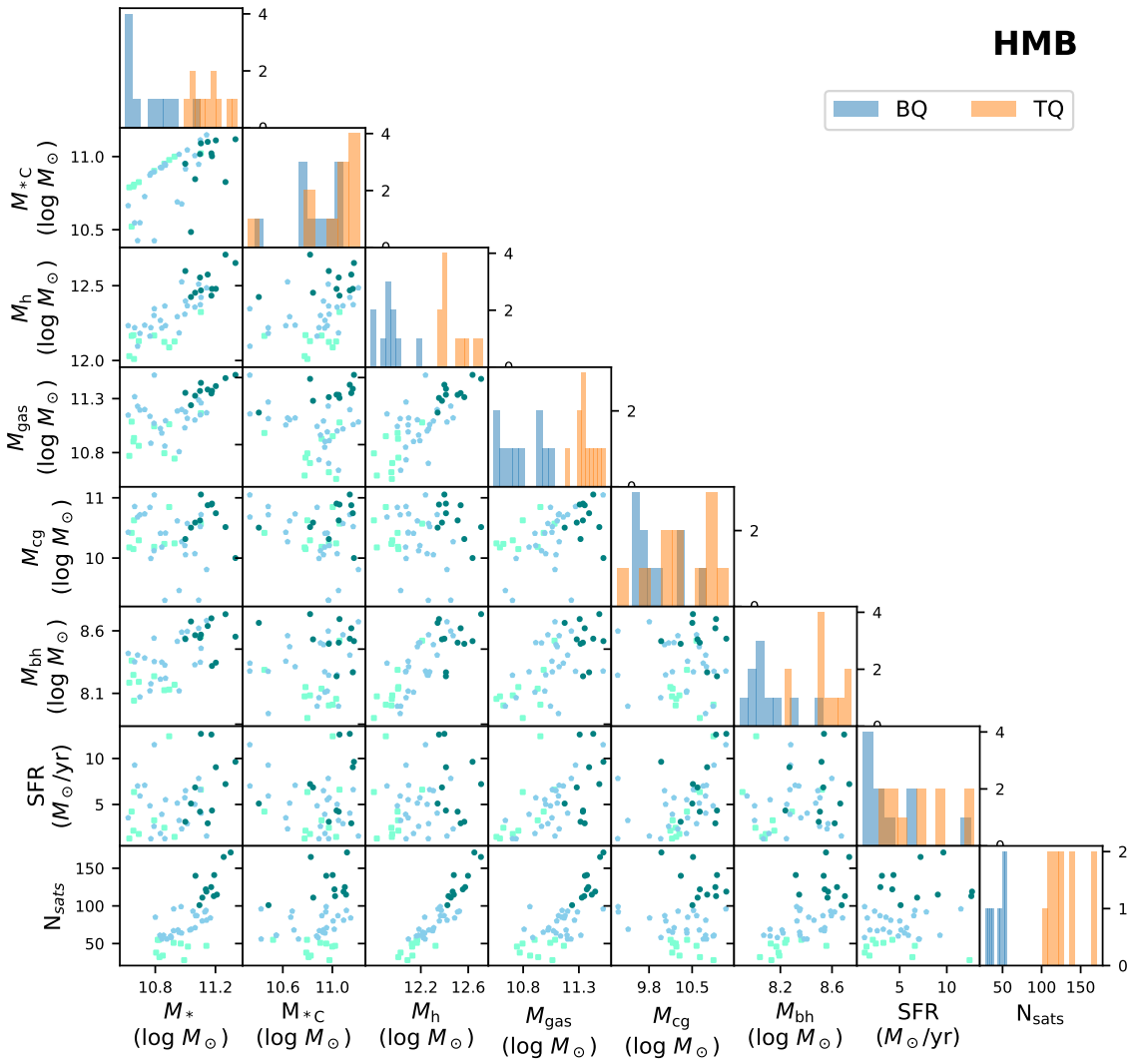

Figure 4.3: Same as Fig. 4.1, but for HMB halos.

Table 4.2: Number of halos in the final fragmented version of our sample. We have three bins (LMB, MMB and HMB) and the 25th (BQ), 50th (IQ) and 75th (TQ) quartiles, as computed for the $N_{\rm sats}$ per halo. As expected, the sum of all the bin and quartile values together adds up to our whole sample of 234 halos.

Quartiles	LMB	MMB	HMB
BQ	25	19	10
IQ	53	48	25
TQ	25	19	10

associated satellites. However, other halo attributes like gas mass, halo mass, stellar mass, SFR, etc. may still have some inter-dependencies that could affect the cold gas masses. This can later be falsely interpreted as purely a signature of satellite properties. Therefore, we generate detailed scatter plots for each of our mass bins (LMB, MMB and HMB in Figs. 4.1, 4.2 and 4.3 respectively) involving various halo attributes like the stellar masses, halo masses, gas masses, BH masses, cold gas masses, SFR and $N_{\rm sats}$. The three sets of points in the scatter plots are colored according to the number of satellites: lowest number of satellites (bottom quartile) in aqua, interquartile range in blue and highest number of satellites (top quartile) in teal. Finally, for the bottom (blue bars) and top (orange bars) quartiles we also plot histograms for each attribute for a straightforward comparison (one can see the ranges of $\rm N_{sats}$ for the quartiles in the $\rm N_{sats}$ histogram).

For all the bins, we see a large spread in values (more so for the LMB and MMB because of their larger sample sizes) for any given pair of halo attributes[5]. Co-variances for halos at the low-end and high-end of each bin also blend-in rather smoothly and do not show any sudden jumps[6]. These scatter plots clearly indicate that the $N_{\rm sats}$ does not correlate with the stellar mass of the central galaxy, by construction.

The correlations between halo attributes are generally similar for the different mass bins. In LMB (Fig.4.1), as one might expect, we see correlations between $\rm M_*$ and $\rm M_{\it h}$, $\rm M_{\it h}$ and $\rm M_{gas}$, and $\rm M_{gas}$ and $\rm M_{cg}$. SFR may correlate very weakly with $\rm M_{\it h}$, $\rm M_{gas}$ and $\rm M_{cg}$. Finally, it appears by eye, that $\rm N_{sats}$ may be correlated with $\rm M_h$ and $\rm M_{gas}$; the difference between the histograms as well as the overlap between the $\bar{X}\pm$ MAD values (as shown in the Appendix A.4) for the corresponding BQ and TQ further supports this inference. The MMB halos again show all the above stated correlations except for $\rm N_{sats}$, which seemingly shows stronger correspondence with more halo attributes (i.e. $\rm M_*$, $\rm M_{\it h}$, $\rm M_{gas}$ and $\rm M_{bh}$) as compared to that for LMB halos. In the HMB sample, like before, $\rm M_*$ and $\rm M_{\it h}$, $\rm M_{\it h}$ and $\rm M_{gas}$ are well correlated, while $\rm M_{cg}$ shows a slightly weaker dependence on $\rm M_{gas}$. $\rm N_{sats}$ again shows robust correlation with more than one halo attribute; however, the overall small sample size of the HMB could evidently overamplify some of the above dependencies.

[5]We see less pronounced scatter for $M_{\rm h}$-M_* and $M_{\rm h}$-$M_{\rm gas}$, since we expect a more massive halo to generally have a correspondingly larger reserve of stellar and gas mass as compared to a less massive halo.

[6]The co-variance between $N_{\rm sats}$ and remaining attributes expectedly shows a bi-modal character since we have a hard demarcation between $N_{\rm sats}$ values for the low and high-end for each bin.

4.3.7 $R_{\mathbf{all}}$ and $R_{\mathbf{10}}$ cases

In the previous subsection we described our iterative trial-and-error approach combined with the 2-sample K-S test in defining our bin limits and subsequently slicing each bin. Now that we have our whole sample neatly fragmented, we can now focus on shaping a strategy to selectively assess the impact satellites might have on the outer halo profiles of their respective hosts. As mentioned earlier, we only take into account the halos constituting the LMB and HMB, owing to the undesirable persistent correlation between $N_{\rm sats}$ and $M_{*\rm C}$ within the MMB halos. Thus, from this point we have a total of 148 halos between the LMB (103 halos) and the HMB (45 halos) that are considered for the subsequent analysis.

As established earlier, each particle in a FoF halo has one of the following three associations– Central, Satellites or the halo (Inner fuzz particles). We treat these associations as a basis for cleanly demarcating the cold gas (as defined in §4.3.5) lying within and beyond each satellite bound to a particular halo. To avoid the influence of ISM, we only compute cold gas beyond $r > 0.1R_{200}$ of each host galaxy.

4.3.7.1 $R_{\mathbf{all}}$: Total halo cold gas

To begin with we want to obtain all the existing cold gas lying within each halo. To do this, we first compute the temperature of each gas cell (dependent on the internal energy, electron abundance and SFR of the gas). All gas cells having a temperature $T < 10^{4.5}$ K are classified as cold gas cells and the rest are categorized as hot gas cells. Finally, we sum up the gas masses for all such cold gas cells to obtain the total cold gas mass within each halo. We refer to this case as $R_{\rm all}$. To sum up, the $R_{\rm all}$ case consists of cold gas lying within the central or the satellite population or the Inner fuzz.

4.3.7.2 $R_{\mathbf{10}}$: Cold gas excluding satellite halo contributions

In the second case, which we refer to as R_{10}, we only include the cold gas cells that are bound either to the central or the Inner fuzz, thus excluding all the cold gas that is gravitationally associated to the satellites. For each satellite in our sample, we assume that all cold gas at $r < 10.0 \cdot R_{0.5}$ (where $R_{0.5}$ is the stellar half mass radius of each satellite) is associated with the ISM and the CGM of that satellite while, the cold gas lying at $r > 10.0 \cdot R_{0.5}$ is outside the gravitational influence of that satellite and is associated with the Central. As in the $R_{\rm all}$ case, we again compute the temperature per gas cell and sort the gas particles as cold and hot. This time, however, we only select the cold gas cells that are at $r > 10.0 \cdot R_{0.5}$ of each satellite. Like before, we sum up the gas masses of these selected cells to obtain the cold gas *outside* of the satellite population.

4.4 Results

Previously we described the process of computing the mass in cold gas phase in each halo with and without satellites ($R_{\rm all}$ and R_{10}, respectively). It is imperative that we first investigate if the presence of satellites indeed has any impact on the extended cold gas profiles of their host halos. Post this, we need to find which of the global satellite population properties has the greatest impact on the cold CGM of the halos.

We first obtain the spherical cold gas density profiles for our halos. This is followed by tracking the changes in cold gas mass ($M_{\rm cg}$) with respect to three different satellite properties

(we refer to them as *probe variables* from now on). Throughout our analysis, we exclude the ISM regions ($r < 0.1\ R_{200}$) for every halo.

4.4.1 Spherical cold gas densities

Since satellites are gravitationally bound systems in themselves, lying within the potentials of their host galaxies, their presence is expected to have an impact on the density profiles of their parent halos. Tidal streams arising from a satellite galaxy's motion through its host halo is one type of an extreme observational evidence in this regard. Detection of tidal streams around Whale galaxy (Richter et al., 2017) or the existence of the Magellanic Stream within our LG (Mastropietro et al., 2005; Connors et al., 2006; Richter et al., 2013) are some excellent examples. The cold gas reservoirs associated with a satellite galaxy travelling through a host galaxy's halo are also expected to feel varied effects such as gravitational forces of the host, drag forces arising from the motion of the satellite either towards or away from the host, small-scale turbulent mixing at the interface of cold clouds and hot ambient medium, etc. Naturally, we expect the satellites to contribute some additional cold gas to the original cold CGM reservoir of the parent galaxy.

The net effects of the above mentioned processes on the extended cold gas phase of halos can be highlighted effectively via the radial spherical cold gas densities for the host galaxies, with and without satellites i.e. in the $R_{\rm all}$ and R_{10} cases, respectively. Accordingly, we plot the mean cold gas spherical densities for all our halos as a function of the normalized radius (from 0.1 to 1.0 R_{200}) in Fig. 4.4. For the sake of clarity we drop the halos in IQ in each mass bin, while for the sake of representational completeness we include the profiles for MMB halos as well. BQ (TQ) halos are represented by blue (red) curves while the $R_{\rm all}$ (R_{10}) case is depicted by solid (dashed) curves. The changes between the similar colored solid and dashed lines represent the effects of satellite population on the halos. Across all our bins, we see smoother density profiles for the R_{10} case (red and blue dashed curves). In comparison, the $R_{\rm all}$ case (red and blue solid curves) shows multiple density peaks, mostly in the regions $0.3 < r < 1.0\ R_{200}$. We remark that the satellite contributions seen in Fig. 4.4 may be due to the cold gas residing within the satellite(s) or some cold gas clouds in the extended halos of the satellite(s) or a combination of both.

On the whole, the cold gas densities drop sharply between $0.1 < r < 0.35\ R_{200}$ and more subtly between $0.35 < r < 1.0\ R_{200}$, thus giving rise to a knee-like feature at $r \simeq 0.35\ R_{200}$. Barring halos in the HMB[7], the TQ halos in both remaining bins generally have higher cold gas densities at $r > 0.35\ R_{200}$ than their counterpart BQ halos. The increase in density contrast between the BQ and TQ densities when including satellites (i.e. $R_{\rm all}$; the difference between blue and red solid lines), as opposed to excluding them (i.e. R_{10}; the difference between blue and red dashed lines), uncovers the impact a satellite population has, as a whole entity, on the extended cold gas density profiles of its associated halo. For the LMB, the average density increases by about 1.7 times from BQ to TQ in absence of satellites. This rises to 3.6 times in presence of satellites i.e. the density contrast roughly doubles. For MMB, without satellites, the average density changes by 2.1 times but with satellites we see almost 4.5 times change (again the density contrast doubles). In fact, close to 1.0 R_{200}, the change in density contrast for MMB is almost 5 times. In case of HMB, a consistent difference between the BQ and TQ densities is not maintained at all impact parameters (unlike that seen for LMB and MMB). A case in point are impact parameters $r \sim 0.35\ R_{200}$ and $r \sim 0.85\ R_{200}$ (see the two corresponding blue

[7]The overlap between the 1-σ shaded regions in the rightmost panel of Fig. 4.4 shows that the corresponding BQ and TQ halos in HMB have similar cold gas densities even at large impact parameters.

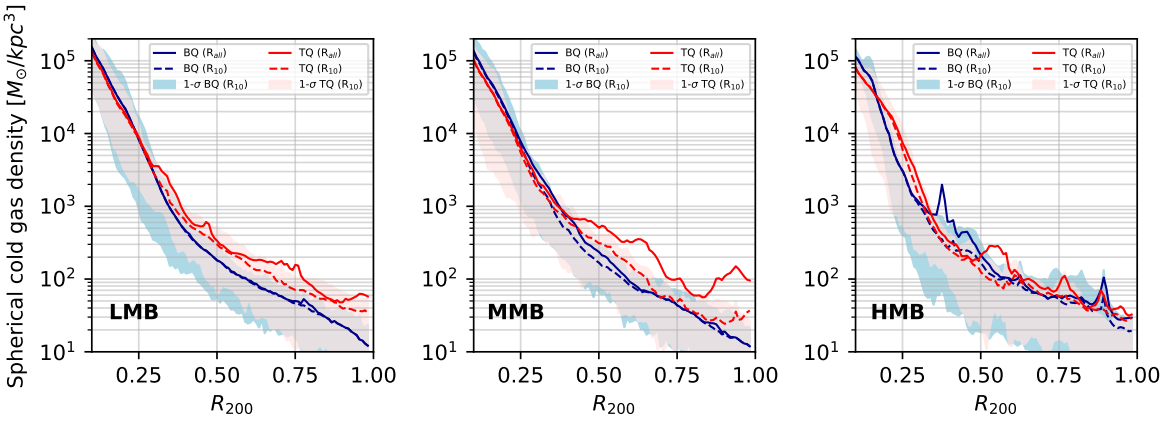

Figure 4.4: *Left-Right*: Comparison between the mean cold gas spherical densities (in $M_\odot$ kpc^{-3}) as a function of normalized radius for $R_{\rm all}$ (*solid lines*) and R_{10} (*dashed lines*), for TNG50 halos belonging to the low-mass (LMB), middle-mass (MMB) and high-mass bins (HMB), for the 25th (*blue*) and 75th (*red*) quartiles. Regions within 0.1 R_{200} have been excluded to avoid ISM. Shaded blue (red) regions indicate 16-84th percentiles for the respective R_{10} cases. Note how differences start creeping between $R_{\rm all}$ and R_{10} mostly in regions at distances $\gtrsim 0.25\ R_{200}$, directly indicating the influence satellites have on the cold gas profiles of typical L* galaxies.

blips in rightmost panel of Fig. 4.4), wherein the $R_{\rm all}$ density for BQ rises sharply above its corresponding TQ value. This could give a preliminary hint that a standalone steady increase in the number of satellites (as in case from BQ to TQ) among the most massive galaxies may not linearly translate to more cold gas in their extended halos.

On average, the TQ halos for all three bins show maximum cold gas contributions from their respective satellite populations as compared to their BQ counterparts. We remark that some of the satellite contributions seen in Fig. 4.4 are due to the cold gas residing within the satellite(s). This is demonstrated in Fig. A.4 where we additionally show the effect of only excluding cold gas lying very close to the satellites.

4.4.2 Number of satellites ($N_{\rm sats}$) and cold gas mass ($M_{\rm cg}$)

§4.4.1 outlines the correlation between the boost in cold gas densities of the host halos and the presence of satellites. The next step is to investigate the effect of various probe variables on the $M_{\rm cg}$ of the halos. Note that we drop the MMB halos from our analysis hereon since we found that there was a non-negligible correlation between the $N_{\rm sats}$ and $M_{*\rm C}$ for the MMB halos (see §4.3.6.1).

We begin with our first probe variable, number of satellites per halo ($N_{\rm sats}$) and plot these against the corresponding $M_{\rm cg}$ values for that halo in Fig. 4.5. We compute the $M_{\rm cg}$ for our $R_{\rm all}$ and R_{10} cases (as described in §4.3.7.1 and §4.3.7.2) and plot those values (differentiated according to the three underlying quartiles) against the $N_{\rm sats}$ for each halo within the LMB and HMB. Respective medians for halos in each quartile (referred hereafter as med$_{\rm s}$) along with their 1-σ errors are also overplotted as colored cross symbols.

As expected, the overall values for both $N_{\rm sats}$ as well as $M_{\rm cg}$ are higher for HMB halos that host more massive galaxies as compared to their counterpart LMB halos which host less massive galaxies (this supports our observations from Figs.4.1 and 4.3); although some overlap is seen for the $M_{\rm cg}$ values between the bins. Notably, for a similar increase in the $N_{\rm sats}$ value from BQ to

TQ ($\simeq$ 3x increase in $\mathrm{med_s}$) in both bins, the M_{cg} in HMB halos shows a much larger increment ($\geq$ 3x increase in $\mathrm{med_s}$) as compared to that for LMB halos ($\simeq$ 1.5x increase in $\mathrm{med_s}$).

Next, we compare the amount of cold gas when including satellites (R_{all}) to that after excluding satellites (R_{10}). For LMB, the BQ $\mathrm{med_s}$ values for the R_{all} and R_{10} cases are almost exactly the same (also true in case of IQ $\mathrm{med_s}$ values); in other words, for halos constituting these quartiles, most of the cold gas really resides outside of the satellites, unlike that for the TQ galaxies (this is also corroborated by the near overlap between the BQ density profiles for R_{all} and R_{10} cases in the leftmost panel in Fig. 4.4). This serves an indication that for the least massive halos the number of satellites associated with the central starts to have an effect on the mass in the cold gas phase found beyond the satellites only after reaching a certain threshold value. For the more massive (HMB) halos there is a small deficit of cold gas mass going from the R_{all} to R_{10} case, indicating the presence of cold gas beyond the corresponding centrals.

4.4.3 Total mass in satellites ($M_{\mathbf{tms}}$) and cold gas mass ($M_{\mathbf{cg}}$)

More massive satellite galaxies could harbor larger reserves of cold gas, potentially contributing more mass to the total cold gas budget of its halo. This time, we plot the total mass (sum of M_*, M_{gas} and M_h) in satellites (M_{tms}) for each halo against the corresponding M_{cg} values in Fig. 4.6, along with their corresponding $\mathrm{med_s}$ with 1-sigma errors (colored cross symbols). It is important to mention that N_{sats} does not perfectly correlate with M_{tms}. In other words, some halos that fall in the BQ on the virtue of their low N_{sats} value do actually have an M_{tms} value higher than some of the halos in other two quartiles. The vice versa is also true for the other two quartiles. A manifestation of the above mentioned effect is indeed seen in Fig. 4.6, wherein the clear demarcation between the quartiles on x-axis (seen earlier in Fig. 4.5) is pretty much lost.

Therefore, we plot two series of median values here. First, using the color scheme from Fig. 4.5, we plot the median M_{tms} and M_{cg} for each of the N_{sats} quartiles ($\mathrm{med_s}$). Note that the y-values of each of these points is the same as in Fig. 4.5. Second, we plot the medians of the bottom, inter and top quartile ranges computed after ranking the M_{tms} values in ascending order (shown as grey/black cross symbols; referred hereafter as $\mathrm{med_q}$).

The singular-most evident impact this has is that it gives us an unbiased picture of how the cold gas mass evolution from the bottom to top quartiles within a bin occurs once we line up the values for M_{tms} from lowest to highest. For the LMB halos, the M_{cg} $\mathrm{med_q}$ value almost stays constant en route BQ to IQ before increasing for TQ. We also do not see much change in the respective $\mathrm{med_s}$ and $\mathrm{med_q}$ values from R_{all} to R_{10} case (something that is also seen for $\mathrm{med_s}$ BQ-IQ values in Fig. 4.5). From this, it appears that the M_{cg} reserves, associated with the halos having small number of as well as less massive satellites, are not impacted much.

On the other hand, the cold gas mass increases monotonically with the total mass in satellites for the HMB halos. For TQ halos, M_{tms} could, therefore, be another factor boosting M_{cg} alongside N_{sats} (see §4.4.2). Even here, an appreciable amount of cold gas is seen beyond the respective centrals (i.e. associated with satellite population) only for the most massive halos in LMB and beyond (seen as a small difference in the y-axis $\mathrm{med_q}$ values between R_{all} to R_{10} cases).

4.4.4 M_* most massive satellite ($M_{*\mathbf{mms}}$) and cold gas mass ($M_{\mathbf{cg}}$)

More massive satellites with correspondingly large stellar and gas mass content could also deposit some extra cold gas in the outer CGM while orbiting within their respective host haloes (Deason et al., 2016; Fattahi et al., 2020). Therefore, we choose the stellar mass of the most massive

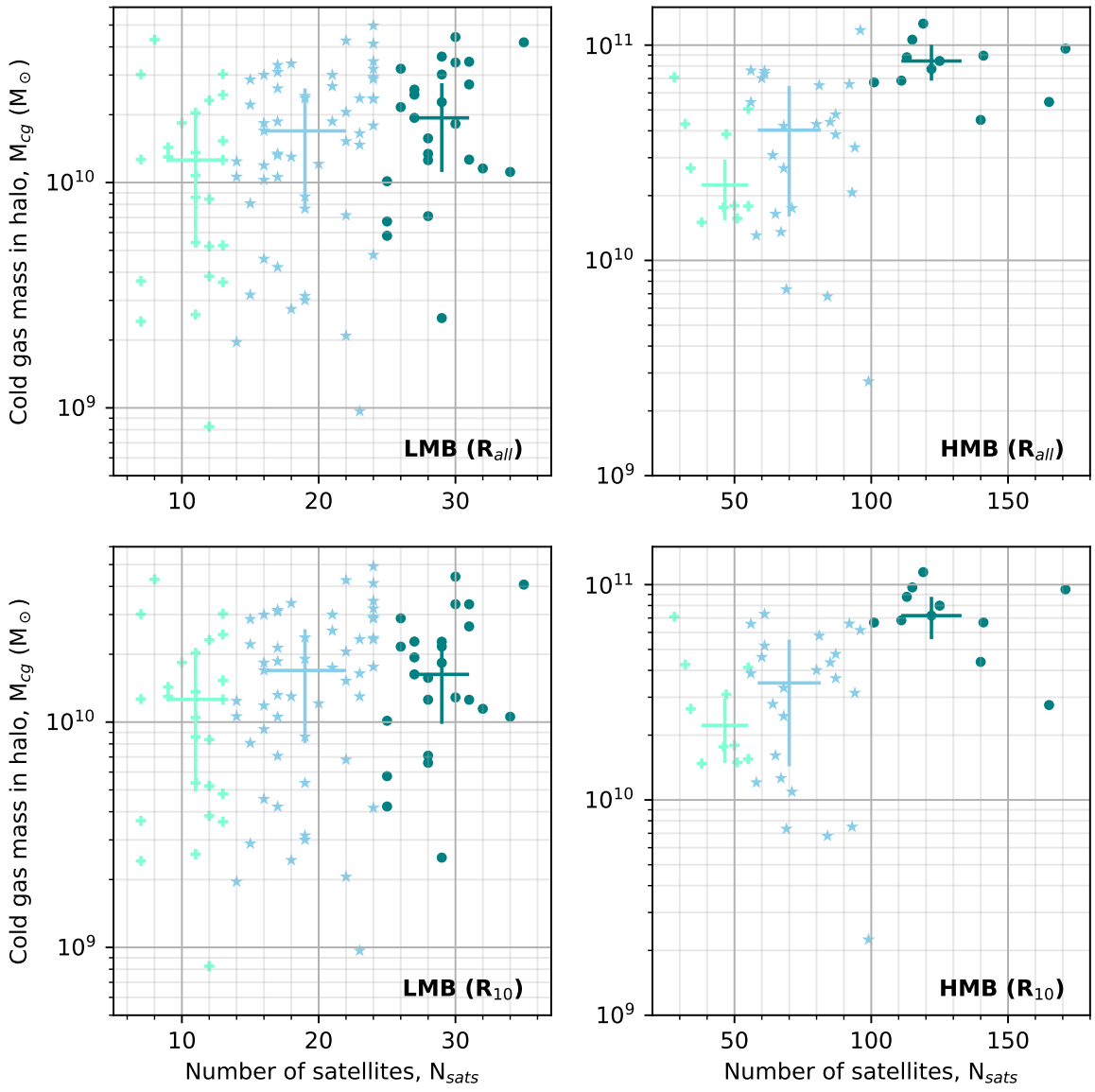

Figure 4.5: Total cold gas mass, $M_{\rm cg}$, (in $M_\odot$) vs number of satellite galaxies per halo ($N_{\rm sats}$) for $R_{\rm all}$ (*top panels*) and R_{10} (*bottom panels*) for the LMB (left panels) and HMB (right panels) halos. Halos belonging to the 25th (*plus symbols*), 50th (*star symbols*) and 75th (*filled circles*) quartiles are shown for each bin. Respective 1-sigma errors (*colored cross symbols*) are shown for each quartile. The effects of satellite population on the halo cold gas only starts building up appreciably beyond a certain $N_{\rm sats}$ value (in this case, seen only for TQ low mass halos and HMB halos).

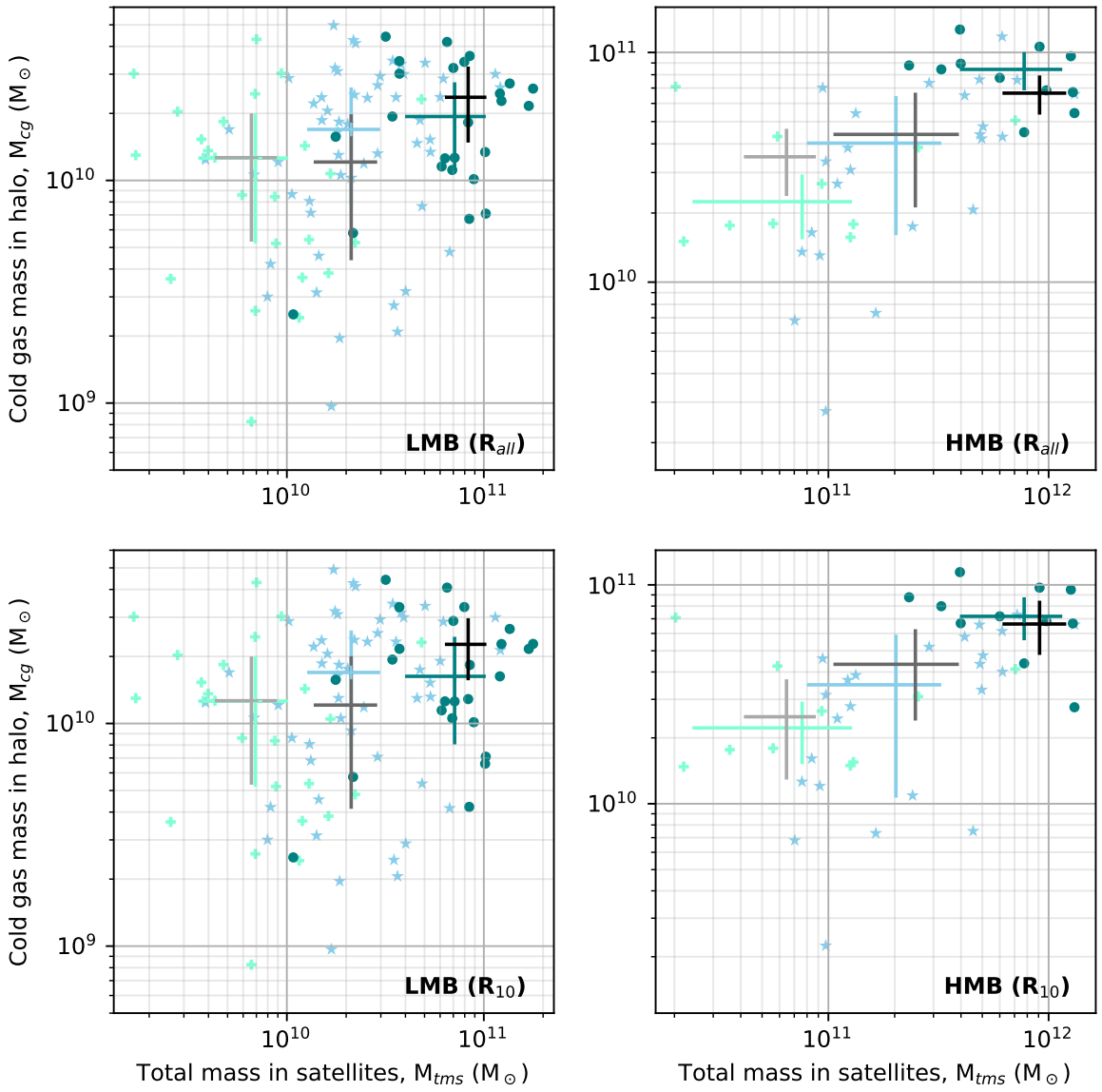

Figure 4.6: Total cold gas mass per halo, $M_{\rm cg}$, (in $M_\odot$) vs Total mass in all satellite galaxies per halo, $M_{\rm tms}$ (in $M_\odot$) for $R_{\rm all}$ (*top panels*) and R_{10} (*bottom panels*) for the LMB (left panels) and HMB (right panels) halos. As in Fig. 4.5, three different quartiles based on the number of satellites are represented by different symbols and corresponding 1-sigma errors (*colored cross symbols*) are shown. Median values of the bottom-, inter- and top quartile-wise bins, defined using the $M_{\rm tms}$ variable, are shown as light grey, grey and black crosses respectively. For LMB halos, $M_{\rm tms}$ shows slightly steeper slope for $M_{\rm cg}$, as compared to that seen due to $N_{\rm sats}$; while for HMB halos, the slope is shallower (see Fig. 4.5).

satellite (alternatively referred as the primary satellite) per halo ($M_{*\mathrm{mms}}$) as our third probe variable and plot it against M_{cg} in Fig. 4.7. Unlike that for N_{sats} and M_{tms} (left panels in Figs. 4.5 and 4.6), $M_{*\mathrm{mms}}$ brings about a fairly linear increase in the M_{cg} values for LMB halos. As we remarked earlier, the underlying dependence of M_{cg} on the central galaxy's mass crops up here as well– even though the median $M_{*\mathrm{mms}}$ in the most massive LMB halos (TQ) exceeds that for the least massive HMB halos (BQ), the median M_{cg} for BQ halos in HMB is still higher than that for TQ LMB halos.

For the higher mass halos, the slope is slightly less steeper than that seen in case of N_{sats} (Fig. 4.5). This is a good indicator that, in this mass range[8], $M_{*\mathrm{mms}}$ cannot be the sole factor impacting the amount of cold gas mass. However, from the above trends it can be safely inferred that the most massive satellite gives away a substantial share of its cold gas to the parent halo.

However, this raises another important question– with what ease does this primary satellite give away some of its cold gas? In other words, how easy or difficult is it to strip cold gas off the primary satellite galaxy? We attempt to answer this question in the next subsection.

4.4.5 Ease of stripping cold gas from the most massive satellite

Recent studies infer that gas in massive satellites, generally, is more difficult to strip off as compared to smaller satellites (Cortese et al., 2021; Wright et al., 2022). The ratio of stellar mass of the most massive satellite in a halo and the stellar mass of the central is a good indicator for quantifying the ease of gas stripping. Thus, we recreate our earlier plot for $M_{*\mathrm{mms}}$ vs. M_{cg} (Fig. 4.7), except this time, we plot the ratio of stellar masses of the primary satellite and its corresponding central ($M_{*\mathrm{mms}}/M_{*\mathrm{C}}$) on the x-axis (see Fig. 4.8).

We observe two important characteristics in this plot. First, a careful comparison with Fig. 4.7 shows that the slope flattens (even though it remains positive across both bins) as we move from $M_{*\mathrm{mms}}$ to the ratio $M_{*\mathrm{mms}}/M_{*\mathrm{C}}$. Secondly, the quartile-wise medians (blue and green cross symbols) for HMB halos have an x-axis overlap, i.e., they have identical $M_{*\mathrm{mms}}/M_{*\mathrm{C}}$ values despite having different amounts of cold gas (y-axis values). From the above two observations we can robustly infer that the ratio, $M_{*\mathrm{mms}}/M_{*\mathrm{C}}$, has a secondary role to play with regards to depositing cold gas in the host CGM as compared to the stellar mass of the most massive satellite, $M_{*\mathrm{mms}}$. Thus, our analysis implies that the ease with which cold gas can be stripped off the most massive satellite within a halo has a positive, yet marginal impact on the cold gas found in that halo.

4.5 Discussion

In this work we have analyzed the extended cold gas distributions for low-mass and high mass TNG galaxies from the perspective of three different probe variables, N_{sats}, M_{tms} and $M_{*\mathrm{mms}}$. We present our main reflections from these results in this section.

One might expect that the amount of cold gas contained in a halo is most closely tied to the central galaxy's mass before having any dependence on the global satellite properties, and, indeed, this agrees with our findings. Both the median values of M_{tms} and $M_{*\mathrm{mms}}$ in the top quartile bin in LMB are higher than the median M_{tms} and $M_{*\mathrm{mms}}$ values in the lowest quartile bin in HMB. However, the M_{cg} value for the lowest HMB quartile remains higher than the M_{cg} value in the highest LMB quartile. Thus, the fact that the median M_{cg} follows the underlying halo mass hierarchy (LMB & HMB), established through our prior binning (instead of following the

[8] Although there could also be a secondary dependence on the number of satellites hosted by a halo.

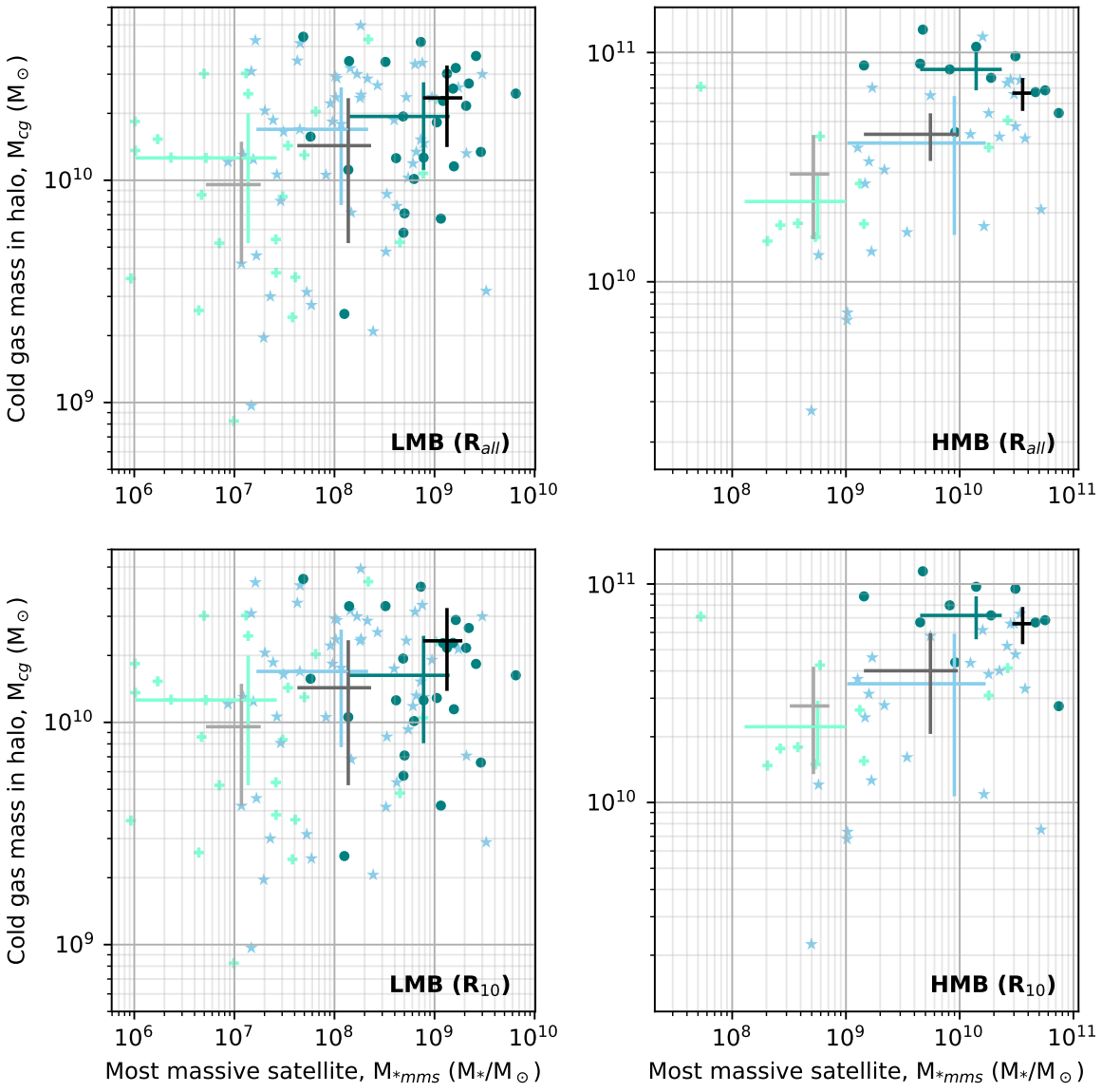

Figure 4.7: Total cold gas mass, $M_{\rm cg}$, (in $M_\odot$) vs the stellar mass of the most massive satellite galaxy in each halo, $M_{*\rm mms}$ (in $M_\odot$). *Left* (*Right*) panels show LMB (HMB) halos while the *top* and *bottom* panels show corresponding $R_{\rm all}$ and R_{10} cases respectively. As in Fig. 4.6, respective quartiles and 1-sigma errors are marked. Low mass halos' cold gas is most affected by $M_{*\rm mms}$ while high mass halos are also appreciably affected by this parameter (though, $N_{\rm sats}$ have the strongest correlation for this mass bin).

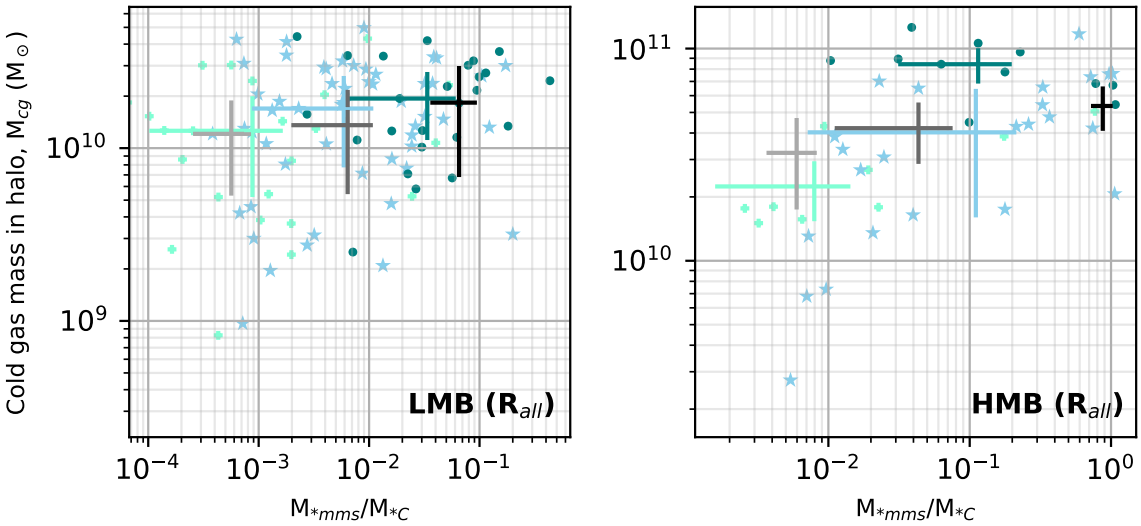

Figure 4.8: Total cold gas mass, $M_{\rm cg}$, (in $M_\odot$) vs the ratio of stellar masses of the primary satellite and its corresponding central in each halo, $M_{*\rm mms}/M_{*\rm C}$ (indicates the ease with which cold gas can be stripped off a satellite galaxy). *Left* (*Right*) panels show LMB (HMB) halos. As in Fig. 4.6, respective quartiles and 1-sigma errors are marked. Across both halo mass bins, we see a positive but very shallow slope, indicating the marginal effect of the ease of cold gas stripping on the halo cold gas reserves.

trends in satellite properties), highlights the importance of our stringent sample fragmentation process.

4.5.1 Satellite population: What matters the most?

It is clear from Figs. 4.5, 4.6 and 4.7 that $N_{\rm sats}$ correlates positively with $M_{\rm cg}$ reserves of an L_* TNG halo irrespective of whether it lies in the low mass or high mass bin. Naturally, a higher $N_{\rm sats}$ should translate in a higher value of $M_{\rm tms}$. It is rather well-known that massive galaxies are generally occur less frequently than their less massive counterparts. Thus, more the number of satellites hosted by a halo, increased are the chances of finding a more massive satellite among them. In other words, a higher $N_{\rm sats}$ should translate to a higher $M_{*\rm mms}$. In the absence of scatter in the stellar mass function for satellites we would have expected to find the exact same relationship between BQ and TQ, irrespective of the probe variable in consideration. The existence of the trends between $M_{\rm cg}$ and our probe variables is, therefore, expected. However, which of these trends presides over the rest, is not very clearly known yet and is, therefore, surprising to find out.

For the low-mass LMB halos, between $N_{\rm sats}$, $M_{\rm tms}$ and $M_{*\rm mms}$, $M_{*\rm mms}$ causes a persistent increase in $M_{\rm cg}$ across all quartiles. This is also the only time wherein the BQ and TQ show a significant difference, with their median plus 1-σ regions overlapping very little. Thus, we can safely infer that for the LMB halos, between the three examined variables, $M_{\rm cg}$ varies the most with $M_{*\rm mms}$.

Within the HMB sample, the difference between $M_{\rm cg}$ in the top and bottom quartiles of halos is significant (no overlap of 1-σ regions) whether we bin by $N_{\rm sats}$, $M_{\rm tms}$, or $M_{*\rm mms}$. Unlike

in the LMB sample, in the HMB sample the strongest difference in $M_{\rm cg}$ between the top and bottom quartiles is found when binning by $N_{\rm sats}$.

4.5.2 Cold gas within most massive satellites across stellar masses

In the context of our earlier analysis about the ease of cold gas stripping (see §4.4.5), the question– does the amount of cold gas within the most massive satellite keep increasing as we move to progressively massive halos (which are expected to host progressively more massive primary satellites)?– merits a closer look. It is worthwhile to remind the readers that we define the bounds of a satellite at $r \sim 10.0 \cdot R_{0.5}$ (labeled as R_{10}). Regions within this parameter constitute the satellite ISM while the rest is dissociated from the gravitational influence of that satellite. This leads us to Fig. 4.9, which shows the changes in cold gas mass within the most massive satellites as we move from the lowest to the highest mass halos.

For the low-mass halos, the median cold gas within their corresponding most massive satellite increases monotonically as we move from the bottom quartile to the top quartile. For the high-mass halos, the increase in median cold gas mass is quite gradual as we transition from the bottom to inter quartile. This is the regime where the median stellar mass of the corresponding most massive satellite goes beyond 10^9 $M_\odot$ (akin to SMC–LMC-mass satellites). Interestingly, moving to even larger satellites (from inter to top quartile) results in a drop in the median values of the cold gas associated with those satellites. In other words, these top quartile HMB satellites do not actually contain as much cold gas within them as is expected from their stellar masses. This could be interpreted as a relative inability of these really massive satellites (as compared to the BQ and IQ satellites in the same bin) in efficiently retaining their cold gas mass reservoirs (and thus depositing some of their cold gas in the extended CGMs of their hosts).

4.5.3 Number of massive satellites associated with a halo

For a particular halo, apart from the role of the most massive satellite, there also may exist a few other less, but still substantially massive satellites. These satellites could also feed the host CGM with their cold gas. Several studies adopt a mass-cut definition for demarcating the low mass from high-mass satellites. Usually, satellites having $M_* < 10^8$ $M_\odot$ are considered are *low-mass* satellites, while those having $M_* > 10^8$ $M_\odot$ are considered as *massive* satellites (McConnachie, 2012; Weisz et al., 2015). As such, it is observationally impossible to detect the complete satellite population for any halo down to the lower end of stellar mass values[9]. This further strengthens our case for looking at the trend between the number of massive satellites vs. $M_{\rm cg}$, instead of $N_{\rm sats}$.

In Fig. 4.10, we find out the impact of the massive satellite population on the cold gas reserve of their host halo. For each halo across our low and high-mass bins, we count the number of satellites which have $M_* > 10^8$ $M_\odot$. As before, we compute the amount of cold gas in that halo when including only these massive satellites. The median number of massive satellites varies from 1 to 3 within the low-mass halos, while the high-mass halos have about median of 4 to 12 massive satellites. The change in median cold gas mass (y-axis) from BQ to TQ for LMB halos is quite small as compared to that seen for HMB halos (for roughly the same three-fold increase in median x-axis values for both samples). Thus, our above–stated points, derived from Fig. 4.10, hint that the amount of cold gas in a halo is certainly dependant, to some degree, on the number of massive satellites it harbors.

[9]Typical observational stellar mass detection limits at low-z for satellites is $M_* > 10^5$ $M_\odot$ (); this can further reduce up to $M_* > 10^{2.5}$ $M_\odot$ for MW satellites (McConnachie, 2012).

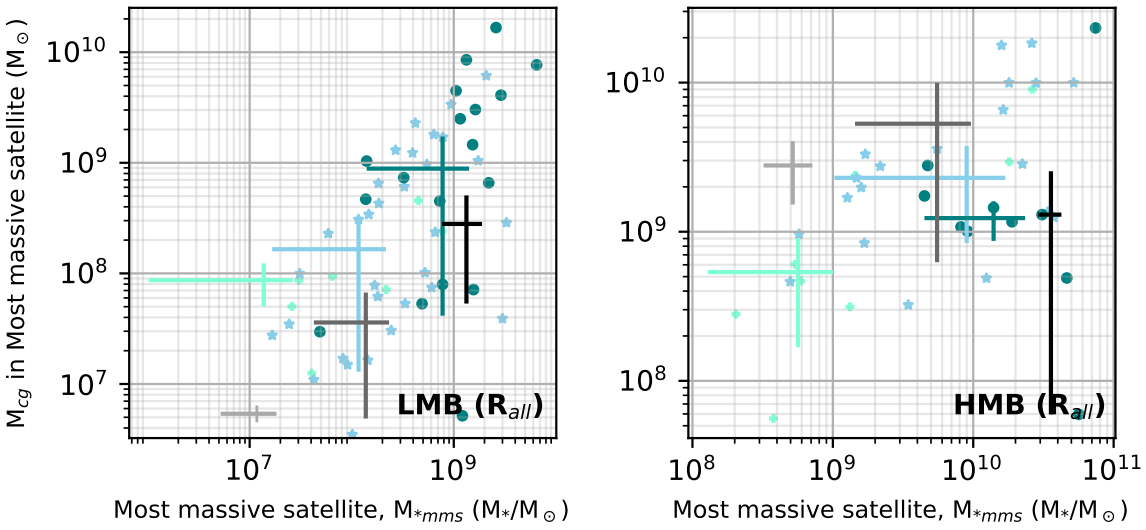

Figure 4.9: Total cold gas mass, $M_{\rm cg}$, (in $M_\odot$) in the most massive satellite vs the stellar mass of the most massive satellite galaxy, $M_{*\rm mms}$. *Left* (*Right*) panels show LMB (HMB) halos. As in Fig. 4.6, respective quartiles and 1-sigma errors are marked. The amount of cold gas contained within the primary satellite gradually increases as we move from low mass to high mass halos. However, the highest mass primary satellites (hosted by the top end of massive halos), contain less cold gas within them as compared to their less massive counterparts in the same halo mass bin.

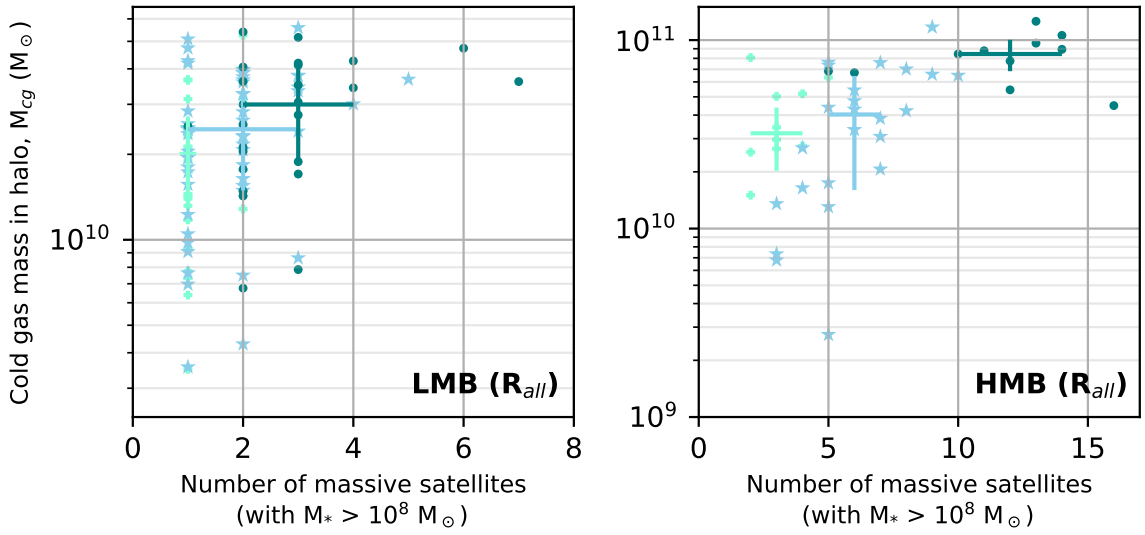

Figure 4.10: Total cold gas mass, $M_{\rm cg}$ (in $M_\odot$) vs the number of massive ($M_* > 10^8$ $M_\odot$) satellites in a halo. *Left* (*Right*) panels show LMB (HMB) halos. As in Fig. 4.6, respective quartiles and 1-sigma errors are marked. LMB halos contain very few massive satellites unlike HMB halos– this is an important factor governing the amount of cold gas ultimately contributed via the satellite population of a halo.

These implications, when taken in the context of our findings from §4.4.4, reveal that the number of massive satellites, in conjunction with the stellar mass of the most massive satellite, might be a key deciding factor towards determining the cold gas mass within a halo. Small halos (LMB) do have massive ($M_* > 10^8$ $M_\odot$) satellites, but they are far too few (1-3) to cause any substantial increase in the cold gas reservoir of their halos. As we move to more massive halos, the number of massive satellites increases in number (as does the stellar mass of the most massive satellite). More cold gas finds its way from these satellites into their parent halo. The most massive halos host the largest pool of massive satellites, which contain huge amounts of cold gas. A fraction of this cold gas eventually gets stripped from the massive satellites. Extremely massive satellites ($M_* > 10^{9.5}$–10^{10} $M_\odot$) are shorn off their cold gas reservoirs the most (as seen by the trends in median values across quartiles in HMB halos in Fig. 4.9).

4.5.4 The supply chain of cold gas in L* galaxies

The substantial scatter (more than an order of magnitude) in the cold gas mass, as seen across Figs. 4.5, 4.6 and 4.7, indicates that satellites are certainly not the primary contributor of cold gas in L* galaxies at low-z. Thus, it is essential to contextualize our results with respect to other known sources of cold gas in galaxies.

Filamentary accretion, in the form of metal-poor gas, from the IGM is one of the most conventional channels through which a galaxy acquires its supply of cold gas (Nelson et al., 2013). For massive galaxies, most of this incoming gas gets shock heated to virial temperatures as it passes through the galactic gravitational potential well– the so-called hot-mode accretion (White & Rees, 1978; White & Frenk, 1991; Birnboim & Dekel, 2003). However, for the halos considered here, the halo potential is only able to heat up the accreting gas to intermediate temperatures– thus, the so-called cold mode accretion (Abadi et al., 2003; Kereš et al., 2005;

Kereš et al., 2009; Dekel et al., 2009). The heated-up gas, later, cools down and rains upon the ISM, eventually contributing to the star-formation process.

Continuous regurgitation of gas between the ISM and halo regions, aka galactic fountain flows, is another potentially important pathway for cold gas accretion (Fraternali & Binney, 2006; Fraternali, 2008). Hot, fast winds driven by supernova feedback are propelled out to CGM distances. On their way out to CGM the baryons in these winds decelerate and lose energy, eventually cooling down and raining back on to the galaxy over a particular timescale. The growth of cool clouds is accelerated via the interaction of feedback-driven winds with the surrounding hot, ambient medium present outside the ISM (Anglés-Alcázar et al., 2017; Suresh et al., 2018).

Radio-mode galactic feedback, arising from accreting SMBHs in low-z universe, to some extent, can alter the phase distributions within the CGM. Resultant AGN winds drive large radio bubbles at kpc distances, which could impact future IGM accretion and transform some of the cold-dense gas phase to a warmer, more diffuse phase (Zinger et al., 2020). At the same time, if these winds are more metal-enriched (i.e., having an enhanced wind metal loading factor), they can increase the efficiency of metal-line cooling in CGM, thus helping the warmer gas condense into cold phase faster (Suresh et al., 2015). This could observationally manifest in terms of small enhancements in, for example, H I covering fractions.

The role of satellites towards the evolution of cold phase CGM of halos is undoubtedly one of the processes acting in concert with those mentioned above. Thus, uncovering the impact of a global satellite population (as undertaken in this study) serves to fit a small but important piece into the giant puzzle of the physics of gas flows around a MW-like galaxy.

4.5.5 Implications in context of the Local Group

Considering that the present study is limited only to L* galaxies, it is imperative to view our findings from the perspective of the LG CGM. It is now observationally as well as theoretically well-established that isolated dwarf galaxies generally contain more gas and are actively star-forming than their counterparts lying within the virial influence of MW-M31 pair (McConnachie, 2012; Fitts et al., 2017). Putman et al. 2021 inferred from their study that the presence of a diffuse halo environment (such as our LG) is crucial in ensuring the depletion of a satellite's gas reservoir and its subsequent quenching. Least massive satellites ($M_* < 10^6$–10^7 $M_\odot$) quench most effectively (i.e. earlier) than the more massive ($M_* \simeq 10^7$–10^8 $M_\odot$) ones, while the most massive satellites ($M_* \simeq 10^8$–10^{10} $M_\odot$) are able to retain most of their cold gas. Multiple simulation-based studies echo similar results (Wetzel et al., 2015; Simpson et al., 2018; Garrison-Kimmel et al., 2019c; Akins et al., 2021; Karunakaran et al., 2021; Font et al., 2021; Joshi et al., 2021).

Our findings resonate with the above statements since we do find negligible cold gas associated with the smallest satellites while an appreciable amount of cold gas is found to be locked within the most massive ones. In other words, the presence of cold gas reservoirs associated with satellites is a robust indicator to whether or not a satellite is quenched. Furthermore, there exists observational evidence that the cold gas streams can be formed during the passage of gas-rich satellite galaxies (e.g., the Magellanic Clouds in the Milky Way halo) through the host galaxy's CGM and that these streams (in case of the Milky Way: the Magellanic Stream and potentially other high-velocity clouds; Richter et al. 2017) could act as a fodder for future star formation (Bekki & Chiba, 2007; Besla et al., 2012; McClure-Griffiths et al., 2018) as well as add substantially to the absorption cross-section of CGM in QSO spectra.

4.6 Summary

We have probed the connection between satellite galaxies and their corresponding centrals in TNG50 simulations from the perspective of the effects on the extended cold CGMs of the host galaxies. Our whole sample of 234 L* halos spans two orders of magnitude in halo mass. Massive haloes tend to have more cold gas and thus subsequent analysis on such an unsegmented sample might give us a highly biased picture about the effects of satellite population on the cold CGM. Therefore, we fragment our dataset into three mass bins, LMB, MMB and HMB such that the mass in cold gas phase of a halo, $M_{\rm cg}$ does not correlate with the stellar mass of its associated central, $M_{*\rm C}$. The effect on cold gas reserves of a halo is studied from the point of view of three different global satellite properties (i.e. probe variables)– $N_{\rm sats}$, $M_{\rm tms}$ and $M_{*\rm mms}$. We summarize our findings below–

- We find that satellites, on the whole, contribute to the extended radial cold gas densities of their respective hosts, across all mass bins.

- Cold gas mass, $M_{\rm cg}$, contributions from satellites towards halos that host a sparse satellite population (containing satellites that are also, overall, less massive), are negligible. In other words, most of the cold gas in smaller halos lies within the centrals and not with their satellites.

- For the LMB halos, after taking into consideration the underlying dependence of $M_{\rm cg}$ on the mass of the central, it becomes clear that only the TQ halos are being fed by the cold gas from the respective most massive satellite. On the other hand, HMB halos show a consistent trend of being fed with cold gas from their most massive satellite across all quartiles. However, the ease with which cold gas is stripped off the most massive satellite (characterized by the stellar mass ratios of the central vs. primary satellite) has minimal effect on the amount of cold gas being deposited in that halo.

- Stellar mass of the most massive satellite, $M_{*\rm mms}$ (Number of satellites, $N_{\rm sats}$), emerges as the most impactful parameter for the low mass (high mass) halos.

- In the regime of LMC/SMC-mass satellites, less $M_{\rm cg}$ is found within the corresponding primary satellite as compared to that in lower quartile primaries of the same bin. Thus, the primary satellites at the top end perform worse in terms of retaining their cold gas as compared to their slightly less massive counterparts.

- Small, less massive halos simply do not contain enough number of massive satellites ($M_* > 10^8\ M_\odot$) that can deposit substantial cold gas; larger, more massive halos, on the other hand, not only contain more massive primary satellites, but also harbor larger number of massive satellites that collectively give away a larger share of their cold gas to their parent halo.

- Among several existent processes such as IGM accretion, galactic fountain flows, galactic feedback and mergers, the role played by satellite populations, with respect to influencing the total cold gas budget of the host galaxy, is small yet crucial. A wholesome understanding about the physics of galactic gas flows would elude us if we do not account for the cold gas contributions made by satellite galaxies.

Data availability

The complete IllustrisTNG suite of simulations (including TNG50) are publicly available at https://www.tng-project.org/data (Nelson et al., 2019a). The scripts and plots for this article can be shared on reasonable request to the corresponding author.

Acknowledgements

The authors sincerely thank the JupyterLab Workspace service (all the scripts and resultant figures in this article have been developed on this web-based user interface), provided as a part of the public data access within IllustrisTNG. We thereby, also acknowledge the role of High Performance Computing Center Stuttgart (HLRS) in Germany, the Gauss Centre for Supercomputing (GCS) and Max Planck Computational Data Facility (MPCDF) in running the simulations.

Chapter 5

Discussion

In the previous chapters, I extensively described three different projects targeted at uncovering different facets of the galaxy–CGM connection and its broader impact on galaxy evolution itself. While each study resulted in some unique insights, there remains, nonetheless, a scope for improvement in certain aspects, both with regards to my work as well as the larger field, in general. I highlight some areas of improvement as well as talk about the possibilities regarding future work in this chapter.

5.1 This work

5.1.1 Improving the sample size of LG simulations

I was able to map the LG CGM over a broad range of temperature-density values (see Fig. 2.1) by implementing post-processed ionization modeling within the HESTIA constrained simulations. Somewhat unexpectedly, I also came across the likelihood of contamination from MW gas clouds as one of the possible pathways contributing to the persistent mismatch between simulation predictions and observed measurements (see Fig. 2.6), especially in the low-z regime. While these results are undoubtedly conclusive, one also cannot simply ignore the fact that their statistical robustness could be greatly improved (Faucher-Giguère, 2017).

One immediate constraint towards upscaling the number of HESTIA realizations is, of course, the high computational cost. This is definitely an area wherein novel, smarter computational techniques need to be devised such that the increase in computational expense can be reduced. Apart from Hestia, there exist some other similar LG simulations like the ELVIS (Garrison-Kimmel et al., 2014c), Apostle simulations (Sawala et al., 2016), Local Group on FIRE (Garrison-Kimmel et al., 2019), SIBELIUS (Sawala et al., 2022), NIHAO-LG (Arora et al., 2022) that could be used for cases highlighted in this thesis as well as other LG-specific problems. While unique insights can be obtained from inter-simulation comparison projects, one needs to be extremely cautious about interpretations about the CGM, since the gravity, hydrodynamical treatments as well as sub–grid modelling differs quite a bit.

5.1.2 Detailed modeling of LG gaseous components

The LG and the broader Local Universe have been long debated to be special in various aspects in terms of its paired host galaxy environment as opposed to most of the other isolated galaxy environments (Libeskind et al., 2020; Arora et al., 2022; Dolag et al., 2023). However, ascertaining the magnitude of this LG characteristic on the satellite population remains tricky because of the observational biases in our LG CGM data. An accurate bias estimate in LG

observations (for example, in the form of modeling contributions from specific LG components like Complex C, Complex M, etc.) would help us probe the uniqueness of LG. Quantifying the sources of observational bias in the existing LG CGM data by analyzing the effect of presence of large substructures like the MS or the LMC-SMC CGM via HESTIA simulations is now practically possible, thanks to the wealth of vastly improved, high-quality, extensive stellar and galactic data from surveys like Gaia eDR3 (Gaia Collaboration et al., 2021), CosmicFlows-4 (Tully et al., 2023), etc.

5.1.3 Generating extensive absorption-line predictions for satellite populations

Since satellites are embedded within the CGMs of their hosts, their life-cycle and fate has a bearing on the CGM of the host galaxy and vice-versa. The morphology of a CGM can very well govern the timescales over which satellites get quenched/feed the host galaxy. Focused studies probing this connection are increasingly being carried out in recent times (Greene et al., 2022; Samuel et al., 2022). Results from my TNG50 study (Chapter 4) conclusively demonstrate that satellite galaxies influence the extended cold gas density profiles of their host haloes (see Fig. 4.4). The trends from the cold gas contributions from satellite galaxies (see Fig. 4.5) with respect to the number of satellite galaxies per halo (N_{sats}), the primary satellite (in M_*) in each halo (see Fig. 4.7) and the number of massive satellites associated with each halo (see Fig. 4.10) collectively provide strong evidence that the number statistics of massive satellites is one of the key factors influencing the amount of cold gas stripping from the satellite population towards the host halos.

One can delve further into the satellite–host galaxy connection by mapping the cool CGM of host halos via low-ions (for example, O I, Si II, S II, Mg II, Si III, etc.). Resulting ion abundances, coupled with detailed kinematics knowledge of satellites in simulations, would give us a better handle on the gas flows between the satellites and host. Subsequent comparisons with existing observations as well as predictions in the event of future missions like LUVOIR (The LUVOIR Team, 2019) could also help shed some light on the missing metals problem in CGM of simulated haloes (Oppenheimer et al., 2018a; Lehner et al., 2020; Ji et al., 2020). An extensive ion mapping study, such as the one proposed above, would be super helpful in conjunction with the existing and upcoming survey datasets.

5.1.4 Investigating the role of CGM in high-z galaxy mergers

Our results from Chapter 3 are proven only within the low-z, gas-rich, major merger regime. While mergers assume a backseat role at low-z, they are thought to be particularly important at high-z. Results, both from surveys (Kartaltepe et al., 2007; Lin et al., 2008; Romano et al., 2021) as well as hydrodynamical simulations (Fakhouri & Ma, 2008; Rodriguez-Gomez et al., 2015; Snyder et al., 2017), indeed show that major mergers were much more frequent in the early universe ($z \gtrsim 2$). We also know that the high-z CGM looked somewhat different than it does at the present epoch. Most of the accreted CGM gas at $z \sim 2$ is in cool phase but at low-z, the same gas is in the hot phase (Hafen et al., 2020). Most of the high-z, extended CGM mass originates via pristine IGM accretion and is still far from being well-mixed, unlike that seen at later epochs (Mitchell et al., 2021).

Observations have detected a metallicity evolution in the LLS associated with the CGM, from early to present times (Lehner et al., 2013; Wotta et al., 2016). The decline in the number density of Mg II absorbers concurrently observed with the constant number density of C IV absorbers, provides strong hints towards the temporal decline and gradual dominance of cool and hot CGM

respectively (Cooksey et al., 2010; Matejek & Simcoe, 2012; Zhu et al., 2013; Cooksey et al., 2013). The reciprocal influence between the CGM and a major merger event at early epochs, is certainly a topic that begs to be investigated. Recent findings from simulations and observations already provide robust evidence that merger-induced outflows can enhance metal mixing and thereby increase the CGM metallicity (Hani et al., 2018; Ginolfi et al., 2020). Such existing and upcoming efforts in this direction could be instrumental in acutely tracking the CGM evolution from the early universe to the present times.

5.2 This field

5.2.1 Addressing spatial resolution concerns with respect to the treatment of cold CGM in simulations

Tackling the treatment of small, cold CGM clumps in simulations has been a thorny issue since the last decade. The much apparent lack of convergence with respect to the cold CGM properties (unlike the well-converged hot CGM phase) across different spatial resolution levels for a cosmological simulation has been a constant feature across most of the simulations available today (Vazza et al., 2010; Miniati, 2014; Genel et al., 2014; Schaye et al., 2015; Wetzel et al., 2016; Hopkins et al., 2018). Small, cold gas clumps can cool isochorically once they reach the spatial resolution limit in the respective simulation. Isochoric cooling would refrain the clumps from disintegrating into small, parsec or even sub-parsec sized droplets, that would have eventually cooled down isobarically and ultimately increased the observable ion covering fractions (Fielding et al., 2020).

Much efforts are being taken to consistently develop novel resolution implementation schemes to increasingly resolve smaller and smaller cold gas clumps in halo regions and alleviate this problem. Some recent developments include employing a small–scale-specific gas refinement technique in the CGM (Peeples et al., 2019; Hummels et al., 2019), introducing extra resolution elements within the virial radius (van de Voort et al., 2019), increasing CGM resolution at the expense of a downgraded ISM resolution (Suresh et al., 2018), implementing shock refinement schemes (Bennett & Sijacki, 2020), idealized simulations of halo-feeding cooling streams (Mandelker et al., 2020), etc. Developing even more sophisticated solutions for effectively managing resolution elements across a given simulated volume while maintaining numerical cost-effectiveness will be important, since this has a direct impact on various mock predictions like covering fractions, cloud sizes, etc (Liang & Remming, 2019). In particular, successfully implementing the insights from idealized and cloud-crushing MHD simulations into cosmological simulations could be a big step towards conclusively characterizing the cold and cool halo gas.

5.2.2 Improvements in ionization modeling

Quasar absorption line studies assume that a single absorber sightline is associated with a spatially isolated cloud having a single set of density, temperature and metallicity values. Naturally, this assumption is also adopted in ionization modeling tools like CLOUDY, which are often employed for generating mock outputs. However, the limited information capacity of absorption-line methods opens up the possibility that the internal phase conditions of a single cloud may be inhomogeneous. In other words, it is realistically possible that multiple spatially distinct gas clouds, sharing the same velocity space, contribute towards a single absorption component. Marra et al. 2022 demonstrated that while low ion absorber components like Si II majorly show single-cloud origins, a lot of the intermediate and high ion absorbers like C IV and O VI have

multiple-cloud origins. Efforts are increasingly being made towards developing evolved, multi-phase ionization models (Zahedy et al., 2019, 2021; Haislmaier et al., 2020; Nielsen et al., 2022). In particular, Sameer et al. 2021, 2022 have developed a novel Bayesian technique that enables individual component modeling within a single absorber, which, in essence, brings the true multi-phase nature of a gas cloud to the fore.

Non-equilibrium effects can dominate in scenarios like in the self-shielding–dominant ISM or in the high-z CGM (where local radiation sources can overpower the effects from the metagalactic UV background) and, hence, violate the primary assumption of PIE/CIE in conventional ionization modeling. Models involving non-equilibrium chemistry along with radiation hydrodynamics are especially important in such cases (Katz, 2022). While almost all existing mainstream CLOUDY models assume a simplistic slab geometry, in reality, astrophysical gas clouds rarely conform to this assumption. Moving towards complex, more realistic cloud geometries in future ionization models is crucial in the context of denser regions where self-shielding starts to dominate (Crighton et al., 2015).

5.2.3 Towards more realistic CGM models

Much of the simulated global ISM and CGM properties of any galaxy depend upon the underlying sub-grid models (Colín et al., 2010; Nuñez-Castiñeyra et al., 2021). While the existing sub-grid recipes are greatly improved as compared to those that were employed about a decade ago, these can certainly be refined further to even more closely resemble the real CGMs. Including full radiation hydrodynamics (Ocvirk et al. 2016; Kannan et al. 2022; Yeh et al. 2023; but see also Puchwein et al. 2023), full CR physics (Pfrommer et al., 2016; Hopkins et al., 2022a), extensively and accurately implementing turbulent processes (Voit, 2018), implementing a more realistic UV background (Puchwein et al., 2015; García & Ryan-Weber, 2020; Acharya & Khaire, 2021), refining the treatment of galactic outflows (Valentini et al., 2017; Schneider & Robertson, 2018), improving upon the mass and metal loading models (Oppenheimer & Davé, 2008), including dust physics (McKinnon et al., 2016; Hou et al., 2017; Aoyama et al., 2018; Gjergo et al., 2018), etc. are some areas that could significantly impact the energy, pressure, metal and baryon budgets as well as the internal morphology of the simulated CGM and hence, deserve a closer look.

It would be certainly beneficial to include efficient post-processing CR schemes like, for example, used in Winner et al. 2019, which can be effectively employed in astrophysical blast wave scenarios like Fermi bubbles, etc. Hopkins et al. 2020 demonstrate the need for investigating the effects of CRs with variable diffusivity, in the quest for pinning down realistic CR models. Very sparse number of low-z simulations including some form of radiative transfer exist to-date and they hint that while radiative transfer could impact the disc morphologies as well as suppress SFR, their role may be over-estimated in simulations employing corresponding sub-grid prescriptions (Wise et al., 2012; Rosdahl et al., 2015). High-resolution, local ISM simulations are now being run in order to characterize the mass rates, temperature phases as well as energy transfer budgets of galactic outflows in unprecedented detail (Kim et al., 2020; Pandya et al., 2021). Improved cosmic ionizing background models, which account for varying magnitude of the AGNs and star-forming galaxies' impact over different epochs, are able to match several constrained parameters such as intergalactic H I and He II photoionization rates upto $z \sim 6$, non-ionizing UV background measurements, galaxy and AGN luminosity functions, etc. (Faucher-Giguère, 2020). While recent dust physics models are able to fairly reproduce the observed dust surface density radial profile in the dust-dominant $z \sim 1$–2 epoch, they fail to obtain enough small dust grains at larger radii, something that is directly at odds with the observed

Mg II reddening curves. However, the effects of shocks and turbulence, which can cause grain shattering, need to be explored further in this context.

Chapter 6

Conclusions

The collective aim of this thesis is to better understand the effects of major merger events, Local Group environments and global satellite properties on the CGM of simulated MW-like, L* galaxies. The broader goal is to improve existing CGM models, thereby taking our current galaxy evolution models a bit more closer to the reality.

6.1 Gas in the Local Group Simulations

In Chapter 2, I presented the findings about the CGM in HESTIA constrained LG simulations at $z = 0$. Across each of the three realizations containing a MW–M31-like galaxy pair, surrounded by a bunch of satellite galaxies, each CGM phase (marked by a corresponding tracer ion) showed distinct extended density profiles that were corroborated by corresponding power spectra. H I and Si III density maps, which broadly represent the cold-dense and cool-ionized CGM, are largely clumpy and distributed close to the galaxies. On the other hand, the highly ionized oxygen ions (O VI, O VII and O VIII), primarily tracing the warm-hot and hot-diffuse CGM, are tenuously distributed throughout the LG and are volume-filling. The extent of the warm-hot and hot CGM, in particular, was seen stretching up to the virial radii of MW-M31.

A comparison of Si III and O VI column densities for M31 revealed that the HESTIA M31, like other simulations, produces less gas on the outskirts as compared to the observed M31 as well as results from low-z galaxies. I designed an observational bias model within my HESTIA sightline-in-a-box analysis framework in order to carefully extract any possible signals from MW CGM that could be falsely attributed to the M31 CGM in observations. This model demonstrated that due to the inherent methodology of spectral-line measurement techniques, some CGM clouds from our MW could be wrongly attributed to the M31 CGM. This could potentially become one of the reasons for long-standing mismatch seen between CGM observations and simulations. Correctly identifying such observational biases could, therefore, help us in better interpretation of the LG CGM observations, thereby helping us improve our current CGM models.

6.2 Bridge formation in merging Galaxies

In Chapter 3, I used four zoom-in major merger simulations, based on Illustris, in a bid to find how the CGM of the merger system impacted some of the observables. The mergers were selected to be gas-rich, occurring between $z \lesssim 0.5$-1.0, with a progenitor mass ratio greater than 1:2 and resulting in MW-mass post merger remnants. Two of the simulations involved multiple passages while the other two were direct collision events. A transient but clear bridge is formed

at the apocenter during the multiple passage mergers while this feature is generally very weak in the direct collision events.

Based on the distance computed for each gas cell from its associated galaxy, I classified it as an ISM, CGM or IGM particle. After continuously monitoring the changes in the distances between the gas particles of merging galaxies through the merger event in every simulation via tracer particle method and implementing CLOUDY post–processing, I obtained H I maps for each system for a set of time stamps spanning the duration of the merger. Excess cold gas (in the form of H I clumps) is funnelled in the bridge regions, causing heightened merger-induced star formation. My analysis revealed that about 33–48 percent of this gas originates in the CGM. Furthermore, kinematical signatures of the gas between the center and outskirts of the galaxies are reflected in the radial velocity profiles. Thus, all of the above results clearly demonstrate the non-trivial role of CGM in influencing some of the post-merger observables in such systems.

6.3 How satellites influence the cold circumgalactic medium in TNG50 simulations

In Chapter 4, I studied the impact of satellites on the cold phase of their host halo CGMs across a range of halo masses. For this, I used galaxies from the TNG50 simulations, one of the flagship varieties within the IllustrisTNG suite. A total of 234 L^* halos were selected based on certain halo, stellar mass and SFR constraints. In order to minimize the primary dependence of satellite properties on the halo masses, I fragmented the sample into low mass bin (LMB), middle mass bin (MMB) and high mass bin (HMB). Each bin was further segmented into bottom, inter and top quartiles (BQ, IQ and TQ) based on the number of satellite galaxies associated per halo. I identified three global satellite properties (termed as probe variables) whose impact on the host cold gas was carefully studied. Number of satellites associated with a halo ($N_{\rm sats}$), total mass in satellites for each halo ($M_{\rm tms}$) and stellar mass of the most massive or primary satellite ($M_{*\rm mms}$) are the three aforementioned probe variables.

Imprints of contribution from satellite populations were found on the extended cold gas density profiles of the host galaxies across all mass bins, except the lowest mass ones. In case of the lowest mass halos, most of the cold gas was found associated with the centrals, rather than their respective satellite population. While $M_{*\rm mms}$ impacted the extended cold CGM in LMB halos the most, only the halos lying in the top end of this mass bin are actually being fed by cold gas from the primary satellite. I also found that the ease with which cold gas is eventually stripped off the primary satellite (characterized by the stellar mass ratio between the primary satellite and the central, $M_{*\rm mms}/M_{*\rm C}$) has very little effect in this context. The high-mass HMB halos' cold gas, on the other hand, was found to be impacted the most by $N_{\rm sats}$.

Extremely massive primary satellites (similar to LMC/SMC masses) are less successful in retaining their cold gas reserves as compared to their lower quartile primaries in the same mass bin. Finally, I found that the lowest mass halos have such few massive ($M_* > 10^8 M_\odot$) satellite galaxies, such that their total satellite population does not ultimately increase the inherent amount of halo cold gas much. The higher mass halos have not only a larger number of massive satellite galaxies but also more massive primary satellites, both of which are able to deposit huge amounts of cold gas in their parent halo CGMs. This study, therefore, shed light on the role of the global satellite population towards the cold CGM of their hosts and demonstrated that satellite stripping is one of the potentially important pathways contributing to the total cold CGM budget of any MW-mass halo.

6.4 Synopsis

In an overarching context, my thesis has primarily contributed to the field of low-z CGM studies in the following distinct ways.

1. The simulated HESTIA galaxies in this work exhibited a rather complex, intricate CGM structure– something that is strongly aligned with the observations.

2. Cosmological environment, local surroundings and merger history all affect CGM properties directly.

3. If the LG is extensively harnessed by both observations as well as simulations, we can better constrain many CGM details, thereby, ruling out some of the less realistic CGM models.

4. More efforts are needed in the direction of expanding the statistical relevance of LG simulations and using them to minutely constrain the LG CGM properties, alleviating spatial resolution convergence concerns and improving the realism of simulated CGM by using better sub–grid models and moving towards ionization models that account for real cloud geometries, non-equilibrium effects and multi-cloud absorber origins.

Bibliography

Aarseth, S. J., Gott, J. R., I., & Turner, E. L. 1979, ApJ, 228, 664, doi: 10.1086/156892

Abadi, M. G., Moore, B., & Bower, R. G. 1999, MNRAS, 308, 947, doi: 10.1046/j.1365-8711.1999.02715.x

Abadi, M. G., Navarro, J. F., Steinmetz, M., & Eke, V. R. 2003, ApJ, 591, 499, doi: 10.1086/375512

Abruzzo, M. W., Bryan, G. L., & Fielding, D. B. 2022a, ApJ, 925, 199, doi: 10.3847/1538-4357/ac3c48

Abruzzo, M. W., Fielding, D. B., & Bryan, G. L. 2022b, arXiv e-prints, arXiv:2210.15679, doi: 10.48550/arXiv.2210.15679

Acharya, A., & Khaire, V. 2021, Monthly Notices of the Royal Astronomical Society, 509, 5559, doi: 10.1093/mnras/stab3316

Adams, E. A., Giovanelli, R., & Haynes, M. P. 2013, The Astrophysical Journal, 768, 77

Adelberger, K. L., Shapley, A. E., Steidel, C. C., et al. 2005, ApJ, 629, 636, doi: 10.1086/431753

Agertz, O., & Kravtsov, A. V. 2015, ApJ, 804, 18, doi: 10.1088/0004-637x/804/1/18

Agertz, O., Teyssier, R., & Moore, B. 2010, Monthly Notices of the Royal Astronomical Society, 410, 1391, doi: 10.1111/j.1365-2966.2010.17530.x

Agertz, O., Moore, B., Stadel, J., et al. 2007, MNRAS, 380, 963, doi: 10.1111/j.1365-2966.2007.12183.x

Agertz, O., Renaud, F., Feltzing, S., et al. 2021, Monthly Notices of the Royal Astronomical Society, 503, 5826, doi: 10.1093/mnras/stab322

Akins, H. B., Christensen, C. R., Brooks, A. M., et al. 2021, The Astrophysical Journal, 909, 139, doi: 10.3847/1538-4357/abe2ab

Alatalo, K., Aladro, R., Nyland, K., et al. 2016, The Astrophysical Journal, 830, 137, doi: 10.3847/0004-637X/830/2/137

Allgood, B., Flores, R. A., Primack, J. R., et al. 2006, MNRAS, 367, 1781, doi: 10.1111/j.1365-2966.2006.10094.x

Anderson, M. E., Churazov, E., & Bregman, J. N. 2016, MNRAS, 455, 227, doi: 10.1093/mnras/stv2314

Andersson, E. P., Agertz, O., Renaud, F., & Teyssier, R. 2022, arXiv e-prints, arXiv:2209.06218, doi: 10.48550/arXiv.2209.06218

Anglés-Alcázar, D., Faucher-Giguère, C.-A., Kereš, D., et al. 2017, MNRAS, 470, 4698, doi: 10.1093/mnras/stx1517

Anglés-Alcázar, D., Faucher-Giguère, C.-A., Kereš, D., et al. 2017, Monthly Notices of the Royal Astronomical Society, 470, 4698, doi: 10.1093/mnras/stx1517

Angulo, R. E., Hahn, O., & Abel, T. 2013, Monthly Notices of the Royal Astronomical Society, 434, 3337, doi: 10.1093/mnras/stt1246

Angulo, R. E., Springel, V., White, S. D. M., et al. 2012, MNRAS, 426, 2046–2062, doi: 10.1111/j.1365-2966.2012.21830.x

Annem, B., & Khoperskov, S. 2022, arXiv e-prints, arXiv:2210.17054. https://arxiv.org/abs/2210.17054

Aoyama, S., Hou, K.-C., Hirashita, H., Nagamine, K., & Shimizu, I. 2018, MNRAS, 478, 4905, doi: 10.1093/mnras/sty1431

Appleby, S., Davé, R., Sorini, D., Storey-Fisher, K., & Smith, B. 2021, MNRAS, 507, 2383, doi: 10.1093/mnras/stab2310

Appleby, S., Davé, R., Sorini, D., Storey-Fisher, K., & Smith, B. 2021, Monthly Notices of the Royal Astronomical Society, 507, 2383, doi: 10.1093/mnras/stab2310

Appleton, P. N., Emonts, B., Lisenfeld, U., et al. 2022, The Astrophysical Journal, 931, 121, doi: 10.3847/1538-4357/ac63b2

Aragon-Calvo, M. A., Neyrinck, M. C., & Silk, J. 2016, arXiv preprint arXiv:1607.07881

Armillotta, L., Fraternali, F., Werk, J. K., Prochaska, J. X., & Marinacci, F. 2017, Monthly Notices of the Royal Astronomical Society, 470, 114, doi: 10.1093/mnras/stx1239

Arora, N., Macciò, A. V., Courteau, S., et al. 2022, MNRAS, 512, 6134, doi: 10.1093/mnras/stac893

Artale, M. C., Pedrosa, S. E., Trayford, J. W., et al. 2017, MNRAS, 470, 1771, doi: 10.1093/mnras/stx1263

Astropy Collaboration, Price-Whelan, A. M., Sipőcz, B. M., et al. 2018, AJ, 156, 123, doi: 10.3847/1538-3881/aabc4f

Augustin, R., Quiret, S., Milliard, B., et al. 2019, MNRAS, 489, 2417, doi: 10.1093/mnras/stz2238

Aumer, M., White, S. D., Naab, T., & Scannapieco, C. 2013, MNRAS, 434, 3142

Babu, G. J., & Feigelson, E. D. 2006, in Astronomical Society of the Pacific Conference Series, Vol. 351, Astronomical Data Analysis Software and Systems XV, ed. C. Gabriel, C. Arviset, D. Ponz, & S. Enrique, 127

Bacon, R., Mary, D., Garel, T., et al. 2021, A&A, 647, A107, doi: 10.1051/0004-6361/202039887

Bahcall, J. N., & Spitzer Jr, L. 1969, ApJ, 156, L63

Bahé, Y. M., Barnes, D. J., Dalla Vecchia, C., et al. 2017, MNRAS, 470, 4186, doi: 10.1093/mnras/stx1403

Barger, K. A., Haffner, L. M., & Bland-Hawthorn, J. 2013, ApJ, 771, 132, doi: 10.1088/0004-637X/771/2/132

Barger, K. A., Madsen, G. J., Fox, A. J., et al. 2017, ApJ, 851, 110, doi: 10.3847/1538-4357/aa992a

Barkana, R., & Loeb, A. 2001, PhR, 349, 125, doi: 10.1016/S0370-1573(01)00019-9

Barmby, P., Ashby, M., Bianchi, L., et al. 2006, The Astrophysical Journal, 650, L45

Barnes, J., & Hut, P. 1986, Nature, 324, 446, doi: 10.1038/324446a0

Barnes, J. E. 1992, ApJ, 393, 484, doi: 10.1086/171522

Barrera-Ballesteros, J. K., Sánchez, S. F., García-Lorenzo, B., et al. 2015, A&A, 579, A45, doi: 10.1051/0004-6361/201425397

Becker, G. D., Pettini, M., Rafelski, M., et al. 2019, The Astrophysical Journal, 883, 163, doi: 10.3847/1538-4357/ab3eb5

Beckett, A., Morris, S. L., Fumagalli, M., et al. 2022, MNRAS, 517, 1020, doi: 10.1093/mnras/stac2630

Behroozi, P. S., Conroy, C., & Wechsler, R. H. 2010a, ApJ, 717, 379

—. 2010b, ApJ, 717, 379–403, doi: 10.1088/0004-637x/717/1/379

Behroozi, P. S., Wechsler, R. H., & Conroy, C. 2013, ApJ, 770, 57

Behroozi, P. S., Wechsler, R. H., & Wu, H.-Y. 2013, ApJ, 762, 109, doi: 10.1088/0004-637X/762/2/109

Bekki, K., & Chiba, M. 2007, Monthly Notices of the Royal Astronomical Society: Letters, 381, L16, doi: 10.1111/j.1745-3933.2007.00357.x

Bekki, K., Couch, W. J., Shioya, Y., & Vazdekis, A. 2005, MNRAS, 359, 949, doi: 10.1111/j.1365-2966.2005.08932.x

Belli, S., Contursi, A., Genzel, R., et al. 2021, ApJL, 909, L11, doi: 10.3847/2041-8213/abe6a6

Bennett, J. S., & Sijacki, D. 2020, MNRAS, 499, 597, doi: 10.1093/mnras/staa2835

Bera, A., Kanekar, N., Weiner, B. J., Sethi, S., & Dwarakanath, K. S. 2018, ApJ, 865, 39, doi: 10.3847/1538-4357/aad698

Berg, M. A., Howk, J. C., Lehner, N., et al. 2019, ApJ, 883, 5, doi: 10.3847/1538-4357/ab378e

Berg, T. A. M., Ellison, S. L., Tumlinson, J., et al. 2018, Monthly Notices of the Royal Astronomical Society, 478, 3890, doi: 10.1093/mnras/sty962

Berger, M. J., & Colella, P. 1989, Journal of Computational Physics, 82, 64, doi: 10.1016/0021-9991(89)90035-1

Berger, M. J., & Oliger, J. 1984, Journal of Computational Physics, 53, 484, doi: 10.1016/0021-9991(84)90073-1

Bergeron, J., & Boissé, P. 1991, Astronomy and Astrophysics, 243, 344

Bergeron, J., & Stasinska, G. 1986, Astronomy and Astrophysics, 169, 1

Bernstein, J., Brown, L. S., & Feinberg, G. 1989, Rev. Mod. Phys., 61, 25, doi: 10.1103/RevModPhys.61.25

Besla, G., Kallivayalil, N., Hernquist, L., et al. 2012, Monthly Notices of the Royal Astronomical Society, 421, 2109, doi: 10.1111/j.1365-2966.2012.20466.x

Bett, P., Eke, V., Frenk, C. S., et al. 2007, MNRAS, 376, 215, doi: 10.1111/j.1365-2966.2007.11432.x

Bhattacharyya, S., Das, S., Gupta, A., Mathur, S., & Krongold, Y. 2022, arXiv e-prints, arXiv:2208.07863, doi: 10.48550/arXiv.2208.07863

Biaus, L., Nuza, S. E., Richter, P., et al. 2022, MNRAS, 517, 6170, doi: 10.1093/mnras/stac2983

Bielby, R. M., Stott, J. P., Cullen, F., et al. 2019, MNRAS, 486, 21, doi: 10.1093/mnras/stz774

Binney, J., & Tremaine, S. 2008, Galactic Dynamics: Second Edition (MNRAS)

Birnboim, Y., & Dekel, A. 2003, MNRAS, 345, 349, doi: 10.1046/j.1365-8711.2003.06955.x

Bish, H. V., Werk, J. K., Peek, J., Zheng, Y., & Putman, M. 2021, ApJ, 912, 8, doi: 10.3847/1538-4357/abeb6b

Bland-Hawthorn, J., & Gerhard, O. 2016, ARA&A, 54, 529, doi: 10.1146/annurev-astro-081915-023441

Boardman, N., Zasowski, G., Newman, J. A., et al. 2020, Monthly Notices of the Royal Astronomical Society, 498, 4943, doi: 10.1093/mnras/staa2731

Bode, P., & Ostriker, J. P. 2003, ApJS, 145, 1, doi: 10.1086/345538

Bogdán, Á., Bourdin, H., Forman, W. R., et al. 2017, ApJ, 850, 98, doi: 10.3847/1538-4357/aa9523

Bogdán, Á., Forman, W. R., Vogelsberger, M., et al. 2013, The Astrophysical Journal, 772, 97, doi: 10.1088/0004-637x/772/2/97

Bogdán, Á., Vogelsberger, M., Kraft, R. P., et al. 2015, ApJ, 804, 72, doi: 10.1088/0004-637X/804/1/72

Boissier, S., & Prantzos, N. 1999, Monthly Notices of the Royal Astronomical Society, 307, 857, doi: 10.1046/j.1365-8711.1999.02699.x

Bondi, H. 1952, Monthly Notices of the Royal Astronomical Society, 112, 195, doi: 10.1093/mnras/112.2.195

Bondi, H., & Hoyle, F. 1944, Monthly Notices of the Royal Astronomical Society, 104, 273, doi: 10.1093/mnras/104.5.273

Boogaard, L. A., Brinchmann, J., Bouché, N., et al. 2018, A&A, 619, A27, doi: 10.1051/0004-6361/201833136

Booth, C., & Schaye, J. 2009, MNRAS, 398, 53

Bordoloi, R., Lilly, S. J., Knobel, C., et al. 2011, ApJ, 743, 10, doi: 10.1088/0004-637X/743/1/10

Bordoloi, R., Tumlinson, J., Werk, J. K., et al. 2014, ApJ, 796, 136

Borrow, J., Schaller, M., & Bower, R. G. 2021, Monthly Notices of the Royal Astronomical Society, 505, 2316, doi: 10.1093/mnras/stab1423

Borthakur, S., Heckman, T., Strickland, D., Wild, V., & Schiminovich, D. 2013, ApJ, 768, 18

Borthakur, S., Heckman, T., Tumlinson, J., et al. 2015, ApJ, 813, 46, doi: 10.1088/0004-637X/813/1/46

—. 2016, ApJ, 833, 259, doi: 10.3847/1538-4357/833/2/259

Borthakur, S., Heckman, T., Tumlinson, J., et al. 2016, The Astrophysical Journal, 833, 259, doi: 10.3847/1538-4357/833/2/259

Böss, L. M., Steinwandel, U. P., Dolag, K., & Lesch, H. 2023, MNRAS, 519, 548, doi: 10.1093/mnras/stac3584

Bouma, S. J. D., Richter, P., & Fechner, C. 2019, A&A, 627, A20, doi: 10.1051/0004-6361/201935078

Bouwens, R. J., Illingworth, G. D., Oesch, P. A., et al. 2012, ApJL, 752, L5, doi: 10.1088/2041-8205/752/1/L5

Bowen, D. V., Tolstoy, E., Ferrara, A., Blades, J. C., & Brinks, E. 1997, The Astrophysical Journal, 478, 530, doi: 10.1086/303823

Boylan-Kolchin, M., Ma, C.-P., & Quataert, E. 2006, Monthly Notices of the Royal Astronomical Society, 369, 1081, doi: 10.1111/j.1365-2966.2006.10379.x

Braine, J., Davoust, E., Zhu, M., et al. 2003, A&A, 408, L13, doi: 10.1051/0004-6361:20031148

Bremer, M. N., Phillipps, S., Kelvin, L. S., et al. 2018, MNRAS, 476, 12, doi: 10.1093/mnras/sty124

Brennan, R., Pandya, V., Somerville, R. S., et al. 2015, MNRAS, 451, 2933, doi: 10.1093/mnras/stv1007

Bryan, G. L., & Norman, M. L. 1995, in American Astronomical Society Meeting Abstracts, Vol. 187, American Astronomical Society Meeting Abstracts, 95.04

Bryan, G. L., Norman, M. L., O'Shea, B. W., et al. 2014, ApJS, 211, 19, doi: 10.1088/0067-0049/211/2/19

Buck, T., Macciò, A. V., Obreja, A., et al. 2017, Monthly Notices of the Royal Astronomical Society, 468, 3628, doi: 10.1093/mnras/stx685

Buck, T., Pfrommer, C., Pakmor, R., Grand, R. J., & Springel, V. 2020, MNRAS, 497, 1712

Buie, Edward, I., Gray, W. J., & Scannapieco, E. 2018, ApJ, 864, 114, doi: 10.3847/1538-4357/aad8bd

Bullock, J. S., Kravtsov, A. V., & Weinberg, D. H. 2001, ApJ, 548, 33, doi: 10.1086/318681

Bundy, K., Fukugita, M., Ellis, R. S., et al. 2009, The Astrophysical Journal, 697, 1369, doi: 10.1088/0004-637X/697/2/1369

Burchett, J. N., Rubin, K. H. R., Prochaska, J. X., et al. 2021, ApJ, 909, 151, doi: 10.3847/1538-4357/abd4e0

Burchett, J. N., Tripp, T. M., Prochaska, J. X., et al. 2019, ApJL, 877, L20, doi: 10.3847/2041-8213/ab1f7f

Bustamante, S., Sparre, M., Springel, V., & Grand, R. J. 2018, Monthly Notices of the Royal Astronomical Society, 479, 3381

Bustard, C., & Gronke, M. 2022, The Astrophysical Journal, 933, 120, doi: 10.3847/1538-4357/ac752b

Bustard, C., Zweibel, E. G., D'Onghia, E., Gallagher, J. S., I., & Farber, R. 2020, ApJ, 893, 29, doi: 10.3847/1538-4357/ab7fa3

Butsky, I. S., Burchett, J. N., Nagai, D., et al. 2019, MNRAS, 490, 4292, doi: 10.1093/mnras/stz2859

Butsky, I. S., Fielding, D. B., Hayward, C. C., et al. 2020, ApJ, 903, 77, doi: 10.3847/1538-4357/abbad2

Butsky, I. S., Nakum, S., Ponnada, S. B., et al. 2023, MNRAS, doi: 10.1093/mnras/stad671

Butsky, I. S., & Quinn, T. R. 2018, ApJ, 868, 108, doi: 10.3847/1538-4357/aaeac2

Calura, F., & Matteucci, F. 2006, MNRAS, 369, 465, doi: 10.1111/j.1365-2966.2006.10329.x

Cautun, M., van de Weygaert, R., Jones, B. J. T., & Frenk, C. S. 2014, Monthly Notices of the Royal Astronomical Society, 441, 2923, doi: 10.1093/mnras/stu768

Ceverino, D., Dekel, A., & Bournaud, F. 2010, MNRAS, 404, 2151

Chadayammuri, U., ZuHone, J., Nulsen, P., et al. 2022, MNRAS, 509, 1201, doi: 10.1093/mnras/stab2629

Chan, T. K., Kereš, D., Gurvich, A. B., et al. 2022, MNRAS, 517, 597, doi: 10.1093/mnras/stac2236

Chen, H.-W., Zahedy, F. S., Johnson, S. D., et al. 2018, MNRAS, 479, 2547, doi: 10.1093/mnras/sty1541

Chen, H.-W., Johnson, S. D., Straka, L. A., et al. 2019, MNRAS, 484, 431, doi: 10.1093/mnras/sty3513

Chen, H.-W., Zahedy, F. S., Boettcher, E., et al. 2020, Monthly Notices of the Royal Astronomical Society, 497, 498, doi: 10.1093/mnras/staa1773

Chen, M. C., Chen, H.-W., Gronke, M., Rauch, M., & Broadhurst, T. 2021, MNRAS, 504, 2629, doi: 10.1093/mnras/stab1041

Chen, Y., Steidel, C. C., Hummels, C. B., et al. 2020, MNRAS, 499, 1721, doi: 10.1093/mnras/staa2808

Chiosi, C., & Matteucci, F. 1984, in Astrophysics and Space Science Library, Vol. 109, Stellar Nucleosynthesis, ed. C. Chiosi & A. Renzini, 359

Chisholm, J., Prochaska, J. X., Schaerer, D., Gazagnes, S., & Henry, A. 2020, MNRAS, 498, 2554, doi: 10.1093/mnras/staa2470

Choi, E., Ostriker, J. P., Naab, T., & Johansson, P. H. 2012, ApJ, 754, 125, doi: 10.1088/0004-637X/754/2/125

Chomiuk, L., & Povich, M. S. 2011, The Astronomical Journal, 142, 197

Churchill, C. W., Klimek, E., Medina, A., & Vander Vliet, J. R. 2014, arXiv e-prints, arXiv:1409.0916, doi: 10.48550/arXiv.1409.0916

Churchill, C. W., Vander Vliet, J. R., Trujillo-Gomez, S., Kacprzak, G. G., & Klypin, A. 2015, ApJ, 802, 10, doi: 10.1088/0004-637X/802/1/10

Cicone, C., De Breuck, C., Chen, C.-C., et al. 2019, arXiv preprint arXiv:1903.04531

Cicone, C., Mainieri, V., Circosta, C., et al. 2021, A&A, 654, L8, doi: 10.1051/0004-6361/202141611

Ciotti, L., Lanzoni, B., & Volonteri, M. 2007, The Astrophysical Journal, 658, 65, doi: 10.1086/510773

Codoreanu, A., Ryan-Weber, E. V., García, L. Á., et al. 2018, MNRAS, 481, 4940, doi: 10.1093/mnras/sty2576

Colavitti, E., Matteucci, F., & Murante, G. 2008, A&A, 483, 401, doi: 10.1051/0004-6361:200809413

Cole, S., Hatton, S., Weinberg, D. H., & Frenk, C. S. 1998, MNRAS, 300, 945, doi: 10.1046/j.1365-8711.1998.01936.x

Cole, S., Lacey, C. G., Baugh, C. M., & Frenk, C. S. 2000, MNRAS, 319, 168, doi: 10.1046/j.1365-8711.2000.03879.x

Colín, P., Avila-Reese, V., Vázquez-Semadeni, E., Valenzuela, O., & Ceverino, D. 2010, ApJ, 713, 535, doi: 10.1088/0004-637X/713/1/535

Comparat, J., Truong, N., Merloni, A., et al. 2022, A&A, 666, A156, doi: 10.1051/0004-6361/202243101

Connors, T. W., Kawata, D., & Gibson, B. K. 2006, MNRAS, 371, 108, doi: 10.1111/j.1365-2966.2006.10659.x

Conroy, C., Naidu, R. P., Zaritsky, D., et al. 2019, The Astrophysical Journal, 887, 237, doi: 10.3847/1538-4357/ab5710

Cooksey, K. L., Kao, M. M., Simcoe, R. A., O'Meara, J. M., & Prochaska, J. X. 2013, ApJ, 763, 37, doi: 10.1088/0004-637X/763/1/37

Cooksey, K. L., Thom, C., Prochaska, J. X., & Chen, H.-W. 2010, ApJ, 708, 868, doi: 10.1088/0004-637X/708/1/868

Cooper, T. J., Simcoe, R. A., Cooksey, K. L., et al. 2019, ApJ, 882, 77, doi: 10.3847/1538-4357/ab3402

Cooper, T. J., Rudie, G. C., Chen, H.-W., et al. 2021, MNRAS, 508, 4359, doi: 10.1093/mnras/stab2869

Cooray, A., & Sheth, R. 2002, PhR, 372, 1, doi: 10.1016/S0370-1573(02)00276-4

Cortese, L., Catinella, B., & Smith, R. 2021, PASA, 38, e035, doi: 10.1017/pasa.2021.18

Cox, D. P. 2005, Annual Review of Astronomy and Astrophysics, 43, 337, doi: 10.1146/annurev.astro.43.072103.150615

Cox, T. J., Jonsson, P., Primack, J. R., & Somerville, R. S. 2006, Monthly Notices of the Royal Astronomical Society, 373, 1013, doi: 10.1111/j.1365-2966.2006.11107.x

Cramer, W. J., Kenney, J. D. P., Sun, M., et al. 2019, ApJ, 870, 63, doi: 10.3847/1538-4357/aaefff

Creasey, P., Scannapieco, C., Nuza, S. E., et al. 2015, ApJL, 800, L4, doi: 10.1088/2041-8205/800/1/L4

Crighton, N. H. M., Hennawi, J. F., Simcoe, R. A., et al. 2015, MNRAS, 446, 18, doi: 10.1093/mnras/stu2088

Cui, W., Knebe, A., Yepes, G., et al. 2018, MNRAS, 480, 2898, doi: 10.1093/mnras/sty2111

Dalla Vecchia, C., & Schaye, J. 2012, Monthly Notices of the Royal Astronomical Society, 426, 140, doi: 10.1111/j.1365-2966.2012.21704.x

Damle, M., Sparre, M., Richter, P., et al. 2022, Monthly Notices of the Royal Astronomical Society, 512, 3717, doi: 10.1093/mnras/stac663

Das, S., Mathur, S., & Gupta, A. 2020a, ApJ, 897, 63, doi: 10.3847/1538-4357/ab93d2

Das, S., Mathur, S., Gupta, A., et al. 2019a, ApJ, 885, 108

Das, S., Mathur, S., Nicastro, F., & Krongold, Y. 2019b, ApJL, 882, L23

Das, S., Sardone, A., Leroy, A. K., et al. 2020b, ApJ, 898, 15, doi: 10.3847/1538-4357/ab97b9

Dattathri, S., & Sharma, P. 2022, MNRAS, 514, 826, doi: 10.1093/mnras/stac1342

Davé, R., Anglés-Alcázar, D., Narayanan, D., et al. 2019, MNRAS, 486, 2827, doi: 10.1093/mnras/stz937

Davé, R., Rafieferantsoa, M. H., Thompson, R. J., & Hopkins, P. F. 2017, MNRAS, 467, 115, doi: 10.1093/mnras/stx108

Davies, L. J. M., Robotham, A. S. G., Lagos, C. d. P., et al. 2019, Monthly Notices of the Royal Astronomical Society, 483, 5444, doi: 10.1093/mnras/sty3393

Davis, M., Efstathiou, G., Frenk, C. S., & White, S. D. M. 1985, ApJ, 292, 371, doi: 10.1086/163168

de Heij, V., Braun, R., & Burton, W. B. 2002, A&A, 391, 159, doi: 10.1051/0004-6361:20020870

De Rossi, M. E., Bower, R. G., Font, A. S., Schaye, J., & Theuns, T. 2017, MNRAS, 472, 3354, doi: 10.1093/mnras/stx2158

Deason, A. J., Mao, Y.-Y., & Wechsler, R. H. 2016, The Astrophysical Journal, 821, 5, doi: 10.3847/0004-637X/821/1/5

Debuhr, J., Quataert, E., Ma, C.-P., & Hopkins, P. 2010, MNRAS, 406, L55, doi: 10.1111/j.1745-3933.2010.00881.x

Deeley, S., Drinkwater, M. J., Cunnama, D., et al. 2017, Monthly Notices of the Royal Astronomical Society, 467, 3934, doi: 10.1093/mnras/stx441

Dehnen, W. 2000, ApJL, 536, L39, doi: 10.1086/312724

Dekel, A., Birnboim, Y., Engel, G., et al. 2009, Nature, 457, 451, doi: 10.1038/nature07648

Desert, F. X., Bazell, D., & Blitz, L. 1990, ApJL, 355, L51, doi: 10.1086/185736

Di Cintio, A., Knebe, A., Libeskind, N. I., et al. 2013, Monthly Notices of the Royal Astronomical Society, 431, 1220, doi: 10.1093/mnras/stt240

Di Matteo, P., Bournaud, F., Martig, M., et al. 2008, A&A, 492, 31, doi: 10.1051/0004-6361:200809480

Di Matteo, T., Springel, V., & Hernquist, L. 2005, Nature, 433, 604, doi: 10.1038/nature03335

Di Teodoro, E. M., & Fraternali, F. 2014, A&A, 567, A68, doi: 10.1051/0004-6361/201423596

Diemand, J., Kuhlen, M., & Madau, P. 2007, ApJ, 667, 859, doi: 10.1086/520573

Diemer, B. 2021, The Astrophysical Journal, 909, 112, doi: 10.3847/1538-4357/abd947

Di Cintio, A., Mostoghiu, R., Knebe, A., & Navarro, J. F. 2021, Monthly Notices of the Royal Astronomical Society, 506, 531, doi: 10.1093/mnras/stab1682

Dolag, K., Borgani, S., Murante, G., & Springel, V. 2009, MNRAS, 399, 497, doi: 10.1111/j.1365-2966.2009.15034.x

Dolag, K., Komatsu, E., & Sunyaev, R. 2016, MNRAS, 463, 1797, doi: 10.1093/mnras/stw2035

Dolag, K., Sorce, J. G., Pilipenko, S., et al. 2023, arXiv e-prints, arXiv:2302.10960, doi: 10.48550/arXiv.2302.10960

D'Onghia, E., & Fox, A. J. 2016, ARA&A, 54, 363, doi: 10.1146/annurev-astro-081915-023251

Donnari, M., Pillepich, A., Nelson, D., et al. 2019, MNRAS, 485, 4817, doi: 10.1093/mnras/stz712

Dou, J., Peng, Y., Renzini, A., et al. 2021, ApJ, 907, 114, doi: 10.3847/1538-4357/abd17c

Doumler, T., Hoffman, Y., Courtois, H., & Gottlöber, S. 2013, Monthly Notices of the Royal Astronomical Society, 430, 888, doi: 10.1093/mnras/sts613

Drake, G. W. 1988, Canadian Journal of Physics, 66, 586, doi: 10.1139/p88-100

Du, X., Shapley, A. E., Topping, M. W., et al. 2021, ApJ, 920, 95, doi: 10.3847/1538-4357/ac1273

Dubois, Y., Pichon, C., Welker, C., et al. 2014, Monthly Notices of the Royal Astronomical Society, 444, 1453, doi: 10.1093/mnras/stu1227

Dupuy, A., Libeskind, N. I., Hoffman, Y., et al. 2022, MNRAS, 516, 4576, doi: 10.1093/mnras/stac2486

Dutta, A., Sharma, P., & Nelson, D. 2021, Monthly Notices of the Royal Astronomical Society, 510, 3561, doi: 10.1093/mnras/stab3653

Dutta, R., Fossati, M., Fumagalli, M., et al. 2023, arXiv e-prints, arXiv:2302.09087, doi: 10.48550/arXiv.2302.09087

Edlén, B. 1979, Physica Scripta, 19, 255, doi: 10.1088/0031-8949/19/3/007

Efstathiou, G. 1979, MNRAS, 187, 117, doi: 10.1093/mnras/187.2.117

Efstathiou, G., Davis, M., White, S. D. M., & Frenk, C. S. 1985, ApJS, 57, 241, doi: 10.1086/191003

Eke, V. R., Cole, S., & Frenk, C. S. 1996, MNRAS, 282, 263, doi: 10.1093/mnras/282.1.263

Ellison, S. L., Catinella, B., & Cortese, L. 2018, Monthly Notices of the Royal Astronomical Society, 478, 3447, doi: 10.1093/mnras/sty1247

Elmegreen, D. M., Elmegreen, B. G., Whitmore, B. C., et al. 2021, The Astrophysical Journal, 908, 121, doi: 10.3847/1538-4357/abd541

Emerick, A., Bryan, G. L., & Mac Low, M.-M. 2019, MNRAS, 482, 1304, doi: 10.1093/mnras/sty2689

Emerick, A., Mac Low, M.-M., Grcevich, J., & Gatto, A. 2016, ApJ, 826, 148

F. Williams, B. 2003, Monthly Notices of the Royal Astronomical Society, 340, 143, doi: 10.1046/j.1365-8711.2003.06274.x

Fabian, A. C., Arnaud, K. A., Bautz, M. W., & Tawara, Y. 1994, ApJL, 436, L63, doi: 10.1086/187633

Faerman, Y., Pandya, V., Somerville, R. S., & Sternberg, A. 2022, The Astrophysical Journal, 928, 37, doi: 10.3847/1538-4357/ac4ca6

Fakhouri, O., & Ma, C.-P. 2008, MNRAS, 386, 577, doi: 10.1111/j.1365-2966.2008.13075.x

Falck, B., Wang, J., Jenkins, A., et al. 2021, MNRAS, 506, 2659, doi: 10.1093/mnras/stab1823

Fang, T., Buote, D., Bullock, J., & Ma, R. 2015, ApJSupplement Series, 217, 21, doi: 10.1088/0067-0049/217/2/21

Farber, R., Ruszkowski, M., Yang, H.-Y. K., & Zweibel, E. G. 2018, The Astrophysical Journal, 856, 112, doi: 10.3847/1538-4357/aab26d

Faridani, S., Flöer, L., Kerp, J., & Westmeier, T. 2014, A&A, 563, A99, doi: 10.1051/0004-6361/201322654

Farina, E. P., Arrigoni-Battaia, F., Costa, T., et al. 2019, ApJ, 887, 196, doi: 10.3847/1538-4357/ab5847

Fasano, G., & Franceschini, A. 1987, Monthly Notices of the Royal Astronomical Society, 225, 155, doi: 10.1093/mnras/225.1.155

Fattahi, A., Deason, A. J., Frenk, C. S., et al. 2020, Monthly Notices of the Royal Astronomical Society, 497, 4459, doi: 10.1093/mnras/staa2221

Faucher-Giguère, C.-A. 2017, in Astrophysics and Space Science Library, Vol. 430, Gas Accretion onto Galaxies, ed. A. Fox & R. Davé, 271

Faucher-Giguère, C.-A. 2020, MNRAS, 493, 1614, doi: 10.1093/mnras/staa302

Faucher-Giguère, C.-A., Lidz, A., Zaldarriaga, M., & Hernquist, L. 2009, ApJ, 703, 1416, doi: 10.1088/0004-637X/703/2/1416

Faucher-Giguère, C.-A. 2017, Monthly Notices of the Royal Astronomical Society, 473, 3717, doi: 10.1093/mnras/stx2595

Feldmann, R., Faucher-Giguère, C.-A., & Kereš, D. 2019, The Astrophysical Journal Letters, 871, L21, doi: 10.3847/2041-8213/aafe80

Feldmann, R., Quataert, E., Hopkins, P. F., Faucher-Giguère, C.-A., & Kereš, D. 2017, MNRAS, 470, 1050, doi: 10.1093/mnras/stx1120

Feldmann, R., Quataert, E., Faucher-Giguère, C.-A., et al. 2022, arXiv e-prints, arXiv:2205.15325, doi: 10.48550/arXiv.2205.15325

Ferland, G. J., Chatzikos, M., Guzmán, F., et al. 2017, RMxAA, 53, 385. https://arxiv.org/abs/1705.10877

Fernandez-Figueroa, A., Lopez, S., Tejos, N., et al. 2022, MNRAS, 517, 2214, doi: 10.1093/mnras/stac2851

Ferrière, K. 2005, in The Magnetized Plasma in Galaxy Evolution, ed. K. T. Chyzy, K. Otmianowska-Mazur, M. Soida, & R.-J. Dettmar, 147–155

Ferrière, K. M. 2001, Reviews of Modern Physics, 73, 1031, doi: 10.1103/RevModPhys.73.1031

Field, G. B., Goldsmith, D. W., & Habing, H. J. 1969, ApJL, 155, L149, doi: 10.1086/180324

Fielding, D., Quataert, E., McCourt, M., & Thompson, T. A. 2017, MNRAS, 466, 3810

Fielding, D. B., & Bryan, G. L. 2022, ApJ, 924, 82, doi: 10.3847/1538-4357/ac2f41

Fielding, D. B., Ostriker, E. C., Bryan, G. L., & Jermyn, A. S. 2020, ApJL, 894, L24, doi: 10.3847/2041-8213/ab8d2c

Fielding, D. B., Tonnesen, S., DeFelippis, D., et al. 2020, ApJ, 903, 32, doi: 10.3847/1538-4357/abbc6d

Fillingham, S. P., Cooper, M. C., Pace, A. B., et al. 2016, MNRAS, 463, 1916

Fitts, A., Boylan-Kolchin, M., Elbert, O. D., et al. 2017, Monthly Notices of the Royal Astronomical Society, 471, 3547, doi: 10.1093/mnras/stx1757

Flores Velázquez, J. A., Gurvich, A. B., Faucher-Giguère, C.-A., et al. 2020, Monthly Notices of the Royal Astronomical Society, 501, 4812, doi: 10.1093/mnras/staa3893

Font, A. S., McCarthy, I. G., & Belokurov, V. 2021, Monthly Notices of the Royal Astronomical Society, 505, 783, doi: 10.1093/mnras/stab1332

Forbes, J. C., Krumholz, M. R., Burkert, A., & Dekel, A. 2014, MNRAS, 443, 168, doi: 10.1093/mnras/stu1142

Ford, A. B., Davé, R., Oppenheimer, B. D., et al. 2014, MNRAS, 444, 1260

Ford, A. B., Oppenheimer, B. D., Davé, R., et al. 2013, MNRAS, 432, 89, doi: 10.1093/mnras/stt393

Ford, G. P., Gear, W. K., Smith, M. W. L., et al. 2013, The Astrophysical Journal, 769, 55, doi: 10.1088/0004-637x/769/1/55

Forero-Romero, J. E., & González, R. 2015, ApJ, 799, 45

Forrest, B., Marsan, Z. C., Annunziatella, M., et al. 2020, ApJ, 903, 47, doi: 10.3847/1538-4357/abb819

Foucaud, S., Conselice, C. J., Hartley, W. G., et al. 2010, Monthly Notices of the Royal Astronomical Society, 406, 147, doi: 10.1111/j.1365-2966.2010.16682.x

Fox, A. J., Savage, B. D., & Wakker, B. P. 2006, ApJS, 165, 229, doi: 10.1086/504800

Fox, A. J., Wakker, B. P., Barger, K. A., et al. 2014, ApJ, 787, 147

Fraternali, F. 2008, Proceedings of the International Astronomical Union, 4, 255–262, doi: 10.1017/s1743921308027671

—. 2017, Gas Accretion via Condensation and Fountains (Cham: Springer International Publishing), 323–353. https://doi.org/10.1007/978-3-319-52512-9_14

Fraternali, F., & Binney, J. J. 2006, Monthly Notices of the Royal Astronomical Society, 366, 449, doi: 10.1111/j.1365-2966.2005.09816.x

Fraternali, F., Marasco, A., Marinacci, F., & Binney, J. 2013, ApJL, 764, L21, doi: 10.1088/2041-8205/764/2/L21

Frigo, M., & Balcells, M. 2017, Monthly Notices of the Royal Astronomical Society, 469, 2184, doi: 10.1093/mnras/stx875

Froning, C. S., & Green, J. C. 2009, Astrophysics and Space Science, 320, 181

Fu, H., Hennawi, J. F., Prochaska, J. X., et al. 2016, ApJ, 832, 52, doi: 10.3847/0004-637X/832/1/52

Fujimoto, S., Ouchi, M., Ferrara, A., et al. 2019, ApJ, 887, 107, doi: 10.3847/1538-4357/ab480f

Furlong, M., Bower, R. G., Theuns, T., et al. 2015, MNRAS, 450, 4486, doi: 10.1093/mnras/stv852

Gabor, J. M., Capelo, P. R., Volonteri, M., et al. 2016, A&A, 592, A62, doi: 10.1051/0004-6361/201527143

Gaia Collaboration, Brown, A. G. A., Vallenari, A., et al. 2018, A&A, 616, A1, doi: 10.1051/0004-6361/201833051

—. 2021, A&A, 649, A1, doi: 10.1051/0004-6361/202039657

Gao, L., Navarro, J. F., Frenk, C. S., et al. 2012, MNRAS, 425, 2169, doi: 10.1111/j.1365-2966.2012.21564.x

Gao, L., White, S. D. M., Jenkins, A., Stoehr, F., & Springel, V. 2004, Monthly Notices of the Royal Astronomical Society, 355, 819, doi: 10.1111/j.1365-2966.2004.08360.x

García, L. A., & Ryan-Weber, E. V. 2020, RMxAA, 56, 97, doi: 10.22201/ia.01851101p.2020.56.01.11

Garrison-Kimmel, S., Boylan-Kolchin, M., Bullock, J. S., & Kirby, E. N. 2014a, MNRAS, 444, 222

Garrison-Kimmel, S., Boylan-Kolchin, M., Bullock, J. S., & Lee, K. 2014b, MNRAS, 438, 2578

—. 2014c, Monthly Notices of the Royal Astronomical Society, 438, 2578, doi: 10.1093/mnras/stt2377

Garrison-Kimmel, S., Hopkins, P. F., Wetzel, A., et al. 2019a, MNRAS, 487, 1380

Garrison-Kimmel, S., Wetzel, A., Hopkins, P. F., et al. 2019b, MNRAS, 489, 4574

—. 2019c, Monthly Notices of the Royal Astronomical Society, 489, 4574, doi: 10.1093/mnras/stz2507

Garrison-Kimmel, S., Hopkins, P. F., Wetzel, A., et al. 2019, MNRAS, 487, 1380, doi: 10.1093/mnras/stz1317

Gatkine, P., Veilleux, S., & Cucchiara, A. 2019, ApJ, 884, 66

Gehren, T., Fried, J., Wehinger, P. A., & Wyckoff, S. 1984, ApJ, 278, 11, doi: 10.1086/161763

Genel, S., Vogelsberger, M., Nelson, D., et al. 2013, Monthly Notices of the Royal Astronomical Society, 435, 1426, doi: 10.1093/mnras/stt1383

Genel, S., Vogelsberger, M., Nelson, D., et al. 2013, MNRAS, 435, 1426, doi: 10.1093/mnras/stt1383

Genel, S., Vogelsberger, M., Springel, V., et al. 2014, Monthly Notices of the Royal Astronomical Society, 445, 175, doi: 10.1093/mnras/stu1654

Ghigna, S., Moore, B., Governato, F., et al. 1998, Monthly Notices of the Royal Astronomical Society, 300, 146, doi: 10.1046/j.1365-8711.1998.01918.x

Gingold, R. A., & Monaghan, J. J. 1977, MNRAS, 181, 375, doi: 10.1093/mnras/181.3.375

Ginolfi, M., Jones, G. C., Béthermin, M., et al. 2020, A&A, 643, A7, doi: 10.1051/0004-6361/202038284

Giovanelli, R., Haynes, M. P., Adams, E. A., et al. 2013, The Astronomical Journal, 146, 15

Girichidis, P., Naab, T., Hanasz, M., & Walch, S. 2018, Monthly Notices of the Royal Astronomical Society, 479, 3042, doi: 10.1093/mnras/sty1653

Gjergo, E., Granato, G. L., Murante, G., et al. 2018, Monthly Notices of the Royal Astronomical Society, 479, 2588, doi: 10.1093/mnras/sty1564

Gnedin, O. Y., Brown, W. R., Geller, M. J., & Kenyon, S. J. 2010, The Astrophysical Journal Letters, 720, L108, doi: 10.1088/2041-8205/720/1/L108

Gonçalves, T. S., Martin, D. C., Menéndez-Delmestre, K., Wyder, T. K., & Koekemoer, A. 2012, ApJ, 759, 67, doi: 10.1088/0004-637X/759/1/67

Górski, K. M., Hivon, E., Banday, A. J., et al. 2005, ApJ, 622, 759, doi: 10.1086/427976

Gottlöber, S., Hoffman, Y., & Yepes, G. 2010, in High Performance Computing in Science and Engineering, Garching/Munich 2009 (Springer), 309–322

Grand, R. J., Gómez, F. A., Marinacci, F., et al. 2017, MNRAS, 467, 179

Grand, R. J. J., Marinacci, F., Pakmor, R., et al. 2021, MNRAS, 507, 4953, doi: 10.1093/mnras/stab2492

Green, J. C., Froning, C. S., Osterman, S., et al. 2011, ApJ, 744, 60

Greene, J. E., Danieli, S., Carlsten, S., et al. 2022, arXiv e-prints, arXiv:2210.14237. https://arxiv.org/abs/2210.14237

Greenstein, J. L., & Schmidt, M. 1964, ApJ, 140, 1, doi: 10.1086/147889

Gronke, M., & Oh, S. P. 2018, MNRAS, 480, L111, doi: 10.1093/mnrasl/sly131

Gronke, M., & Oh, S. P. 2020, Monthly Notices of the Royal Astronomical Society: Letters, 494, L27, doi: 10.1093/mnrasl/slaa033

Gronke, M., Oh, S. P., Ji, S., & Norman, C. 2021, Monthly Notices of the Royal Astronomical Society, 511, 859, doi: 10.1093/mnras/stab3351

Guedes, J., Callegari, S., Madau, P., & Mayer, L. 2011, ApJ, 742, 76, doi: 10.1088/0004-637X/742/2/76

Gunn, J. E., & Gott, J. Richard, I. 1972a, ApJ, 176, 1, doi: 10.1086/151605

—. 1972b, ApJ, 176, 1, doi: 10.1086/151605

Guo, Q., White, S., Li, C., & Boylan-Kolchin, M. 2010, MNRAS, 404, 1111

Gupta, A., Mathur, S., Krongold, Y., Nicastro, F., & Galeazzi, M. 2012, ApJL, 756, L8

Gurvich, A. B., Faucher-Giguère, C.-A., Richings, A. J., et al. 2020, MNRAS, 498, 3664, doi: 10.1093/mnras/staa2578

Gutcke, T. A., Pakmor, R., Naab, T., & Springel, V. 2021, MNRAS, 501, 5597, doi: 10.1093/mnras/staa3875

Haardt, F., & Madau, P. 2012, ApJ, 746, 125, doi: 10.1088/0004-637X/746/2/125

Hadzhiyska, B., Eisenstein, D., Bose, S., Garrison, L. H., & Maksimova, N. 2021, Monthly Notices of the Royal Astronomical Society, 509, 501, doi: 10.1093/mnras/stab2980

Hafen, Z., Faucher-Giguère, C.-A., Anglés-Alcázar, D., et al. 2019, MNRAS, 488, 1248

—. 2020, MNRAS, 494, 3581

Hafen, Z., Stern, J., Bullock, J., et al. 2022, MNRAS, 514, 5056, doi: 10.1093/mnras/stac1603

Haffner, L. M., Reynolds, R. J., & Tufte, S. L. 2001, The Astrophysical Journal, 556, L33, doi: 10.1086/322867

Haislmaier, K. J., Tripp, T. M., Katz, N., et al. 2020, Monthly Notices of the Royal Astronomical Society, 502, 4993, doi: 10.1093/mnras/staa3544

Hammer, F., Yang, Y., Fouquet, S., et al. 2013, MNRAS, 431, 3543

Hani, M. H., Ellison, S. L., Sparre, M., et al. 2019, MNRAS, 488, 135–152, doi: 10.1093/mnras/stz1708

Hani, M. H., Gosain, H., Ellison, S. L., Patton, D. R., & Torrey, P. 2020, Monthly Notices of the Royal Astronomical Society, 493, 3716, doi: 10.1093/mnras/staa459

Hani, M. H., Sparre, M., Ellison, S. L., Torrey, P., & Vogelsberger, M. 2018, MNRAS, 475, 1160, doi: 10.1093/mnras/stx3252

Hausammann, L., Revaz, Y., & Jablonka, P. 2019, A&A, 624, A11, doi: 10.1051/0004-6361/201834871

Hayward, C. C., Behroozi, P. S., Somerville, R. S., et al. 2013, MNRAS, 434, 2572, doi: 10.1093/mnras/stt1202

Hayward, C. C., Narayanan, D., Kereš, D., et al. 2012, Monthly Notices of the Royal Astronomical Society, 428, 2529, doi: 10.1093/mnras/sts222

Hayward, C. C., Torrey, P., Springel, V., Hernquist, L., & Vogelsberger, M. 2014, Monthly Notices of the Royal Astronomical Society, 442, 1992, doi: 10.1093/mnras/stu957

Heckman, T., Borthakur, S., Wild, V., Schiminovich, D., & Bordoloi, R. 2017, ApJ, 846, 151, doi: 10.3847/1538-4357/aa80dc

Heitmann, K., White, M., Wagner, C., Habib, S., & Higdon, D. 2010, ApJ, 715, 104, doi: 10.1088/0004-637X/715/1/104

Hellwing, W. A., Frenk, C. S., Cautun, M., et al. 2016, MNRAS, 457, 3492, doi: 10.1093/mnras/stw214

Henley, D. B., Shelton, R. L., & Kwak, K. 2014, ApJ, 791, 41, doi: 10.1088/0004-637X/791/1/41

Hennawi, J. F., Prochaska, J. X., Cantalupo, S., & Arrigoni-Battaia, F. 2015, Science, 348, 779, doi: 10.1126/science.aaa5397

Henriques, B. M. B., White, S. D. M., Lilly, S. J., et al. 2019, Monthly Notices of the Royal Astronomical Society, 485, 3446, doi: 10.1093/mnras/stz577

Henry, A., Scarlata, C., Martin, C. L., & Erb, D. 2015, ApJ, 809, 19, doi: 10.1088/0004-637X/809/1/19

Herenz, P., Richter, P., Charlton, J. C., & Masiero, J. R. 2013, A&A, 550, A87, doi: 10.1051/0004-6361/201220531

Hernquist, L., Katz, N., Weinberg, D. H., & Miralda-Escudé, J. 1996, ApJL, 457, L51, doi: 10.1086/309899

Hockney, R. W., & Eastwood, J. W. 1981, Computer Simulation Using Particles (McGraw-Hill)

Hoffman, Y., & Ribak, E. 1991, ApJ, 380, L5

Hopkins, P. F., Butsky, I. S., & Ji, S. 2022a, arXiv e-prints, arXiv:2211.05811, doi: 10.48550/arXiv.2211.05811

Hopkins, P. F., Butsky, I. S., Panopoulou, G. V., et al. 2022b, MNRAS, 516, 3470, doi: 10.1093/mnras/stac1791

Hopkins, P. F., Chan, T. K., Ji, S., et al. 2020, Monthly Notices of the Royal Astronomical Society, 501, 3640, doi: 10.1093/mnras/staa3690

Hopkins, P. F., Hernquist, L., Cox, T. J., & Kereš, D. 2008, The Astrophysical Journal Supplement Series, 175, 356, doi: 10.1086/524362

Hopkins, P. F., Kereš, D., Oñorbe, J., et al. 2014, MNRAS, 445, 581, doi: 10.1093/mnras/stu1738

Hopkins, P. F., Wetzel, A., Kereš, D., et al. 2018, MNRAS, 480, 800, doi: 10.1093/mnras/sty1690

Hopkins, P. F., Wetzel, A., Kereš, D., et al. 2018, MNRAS, 480, 800

Hou, K.-C., Hirashita, H., Nagamine, K., Aoyama, S., & Shimizu, I. 2017, MNRAS, 469, 870, doi: 10.1093/mnras/stx877

Hoyle, F., & Burbidge, G. R. 1966, ApJ, 144, 534, doi: 10.1086/148635

Hsu, W. H., Putman, M. E., Heitsch, F., et al. 2011, AJ, 141, 57, doi: 10.1088/0004-6256/141/2/57

Huang, S., Ho, L. C., Peng, C. Y., Li, Z.-Y., & Barth, A. J. 2016, The Astrophysical Journal, 821, 114, doi: 10.3847/0004-637X/821/2/114

Hubble, E. P. 1929, ApJ, 69, 103, doi: 10.1086/143167

Hummels, C. B., Bryan, G. L., Smith, B. D., & Turk, M. J. 2013, MNRAS, 430, 1548

Hummels, C. B., Smith, B. D., & Silvia, D. W. 2017, ApJ, 847, 59, doi: 10.3847/1538-4357/aa7e2d

Hummels, C. B., Smith, B. D., Hopkins, P. F., et al. 2019, ApJ, 882, 156, doi: 10.3847/1538-4357/ab378f

Hummels, C. B., Smith, B. D., Hopkins, P. F., et al. 2019, ApJ, 882, 156, doi: 10.3847/1538-4357/ab378f

Hunt, L. K., Tortora, C., Ginolfi, M., & Schneider, R. 2020, A&A, 643, A180, doi: 10.1051/0004-6361/202039021

Hunt, R. 1975, MNRAS, 173, 465, doi: 10.1093/mnras/173.2.465

Huško, F., Lacey, C. G., Schaye, J., Schaller, M., & Nobels, F. S. J. 2022, Monthly Notices of the Royal Astronomical Society, 516, 3750, doi: 10.1093/mnras/stac2278

Ibata, R. A., Lewis, G. F., Conn, A. R., et al. 2013, Nature, 493, 62

Irodotou, D., Fragkoudi, F., Pakmor, R., et al. 2021, arXiv e-prints, arXiv:2110.11368. https://arxiv.org/abs/2110.11368

Janowiecki, S., Catinella, B., Cortese, L., et al. 2017, Monthly Notices of the Royal Astronomical Society, 466, 4795, doi: 10.1093/mnras/stx046

Jenkins, A., Frenk, C. S., Pearce, F. R., et al. 1998, ApJ, 499, 20, doi: 10.1086/305615

Jentschura, U. D., Kotochigova, S. A., Mohr, P. J., Taylor, B. N., et al. 2005, Energy Levels of Hydrogen and Deuterium

Ji, S., Chan, T., Hummels, C. B., et al. 2020, MNRAS, 496, 4221

Jiang, Y.-F., & Oh, S. P. 2018, ApJ, 854, 5, doi: 10.3847/1538-4357/aaa6ce

jie Peng, Y., Lilly, S. J., Kovač, K., et al. 2010, The Astrophysical Journal, 721, 193, doi: 10.1088/0004-637X/721/1/193

Jing, Y. P. 2002, MNRAS, 335, L89, doi: 10.1046/j.1365-8711.2002.05899.x

Johnson, S. D., Chen, H.-W., & Mulchaey, J. S. 2015, MNRAS, 449, 3263

Johnson, S. D., Chen, H.-W., Mulchaey, J. S., Schaye, J., & Straka, L. A. 2017, The Astrophysical Journal Letters, 850, L10, doi: 10.3847/2041-8213/aa9370

Johnson, W., & Soff, G. 1985, Atomic Data and Nuclear Data Tables, 33, 405, doi: https://doi.org/10.1016/0092-640X(85)90010-5

Joshi, G. D., Pillepich, A., Nelson, D., et al. 2021, Monthly Notices of the Royal Astronomical Society, 508, 1652, doi: 10.1093/mnras/stab2573

Kaaret, P., Koutroumpa, D., Kuntz, K. D., et al. 2020, Nature Astronomy, 4, 1072, doi: 10.1038/s41550-020-01215-w

Kacprzak, G. G., Churchill, C. W., & Nielsen, N. M. 2012, ApJL, 760, L7, doi: 10.1088/2041-8205/760/1/L7

Kanjilal, V., Dutta, A., & Sharma, P. 2021, MNRAS, 501, 1143, doi: 10.1093/mnras/staa3610

Kannan, R., Garaldi, E., Smith, A., et al. 2022, MNRAS, 511, 4005, doi: 10.1093/mnras/stab3710

Kannan, R., Springel, V., Pakmor, R., Marinacci, F., & Vogelsberger, M. 2016, MNRAS, 458, 410, doi: 10.1093/mnras/stw294

Kant, I. 1755, Allgemeine Naturgeschichte und Theorie des Himmels, nach Newtonischen Grundsätzen abgehandelt (Petersen)

Karman, W., Macciò, A. V., Kannan, R., Moster, B. P., & Somerville, R. S. 2015, MNRAS, 452, 2984, doi: 10.1093/mnras/stv1508

Kartaltepe, J. S., Sanders, D. B., Scoville, N. Z., et al. 2007, ApJS, 172, 320, doi: 10.1086/519953

Karunakaran, A., Spekkens, K., Oman, K. A., et al. 2021, The Astrophysical Journal Letters, 916, L19, doi: 10.3847/2041-8213/ac0e3a

Karwin, C. M., Murgia, S., Campbell, S., & Moskalenko, I. V. 2019, The Astrophysical Journal, 880, 95, doi: 10.3847/1538-4357/ab2880

Katz, H. 2022, Monthly Notices of the Royal Astronomical Society, 512, 348, doi: 10.1093/mnras/stac423

Kaviraj, S., Devriendt, J., Dubois, Y., et al. 2015, Monthly Notices of the Royal Astronomical Society, 452, 2845, doi: 10.1093/mnras/stv1500

Kaviraj, S., Laigle, C., Kimm, T., et al. 2017, MNRAS, 467, 4739, doi: 10.1093/mnras/stx126

Kennicutt, Robert C., J. 1998, ApJ, 498, 541, doi: 10.1086/305588

Kereš, D., & Hernquist, L. 2009, ApJL, 700, L1, doi: 10.1088/0004-637X/700/1/L1

Kereš, D., Katz, N., Weinberg, D. H., & Davé, R. 2005, MNRAS, 363, 2, doi: 10.1111/j.1365-2966.2005.09451.x

Kereš, D., Vogelsberger, M., Sijacki, D., Springel, V., & Hernquist, L. 2012, MNRAS, 425, 2027, doi: 10.1111/j.1365-2966.2012.21548.x

Kereš, D., Katz, N., Fardal, M., Davé, R., & Weinberg, D. H. 2009, Monthly Notices of the Royal Astronomical Society, 395, 160, doi: 10.1111/j.1365-2966.2009.14541.x

Kerp, J., Mack, K. H., Egger, R., et al. 1996, A&A, 312, 67

Khandai, N., Di Matteo, T., Croft, R., et al. 2015, MNRAS, 450, 1349, doi: 10.1093/mnras/stv627

Khochfar, S., & Silk, J. 2006, The Astrophysical Journal, 648, L21, doi: 10.1086/507768

Khoperskov, S., Minchev, I., Libeskind, N., et al. 2022, arXiv e-prints, arXiv:2206.05491, doi: 10.48550/arXiv.2206.05491

Kim, C.-G., Ostriker, E. C., Somerville, R. S., et al. 2020, ApJ, 900, 61, doi: 10.3847/1538-4357/aba962

Kimble, R. A., Woodgate, B. E., Bowers, C. W., et al. 1998, The Astrophysical Journal, 492, L83, doi: 10.1086/311102

Klein, R. I., McKee, C. F., & Colella, P. 1994, ApJ, 420, 213, doi: 10.1086/173554

Kleiner, D., Pimbblet, K. A., Jones, D. H., Koribalski, B. S., & Serra, P. 2017, Monthly Notices of the Royal Astronomical Society, 466, 4692

Klypin, A., Kravtsov, A. V., Valenzuela, O., & Prada, F. 1999, ApJ, 522, 82

Klypin, A. A., & Shandarin, S. F. 1983, MNRAS, 204, 891, doi: 10.1093/mnras/204.3.891

Klypin, A. A., Trujillo-Gomez, S., & Primack, J. 2011, ApJ, 740, 102, doi: 10.1088/0004-637X/740/2/102

Knebe, A., Libeskind, N. I., Knollmann, S. R., et al. 2011, Monthly Notices of the Royal Astronomical Society, 412, 529, doi: 10.1111/j.1365-2966.2010.17924.x

Knollmann, S. R., & Knebe, A. 2009, ApJSupplement Series, 182, 608

Kolmogorov, A. 1933, Inst. Ital. Attuari, Giorn., 4, 83

Kolokythas, K., Vaddi, S., O'Sullivan, E., et al. 2022, MNRAS, 510, 4191, doi: 10.1093/mnras/stab3699

Kopenhafer, C., O'Shea, B. W., & Voit, G. M. 2022, arXiv e-prints, arXiv:2206.04706, doi: 10.48550/arXiv.2206.04706

Kormendy, J., & Ho, L. C. 2013, ARA&A, 51, 511, doi: 10.1146/annurev-astro-082708-101811

Kormendy, J., & Richstone, D. 1995, ARA&A, 33, 581, doi: 10.1146/annurev.aa.33.090195.003053

Kotera, K., & Olinto, A. V. 2011, ARA&A, 49, 119, doi: 10.1146/annurev-astro-081710-102620

Kourkchi, E., Tully, R. B., Eftekharzadeh, S., et al. 2020, ApJ, 902, 145, doi: 10.3847/1538-4357/abb66b

Kraljic, K., Arnouts, S., Pichon, C., et al. 2017, Monthly Notices of the Royal Astronomical Society, 474, 547, doi: 10.1093/mnras/stx2638

Kraljic, K., Pichon, C., Codis, S., et al. 2020, Monthly Notices of the Royal Astronomical Society, 491, 4294

Kravtsov, A. V., Klypin, A. A., & Khokhlov, A. M. 1997, ApJS, 111, 73, doi: 10.1086/313015

Krolik, J. H. 1999, Active galactic nuclei : from the central black hole to the galactic environment (Princeton University Press)

Kruijssen, J. M. D., Pelupessy, F. I., Lamers, H. J. G. L. M., et al. 2012, Monthly Notices of the Royal Astronomical Society, 421, 1927, doi: 10.1111/j.1365-2966.2012.20322.x

Krumholz, M. R., & Gnedin, N. Y. 2011, ApJ, 729, 36, doi: 10.1088/0004-637X/729/1/36

Kwak, K., Shelton, R. L., & Raley, E. A. 2009, ApJ, 699, 1775, doi: 10.1088/0004-637X/699/2/1775

Lan, T.-W., & Mo, H. 2018, ApJ, 866, 36, doi: 10.3847/1538-4357/aadc08

Langen, V., Cantalupo, S., Steidel, C. C., et al. 2023, MNRAS, 519, 5099, doi: 10.1093/mnras/stac3205

Lapi, A., Pantoni, L., Boco, L., & Danese, L. 2020, ApJ, 897, 81, doi: 10.3847/1538-4357/ab9812

Larson, R. B. 1972, Nature Physical Science, 236, 7, doi: 10.1038/physci236007a0

Larson, R. B., Tinsley, B. M., & Caldwell, C. N. 1980, ApJ, 237, 692, doi: 10.1086/157917

Lau, M. W., Prochaska, J. X., & Hennawi, J. F. 2016, The Astrophysical Journal Supplement Series, 226, 25

Leclercq, F., Bacon, R., Wisotzki, L., et al. 2017, A&A, 608, A8, doi: 10.1051/0004-6361/201731480

Leclercq, F., Bacon, R., Verhamme, A., et al. 2020, A&A, 635, A82, doi: 10.1051/0004-6361/201937339

Lehner, N., Howk, J. C., Marasco, A., & Fraternali, F. 2022, MNRAS, 513, 3228, doi: 10.1093/mnras/stac987

Lehner, N., Howk, J. C., Thom, C., et al. 2012, MNRAS, 424, 2896, doi: 10.1111/j.1365-2966.2012.21428.x

Lehner, N., Wotta, C. B., Howk, J. C., et al. 2018, ApJ, 866, 33, doi: 10.3847/1538-4357/aadd03

Lehner, N., Howk, J., Tripp, T., et al. 2013, ApJ, 770, 138

Lehner, N., Berek, S. C., Howk, J. C., et al. 2020, ApJ, 900, 9, doi: 10.3847/1538-4357/aba49c

Lehnert, M. D., Heckman, T. M., & Weaver, K. A. 1999, ApJ, 523, 575, doi: 10.1086/307762

Lehnert, M. D., van Driel, W., & Minchin, R. 2016, A&A, 590, A51, doi: 10.1051/0004-6361/201525743

Leitner, S. N., & Kravtsov, A. V. 2011, The Astrophysical Journal, 734, 48, doi: 10.1088/0004-637X/734/1/48

Leung, G. C. K., Coil, A. L., Rupke, D. S. N., & Perrotta, S. 2021, ApJ, 914, 17, doi: 10.3847/1538-4357/abf4da

Lewis, A. R., Dolphin, A. E., Dalcanton, J. J., et al. 2015, ApJ, 805, 183, doi: 10.1088/0004-637X/805/2/183

Li, C., Qiu, K., Hu, B., & Cao, Y. 2021a, ApJL, 918, L2, doi: 10.3847/2041-8213/ac19bc

Li, H., Wang, H., Mo, H. J., et al. 2022, arXiv e-prints, arXiv:2209.07711. https://arxiv.org/abs/2209.07711

Li, J., Emonts, B. H. C., Cai, Z., et al. 2021b, ApJL, 922, L29, doi: 10.3847/2041-8213/ac390d

Li, J.-T., Bregman, J. N., Wang, Q. D., Crain, R. A., & Anderson, M. E. 2018, The Astrophysical Journal Letters, 855, L24, doi: 10.3847/2041-8213/aab2af

Li, J.-T., Bregman, J. N., Wang, Q. D., et al. 2017, ApJS, 233, 20, doi: 10.3847/1538-4365/aa96fc

Li, M., & Tonnesen, S. 2020, ApJ, 898, 148

Li, Y., Bryan, G. L., & Quataert, E. 2019, ApJ, 887, 41, doi: 10.3847/1538-4357/ab4bca

Liang, C. J., & Chen, H.-W. 2014, Monthly Notices of the Royal Astronomical Society, 445, 2061, doi: 10.1093/mnras/stu1901

Liang, C. J., Kravtsov, A. V., & Agertz, O. 2018, MNRAS, 479, 1822, doi: 10.1093/mnras/sty1668

Liang, C. J., & Remming, I. 2019, Monthly Notices of the Royal Astronomical Society, 491, 5056, doi: 10.1093/mnras/stz3403

Liang, C. J., & Remming, I. 2020, MNRAS, 491, 5056, doi: 10.1093/mnras/stz3403

Libeskind, N. I., Knebe, A., Hoffman, Y., Gottlöber, S., & Yepes, G. 2011, Monthly Notices of the Royal Astronomical Society, 418, 336, doi: 10.1111/j.1365-2966.2011.19487.x

Libeskind, N. I., van de Weygaert, R., Cautun, M., et al. 2017, Monthly Notices of the Royal Astronomical Society, 473, 1195, doi: 10.1093/mnras/stx1976

Libeskind, N. I., Carlesi, E., Grand, R. J. J., et al. 2020, MNRAS, 498, 2968, doi: 10.1093/mnras/staa2541

Lin, L., Koo, D. C., Weiner, B. J., et al. 2007, The Astrophysical Journal, 660, L51, doi: 10.1086/517919

Lin, L., Patton, D. R., Koo, D. C., et al. 2008, ApJ, 681, 232, doi: 10.1086/587928

Lochhaas, C., Bryan, G. L., Li, Y., Li, M., & Fielding, D. 2020, Monthly Notices of the Royal Astronomical Society, 493, 1461, doi: 10.1093/mnras/staa358

Lochhaas, C., Tumlinson, J., Peeples, M. S., et al. 2022, arXiv e-prints, arXiv:2206.09925, doi: 10.48550/arXiv.2206.09925

Lockman, F. J., Benjamin, R. A., Pichette, N., & Thibodeau, C. 2023, ApJ, 943, 55, doi: 10.3847/1538-4357/aca764

Lockman, F. J., Murphy, E. M., Petty-Powell, S., & Urick, V. J. 2002, ApJS, 140, 331, doi: 10.1086/339371

Lofthouse, E. K., Fumagalli, M., Fossati, M., et al. 2020, MNRAS, 491, 2057, doi: 10.1093/mnras/stz3066

Lokhorst, D., Abraham, R., van Dokkum, P., Wijers, N., & Schaye, J. 2019, ApJ, 877, 4, doi: 10.3847/1538-4357/ab184e

Lotz, J. M., Jonsson, P., Cox, T. J., & Primack, J. R. 2008, Monthly Notices of the Royal Astronomical Society, 391, 1137, doi: 10.1111/j.1365-2966.2008.14004.x

Lovell, C. C., Vijayan, A. P., Thomas, P. A., et al. 2021, MNRAS, 500, 2127, doi: 10.1093/mnras/staa3360

Lovell, M. R., & Zavala, J. 2023, MNRAS, 520, 1567, doi: 10.1093/mnras/stad216

Lovell, M. R., Bose, S., Boyarsky, A., et al. 2017, MNRAS, 468, 4285

Lu, L.-Y., Li, J.-T., Vargas, C. J., et al. 2023, MNRAS, 519, 6098, doi: 10.1093/mnras/stad006

Lucchini, S., D'Onghia, E., Fox, A. J., et al. 2020, Nature, 585, 203. https://arxiv.org/abs/2009.04368

Lucy, L. B. 1977, AJ, 82, 1013, doi: 10.1086/112164

Mackenzie, R., Fumagalli, M., Theuns, T., et al. 2019, MNRAS, 487, 5070, doi: 10.1093/mnras/stz1501

Maksimova, N. A., Garrison, L. H., Eisenstein, D. J., et al. 2021, MNRAS, 508, 4017, doi: 10.1093/mnras/stab2484

Maller, A. H., & Bullock, J. S. 2004, Monthly Notices of the Royal Astronomical Society, 355, 694, doi: 10.1111/j.1365-2966.2004.08349.x

Maloney, P. R., & Putman, M. E. 2003, The Astrophysical Journal, 589, 270, doi: 10.1086/374547

Man, A., & Belli, S. 2018, Nature Astronomy, 2, 695, doi: 10.1038/s41550-018-0558-1

Mandelker, N., Nagai, D., Aung, H., et al. 2020, MNRAS, 494, 2641, doi: 10.1093/mnras/staa812

Marinacci, F., Pakmor, R., & Springel, V. 2013, Monthly Notices of the Royal Astronomical Society, 437, 1750, doi: 10.1093/mnras/stt2003

—. 2014, MNRAS, 437, 1750

Marinacci, F., Sales, L. V., Vogelsberger, M., Torrey, P., & Springel, V. 2019, MNRAS, 489, 4233, doi: 10.1093/mnras/stz2391

Marinacci, F., & Vogelsberger, M. 2016, MNRAS, 456, L69, doi: 10.1093/mnrasl/slv176

Marinacci, F., Vogelsberger, M., Pakmor, R., et al. 2018, Monthly Notices of the Royal Astronomical Society, 480, 5113, doi: 10.1093/mnras/sty2206

Marra, R., Churchill, C. W., Kacprzak, G. G., et al. 2022, arXiv preprint arXiv:2202.12228

Martig, M., & Bournaud, F. 2008, Monthly Notices of the Royal Astronomical Society: Letters, 385, L38, doi: 10.1111/j.1745-3933.2008.00429.x

Martig, M., Bournaud, F., Teyssier, R., & Dekel, A. 2009, The Astrophysical Journal, 707, 250, doi: 10.1088/0004-637X/707/1/250

Martin, C. L. 2006, ApJ, 647, 222, doi: 10.1086/504886

Martin, W. C., & Zalubas, R. 1983, Journal of Physical and Chemical Reference Data, 12, 323, doi: 10.1063/1.555685

Martín-Navarro, I., Pillepich, A., Nelson, D., et al. 2021, Nature, 594, 187, doi: 10.1038/s41586-021-03545-9

Marulli, F., Bolzonella, M., Branchini, E., et al. 2013, A&A, 557, A17, doi: 10.1051/0004-6361/201321476

Mastropietro, C., Moore, B., Mayer, L., Wadsley, J., & Stadel, J. 2005, MNRAS, 363, 509, doi: 10.1111/j.1365-2966.2005.09435.x

Matejek, M. S., & Simcoe, R. A. 2012, ApJ, 761, 112

Mathew, S. S., & Federrath, C. 2020, Monthly Notices of the Royal Astronomical Society, 496, 5201, doi: 10.1093/mnras/staa1931

Mathewson, D. S., Cleary, M. N., & Murray, J. D. 1974, ApJ, 190, 291, doi: 10.1086/152875

McAlpine, S., Helly, J. C., Schaller, M., et al. 2022, MNRAS, 512, 5823, doi: 10.1093/mnras/stac295

McCabe, T., Borthakur, S., Heckman, T., et al. 2021, ApJ, 923, 189, doi: 10.3847/1538-4357/ac283c

McClure-Griffiths, N. M., Dénes, H., Dickey, J. M., et al. 2018, Nature Astronomy, 2, 901, doi: 10.1038/s41550-018-0608-8

McConnachie, A. W. 2012, The Astronomical Journal, 144, 4, doi: 10.1088/0004-6256/144/1/4

McCourt, M., Oh, S. P., O'Leary, R., & Madigan, A.-M. 2017, Monthly Notices of the Royal Astronomical Society, 473, 5407, doi: 10.1093/mnras/stx2687

McCourt, M., Oh, S. P., O'Leary, R., & Madigan, A.-M. 2018, MNRAS, 473, 5407, doi: 10.1093/mnras/stx2687

McGaugh, S. S., Schombert, J. M., De Blok, W., & Zagursky, M. J. 2009, ApJL, 708, L14

McKee, C. F., & Williams, J. P. 1997, ApJ, 476, 144, doi: 10.1086/303587

McKinnon, R., Torrey, P., & Vogelsberger, M. 2016, MNRAS, 457, 3775, doi: 10.1093/mnras/stw253

McLeod, M., Libeskind, N., Lahav, O., & Hoffman, Y. 2017, Journal of Cosmology and Astroparticle Physics, 2017, 034

McPartland, C., Ebeling, H., Roediger, E., & Blumenthal, K. 2016, MNRAS, 455, 2994

Méndez-Hernández, H., Cassata, P., Ibar, E., et al. 2022, A&A, 666, A56, doi: 10.1051/0004-6361/202142553

Meneux, B., Guzzo, L., Garilli, B., et al. 2008, A&A, 478, 299, doi: 10.1051/0004-6361:20078182

Metuki, O., Libeskind, N. I., Hoffman, Y., Crain, R. A., & Theuns, T. 2015, MNRAS, 446, 1458

Mihos, J. C., & Hernquist, L. 1994, ApJL, 425, L13, doi: 10.1086/187299

—. 1996, ApJ, 464, 641, doi: 10.1086/177353

Miller, M. J., & Bregman, J. N. 2015, ApJ, 800, 14

Miniati, F. 2014, ApJ, 782, 21, doi: 10.1088/0004-637X/782/1/21

Mintz, A., Rafelski, M., Jorgenson, R. A., et al. 2022, AJ, 164, 51, doi: 10.3847/1538-3881/ac764d

Mitchell, P. D., Blaizot, J., Cadiou, C., et al. 2021, MNRAS, 501, 5757, doi: 10.1093/mnras/stab035

Monaghan, J. J. 1992, ARA&A, 30, 543, doi: 10.1146/annurev.aa.30.090192.002551

Moore, B., Ghigna, S., Governato, F., et al. 1999, ApJL, 524, L19, doi: 10.1086/312287

Moore, B., Katz, N., Lake, G., Dressler, A., & Oemler, A. 1996, Nature, 379, 613, doi: 10.1038/379613a0

Moos, H. W., Cash, W. C., Cowie, L. L., et al. 2000, ApJ, 538, L1–L6, doi: 10.1086/312795

Moran, E. C., Shahinyan, K., Sugarman, H. R., Vélez, D. O., & Eracleous, M. 2014, AJ, 148, 136, doi: 10.1088/0004-6256/148/6/136

Moreno, J., Torrey, P., Ellison, S. L., et al. 2019, Monthly Notices of the Royal Astronomical Society, 485, 1320, doi: 10.1093/mnras/stz417

Moster, B. P., Naab, T., & White, S. D. M. 2013, MNRAS, 428, 3121, doi: 10.1093/mnras/sts261

Müller, A., Poggianti, B. M., Pfrommer, C., et al. 2020, Nature Astronomy, doi: 10.1038/s41550-020-01234-7

Munch, G. 1952, Publications of the Astronomical Society of the Pacific, 64, 312, doi: 10.1086/126507

Münch, G., & Zirin, H. 1961, ApJ, 133, 11

Munshi, F., Governato, F., Brooks, A., et al. 2013, ApJ, 766, 56

Muratov, A. L., Kereš, D., Faucher-Giguère, C.-A., et al. 2015, MNRAS, 454, 2691

Muzahid, S., Fonseca, G., Roberts, A., et al. 2018, Monthly Notices of the Royal Astronomical Society, 476, 4965, doi: 10.1093/mnras/sty529

Muzahid, S., Schaye, J., Cantalupo, S., et al. 2021, MNRAS, 508, 5612, doi: 10.1093/mnras/stab2933

Naidoo, K., Hellwing, W., Bilicki, M., et al. 2022, arXiv e-prints, arXiv:2209.14386, doi: 10.48550/arXiv.2209.14386

Naiman, J. P., Pillepich, A., Springel, V., et al. 2018, MNRAS, 477, 1206, doi: 10.1093/mnras/sty618

Naiman, J. P., Pillepich, A., Springel, V., et al. 2018, Monthly Notices of the Royal Astronomical Society, 477, 1206, doi: 10.1093/mnras/sty618

Navarro, J. F., Frenk, C. S., & White, S. D. M. 1996, ApJ, 462, 563, doi: 10.1086/177173

—. 1997, ApJ, 490, 493, doi: 10.1086/304888

Navarro, J. F., Ludlow, A., Springel, V., et al. 2010, Monthly Notices of the Royal Astronomical Society, 402, 21, doi: 10.1111/j.1365-2966.2009.15878.x

Nelson, D., Vogelsberger, M., Genel, S., et al. 2013, MNRAS, 429, 3353, doi: 10.1093/mnras/sts595

Nelson, D., Pillepich, A., Springel, V., et al. 2017, Monthly Notices of the Royal Astronomical Society, 475, 624, doi: 10.1093/mnras/stx3040

Nelson, D., Springel, V., Pillepich, A., et al. 2019a, Computational Astrophysics and Cosmology, 6, 2, doi: 10.1186/s40668-019-0028-x

Nelson, D., Pillepich, A., Springel, V., et al. 2019b, MNRAS, 490, 3234, doi: 10.1093/mnras/stz2306

—. 2019c, MNRAS, 490, 3234, doi: 10.1093/mnras/stz2306

Nelson, D., Sharma, P., Pillepich, A., et al. 2020, MNRAS, 498, 2391, doi: 10.1093/mnras/staa2419

Newton, O., Di Cintio, A., Cardona-Barrero, S., et al. 2022, arXiv e-prints, arXiv:2212.05066, doi: 10.48550/arXiv.2212.05066

Nicastro, F., Senatore, F., Krongold, Y., Mathur, S., & Elvis, M. 2016, ApJL, 828, L12, doi: 10.3847/2041-8205/828/1/L12

Nielsen, N. M., Churchill, C. W., Kacprzak, G. G., & Murphy, M. T. 2013, ApJ, 776, 114, doi: 10.1088/0004-637x/776/2/114

Nielsen, N. M., Kacprzak, G. G., Sameer, et al. 2022, MNRAS, 514, 6074, doi: 10.1093/mnras/stac1824

Niemi, S.-M., Heinämäki, P., Nurmi, P., & Saar, E. 2010, Monthly Notices of the Royal Astronomical Society, 405, 477, doi: 10.1111/j.1365-2966.2010.16457.x

Nobels, F. S. J., Schaye, J., Schaller, M., Bahé, Y. M., & Chaikin, E. 2022, MNRAS, 515, 4838, doi: 10.1093/mnras/stac2061

Nuñez-Castiñeyra, A., Nezri, E., Devriendt, J., & Teyssier, R. 2021, MNRAS, 501, 62, doi: 10.1093/mnras/staa3233

Nuza, S. E., Dolag, K., & Saro, A. 2010, MNRAS, 407, 1376, doi: 10.1111/j.1365-2966.2010.16926.x

Nuza, S. E., Kitaura, F.-S., Heß, S., Libeskind, N. I., & Müller, V. 2014, MNRAS, 445, 988, doi: 10.1093/mnras/stu1746

Nuza, S. E., Parisi, F., Scannapieco, C., et al. 2014, MNRAS, 441, 2593

Nuza, S. E., Scannapieco, C., Chiappini, C., et al. 2019, MNRAS, 482, 3089, doi: 10.1093/mnras/sty2882

Nuza, S. E., Sánchez, A. G., Prada, F., et al. 2013, MNRAS, 432, 743, doi: 10.1093/mnras/stt513

Ocvirk, P., Gillet, N., Shapiro, P. R., et al. 2016, MNRAS, 463, 1462

Ocvirk, P., Aubert, D., Sorce, J. G., et al. 2020, Monthly Notices of the Royal Astronomical Society, 496, 4087, doi: 10.1093/mnras/staa1266

Okoshi, K., Minowa, Y., Kashikawa, N., et al. 2021, The Astronomical Journal, 162, 175, doi: 10.3847/1538-3881/ac0bbb

Oku, Y., Tomida, K., Nagamine, K., Shimizu, I., & Cen, R. 2022, ApJS, 262, 9, doi: 10.3847/1538-4365/ac77ff

Oppenheimer, B., Schaye, J., Crain, R., Werk, J., & Richings, A. 2017, MNRAS, 481, 835

Oppenheimer, B. D., & Davé, R. 2008, MNRAS, 387, 577

Oppenheimer, B. D., Davé, R., Kereš, D., et al. 2010, Monthly Notices of the Royal Astronomical Society, 406, 2325, doi: 10.1111/j.1365-2966.2010.16872.x

Oppenheimer, B. D., Schaye, J., Crain, R. A., Werk, J. K., & Richings, A. J. 2018a, Monthly Notices of the Royal Astronomical Society, 481, 835, doi: 10.1093/mnras/sty2281

—. 2018b, Monthly Notices of the Royal Astronomical Society, 481, 835

Oppenheimer, B. D., Crain, R. A., Schaye, J., et al. 2016, MNRAS, 460, 2157

Oppenheimer, B. D., Bogdán, Á., Crain, R. A., et al. 2020, ApJL, 893, L24, doi: 10.3847/2041-8213/ab846f

Orr, M. E., Hatchfield, H. P., Battersby, C., et al. 2021, ApJL, 908, L31, doi: 10.3847/2041-8213/abdebd

O'Sullivan, D. B., Martin, C., Matuszewski, M., et al. 2020, ApJ, 894, 3, doi: 10.3847/1538-4357/ab838c

Owers, M. S., Couch, W. J., Nulsen, P. E., & Randall, S. W. 2012, ApJL, 750, L23

Pacifici, C., Kassin, S. A., Weiner, B. J., et al. 2016, ApJ, 832, 79, doi: 10.3847/0004-637X/832/1/79

Pakmor, R., Bauer, A., & Springel, V. 2011, MNRAS, 418, 1392, doi: 10.1111/j.1365-2966.2011.19591.x

Pakmor, R., Guillet, T., Pfrommer, C., et al. 2018, MNRAS, 481, 4410, doi: 10.1093/mnras/sty2601

Pakmor, R., Pfrommer, C., Simpson, C. M., & Springel, V. 2016a, The Astrophysical Journal Letters, 824, L30, doi: 10.3847/2041-8205/824/2/L30

Pakmor, R., & Springel, V. 2013, MNRAS, 432, 176, doi: 10.1093/mnras/stt428

Pakmor, R., Springel, V., Bauer, A., et al. 2016b, MNRAS, 455, 1134

Pakmor, R., Gómez, F. A., Grand, R. J. J., et al. 2017, Monthly Notices of the Royal Astronomical Society, 469, 3185–3199, doi: 10.1093/mnras/stx1074

Pakmor, R., van de Voort, F., Bieri, R., et al. 2020, MNRAS, 498, 3125–3137, doi: 10.1093/mnras/staa2530

Pan, H.-A., Lin, L., Hsieh, B.-C., et al. 2018, The Astrophysical Journal, 868, 132, doi: 10.3847/1538-4357/aaeb92

Pandya, V., Fielding, D. B., Anglés-Alcázar, D., et al. 2021, MNRAS, 508, 2979, doi: 10.1093/mnras/stab2714

Pandya, V., Fielding, D. B., Bryan, G. L., et al. 2022, arXiv e-prints, arXiv:2211.09755. https://arxiv.org/abs/2211.09755

Park, G., Koo, B.-C., Kang, J.-h., et al. 2016, ApJL, 827, L27, doi: 10.3847/2041-8205/827/2/L27

Patel, E., Besla, G., Mandel, K., & Sohn, S. T. 2018, The Astrophysical Journal, 857, 78, doi: 10.3847/1538-4357/aab78f

Patton, D. R., Wilson, K. D., Metrow, C. J., et al. 2020, Monthly Notices of the Royal Astronomical Society, 494, 4969, doi: 10.1093/mnras/staa913

Pawlik, M. M., McAlpine, S., Trayford, J. W., et al. 2019, Nature Astronomy, 3, 440, doi: 10.1038/s41550-019-0725-z

Pawlowski, M. S., Ibata, R. A., & Bullock, J. S. 2017, ApJ, 850, 132

Pawlowski, M. S., & Kroupa, P. 2020, MNRAS, 491, 3042

Peacock, J. A. 1983, Monthly Notices of the Royal Astronomical Society, 202, 615, doi: 10.1093/mnras/202.3.615

Peebles, P. J. E. 1968, ApJ, 153, 1, doi: 10.1086/149628

Peek, J. E. G., Heiles, C., Putman, M. E., & Douglas, K. 2009, ApJ, 692, 827, doi: 10.1088/0004-637X/692/1/827

Peeples, M. S., Werk, J. K., Tumlinson, J., et al. 2014, ApJ, 786, 54

Peeples, M. S., Corlies, L., Tumlinson, J., et al. 2019, ApJ, 873, 129, doi: 10.3847/1538-4357/ab0654

Peng, Y., Maiolino, R., & Cochrane, R. 2015, Nature, 521, 192, doi: 10.1038/nature14439

Peterson, J. R., & Fabian, A. C. 2006, PhR, 427, 1, doi: 10.1016/j.physrep.2005.12.007

Pfleiderer, J. 1963, ZA, 58, 12

Pfleiderer, J., & Siedentopf, H. 1961, ZA, 51, 201

Pfrommer, C., Pakmor, R., Schaal, K., Simpson, C. M., & Springel, V. 2016, Monthly Notices of the Royal Astronomical Society, 465, 4500, doi: 10.1093/mnras/stw2941

Piffl, T., Binney, J., McMillan, P. J., et al. 2014, Monthly Notices of the Royal Astronomical Society, 445, 3133, doi: 10.1093/mnras/stu1948

Pillepich, A., Nelson, D., Hernquist, L., et al. 2017, Monthly Notices of the Royal Astronomical Society, 475, 648, doi: 10.1093/mnras/stx3112

Pillepich, A., Springel, V., Nelson, D., et al. 2018, MNRAS, 473, 4077, doi: 10.1093/mnras/stx2656

Pillepich, A., Nelson, D., Springel, V., et al. 2019, MNRAS, 490, 3196, doi: 10.1093/mnras/stz2338

Planck Collaboration, Ade, P. A. R., Aghanim, N., et al. 2014, A&A, 571, A16, doi: 10.1051/0004-6361/201321591

—. 2016, A&A, 594, A13, doi: 10.1051/0004-6361/201525830

Poggianti, B. M., Moretti, A., Gullieuszik, M., et al. 2017, ApJ, 844, 48, doi: 10.3847/1538-4357/aa78ed

Ponti, G., Sanders, J. S., Locatelli, N., et al. 2022, arXiv e-prints, arXiv:2211.02060. https://arxiv.org/abs/2211.02060

Posti, L., & Helmi, A. 2019, A&A, 621, A56, doi: 10.1051/0004-6361/201833355

Predehl, P., Sunyaev, R. A., Becker, W., et al. 2020, Nature, 588, 227, doi: 10.1038/s41586-020-2979-0

Price, D. J. 2012, Journal of Computational Physics, 231, 759, doi: 10.1016/j.jcp.2010.12.011

Price, D. J., & Monaghan, J. J. 2007, Monthly Notices of the Royal Astronomical Society, 374, 1347, doi: 10.1111/j.1365-2966.2006.11241.x

Privon, G. C., Barnes, J. E., Evans, A. S., et al. 2013, ApJ, 771, 120, doi: 10.1088/0004-637X/771/2/120

Prochaska, J. X., & Hennawi, J. F. 2008, The Astrophysical Journal, 690, 1558

Prochaska, J. X., Hennawi, J. F., & Simcoe, R. A. 2013, ApJL, 762, L19, doi: 10.1088/2041-8205/762/2/L19

Prochaska, J. X., Weiner, B., Chen, H. W., Cooksey, K. L., & Mulchaey, J. S. 2011, ApJS, 193, 28, doi: 10.1088/0067-0049/193/2/28

Prochaska, J. X., Bloom, J. S., Chen, H.-W., et al. 2004, ApJ, 611, 200

Prochaska, J. X., Werk, J. K., Worseck, G., et al. 2017, ApJ, 837, 169, doi: 10.3847/1538-4357/aa6007

Puchwein, E., Bolton, J. S., Haehnelt, M. G., et al. 2015, MNRAS, 450, 4081, doi: 10.1093/mnras/stv773

Puchwein, E., Bolton, J. S., Keating, L. C., et al. 2023, MNRAS, 519, 6162, doi: 10.1093/mnras/stac3761

Putman, M. E., Peek, J. E. G., & Joung, M. R. 2012, ARA&A, 50, 491, doi: 10.1146/annurev-astro-081811-125612

Putman, M. E., Saul, D. R., & Mets, E. 2011, MNRAS, 418, 1575, doi: 10.1111/j.1365-2966.2011.19524.x

Putman, M. E., Zheng, Y., Price-Whelan, A. M., et al. 2021, The Astrophysical Journal, 913, 53, doi: 10.3847/1538-4357/abe391

Putman, M. E., de Heij, V., Staveley-Smith, L., et al. 2002, The Astronomical Journal, 123, 873, doi: 10.1086/338088

Qu, Z., Chen, H.-W., Rudie, G. C., et al. 2022, MNRAS, 516, 4882, doi: 10.1093/mnras/stac2528

Quai, S., Hani, M. H., Ellison, S. L., Patton, D. R., & Woo, J. 2021, Monthly Notices of the Royal Astronomical Society, 504, 1888, doi: 10.1093/mnras/stab988

Rahmani, S., Lianou, S., & Barmby, P. 2016, Monthly Notices of the Royal Astronomical Society, 456, 4128, doi: 10.1093/mnras/stv2951

Rahmati, A., Schaye, J., Pawlik, A. H., & Raivcevic, M. 2013, MNRAS, 431, 2261

Ramesh, R., Nelson, D., & Pillepich, A. 2022, arXiv e-prints, arXiv:2211.00020. https://arxiv.org/abs/2211.00020

Rauch, M., Sargent, W. L. W., & Barlow, T. A. 1999, The Astrophysical Journal, 515, 500, doi: 10.1086/307060

Reed, D., Gardner, J., Quinn, T., et al. 2003, MNRAS, 346, 565, doi: 10.1046/j.1365-2966.2003.07113.x

Renaud, F., Agertz, O., Read, J. I., et al. 2021, Monthly Notices of the Royal Astronomical Society, 503, 5846, doi: 10.1093/mnras/stab250

Renaud, F., Bournaud, F., & Duc, P.-A. 2014, Monthly Notices of the Royal Astronomical Society, 446, 2038, doi: 10.1093/mnras/stu2208

Renaud, F., & Gieles, M. 2013, Monthly Notices of the Royal Astronomical Society: Letters, 431, L83, doi: 10.1093/mnrasl/slt013

Rey, M. P., Katz, H. B., Cameron, A. J., Devriendt, J., & Slyz, A. 2023, arXiv e-prints, arXiv:2302.08521, doi: 10.48550/arXiv.2302.08521

Rhodin, N. H. P., Agertz, O., Christensen, L., Renaud, F., & Fynbo, J. P. U. 2019, MNRAS, 488, 3634, doi: 10.1093/mnras/stz1479

Richter, P. 2020, ApJ, 892, 33, doi: 10.3847/1538-4357/ab7937

Richter, P., Charlton, J. C., Fangano, A. P. M., Bekhti, N. B., & Masiero, J. R. 2009, The Astrophysical Journal, 695, 1631, doi: 10.1088/0004-637x/695/2/1631

Richter, P., Fox, A. J., Wakker, B. P., et al. 2013, ApJ, 772, 111

Richter, P., Paerels, F. B. S., & Kaastra, J. S. 2008, SSRv, 134, 25, doi: 10.1007/s11214-008-9325-4

Richter, P., Sembach, K., & Howk, J. 2003, Astronomy & Astrophysics, 405, 1013

Richter, P., Sembach, K. R., Wakker, B. P., & Savage, B. D. 2001a, The Astrophysical Journal, 562, L181, doi: 10.1086/338050

Richter, P., Sembach, K. R., Wakker, B. P., et al. 2001b, ApJ, 559, 318

Richter, P., Wakker, B. P., Fechner, C., et al. 2016, A&A, 590, A68, doi: 10.1051/0004-6361/201527038

Richter, P., Westmeier, T., & Brüns, C. 2005, A&A, 442, L49, doi: 10.1051/0004-6361:200500182

Richter, P., Nuza, S. E., Fox, A. J., et al. 2017, A&A, 607, A48, doi: 10.1051/0004-6361/201630081

Rodriguez-Gomez, V., Genel, S., Vogelsberger, M., et al. 2015, MNRAS, 449, 49, doi: 10.1093/mnras/stv264

Rodriguez-Gomez, V., Sales, L. V., Genel, S., et al. 2017, Monthly Notices of the Royal Astronomical Society, 467, 3083

Röhser, T., Kerp, J., Lenz, D., & Winkel, B. 2016, A&A, 596, A94, doi: 10.1051/0004-6361/201629141

Romano, M., Cassata, P., Morselli, L., et al. 2021, A&A, 653, A111, doi: 10.1051/0004-6361/202141306

Rosdahl, J., Schaye, J., Teyssier, R., & Agertz, O. 2015, MNRAS, 451, 34, doi: 10.1093/mnras/stv937

Röttgers, B., Naab, T., Cernetic, M., et al. 2020, MNRAS, 496, 152, doi: 10.1093/mnras/staa1490

Rubin, K. H., Diamond-Stanic, A. M., Coil, A. L., Crighton, N. H., & Moustakas, J. 2018, ApJ, 853, 95

Rubin, K. H. R., Prochaska, J. X., Koo, D. C., & Phillips, A. C. 2012, ApJL, 747, L26, doi: 10.1088/2041-8205/747/2/L26

Rubin, K. H. R., Prochaska, J. X., Koo, D. C., & Phillips, A. C. 2012, The Astrophysical Journal Letters, 747, L26, doi: 10.1088/2041-8205/747/2/L26

Rudie, G. C., Steidel, C. C., Trainor, R. F., et al. 2012, ApJ, 750, 67, doi: 10.1088/0004-637X/750/1/67

Rupke, D. S., Coil, A., Geach, J. E., et al. 2019, Nature, 574, 643

Ruszkowski, M., Yang, H. Y. K., & Zweibel, E. 2017, ApJ, 834, 208, doi: 10.3847/1538-4357/834/2/208

Salem, M., Besla, G., Bryan, G., et al. 2015a, The Astrophysical Journal, 815, 77, doi: 10.1088/0004-637x/815/1/77

—. 2015b, The Astrophysical Journal, 815, 77, doi: 10.1088/0004-637X/815/1/77

Salem, M., Bryan, G. L., & Corlies, L. 2016, MNRAS, 456, 582

Salem, M., Bryan, G. L., & Hummels, C. 2014, The Astrophysical Journal, 797, L18, doi: 10.1088/2041-8205/797/2/l18

Salpeter, E. E. 1959, ApJ, 129, 608, doi: 10.1086/146660

Sameer, Charlton, J. C., Norris, J. M., et al. 2021, MNRAS, 501, 2112, doi: 10.1093/mnras/staa3754

Sameer, Charlton, J. C., Kacprzak, G. G., et al. 2022, MNRAS, 510, 5796, doi: 10.1093/mnras/stac052

Samuel, J., Wetzel, A., Chapman, S., et al. 2021, MNRAS, 504, 1379, doi: 10.1093/mnras/stab955

Samuel, J., Wetzel, A., Santistevan, I., et al. 2022, MNRAS, 514, 5276, doi: 10.1093/mnras/stac1706

Samuel, J., Wetzel, A., Tollerud, E., et al. 2020, MNRAS, 491, 1471

Sanchez, N. N., Bellovary, J. M., Holley-Bockelmann, K., et al. 2018, The Astrophysical Journal, 860, 20, doi: 10.3847/1538-4357/aac015

Sancisi, R., Fraternali, F., Oosterloo, T., & van der Hulst, T. 2008, A&A Rv, 15, 189, doi: 10.1007/s00159-008-0010-0

Sanders, D. B., & Mirabel, I. F. 1996, Annual Review of Astronomy and Astrophysics, 34, 749, doi: 10.1146/annurev.astro.34.1.749

Sanders, N. E., Caldwell, N., McDowell, J., & Harding, P. 2012, ApJ, 758, 133, doi: 10.1088/0004-637X/758/2/133

Sardone, A., Pisano, D. J., Pingel, N. M., et al. 2021, ApJ, 910, 69, doi: 10.3847/1538-4357/abde45

Sargent, W. L. W., Young, P. J., Boksenberg, A., & Tytler, D. 1980, ApJS, 42, 41, doi: 10.1086/190644

Savage, B., Sembach, K., Wakker, B., et al. 2003, ApJSupplement Series, 146, 125

Savage, B. D., Sembach, K. R., Jenkins, E. B., et al. 2000, ApJ, 538, L27, doi: 10.1086/312792

Savorgnan, G. A. D., Graham, A. W., Marconi, A., & Sani, E. 2016, ApJ, 817, 21, doi: 10.3847/0004-637X/817/1/21

Sawala, T., McAlpine, S., Jasche, J., et al. 2022, MNRAS, 509, 1432, doi: 10.1093/mnras/stab2684

Sawala, T., Frenk, C. S., Fattahi, A., et al. 2016, MNRAS, 457, 1931

Scannapieco, C., Creasey, P., Nuza, S. E., et al. 2015, A&A, 577, A3, doi: 10.1051/0004-6361/201425494

Schawinski, K., Dowlin, N., Thomas, D., Urry, C. M., & Edmondson, E. 2010, The Astrophysical Journal Letters, 714, L108, doi: 10.1088/2041-8205/714/1/L108

Schaye, J., Crain, R. A., Bower, R. G., et al. 2015, MNRAS, 446, 521

Schiavi, Riccardo, Capuzzo-Dolcetta, Roberto, Arca-Sedda, Manuel, & Spera, Mario. 2020, A&A, 642, A30, doi: 10.1051/0004-6361/202038674

Schiminovich, D., Catinella, B., Kauffmann, G., et al. 2010, MNRAS, 408, 919

Schmidt, M. 1959, ApJ, 129, 243, doi: 10.1086/146614

—. 1963, Nature, 197, 1040, doi: 10.1038/1971040a0

Schneider, A. 2015, Monthly Notices of the Royal Astronomical Society, 451, 3117, doi: 10.1093/mnras/stv1169

Schneider, E. E., & Robertson, B. E. 2018, ApJ, 860, 135, doi: 10.3847/1538-4357/aac329

Scholtz, J., Maiolino, R., Jones, G. C., & Carniani, S. 2023, MNRAS, 519, 5246, doi: 10.1093/mnras/stac3787

Sembach, K., Wakker, B., Savage, B., et al. 2003, ApJSupplement Series, 146, 165

Sembach, K. R., Savage, B. D., Shull, J. M., et al. 2000, ApJ, 538, L31, doi: 10.1086/312785

Shaban, A., Bordoloi, R., Chisholm, J., et al. 2022, ApJ, 936, 77, doi: 10.3847/1538-4357/ac7c65

Sharma, P., Colella, P., & Martin, D. F. 2010, SIAM Journal on Scientific Computing, 32, 3564, doi: 10.1137/100792135

Sharma, P., & Hammett, G. W. 2007, Journal of Computational Physics, 227, 123, doi: 10.1016/j.jcp.2007.07.026

Shen, S., Mo, H. J., White, S. D. M., et al. 2003, Monthly Notices of the Royal Astronomical Society, 343, 978, doi: 10.1046/j.1365-8711.2003.06740.x

Sheth, R. K., & Tormen, G. 2002, Monthly Notices of the Royal Astronomical Society, 329, 61, doi: 10.1046/j.1365-8711.2002.04950.x

Shields, J. C., Walcher, C. J., Böker, T., et al. 2008, ApJ, 682, 104, doi: 10.1086/589680

Shull, J. M., Jones, J. R., Danforth, C. W., & Collins, J. A. 2009, The Astrophysical Journal, 699, 754, doi: 10.1088/0004-637X/699/1/754

Sick, J., Courteau, S., Cuillandre, J.-C., et al. 2015, Galaxy Masses as Constraints of Formation Models, 311, 82

Sijacki, D., Springel, V., Di Matteo, T., & Hernquist, L. 2007, MNRAS, 380, 877, doi: 10.1111/j.1365-2966.2007.12153.x

Sijacki, D., Vogelsberger, M., Genel, S., et al. 2015, Monthly Notices of the Royal Astronomical Society, 452, 575, doi: 10.1093/mnras/stv1340

Simons, R. C., Peeples, M. S., Tumlinson, J., et al. 2020, The Astrophysical Journal, 905, 167, doi: 10.3847/1538-4357/abc5b8

Simpson, C. M., Grand, R. J., Gómez, F. A., et al. 2018, MNRAS, 478, 548

Simpson, C. M., Pakmor, R., Marinacci, F., et al. 2016, The Astrophysical Journal, 827, L29, doi: 10.3847/2041-8205/827/2/l29

Skillman, S. W., Warren, M. S., Turk, M. J., et al. 2014, arXiv e-prints, arXiv:1407.2600, doi: 10.48550/arXiv.1407.2600

Smailagić, M., Prochaska, J. X., Burchett, J., Zhu, G., & Ménard, B. 2018, ApJ, 867, 106, doi: 10.3847/1538-4357/aae384

Smart, B. M., Haffner, L. M., Barger, K. A., Hill, A., & Madsen, G. 2019, ApJ, 887, 16, doi: 10.3847/1538-4357/ab4d58

Smirnov, N. 1948, The Annals of Mathematical Statistics, 19, 279 , doi: 10.1214/aoms/1177730256

Smith, B. J., Struck, C., Hancock, M., et al. 2007, The Astronomical Journal, 133, 791, doi: 10.1086/510350

Smith, M. C., Sijacki, D., & Shen, S. 2019, MNRAS, 485, 3317, doi: 10.1093/mnras/stz599

Smith, M. C., Fielding, D. B., Bryan, G. L., et al. 2023, arXiv e-prints, arXiv:2301.07116, doi: 10.48550/arXiv.2301.07116

Smith, R., Shinn, J.-H., Tonnesen, S., et al. 2022, ApJ, 934, 86, doi: 10.3847/1538-4357/ac7ab5

Smith, R. J., Lucey, J. R., Hammer, D., et al. 2010, MNRAS, 408, 1417

Snyder, G. F., Cox, T. J., Hayward, C. C., Hernquist, L., & Jonsson, P. 2011, ApJ, 741, 77, doi: 10.1088/0004-637X/741/2/77

Snyder, G. F., Lotz, J. M., Rodriguez-Gomez, V., et al. 2017, MNRAS, 468, 207, doi: 10.1093/mnras/stx487

Solimano, M., González-López, J., Aravena, M., et al. 2022, ApJ, 935, 17, doi: 10.3847/1538-4357/ac7c1a

Somerville, R. S., & Davé, R. 2015, Annual Review of Astronomy and Astrophysics, 53, 51

Somerville, R. S., Hopkins, P. F., Cox, T. J., Robertson, B. E., & Hernquist, L. 2008, MNRAS, 391, 481, doi: 10.1111/j.1365-2966.2008.13805.x

Somerville, R. S., Popping, G., & Trager, S. C. 2015, MNRAS, 453, 4337, doi: 10.1093/mnras/stv1877

Sorce, J. G. 2015, Monthly Notices of the Royal Astronomical Society, 450, 2644, doi: 10.1093/mnras/stv760

Sorce, J. G., Courtois, H. M., Gottlöber, S., Hoffman, Y., & Tully, R. B. 2013, Monthly Notices of the Royal Astronomical Society, 437, 3586, doi: 10.1093/mnras/stt2153

Sorce, J. G., Gottlöber, S., Yepes, G., et al. 2015, MNRAS, 455, 2078, doi: 10.1093/mnras/stv2407

Sparre, M., Hayward, C. C., Feldmann, R., et al. 2017, MNRAS, 466, 88, doi: 10.1093/mnras/stw3011

Sparre, M., Pfrommer, C., & Ehlert, K. 2020, MNRAS, 499, 4261, doi: 10.1093/mnras/staa3177

Sparre, M., Pfrommer, C., & Vogelsberger, M. 2018, Monthly Notices of the Royal Astronomical Society, 482, 5401, doi: 10.1093/mnras/sty3063

Sparre, M., Pfrommer, C., & Vogelsberger, M. 2019, MNRAS, 482, 5401, doi: 10.1093/mnras/sty3063

Sparre, M., & Springel, V. 2016, Monthly Notices of the Royal Astronomical Society, 462, 2418, doi: 10.1093/mnras/stw1793

Sparre, M., & Springel, V. 2016, MNRAS, 462, 2418, doi: 10.1093/mnras/stw1793

Sparre, M., & Springel, V. 2017, Monthly Notices of the Royal Astronomical Society, 470, 3946, doi: 10.1093/mnras/stx1516

Sparre, M., Hayward, C. C., Springel, V., et al. 2015, MNRAS, 447, 3548, doi: 10.1093/mnras/stu2713

Speagle, J. S., Steinhardt, C. L., Capak, P. L., & Silverman, J. D. 2014, ApJS, 214, 15, doi: 10.1088/0067-0049/214/2/15

Spekkens, K., Urbancic, N., Mason, B. S., Willman, B., & Aguirre, J. E. 2014, ApJL, 795, L5

Spilker, J. S., Suess, K. A., Setton, D. J., et al. 2022, ApJL, 936, L11, doi: 10.3847/2041-8213/ac75ea

Spitzer Jr, L. 1956, ApJ, 124, 20

Springel, V. 2005, MNRAS, 364, 1105, doi: 10.1111/j.1365-2966.2005.09655.x

Springel, V. 2010, MNRAS, 401, 791

Springel, V. 2010, ARA&A, 48, 391, doi: 10.1146/annurev-astro-081309-130914

Springel, V., Di Matteo, T., & Hernquist, L. 2005a, MNRAS, 361, 776, doi: 10.1111/j.1365-2966.2005.09238.x

—. 2005b, MNRAS, 361, 776, doi: 10.1111/j.1365-2966.2005.09238.x

Springel, V., & Hernquist, L. 2003, MNRAS, 339, 289

—. 2005, The Astrophysical Journal, 622, L9, doi: 10.1086/429486

Springel, V., Pakmor, R., Zier, O., & Reinecke, M. 2021, MNRAS, 506, 2871, doi: 10.1093/mnras/stab1855

Springel, V., White, S. D. M., Tormen, G., & Kauffmann, G. 2001, MNRAS, 328, 726, doi: 10.1046/j.1365-8711.2001.04912.x

Springel, V., White, S. D. M., Jenkins, A., et al. 2005c, Nature, 435, 629, doi: 10.1038/nature03597

Springel, V., Wang, J., Vogelsberger, M., et al. 2008, MNRAS, 391, 1685, doi: 10.1111/j.1365-2966.2008.14066.x

Springel, V., Pakmor, R., Pillepich, A., et al. 2018, MNRAS, 475, 676, doi: 10.1093/mnras/stx3304

Stadel, J., Potter, D., Moore, B., et al. 2009, Monthly Notices of the Royal Astronomical Society: Letters, 398, L21, doi: 10.1111/j.1745-3933.2009.00699.x

Stanimirović, S., Hoffman, S., Heiles, C., et al. 2008, ApJ, 680, 276, doi: 10.1086/587480

Steidel, C. C., Erb, D. K., Shapley, A. E., et al. 2010, ApJ, 717, 289, doi: 10.1088/0004-637X/717/1/289

Steinwandel, U. P., Kim, C.-G., Bryan, G. L., et al. 2022, arXiv e-prints, arXiv:2212.03898, doi: 10.48550/arXiv.2212.03898

Stern, J., Faucher-Giguère, C.-A., Hennawi, J. F., et al. 2018, The Astrophysical Journal, 865, 91, doi: 10.3847/1538-4357/aac884

Stern, J., Fielding, D., Faucher-Giguère, C.-A., & Quataert, E. 2019, Monthly Notices of the Royal Astronomical Society, 488, 2549, doi: 10.1093/mnras/stz1859

—. 2020, Monthly Notices of the Royal Astronomical Society, 492, 6042, doi: 10.1093/mnras/staa198

Stern, J., Hennawi, J. F., Prochaska, J. X., & Werk, J. K. 2016, ApJ, 830, 87, doi: 10.3847/0004-637X/830/2/87

Sternberg, A., McKee, C. F., & Wolfire, M. G. 2002, The Astrophysical Journal Supplement Series, 143, 419, doi: 10.1086/343032

Stierwalt, S., Besla, G., Patton, D., et al. 2015, The Astrophysical Journal, 805, 2, doi: 10.1088/0004-637X/805/1/2

Stinson, G., Seth, A., Katz, N., et al. 2006, MNRAS, 373, 1074, doi: 10.1111/j.1365-2966.2006.11097.x

Stinson, G. S., Brook, C., Macciò, A. V., et al. 2013, MNRAS, 428, 129, doi: 10.1093/mnras/sts028

Stocke, J. T., Keeney, B. A., Danforth, C. W., et al. 2013, ApJ, 763, 148

Strawn, C., Roca-Fàbrega, S., & Primack, J. 2022, Monthly Notices of the Royal Astronomical Society, 519, 1, doi: 10.1093/mnras/stac3567

Struck, C. 1999, PhR, 321, 1, doi: 10.1016/S0370-1573(99)00030-7

Su, K.-Y., Hopkins, P. F., Hayward, C. C., et al. 2019, Monthly Notices of the Royal Astronomical Society, 491, 1190, doi: 10.1093/mnras/stz3011

Suresh, J., Bird, S., Vogelsberger, M., et al. 2015, MNRAS, 448, 895

Suresh, J., Nelson, D., Genel, S., Rubin, K. H. R., & Hernquist, L. 2018, Monthly Notices of the Royal Astronomical Society, 483, 4040, doi: 10.1093/mnras/sty3402

Suresh, J., Nelson, D., Genel, S., Rubin, K. H. R., & Hernquist, L. 2019, MNRAS, 483, 4040, doi: 10.1093/mnras/sty3402

Suresh, J., Rubin, K. H. R., Kannan, R., et al. 2016, MNRAS, 465, 2966–2982, doi: 10.1093/mnras/stw2499

Sutherland, R. S., & Dopita, M. A. 1993, ApJS, 88, 253, doi: 10.1086/191823

Tabatabaei, F. S., & Berkhuijsen, E. M. 2010, A&A, 517, A77, doi: 10.1051/0004-6361/200913593

Talbot, Raymond J., J., & Arnett, W. D. 1971, ApJ, 170, 409, doi: 10.1086/151228

Tan, B., Oh, S. P., & Gronke, M. 2022, arXiv e-prints, arXiv:2210.06493. https://arxiv.org/abs/2210.06493

Tantalo, R., Chiosi, C., Bressan, A., Marigo, P., & Portinari, L. 1998, A&A, 335, 823, doi: 10.48550/arXiv.astro-ph/9710079

Tasker, E. J., Brunino, R., Mitchell, N. L., et al. 2008, MNRAS, 390, 1267, doi: 10.1111/j.1365-2966.2008.13836.x

Tchernyshyov, K., Werk, J. K., Wilde, M. C., et al. 2022, ApJ, 927, 147, doi: 10.3847/1538-4357/ac450c

Teyssier, R. 2002, A&A, 385, 337, doi: 10.1051/0004-6361:20011817

Teyssier, R., Pontzen, A., Dubois, Y., & Read, J. I. 2013, MNRAS, 429, 3068, doi: 10.1093/mnras/sts563

The LUVOIR Team. 2019, arXiv e-prints, arXiv:1912.06219, doi: 10.48550/arXiv.1912.06219

Thomas, T., & Pfrommer, C. 2019, MNRAS, 485, 2977

Thompson, T. A., Quataert, E., Zhang, D., & Weinberg, D. H. 2016, MNRAS, 455, 1830, doi: 10.1093/mnras/stv2428

Thorp, M. D., Ellison, S. L., Simard, L., Sánchez, S. F., & Antonio, B. 2018, Monthly Notices of the Royal Astronomical Society: Letters, 482, L55, doi: 10.1093/mnrasl/sly185

Tibaldo, L., Digel, S. W., Casandjian, J. M., et al. 2015, The Astrophysical Journal, 807, 161, doi: 10.1088/0004-637X/807/2/161

Tielens, A. G. G. M. 2005, The Physics and Chemistry of the Interstellar Medium (Cambridge University Press)

Tinker, J., Kravtsov, A. V., Klypin, A., et al. 2008, The Astrophysical Journal, 688, 709, doi: 10.1086/591439

Tinsley, B. M. 1974, ApJ, 192, 629, doi: 10.1086/153099

Tolstoy, E., Hill, V., & Tosi, M. 2009, Annual Review of Astronomy and Astrophysics, 47, 371

Tonnesen, S., & Bryan, G. L. 2021, ApJ, 911, 68, doi: 10.3847/1538-4357/abe7e2

Toomre, A., & Toomre, J. 1972, ApJ, 178, 623, doi: 10.1086/151823

Torrey, P., Vogelsberger, M., Genel, S., et al. 2014a, MNRAS, 438, 1985, doi: 10.1093/mnras/stt2295

—. 2014b, MNRAS, 438, 1985, doi: 10.1093/mnras/stt2295

Torrey, P., Vogelsberger, M., Marinacci, F., et al. 2019, Monthly Notices of the Royal Astronomical Society, 484, 5587, doi: 10.1093/mnras/stz243

Travascio, A., Zappacosta, L., Cantalupo, S., et al. 2020, A&A, 635, A157, doi: 10.1051/0004-6361/201936197

Trayford, J. W., Theuns, T., Bower, R. G., et al. 2015, Monthly Notices of the Royal Astronomical Society, 452, 2879, doi: 10.1093/mnras/stv1461

Tremmel, M., Karcher, M., Governato, F., et al. 2017, MNRAS, 470, 1121, doi: 10.1093/mnras/stx1160

Tremmel, M., Quinn, T. R., Ricarte, A., et al. 2018, Monthly Notices of the Royal Astronomical Society, 483, 3336, doi: 10.1093/mnras/sty3336

Tremonti, C. A., Heckman, T. M., Kauffmann, G., et al. 2004, ApJ, 613, 898, doi: 10.1086/423264

Tripp, T. M., Sembach, K. R., Bowen, D. V., et al. 2008, ApJSupplement Series, 177, 39

Tripp, T. M., Meiring, J. D., Prochaska, J. X., et al. 2011, Science, 334, 952, doi: 10.1126/science.1209850

Tufte, S. L., Reynolds, R. J., & Haffner, L. M. 1998, The Astrophysical Journal, 504, 773, doi: 10.1086/306103

Tully, R. B., Courtois, H. M., & Sorce, J. G. 2016, AJ, 152, 50, doi: 10.3847/0004-6256/152/2/50

Tully, R. B., Courtois, H. M., Dolphin, A. E., et al. 2013, The Astronomical Journal, 146, 86

Tully, R. B., Kourkchi, E., Courtois, H. M., et al. 2023, ApJ, 944, 94, doi: 10.3847/1538-4357/ac94d8

Tumlinson, J., Peeples, M. S., & Werk, J. K. 2017, ARA&A, 55, 389, doi: 10.1146/annurev-astro-091916-055240

Tumlinson, J., Thom, C., Werk, J. K., et al. 2011, Science, 334, 948

—. 2013a, ApJ, 777, 59

—. 2013b, ApJ, 777, 59, doi: 10.1088/0004-637x/777/1/59

Tuominen, T., Nevalainen, J., Tempel, E., et al. 2021, A&A, 646, A156, doi: 10.1051/0004-6361/202039221

Turk, M. J., Smith, B. D., Oishi, J. S., et al. 2011, ApJS, 192, 9, doi: 10.1088/0067-0049/192/1/9

Turner, M. L., Schaye, J., Steidel, C. C., Rudie, G. C., & Strom, A. L. 2015, MNRAS, 450, 2067, doi: 10.1093/mnras/stv750

Turner, M. L., Schaye, J., Steidel, C. C., Rudie, G. C., & Strom, A. L. 2015, MNRAS, 450, 2067

Uhlig, M., Pfrommer, C., Sharma, M., et al. 2012, Monthly Notices of the Royal Astronomical Society, 423, 2374, doi: 10.1111/j.1365-2966.2012.21045.x

Valentini, M., Murante, G., Borgani, S., et al. 2017, MNRAS, 470, 3167, doi: 10.1093/mnras/stx1352

van de Voort, F., Springel, V., Mandelker, N., van den Bosch, F. C., & Pakmor, R. 2019, MNRAS, 482, L85, doi: 10.1093/mnrasl/sly190

van de Voort, F., Springel, V., Mandelker, N., van den Bosch, F. C., & Pakmor, R. 2019, MNRAS: Letters, 482, L85

Van Den Bosch, F. C., Aquino, D., Yang, X., et al. 2008, Monthly Notices of the Royal Astronomical Society, 387, 79, doi: 10.1111/j.1365-2966.2008.13230.x

Van der Marel, R. P., Fardal, M., Besla, G., et al. 2012, ApJ, 753, 8

van de Voort, F., Bieri, R., Pakmor, R., et al. 2021, Monthly Notices of the Royal Astronomical Society, 501, 4888, doi: 10.1093/mnras/staa3938

Vazza, F., Brunetti, G., Gheller, C., & Brunino, R. 2010, NewA, 15, 695, doi: 10.1016/j.newast.2010.05.003

Violino, G., Ellison, S. L., Sargent, M., et al. 2018, Monthly Notices of the Royal Astronomical Society, 476, 2591, doi: 10.1093/mnras/sty345

Vogelsberger, M., Genel, S., Sijacki, D., et al. 2013, MNRAS, 436, 3031

Vogelsberger, M., Marinacci, F., Torrey, P., & Puchwein, E. 2020, Nature Reviews Physics, 2, 42, doi: 10.1038/s42254-019-0127-2

Vogelsberger, M., Genel, S., Springel, V., et al. 2014a, Nature, 509, 177, doi: 10.1038/nature13316

—. 2014b, MNRAS, 444, 1518, doi: 10.1093/mnras/stu1536

—. 2014c, Nature, 509, 177, doi: 10.1038/nature13316

Voit, G. M. 2018, ApJ, 868, 102, doi: 10.3847/1538-4357/aae8e2

Voit, G. M., Donahue, M., Bryan, G. L., & McDonald, M. 2015, Nature, 519, 203, doi: 10.1038/nature14167

Vollmer, B., Braine, J., Mazzilli-Ciraulo, B., & Schneider, B. 2021, A&A, 647, A138, doi: 10.1051/0004-6361/202037887

Vollmer, B., Braine, J., & Soida, M. 2012, A&A, 547, A39, doi: 10.1051/0004-6361/201219668

Wadsley, J. W., Veeravalli, G., & Couchman, H. M. P. 2008, Monthly Notices of the Royal Astronomical Society, 387, 427, doi: 10.1111/j.1365-2966.2008.13260.x

Wagner, C. R., Courteau, S., Brodwin, M., et al. 2017, ApJ, 834, 53, doi: 10.3847/1538-4357/834/1/53

Wake, D. A., Whitaker, K. E., Labbé, I., et al. 2011, The Astrophysical Journal, 728, 46, doi: 10.1088/0004-637X/728/1/46

Wakker, B., Howk, J. C., Chu, Y.-H., Bomans, D., & Points, S. D. 1998, ApJL, 499, L87, doi: 10.1086/311334

Wakker, B., Savage, B., Sembach, K. e. . a., et al. 2003, ApJSupplement Series, 146, 1

Wakker, B. P., & van Woerden, H. 1991, A&A, 250, 509

—. 1997, ARA&A, 35, 217, doi: 10.1146/annurev.astro.35.1.217

Wakker, B. P., York, D. G., Wilhelm, R., et al. 2008, ApJ, 672, 298, doi: 10.1086/523845

Wakker, B. P., York, D. G., Howk, J. C., et al. 2007, ApJL, 670, L113, doi: 10.1086/524222

Wang, L., Dutton, A. A., Stinson, G. S., et al. 2015, MNRAS, 454, 83, doi: 10.1093/mnras/stv1937

Wang, L., Dutton, A. A., Stinson, G. S., et al. 2017, Monthly Notices of the Royal Astronomical Society, 466, 4858, doi: 10.1093/mnras/stx066

Wannier, P., & Wrixon, G. T. 1972, ApJL, 173, L119, doi: 10.1086/180930

Warren, M. S., Abazajian, K., Holz, D. E., & Teodoro, L. 2006, ApJ, 646, 881, doi: 10.1086/504962

Weigel, A. K., Schawinski, K., Caplar, N., et al. 2017, The Astrophysical Journal, 845, 145, doi: 10.3847/1538-4357/aa8097

Weinberger, R., & Hernquist, L. 2023, MNRAS, 519, 3011, doi: 10.1093/mnras/stac3708

Weinberger, R., Springel, V., & Pakmor, R. 2020, ApJSupplement Series, 248, 32

Weinberger, R., Springel, V., Hernquist, L., et al. 2017, MNRAS, 465, 3291, doi: 10.1093/mnras/stw2944

Weinberger, R., Su, K.-Y., Ehlert, K., et al. 2022, arXiv e-prints, arXiv:2211.11771, doi: 10.48550/arXiv.2211.11771

Weisz, D. R., Dolphin, A. E., Skillman, E. D., et al. 2015, The Astrophysical Journal, 804, 136, doi: 10.1088/0004-637X/804/2/136

Werk, J. K., Prochaska, J. X., Thom, C., et al. 2013, ApJS, 204, 17, doi: 10.1088/0067-0049/204/2/17

Werk, J. K., Prochaska, J. X., Tumlinson, J., et al. 2014, ApJ, 792, 8

Werk, J. K., Prochaska, J. X., Cantalupo, S., et al. 2016a, The Astrophysical Journal, 833, 54

—. 2016b, The Astrophysical Journal, 833, 54, doi: 10.3847/1538-4357/833/1/54

Westmeier, T., Braun, R., & Thilker, D. 2005a, A&A, 436, 101, doi: 10.1051/0004-6361:20052867

Westmeier, T., Brüns, C., & Kerp, J. 2005b, A&A, 432, 937, doi: 10.1051/0004-6361:20041246

Westmeier, T., Staveley-Smith, L., Calabretta, M., et al. 2015, MNRAS, 453, 338

Wetzel, A. R., Deason, A. J., & Garrison-Kimmel, S. 2015, ApJ, 807, 49

Wetzel, A. R., Hopkins, P. F., Kim, J.-h., et al. 2016, ApJL, 827, L23

Whitaker, K. E., Van Dokkum, P. G., Brammer, G., & Franx, M. 2012, ApJL, 754, L29

White, S. D. M., & Frenk, C. S. 1991, ApJ, 379, 52, doi: 10.1086/170483

White, S. D. M., & Rees, M. J. 1978, MNRAS, 183, 341, doi: 10.1093/mnras/183.3.341

Whittingham, J., Sparre, M., Pfrommer, C., & Pakmor, R. 2021, Monthly Notices of the Royal Astronomical Society, 506, 229, doi: 10.1093/mnras/stab1425

Whittingham, J., Sparre, M., Pfrommer, C., & Pakmor, R. 2023, arXiv e-prints, arXiv:2301.13208, doi: 10.48550/arXiv.2301.13208

Wiersma, R. P. C., Schaye, J., Theuns, T., Dalla Vecchia, C., & Tornatore, L. 2009, MNRAS, 399, 574, doi: 10.1111/j.1365-2966.2009.15331.x

Wijers, N. A., Schaye, J., & Oppenheimer, B. D. 2020, The warm-hot circumgalactic medium around EAGLE-simulation galaxies and its detection prospects with X-ray and UV line absorption. https://arxiv.org/abs/2004.05171

Wild, V., Walcher, C. J., Johansson, P. H., et al. 2009, MNRAS, 395, 144, doi: 10.1111/j.1365-2966.2009.14537.x

Wilde, M. C., Werk, J. K., Burchett, J. N., et al. 2021, ApJ, 912, 9, doi: 10.3847/1538-4357/abea14

Williams, B. F. 2003, The Astronomical Journal, 126, 1312

Winner, G., Pfrommer, C., Girichidis, P., & Pakmor, R. 2019, MNRAS, 488, 2235, doi: 10.1093/mnras/stz1792

Wise, J. H., Abel, T., Turk, M. J., Norman, M. L., & Smith, B. D. 2012, MNRAS, 427, 311, doi: 10.1111/j.1365-2966.2012.21809.x

Wolfire, M. G., Hollenbach, D., McKee, C. F., Tielens, A. G. G. M., & Bakes, E. L. O. 1995, ApJ, 443, 152, doi: 10.1086/175510

Woodgate, B. E., Kimble, R. A., Bowers, C. W., et al. 1998, Publications of the Astronomical Society of the Pacific, 110, 1183, doi: 10.1086/316243

Wotta, C. B., Lehner, N., Howk, J. C., O'Meara, J. M., & Prochaska, J. X. 2016, The Astrophysical Journal, 831, 95, doi: 10.3847/0004-637X/831/1/95

Wright, R. J., Lagos, C. d. P., Power, C., & Correa, C. A. 2021, MNRAS, 504, 5702, doi: 10.1093/mnras/stab1057

Wright, R. J., Lagos, C. d. P., Power, C., et al. 2022, MNRAS, 516, 2891, doi: 10.1093/mnras/stac2042

Yang, X., Mo, H. J., Jing, Y. P., van den Bosch, F. C., & Chu, Y. 2004, MNRAS, 350, 1153, doi: 10.1111/j.1365-2966.2004.07744.x

Yao, Y., Shull, J. M., Wang, Q. D., & Cash, W. 2012, ApJ, 746, 166, doi: 10.1088/0004-637X/746/2/166

Yeager, T., & Struck, C. 2020, The Astrophysical Journal, 905, 118, doi: 10.3847/1538-4357/abc82a

Yeh, J. Y. C., Smith, A., Kannan, R., et al. 2023, MNRAS, 520, 2757, doi: 10.1093/mnras/stad210

Yin, J., Hou, J. L., Prantzos, N., et al. 2009, A&A, 505, 497, doi: 10.1051/0004-6361/200912316

York, D. G., Khare, P., Vanden Berk, D., et al. 2006, MNRAS, 367, 945, doi: 10.1111/j.1365-2966.2005.10018.x

Yoshii, Y. 1981, A&A, 97, 280

Yung, L. Y. A., Somerville, R. S., Ferguson, H. C., et al. 2022, MNRAS, 515, 5416, doi: 10.1093/mnras/stac2139

Yıldırım, A., van den Bosch, R. C. E., van de Ven, G., et al. 2017, Monthly Notices of the Royal Astronomical Society, 468, 4216, doi: 10.1093/mnras/stx732

Zabl, J., Bouché, N. F., Wisotzki, L., et al. 2021, MNRAS, 507, 4294, doi: 10.1093/mnras/stab2165

Zahedy, F. S., Chen, H.-W., Johnson, S. D., et al. 2019, MNRAS, 484, 2257, doi: 10.1093/mnras/sty3482

Zahedy, F. S., Chen, H.-W., Cooper, T. M., et al. 2021, MNRAS, 506, 877, doi: 10.1093/mnras/stab1661

Zahid, H. J., Bresolin, F., Kewley, L. J., Coil, A. L., & Davé, R. 2012, The Astrophysical Journal, 750, 120, doi: 10.1088/0004-637X/750/2/120

Zanella, A., Le Floc'h, E., Harrison, C. M., et al. 2019, MNRAS, 489, 2792, doi: 10.1093/mnras/stz2099

Zee, W.-B. G., Yoon, S.-J., Moon, J.-S., et al. 2022, ApJ, 935, 48, doi: 10.3847/1538-4357/ac7462

Zel'dovich, Y. B., Kurt, V. G., & Syunyaev, R. A. 1969, Soviet Journal of Experimental and Theoretical Physics, 28, 146

Zhang, Y., Liu, R.-Y., Li, H., et al. 2021, The Astrophysical Journal, 911, 58, doi: 10.3847/1538-4357/abe9b6

Zheng, Y., Emerick, A., Putman, M. E., et al. 2020, The Astrophysical Journal, 905, 133, doi: 10.3847/1538-4357/abc875

Zheng, Y., Peek, J., Putman, M., & Werk, J. 2019a, ApJ, 871, 35

Zheng, Y., Putman, M. E., Emerick, A., et al. 2019b, Monthly Notices of the Royal Astronomical Society, 490, 467, doi: 10.1093/mnras/stz2563

Zhu, G., & Ménard, B. 2013, ApJ, 770, 130, doi: 10.1088/0004-637X/770/2/130

Zhu, G., Menard, B., Bizyaev, D., et al. 2013, MNRAS, 439, doi: 10.1093/mnras/stu186

Zhu, W., Zhang, F., & Feng, L.-L. 2022, The Astrophysical Journal, 924, 132

Zinger, E., Pillepich, A., Nelson, D., et al. 2020, Monthly Notices of the Royal Astronomical Society, 499, 768, doi: 10.1093/mnras/staa2607

Zonca, A., Singer, L., Lenz, D., et al. 2019, Journal of Open Source Software, 4, 1298, doi: 10.21105/joss.01298

Appendix A

A.1 Radial gas metallicity profiles

We obtain the radial gas metallicity profiles in spherical shells equally spaced in the logarithmic radius ($\log r$) for the HESTIA galaxies in Fig. A.1. Overall, the gas metallicities for MW and M31 look similar. The HESTIA galaxies are metal-rich in the inner disc regions (3-10 times the solar metallicity inside 10 kpc), after which the metallicity drops sharply out to the CGM regions (as low as 0.2 times solar metallicity at 500 kpc). Beyond this point, the metallicities rise again due to the presence of the pairing galaxy at those distances. As observed by Conroy et al. 2019, we also see our galaxies exhibiting a turn-over from being metal-rich (at $r < 10$ kpc) to metal-poor (at $r > 30$ kpc).

For the MW in 17-11 and M31 in 37-11 the central gas metallicities reach values as high as 10 $Z_{\odot}$. These values are clearly a factor of 2-3 higher than for M31 observations (Sanders et al., 2012), and these also exceed our expectations for MW-like galaxies (see fig. 10 in Torrey et al. 2014a for a compilation of observations of MW-mass galaxies). We, therefore, conclude that HESTIA produces a disc metallicity, which is up to a factor of 3 higher than expected from observations. There are no strong observational constraints on the MW and M31 CGM metallicity, but when comparing to observations we keep in mind the possibility that our simulations might have a CGM metallicity, which is up to a factor of 3 too high in comparison to *real galaxies*.

A.2 A listing of the most relevant parameters for the most massive galaxies in each realization

In Table A.1, A.2 and A.3 we show properties of the satellite galaxies in each of the simulations. The galaxy numbers appear in Fig. 2.1 of the main paper, and we see that all the dense H I regions are associated with one of the galaxies listed in the tables.

A.3 Column density profiles for the MW

In Fig. A.2 we show the radial column density profile of the simulated MW for the different ions. This is complementary to the M31 column density profiles in Fig. 2.4.

A.4 Convergence test

We perform a convergence test, where we compare the high-resolution HESTIA simulations, which we presented in the main paper, to intermediate-resolution simulations with an eight times lower mass of the dark matter particles. In Fig. A.3, we test whether the column density profiles of

Table A.1: A list of properties for the most massive galaxies in the 09−18 realization. Galaxy no. 0 corresponds to the M31, while galaxy no. 9 corresponds to the MW. Remaining galaxies can be correlated with their respective galaxy nos. in Fig. 2.1. Dist. (kpc) refers to the distance of the corresponding galaxy from the LG centre, in kpc.

Galaxy no.	log M_* ($M_\odot$)	log $M_{\rm dm}$ ($M_\odot$)	log $M_{\rm gas}$ ($M_\odot$)	Dist. (kpc)
0	11.113	12.275	11.195	433.19
1	9.184	10.338	9.627	494.37
2	8.755	10.164	9.385	585.21
3	8.445	10.033	9.258	622.04
4	8.807	9.614	8.902	474.55
5	8.973	9.038	8.666	420.03
6	8.665	9.540	8.636	478.16
7	7.854	9.729	8.453	328.25
8	8.189	9.098	7.599	335.97
9	10.911	12.156	11.078	433.19
10	10.390	11.111	10.207	554.78
11	9.220	10.345	9.707	658.60
12	8.896	10.254	9.596	767.30
13	9.026	9.952	9.503	415.00
14	8.640	10.133	9.419	547.98
15	8.718	9.748	9.207	525.90
16	8.012	9.907	8.967	549.84
17	7.983	9.771	9.025	152.61
18	8.638	9.469	8.839	420.42
19	6.909	9.152	8.151	572.19
20	7.010	9.237	7.800	684.53
21	7.769	9.052	7.444	508.79
22	5.203	9.241	5.246	421.25
23	8.181	9.944	9.138	387.82
24	7.261	9.910	8.785	683.50
25	7.389	9.822	8.931	641.68
26	7.497	9.556	8.419	658.64

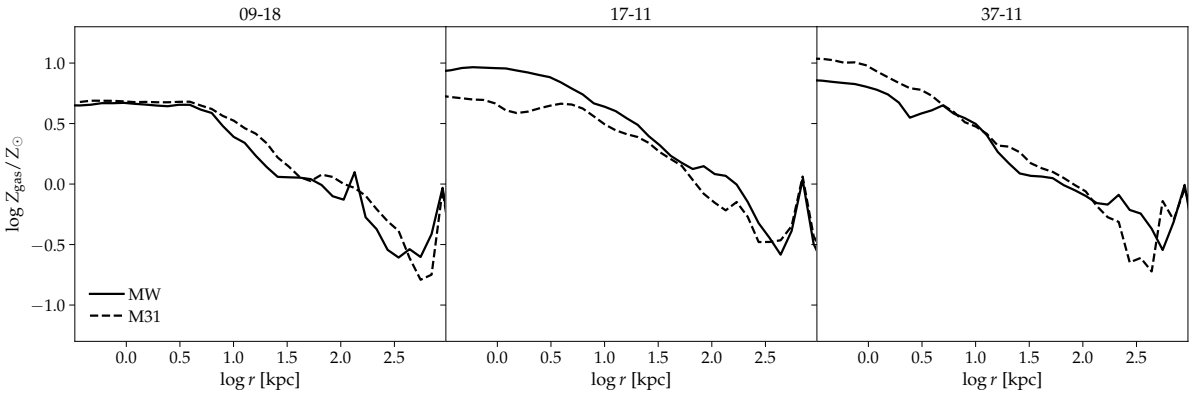

Figure A.1: Radial gas metallicity profiles for the HESTIA galaxies. The profiles show two distinct regimes– metal-rich in the inner disc regions ($r < 10$ kpc) and metal-poor in the CGM regions ($r > 30$ kpc). The rise in metallicities at $r > 500$ kpc occurs due to the presence of the pairing galaxy at these distances.

Table A.2: Same as A.1, but for the 17−11. Galaxy no. 0 corresponds to the M31, while galaxy no. 1 corresponds to the MW.

Galaxy no.	log M_* ($M_\odot$)	log M_{dm} ($M_\odot$)	log M_{gas} ($M_\odot$)	Dist. (kpc)
0	11.079	12.310	11.212	338.01
1	11.062	12.184	10.919	338.00
2	9.648	10.330	9.422	455.76
3	8.985	10.429	9.697	259.56
4	8.686	10.282	9.745	244.43
5	9.461	10.074	9.414	306.94
6	8.745	10.304	9.593	640.84
7	8.977	10.023	9.619	114.45
8	9.334	9.702	8.899	389.40
9	8.469	9.654	9.248	233.49
10	8.195	9.843	9.044	409.12
11	8.029	9.246	8.753	240.47
12	7.028	9.620	8.369	263.22
13	6.871	9.401	8.495	422.59
14	7.285	9.435	8.344	336.52
15	7.446	9.407	8.141	400.67
16	6.860	9.416	7.818	499.36
17	7.486	5.304	8.611	324.31
18	6.725	5.605	8.539	359.37
19	6.036	-	7.750	383.76
20	7.894	9.880	8.906	676.74
21	7.563	9.801	8.635	696.55
22	7.364	9.631	8.607	491.8
23	7.617	9.571	8.240	788.02
24	6.538	9.460	8.057	466.96
25	6.772	9.498	7.998	678.25
26	5.953	9.460	7.092	496.14

Table A.3: Same as A.1, but for the 37−11. Galaxy no. 0 corresponds to the M31, while galaxy no. 11 corresponds to the MW.

Galaxy no.	log M_* ($M_\odot$)	log $M_{\rm dm}$ ($M_\odot$)	log $M_{\rm gas}$ ($M_\odot$)	Dist. (kpc)
0	10.719	11.955	10.871	425.30
1	8.919	10.599	9.809	484.08
2	9.299	10.349	9.799	584.03
3	8.956	10.209	9.678	471.87
4	8.246	10.297	9.315	517.37
5	7.086	9.974	8.205	637.63
6	8.380	9.493	8.765	475.21
7	7.640	9.530	8.772	635.12
8	7.046	9.439	8.489	518.32
9	6.647	9.031	7.611	510.55
10	6.593	7.969	6.532	519.30
11	10.774	11.954	10.761	425.29
12	9.517	10.706	9.876	473.75
13	7.153	9.533	8.198	353.56
14	6.882	9.357	7.818	317.15
15	6.934	9.267	7.870	567.53
16	7.669	8.939	8.092	325.65
17	6.536	9.223	6.542	516.28
18	10.040	11.377	10.343	645.13
19	8.356	9.781	9.202	611.27
20	8.326	9.339	8.767	683.16
21	7.515	9.440	8.630	705.46
22	7.133	9.487	8.331	504.48
23	9.675	10.895	9.841	698.75
24	8.470	10.121	9.270	728.57
25	7.693	10.049	8.944	638.65
26	7.411	9.746	8.482	230.93
27	7.151	9.581	8.348	576.87
28	5.682	9.580	7.388	744.04
29	6.073	9.515	6.705	426.66
30	6.534	9.465	7.609	731.14
31	6.536	9.204	6.780	574.73

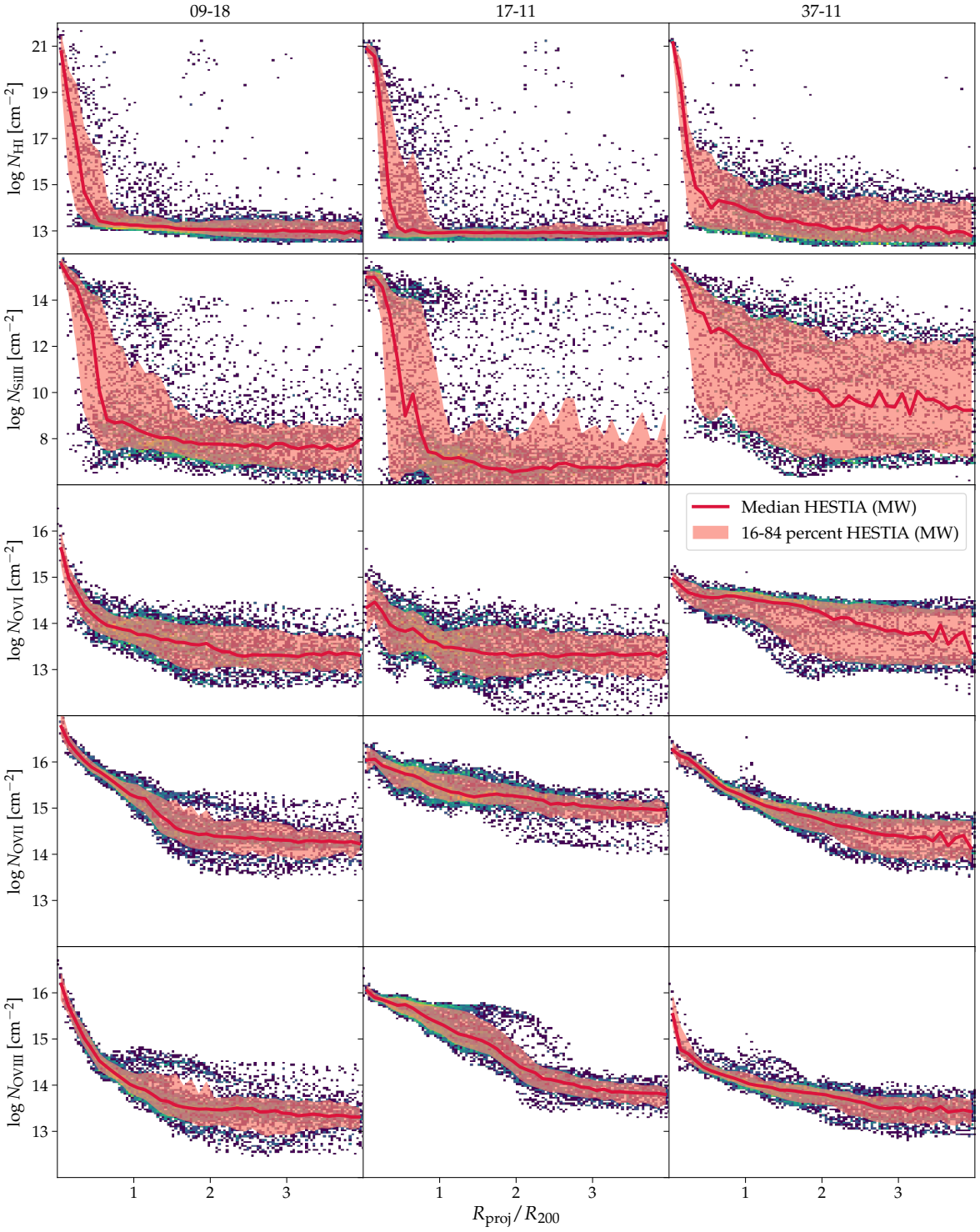

Figure A.2: Same as Fig. 2.4, but for MW. A distinct blob of H I column density absorbers, which can be seen at a distance of ~ 2.0 R_{200} in the H I profile for 09−18, can be correlated with the satellite galaxy numbered 17 in the corresponding skymap (H I skymap for 09−18 in Fig. 2.1).

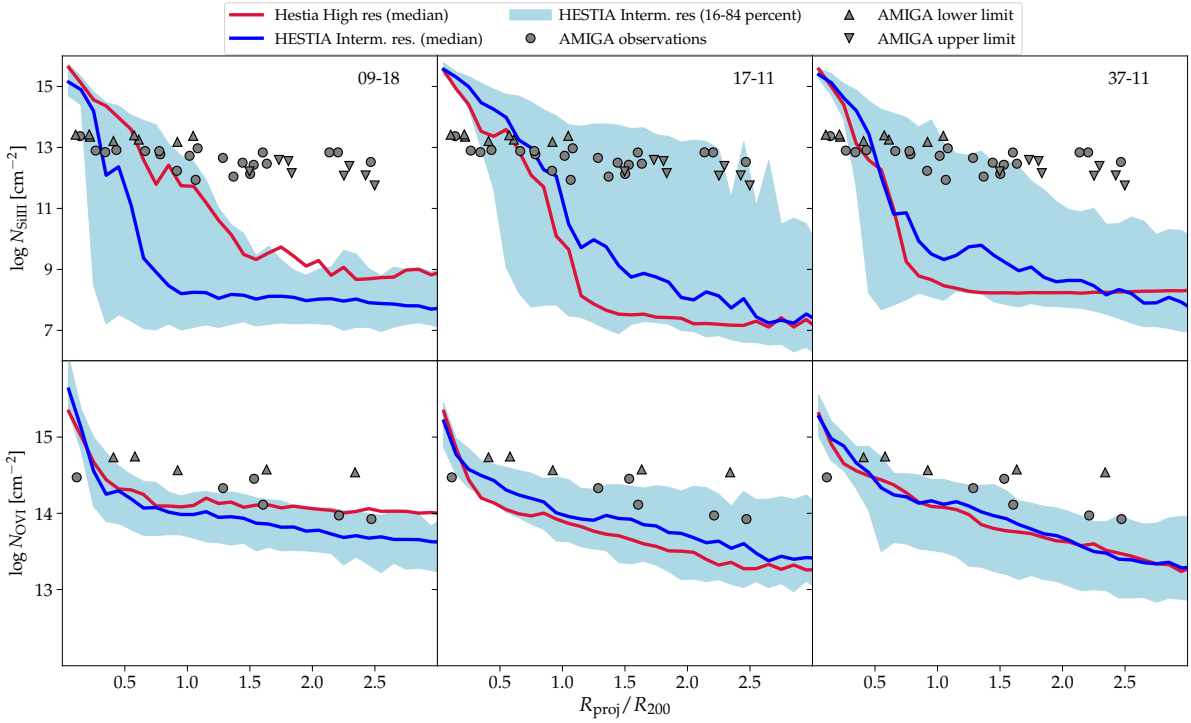

Figure A.3: We perform a convergence test of Fig. 2.5. The thick red line shows the median of the high-resolution HESTIA simulations, which was also shown in Fig. 2.5. The blue line and contour show the median and 16-84 percentiles, respectively, of intermediate resolution simulations with an eight times lower mass resolution (dark matter particles have an eight times higher mass) in comparison to the high resolution simulations. Examination of the median profiles does not indicate a lack of convergence, so our column density profiles are well converged.

Si III and O VI are converged. In simulation 09-18, the column densities at $\gtrsim R_{200}$ are higher in the intermediate resolution simulation in comparison to the high-resolution simulations. For 17-11 and 37-11, we have the opposite trend – we see the highest column densities in the high-resolution simulations. The median profiles of O VI are only slightly affected by resolution with the difference between intermediate and high resolution simulations being less than a factor of two. We conclude that, on the whole, the column density profiles are well converged.

A.5 Density profiles for different radial cuts of satellite population

In Fig. 4.4, for all our halos, we computed the spherical cold gas densities when including all available cold gas in each halo ($R_{\rm all}$) and that when excluding the cold gas lying within the radial cut, r $\gtrsim 10.0 \cdot$ R$_{0.5}$ (R_{10}). In Fig. A.4, we additionally compute and overlay the spherical cold gas densities for two other radial cuts, R_5 (r $\gtrsim 5.0 \cdot$ R$_{0.5}$; *dashed dark blue (dark red)*) and R_2 (r $\gtrsim 2.0 \cdot$ R$_{0.5}$; *dashed teal (maroon)*). The R_2 curves almost overlap with the corresponding $R_{\rm all}$ curves since the cold gas within R_2 is essentially associated with the very ISM of each satellite, rather than its extended environment. A comparison between the similarly colored dashed lines, thus, indicates how much cold gas lies in the extended regions of the satellites.

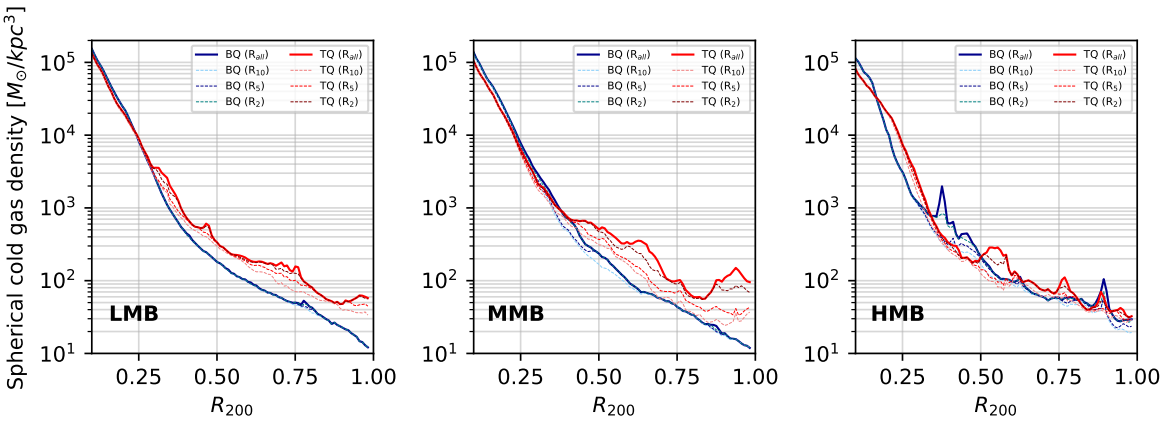

Figure A.4: Same as Fig. 4.4 but now also with two other radial cuts for the satellite populations. This time along with plotting all cold gas at r $\gtrsim 10.0 \cdot$ R$_{0.5}$ (i.e. R_{10} case; *dashed light blue (light red)*) of each satellite within a halo, we also show the mean cold gas spherical densities for R_5 (r $\gtrsim 5.0 \cdot$ R$_{0.5}$; *dashed dark blue (dark red)*) and R_2 (r $\gtrsim 2.0 \cdot$ R$_{0.5}$; *dashed teal (maroon)*). As before, the density profiles for $R_{\rm all}$ are depicted with solid lines. As expected, the R_2 curves lie closest to the respective $R_{\rm all}$ curves since we exclude only the cold gas lying within each satellite rather than its extended environment. Nonetheless, a perfect overlap between these two curves is still missing. Thus, the difference between similarly colored dashed lines is an indicator of the cold gas lying solely in the extended environments of satellites.

A.6 Total cold gas mass within satellites

We compute the total cold gas mass lying within R_{10} against the total available cold gas mass in the entire halo ($R_{\rm all}$) in Fig. A.5. It is worthy to note how the amount of median cold gas within the most massive satellites (black cross symbol) is somewhat less than that lying in the satellites in its predecessor quartile (grey cross symbol).

A.7 Median and MAD values

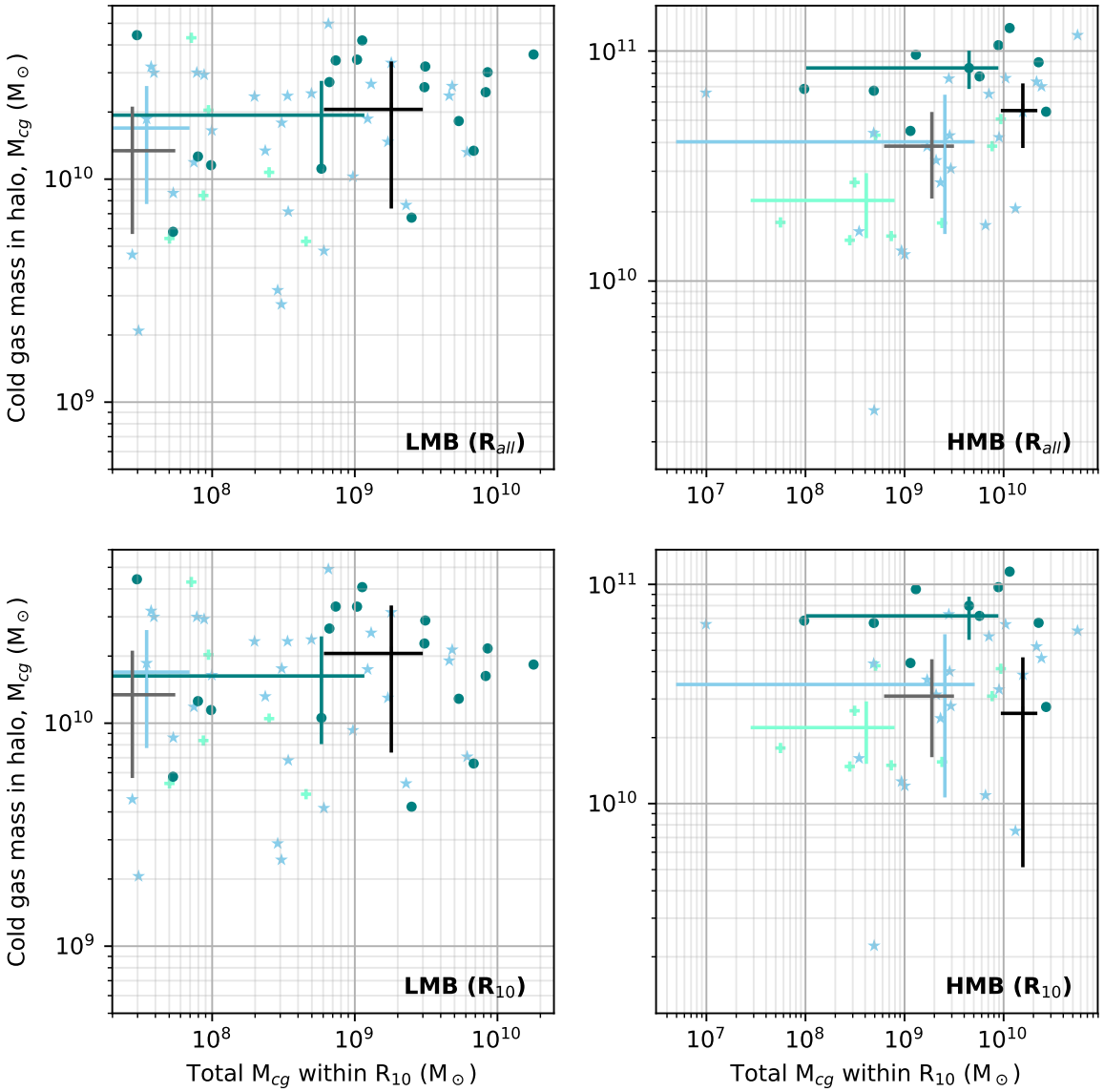

Figure A.5: Total cold gas mass, $M_{\rm cg}$, (in $M_\odot$) *within* R_{10} vs the total cold gas mass in each halo (in $M_\odot$) for $R_{\rm all}$ (*top panels*) and R_{10} (*bottom panels*) for the LMB (left panels) and HMB (right panels) halos. As in Fig.4.6, respective quartiles and 1-sigma errors are marked.

Table A.4: The inter-bin $\bar{X}$ and MAD values for the halos belonging to the bottom and top quartiles for M_h, M_{gas}, M_{bh} and SFR. Except for the SFR $\bar{X} \pm$ MAD values for MMB and HMB halos, the $\bar{X} \pm$ MAD values for respective quartiles nicely overlap with each other for every other halo attribute. Such an overlap is indicative of a similar distribution for the corresponding halo attribute within a bin.

Samples	M_h ($M_\odot$)		M_{gas} ($M_\odot$)		M_{bh} ($M_\odot$)		SFR ($M_\odot$ yr^{-1})	
	$\bar{X}_{BQ}$ (MAD$_{BQ}$)	$\bar{X}_{TQ}$ (MAD$_{TQ}$)	$\bar{X}_{BQ}$ (MAD$_{BQ}$)	$\bar{X}_{TQ}$ (MAD$_{TQ}$)	$\bar{X}_{BQ}$ (MAD$_{BQ}$)	$\bar{X}_{TQ}$ (MAD$_{TQ}$)	$\bar{X}_{BQ}$ (MAD$_{BQ}$)	$\bar{X}_{TQ}$ (MAD$_{TQ}$)
LMB	**3.98e+11 (5.88e+10)**	**4.88e+11 (4.06e+10)**	**3.50e+10 (7.03e+09)**	**5.71e+10 (1.15e+10)**	**4.46e+07 (1.47e+07)**	**4.47e+07 (2.07e+07)**	**1.797 (0.626)**	**2.970 (0.624)**
MMB	**5.46e+11 (4.58e+10)**	**9.02e+11 (1.93e+11)**	**4.62e+10 (1.08e+10)**	**7.39e+10 (1.71e+10)**	**6.36e+07 (2.47e+07)**	**8.57e+07 (3.65e+07)**	2.315 (0.604)	2.775 (0.925)
HMB	**1.19e+12 (6.57e+10)**	**2.11e+12 (4.26e+11)**	**6.35e+10 (1.22e+10)**	**1.15e+11 (4.88e+10)**	**1.45e+08 (1.86e+07)**	**2.29e+08 (5.22e+07)**	2.148 (0.783)	1.771 (0.523)